Dissertation
submitted to the
Combined Faculties for the Natural Sciences and for Mathematics
of the Ruperto-Carola University of Heidelberg, Germany
for the degree of
Doctor of Natural Sciences

Put forward by
Pablo, Botas Sanmartín
Born in: A Coruña, Spain
Oral examination: January 9th, 2019

Adaptive proton radiation therapy via fast Monte Carlo dose calculation to correct for inter- and intra-fraction motion and geometry changes

Referees: Prof. Dr. Joao Seco

Prof. Dr. Oliver Jäkel

Abstract

Intensity modulated proton therapy (IMPT) plans precisely balance thousands of proton beamlets, giving high dose to the tumor while trying to spare healthy tissues. However, plan quality is affected by factors including: 1) dose calculation inaccuracies, 2) underestimation of the biological effect of the dose in sensitive areas and geometrical changes like 3) patient movement or 4) changes in posture and anatomy. All these factors are addressed in the projects here presented.

Project 1, in collaboration, introduces an upgraded version of a Monte Carlo package for graphics processing units (GPU-MC) to provide fast and accurate dose calculations. This package is extended to serve as the unique dose calculation engine in the following projects.

Project 2, in collaboration, presents a prioritized optimization method to reduce the potential biological effect of the radiation in organs at risk near the tumor.

Project 3 compares computationally efficient strategies to take into account the patient respiratory motion by defining planning target volumes based on a 4DCT of the patient. Density overwrites considering water-equivalent-path-length to voxels across the 4DCT targets works best.

Project 4 demonstrates an online algorithm that maintains IMPT plan quality through treatment, adapting it to the daily patient posture and anatomy using GPU-MC calculations.

Kurzfassung

In der Bestrahlungsplanung für intensitätsmodulierten Protonentherapie (IMPT) werden tausende von Protonenbündeln präzise addiert mit dem Ziel einer hohen Tumordosis bei gleichzeitigem schonen von gesundem Gewebe. Die Qualität des Bestrahlungsplans wird jedoch durch folgende Faktoren beeinflusst: 1) Dosisberechnungsungenauigkeiten, 2) Unterschätzung der biologischen Wirkung der Dosis in sensiblen Bereichen und geometrische Veränderungen hervorgerufen durch 3) Bewegung des Patienten oder 4) Veränderungen in Haltung und Anatomie. All diese Faktoren werden in den hier vorgestellten Projekten behandelt.

Projekt 1 (in Zusammenarbeit) führt eine verbesserte Version eines Monte-Carlo Programs für Grafikprozessoren (GPU-MC) ein, um schnelle und genaue Dosisberechnungen zu ermöglichen. Dieses Program wurde erweitert, um in den folgenden Projekten als bevorzugte Dosisberechnungsmethode zu dienen.

Projekt 2 (in Zusammenarbeit) präsentiert eine priorisierte Optimierungsmethode, um die potentielle biologische Wirkung der Strahlung in gefährdeten Organen in der Nähe des Tumors zu reduzieren.

Projekt 3 vergleicht recheneffiziente Strategien, um die Atembewegung des Patienten zu berücksichtigen basierend auf Planungszielvolumina definiert mit Hilfe von 4DCT des Patienten. Dichteüberschreibungen unter Berücksichtigung der Wasseräquivalenz-Pfadlänge zu Voxeln über die 4DCT-Ziele sind hier am genauesten.

Projekt 4 demonstriert einen Online-Algorithmus, der die Qualität des IMPT-Plans während der fraktioniertene Behandlung garantiert und sie mit Hilfe von GPU-MC- Berechnungen an die tägliche Haltung und Anatomie des Patienten anpasst.

Acknowledgements

First and foremost I would like to acknowledge Prof. Paganetti for supporting me during the thesis. Harald allowed me to participate and learn from great projects during what came to be my most inspiring and interesting years to date. Being part of such a nice research group has been a unique experience that I wish everyone could have. It's amazing all the projects he's lead over the many, many, many years (not calling him old here) and how he manages them on the personal and professional levels.

I don't want to forget colleagues like Aimee, Jungwook, Maria, the Jans and the Davids (too bad you have such common names ☺), Drosoula, Maryam, Joost, Nadya, Abdel, Ali, Wonmo, Tom, Brian, Greg and many others. My supervisors at Heidelberg also helped me a lot along this way. Fernando was a major addition to our little community, too bad he didn't cook more *paellas*, that's something I won't forgive. I guess he was busy cleaning the 5000 kilos of rock from his backyard. I want to specially thank Clemens for all the great times in the lab and outside of it. Since I came into the group he took me under his wing and was always there to answer every question I could possibly have... and lately ask some himself.

All my friends during these years have been great, I'm not giving many names so nobody feels bad. Also, I doubt anyone will ever read these lines ☺. Still, some have to be mentioned: *quieres-ser-mi-amigo* Victor *este-chile-está-dulce* and the `Food for All®` guys, Joan *the let's-go-to-a-bar-scientist*, *sleepless-life-beast*-Nadine, Andres *Ay,-lo-amo-voy-a-estudiar*, Meli *for-president* and *come-back-to-this-reality* Gabi were just stupid enough to end up hanging out with Lili and I. I hope we can meet soon!!

A mis padres Lola y Calilo, que son simplemente unos cracks a los que nunca les agradeceré nada lo suficiente. A mis súper-hermanas y -hermano Carla, Sara y Martín, que siempre te hacen tener los pies en el suelo aprovechando de cada oportunidad para reírse un poquito. Son los mejores. Sus parejas no están nada mal tampoco.

Finalmente a Lili. Muchas gracias por todo el apoyo y amor durante todo este tiempo de principio a fin. Sin ti no hubiera llegado hasta aquí. Te aseguras de que nadie a tu alrededor se olvide de lo preciosa que la vida puede ser. El 25 de Agosto trajiste a una pequeña de ojos profundos ávidos de sonrisas que nos está robando el corazon día a día. Así que, especialemte, quiero dedicar a mis estrellas fugaces amarillas todo el esfuerzo y el trabajo que espero demostrar en este escrito. Y a l@s que vengan.

Thanks a lot to everyone!

Pablo

A mis estrellas fugaces amarillas habidas y por haber

Table of contents

List of tables

List of figures

List of symbols

β	Fraction of speed of light: v/c
χ_c	Characteristic single scattering angle in Molière's theory
γ	Lorentz factor: $\left(1-\beta^2\right)^{-1/2}$
$\hbar$	Reduced Planck's constant (6.58×10^{-16} eV s)
ρ	Material mass density
A	Mass number
c	Speed of light
D	Dose-influence matrix used for optimization
e	Electron charge: 1.6022×10^{-19} C
I	Mean excitation energy of a material
L_R	Radiation length
LET_D	Dose-averaged LET
m_e	Electron mass: 511 keV
n_e	Electron density
p	Momentum
S	Total stopping power
S_{col}/S_{el}	Collision/electronic stopping power
S_{rad}	Radiative stopping power
Z	Atomic number
z	Projectile charge in units of e
4DCT	4-dimensional CT
ADC	Analytical dose calculation
AIP	Average image projection
C100	Constant intensity IGTV filling with 100 HU
C50	Constant intensity IGTV filling with 50 HU
CDF	Cumulative density function
CHII	Condense history method class II
CT	Computed tomography
CTV	Clinical target volume
DIR	Deformable image registration
DS	Double scattering

gEUD	Generalized equivalent uniform dose
GPU	Graphics processing unit
GTV	Gross tumor volume
Gy	Gray, unit of dose: 1 Gy = 1 J/kg
ICTV	Internal clinical target volume
IGTV	Internal gross tumor volume
IMPT	Intensity modulated proton therapy
IMRT	Intensity modulated radiation therapy
ITV	Internal tumor volume
LBTE	Linear Boltzmann transport equation
LET	Linear energy transfer
MC	Monte Carlo
MCS	Multiple Coulomb scattering
MFO	Multi-field optimization
MIP	Maximum image projection
MLD	Mean lung dose
MSE	Mean squared error
NSCLC	Non-small-cell lung cancer
OAR	Organ at risk
PBS	Pencil beam scanning
PDF	Probability density function
PET	Positron emission tomography
PS	Passive scattering proton delivery technique
PTCOG	Particle Therapy Co-Operative Group
PTV	Planning target volume
RBE	Relative biological effect
SFO	Single field optimization
SFUD	Single field uniform dose
SOBP	Spread-out Bragg peak
vCT	Virtual CT
VRT	Variance reduction technique
WED	Water equivalent distance
WEPL	Water equivalent path length

Chapter 1

Introduction

Proton therapy is a type of radiation therapy that leverages the nature of proton interactions with matter to irradiate tumors, while trying to spare the healthy tissues as much as possible. As such, the behavior of the radiation field and therefore its therapeutic effectiveness ultimately shares its dependencies with the basic physics laws that governs the interactions of protons with matter.

It would be ideal to be able to perfectly predict what radiation field a patient will receive during treatment and what the particular effect the field will have. However, errors and uncertainties arise from several sources and steps, some of which are:

1. Calculation of a proton field in a known, static geometry, like a patient.
2. Nonexistence of a static 3D geometry to irradiate, due to patient movements like respiration.
3. Variation of the static 3D geometry to irradiate after its initial determination, due to patient positioning and/or anatomy evolution.
4. Lack of understanding of the biological effect of the energy deposited in the patient.

The potential effects these uncertainty sources produce should be minimize, to improve proton treatments quality. Hence, this thesis leverages the understanding of particle interactions with matter to propose solutions to specific aspects of the previous four items.

In order to motivate the goals of this thesis and to present the core concepts in proton therapy, this chapter gives an introduction to proton therapy, explaining its rationale, the current practice workflow and how it is delivered to the patient. Then, the previous points are explained and, finally, the thesis structure and goals are defined. The basics of the interactions of protons with matter are given separately in chapter 2 due to its extension and will be

often referred from this introduction. If the reader is not familiar with the physics basics or quantities of interest in proton therapy, it is recommended to acquire the basic notions by referring to the aforementioned chapter.

Finally, in occasions throughout this thesis many publications could be cited that support a certain claim, however only a few references may be given for clarity and to avoid too long citation list that would otherwise affect the document readibility. It is not the intention of the author to remove any recognition from the uncited publications.

1.1 Proton therapy background

1.1.1 Rationale and history

Proton therapy is a type of external radiation therapy for cancer treatment. The radiation field aims to give a homogeneous dose (energy per unit mass) to the tumor, while trying to spare healthy tissues. As opposed to the more common radiation therapy that employs X-ray beams, proton therapy delivers the therapeutic radiation field by way of proton beams. There are geometric advantages in the achievable dose distribution employing this type of radiation due to the manner protons interact with the human body. Protons, and other ions, deposit most of their energy in the medium at the end of their range, forming the so-called *Bragg peak*, shown in figure 1.1, and allowing the deposition of high dose levels at the tumor position. The proton dose stops at a certain point and downstream tissues are not irradiated. For an in-depth explanation of why this happens, refer to chapter 2.

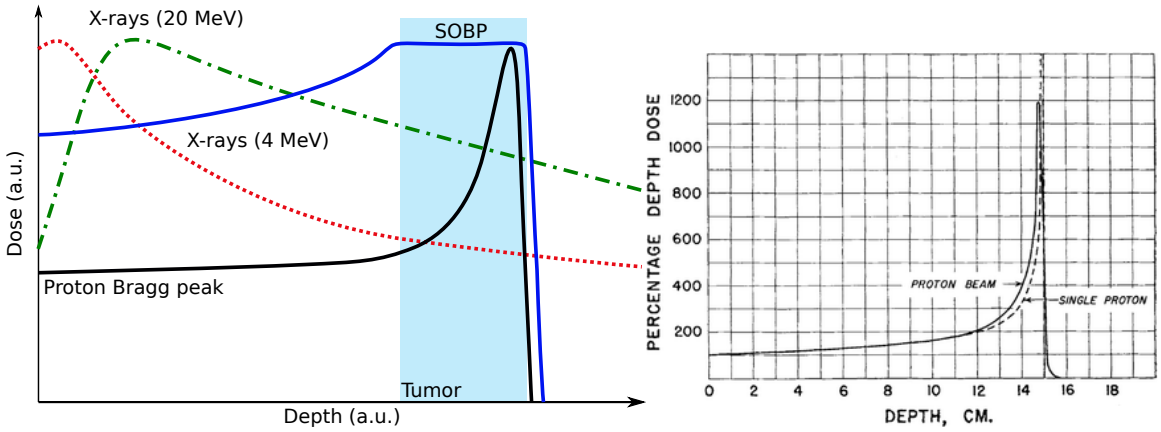

(a) (b)

Fig. 1.1 Proton pencil beam dose deposition as a function of depth. a) compared with X-rays. b) original figure by R. Wilson in his 1946 publication [Wil46].

The comparisons in figure 1.1a show that protons can be used to deliver a bigger fraction of the total dose to the tumor than X-rays, better sparing the healthy tissue from being damaged. This was the observation initially published by Robert Wilson in 1946 [Wil46], where he suggested the usage of collimated proton beams to treat deep-seated tumors. This publication, illustrated with image 1.1b extracted from it, effectively started the proton therapy field, even suggesting to modulate the penetration of a continuously delivered proton beam by a rotating wheel to create the *spread-out Bragg peak* (SOBP). The SOBP, shown in figure 1.1a, is the result of summing the dose contributed by many single beamlets to create homogeneous dose fields.

The first proton therapy patients were treated at Berkeley in 1954 and by the end of 2016, a total of ~150000 patients had received proton therapy. In the last decades, the number of patients have increased exponentially and so has the number of active proton centers: 80 active, 46 under construction and 25 in planning stage (patient data from December of 2016 and center totals as of this date, both according to the Particle Therapy Co-Operative Group, PTCOG, website: https://www.ptcog.ch).

Despite the dose-depth profiles shown in figure 1.1 display a distribution favourable to the proton modality as compared to the X-rays', it is not to be concluded that protons will always perform significantly better than X-rays in the treatment of cancer. In fact, the selection of cases that would benefit the most from such technique is an active area of research (see [PK10] for example). There are many aspects that may make a modality more favourable than the other, being the economic and the availability of appropriate treatment centers two of the most simple, yet important, factors. It is widely accepted, however, that most ocular and pediatric tumors and tumors with the target very close to sensitive organs should in principle benefit from proton therapy [PK10]. Moreover, the ceiling of the quality achievable by a proton therapy plan depends on many aspects, some of which are specific to the way the radiation field is delivered to the patient.

1.1.2 Workflow

It is important in order to follow this thesis to understand what workflow is implemented in proton therapy since the patient receives a diagnostic until the treatment finalizes. Generally, all proton plans follow these steps:

1. Diagnosis and prescription: A physician closely studies a patient scan and produces a diagnosis with a prescription of dose to the tumor and dose limits to the healthy organs.

   Along with the total dose prescribed to the tumor, the delivery schedule is also specified. Plans are generally delivered daily for several weeks. Each daily session is called a

fraction and the selection of total fractions and how often they are delivered is referred to as fractionation scheme. Section 1.1.4 explains fractionation and its impact on the uncertainties studied in this thesis. An example of prescribed dose to the target is 60 Gray (Gy) in 30 daily fractions.

2. Planning computed tomography (CT) scan: A CT scan is taken if not yet available to have an image of the patient that can be related to material information and proton stopping power. In preparation for this scan, the patient is immobilized in a specific setup that must be reproduced for each fraction. The CT scan consists of a 3D cube divided in a number of voxels of a given size, for example $512 \times 512 \times 250$ $0.5 \times 0.5 \times 2.5$ mm^3. Each voxel contains a value in Hounsfield units, which is a scale representing the total attenuation coefficient of the X-rays generated in the CT at each patient position. From this scale, it is possible to infer the material composition of the patient and the other physical quantities required to calculate the proton treatment.

3. Definition of patient structures in the CT: Information from all available scans are used in order to define a set of contoured regions in the CT image that enclose the different patient structures. Common delineated structures are the patient him-/herself, important organs at risk (OARs), tumor/s, areas the radiation fields should not traverse, etc. This is a laborious process that can take several hours. It is common to refer to the resultant defined regions as *structures* or *contours* and both terms are employed in this thesis.

4. Field definitions: The direction of the proton fields and the target they aim for are defined. They are chosen trying to avoid OARs or areas that can cause uncertainty in the final dose distribution. Usually 3-4 fields are used with initial proton energies in the range of 50-300 MeV.

5. Plan optimization: The contribution of all individual fields is carefully optimized to deliver the prescription dose to the target while minimizing the dose to the OARs (following clinical criteria). The optimization process depends on the delivery technique. If the optimized fluence from each field does not produce a satisfactory dose distribution, the process may be sent back to item 3 or 4.

6. Patient setup: Before each fraction is delivered, the patient is carefully setup in the same position recorded in the CT. If this is achieved, the planned dose distribution can be reproduced at the fraction.

7. Fraction delivering: The fraction is delivered to the patient. The patient should maintain the position during the fraction delivery.

At any point during treatment, the original plan can be re-evaluated.

1.1.3 Delivery techniques

The potential benefit of a proton therapy treatment is dependent on what treatment delivery technique is used. Proton therapy treatments are mainly delivered with two techniques: *passive scattering* (PS) and *pencil beam scanning* (PBS).

1.1.3.1 Passive scattering

In passive scattering the desired dose distribution is delivered to the target using one or several continuous radiation fields, each generally covering the whole tumor. Depending on the number of scattering foils used, passive scattering is divided into single and double scattering (DS). Double scattering is more widely used because of the limited dose homogeneity that single scattering can provide, however, single scattering can be employed for very small targets, such as choroidal melanoma [Kim+18]. The following explanation corresponds to double scattering, the working principles of single sattering can be derived from it.

A schematic representation of the beamline is shown in figure 1.2, with the beam in blue going from left to right as it leaves the particle accelerator and traverses each of the main components until it reaches the target. This representation is a simple example that aims to explain the underlying ideas of each component, the real design of the beamline is much more complex.

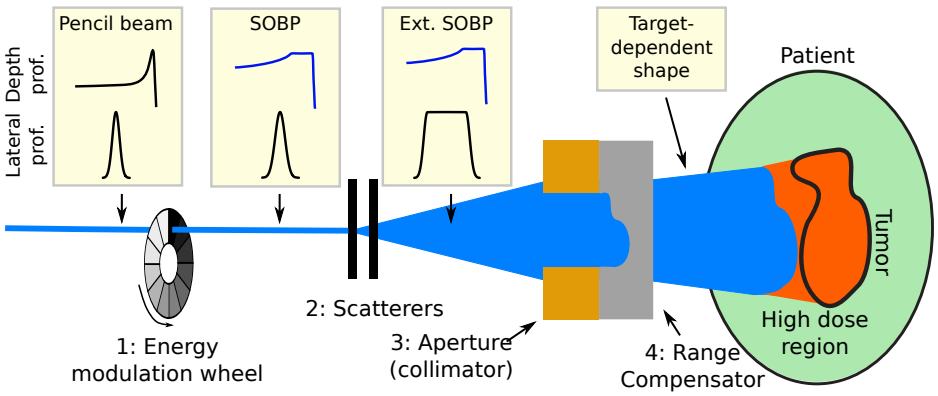

Fig. 1.2 Double scattering beamline schematic representation. A pencil beam is shaped to provide tumor coverage, but the SOBP modulation (SOBP width) causes high dose to be deposited on the healthy tissue located close to the proximal end of the target.

A nearly monoenergetic pencil beam undergoes the following transformations (numbering respected in the figure):

1. A modulator wheel is employed to create a SOBP (as suggested by R. Wilson [Wil46]). The wheel spins, making the initial pencil beam traverse different material thicknesses, losing different amounts of energy depending on the wheel position. The size of the resultant SOBP is called *modulation* and is generally fixed across the field (orange area in figure 1.2). Of course, designs other than a wheel are possible, but they all share the same working principle.

2. A double scattering system widens the mixed energy beam creating a beam with homogeneous fluence on a wide cross section. The first of the scatterers increases the beam emittance due to the multiple Coulomb scattering in the material (a process explained in section 2). Because the result is a nearly-Gaussian profile, a second scatterer is employed to flatten the distribution. The design and composition of this second scatterer was an active topic of research with different models proposed, but the underlying idea that was found to work best was to act differently at different radial positions of the field, scattering more the central part (refer to [Tak94; Tak02; KSS77; Gru+94] for further details).

3. An aperture fabricated from a high absorbent material adjusts the proton field to the beam's-eye-view tumor contour per field.

4. A range compensator takes the tumor's distal shape into account by absorbing more or less energy depending on the position within the field.

The main limitation of this delivery modality is the fixed modulation across the radiation field. The components described above do not conform the field to the proximal end of the target due to the fixed modulation. To alleviate this, complex patching techniques can be used to increase the conformity of the dose to the required desired distribution by blocking certain regions for specific fields. This limitations is naturally solved using PBS, increasing the conformity of the dose to the target. This is the reason why PBS is slowly being replacing DS in many applications.

1.1.3.2 Pencil Beam Scanning

In PBS, the desired dose distribution is delivered by hundreds or thousands of individual quasi-monoenergetic pencil beams that are deflected by magnets to deposit their energy along a desired path. The beamlets are organized in fields, impinging on the target from

different angles. The total dose is generated by summing the dose given by each individual pencil beam. The beamlers are delivered in a sequential manner and it takes time to adjust the machine parameters preparing for the next beamlet, creating a delivery time structure. Because changing the energy between beamlets is the most time consuming operation, each treatment field is usually organized in energy layers.

The treatment modality used with this delivery is termed *intensity modulated proton therapy* (IMPT), in a parallelism to its X-ray counter part: intensity modulated radiation therapy (IMRT). It should be noted that in IMPT, not only the beamlets intensity is modulated, but also the energy, making the term slightly misleading.

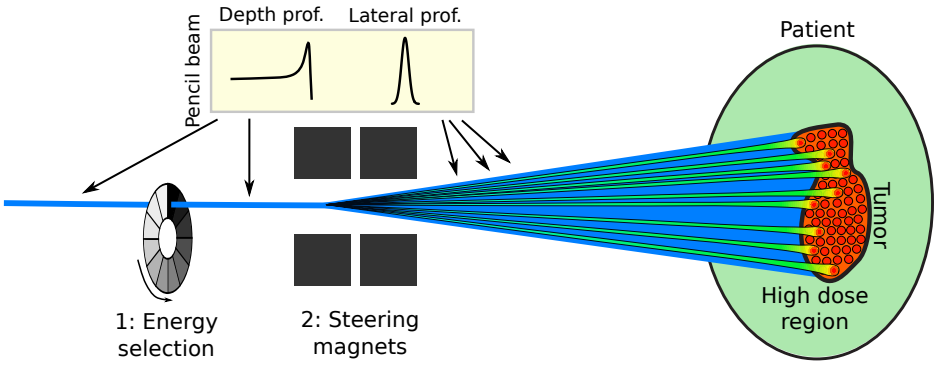

Fig. 1.3 Pencil beam scanning beamline schematic representation. Many pencil beams are produced one after the other and deflected by the magnets to reach the desired destination in the tumor.

The number of protons per beamlet in IMPT plans is optimized to provide the desired dose to the target while maintaining the dose to the healthy tissue as low as possible. This optimization procedure allows high conformity of the dose to the desired distribution and a brief introduction to it is given in section 3.2. The result of the optimization procedure is usually that each field utilized during the treatment gives a inhomogeneous dose to the tumor, but the dose from all fields creates a homogeneous dose in it, just like the plan shown in figure 1.4.

Because the dose per field is inhomogeneous, there is no fixed modulation as in DS, improving dose conformity to the target. This is possible when multi-field optimization (MFO) is used. Nevertheless, if homogeneous doses per field are desirable in a particular situation, single field optimization (SFO) can be employed to create single field uniform dose (SFUD) plans.

While the increased dose conformity is a positive trait, IMPT plans are very sensitive to geometry changes. As it will be explained in chapter 2, the shape and penetration depth of each beamlet highly depends on the tissues traversed. Due to the high degree of dependency

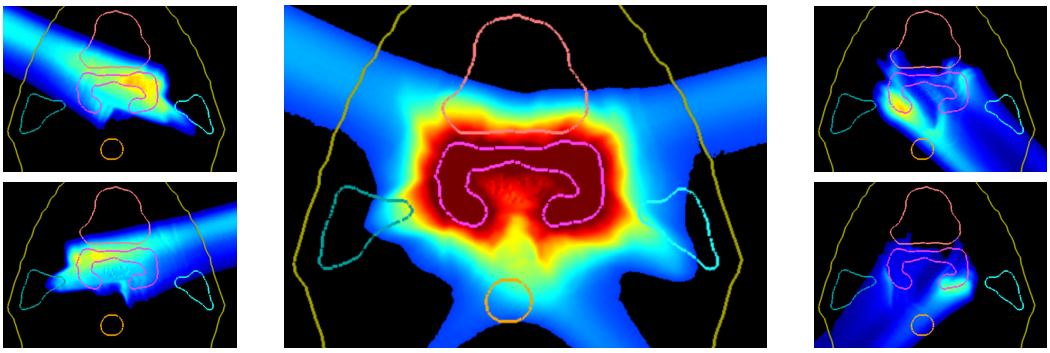

Fig. 1.4 Example of a homogeneous IMPT dose distribution (center) delivered by 4 inhomogeneous dose distributions (left and right).

of the total dose on the dose of each beamlet, changes in the tissues traversed by each beamlet impact the total dose. Therefore, geometrical changes like a setup error causing patient mispositioning, breathing motion or anatomical changes through the course of treatment impact the plan quality. Additionally, the high dose inhomogeneity given by each field may have radiobiological implications, potentially increasing the impact of the dose in healthy tissues. Section 1.2 analyzes these aspects.

1.1.4 Treatment fractionation

Before entering the treatment uncertainties section, it is important to discuss the time scales present in proton therapy. Proton therapy is usually given in a fractionated schedule. For example, a 60 Gy plan may be delivered in a 2 Gy per week-day schedule until the total dose is given to the tumor. In each fraction the same dose distribution is usually delivered, unless otherwise decided. Depending on the complexity of the plan, fractions for a given case might take longer than for others, but 30 min can be given as representative figure, mostly due to preparation and positioning of the patient on the treatment couch. However, the irradiation time is just a few minutes, around 5 min for the purpose of the discussion here. Splitting the radiation treatment into fractions is not an arbitrary decision or motivated by scheduling or management of the treatments of many patients. After all, most time is dedicated to preparation. The reason behind fractionation is to improve the treatment quality by better sparing the healthy tissues.

The traditional fractionation wisdom relies on what is known as the 4 Rs of radiobiology: repair, reassortment, repopulation and reoxygenation. The detailed analysis of each of these is beyond the scope of this thesis, but it is still important to note them because they are the ultimate reason radiation therapy works. After giving a fraction, normal cells repair sublethal DNA damage better than tumor cells due to their better repairing mechanisms, survivor

tumor cells may cycle into more sensitive phases of the cell cycle and become more sensitive in the next fraction (reassortment), healthy tissues recover through cell repopulation and, finally, the tumor radiation sensitivity may be increased by reoxygenation. These improves the therapeutic impact of radiation as opposed to give all the dose in a single delivery, which could seriously damage healthy tissues.

The fractionated schedule is taken as reference to define the time frame some particular effects and uncertainties act on. Notably for this thesis, on the one hand, intrafractional geometrical changes refer to patient movements while the fraction is being delivered. By far, the most important of which is the respiratory motion, although bowel movements may also have some limited impact. On the other hand, interfractional geometrical changes refer to the patient being positioned at each fraction slightly different from the reference planning position, in what is called a setup error. Another source of uncertainty in the interfractional scale is the anatomy of the patient changing throughout treatment via weight loss or tumor shrinkage, for example. Importantly, some of the random fluctuations caused by these uncertainties on both intra- and interfraction scales, might average out to some degree as more and more fractions are delivered to the patient. Therefore, fractionation can also be seen as a forgiving situation for uncertainties causing random errors. However, the traditional fractionated delivery has been challenged in recent years, proposing to deliver the treatment in a hypofractionated schedule giving more dose per fraction and less total fractions obtaining an improve therapeutic ratio [Lai+16].

The main driver behind hypofrationation is that the increased dose conformity to the tumor of modern radiation techniques spares better the healthy tissues [Lai+16]. Hypofractionation has been mainly studied for X-rays in breast [Smi+11; Kar+14; RSK15], prostate [DP99; RSK15; BTD17] and brain metastases [Ino+14]. However, proton treatments are also expected to benefit from it and have already been investigated in lung (non-small cell lung cancer) [Nih+06; Hat+07; Bus+13], liver [Chi+05; Fuk+09; Bus+11; Kom+11] and prostate [Shi+95; Sla+04; Zie+10]. See [Lai+16] for a review on hypofractionation results with X-rays, protons and carbon ions, including a brief radiobiological discussion.

Under the scope of this thesis, it is important to discuss the consequences of hypo- and hyperfractionation on the studied uncertainties. In hypofractionated treatments, random fluctuations may not even out as each fraction has a bigger importance, making the plan more sensitive to random errors such as patient mispositioning on the treatment couch. The specific relation between the fractionation and treatment uncertainties is discussed at each uncertainty section below.

1.2 Treatment uncertainties under the scope of this thesis

The following subsections explain the uncertainties tackled in this thesis, along with the strategy employed to analyze and reduce them. One uncertainty is approached per project. The sections respect the same order as the publications included in chapters 4–7.

1.2.1 Dose calculation uncertainty

The presence of uncertainties in dose calculation limits the achievable quality of IMPT plans [Pag12]. In order to generate IMPT plans, the dose in each point of a patient has to be calculated for each individual beamlet. To calculate the 3D dose distribution in a patient, one should solve the linear Boltzmann transport equation (LBTE) describing how protons traverse a medium, however this is a very complicated task in a geometry such as a human being. In the clinical practice, the so-called *analytical dose calculation* (ADC) algorithms are usually employed. These algorithms are a way of approximating the LBTE and they have been shown to present inaccuracies in areas of high tissue heterogeneity, like lung or head and neck [Saw+08; Pag12; Gra+14; Sch+15; Yep+18] (among other authors), usually due to the miscalculation of the scattering component of the equation [Saw+08]. On the contrary to ADC, Monte Carlo (MC) particle transport simulations converge to the exact solution of the LBTE and are considered the gold standard for dose calculations.

Monte Carlo simulations allow the statistical estimation of macroscopic quantities, such as deposited energy inside a region in a patient, arising from the step-by-step evaluation of the interaction probabilities of particles with their microscopic environment and the sampling of the products of these interactions. MC simulations of proton plans consist of the transport of millions of primary protons and the secondaries they create until all particles have lost all their initial kinetic energy through interactions or have left the region of interest and therefore cannot affect the patient anymore and are discarded. Of course, there are uncertainties present in MC simulations, specifically, in the interaction cross-sections and models, which might not be well understood. However, within the scope of proton therapy dose calculations in patients, MC presents high accuracy [Pag12], comparable to the experimental measurements used to verify the treatment plans [Tes+13]. Section 3.1 includes a brief introduction of how the simulations in gPMC work, which illustrates the functioning of most MC codes.

Dose calculation uncertainties have a high impact in treatment quality due to the ballistic properties of protons and their influence on the range determination. Range uncertainties, some of which are produced by the dose calculation, can be handled either by extending the region considered as target adding safety margins or by considering several error scenarios and performing robust treatment optimization on them. Without getting into details in either

option, both of them have the common consequence of increasing the area irradiated with high dose, giving higher doses to healthy tissue [Wat+16]. Reducing the dose calculation uncertainty by employing MC simulations would have a positive impact, shrinking the region receiving high dose levels [Pag12].

Despite the high potential of MC simulations to reduce this uncertainty, their clinical usage is not widespread due to their low computation efficiency. As briefly explained before, MC simulations explicitly consider all the interactions suffered by every particle, which produces calculation times too long to be used in the clinical routine. Therefore, MC simulations have historically been relegated to a second-opinion tool to evaluate already-created treatment plans with high risk or when the ADC result was not trusted. However, modern implementations of MC engines on highly parallelizable devices such as graphics processing units (GPU) have drastically improved the efficiency of the simulations, making them viable for calculations within the clinical context [Jia+12; Ma+14; TMB15; Wan+16].

The GPU-MC package gPMC was previously developed in collaboration with UT Southwestern [Jia+12]. However, the validation of the code in patient cases against TOPAS showed errors attributable to the different handling of nuclear interactions in gPMC and TOPAS [Gia+15]. TOPAS [Per+12], TOol for PArticle Simulation, is a sophisticated wrapper around Geant4 [Ago+03] that allows easy and reliable simulations with greatly reduced development time and has been extensively benchmarked against experimental data [Tes+13].

Project 1 was dedicated to improve gPMC, making possible its reliable use by improving the nuclear interaction models. Also, to facilitate its usage in a wide variety of GPU and CPU devices, translation from the original CUDA language [Nic+08] to OpenCL [SGS10] was intended. Additionally, the improvements may bring the usage of MC simulations in routine calculations in the clinic one step closer. Finally, its capabilities were extended to tally fluence and LET to allow other studies, like the one introduced in the following section.

1.2.2 Radiobiological effect uncertainty

When protons traverse matter, they lose energy to the medium as they slow down. This energy is transferred by ionizing the medium's atoms or by reactions with the nuclei. Either way, subproducts like electrons, secondary protons and others travel some distance while reacting, further dispersing the initial energy in a chain reaction. When occurring in a biological system, all this reaction may destroy molecules or distort their structure, changes that may end up being fatal.

The particular radiobiological effect a radiation field will have in a tissue is very hard to predict. It depends, for example, on the radiation sensitivity of the tissue and the density and type of secondary particles liberated in the medium. Additionally, the radiation sensitivity of

a given tissue is patient-dependent and currently can only be taken into account by observing the effect of the treatment as it progresses. However, the energy captured by a region per unit length, or linear energy transfer (LET), has been found to be a good surrogate of the amount of entities capable of causing damage in the tissue. Therefore, the LET of a radiation field should be somehow proportional to its radiobiological effect. The LET is a property of each particle, but in this case it is intended as a well-defined property at each patient position crossed by many particles. Reality is that when LET is referred to a patient location, it is usually assumed that the LET values presented by all the particles in that location are somehow averaged, in the case of this project, the dose-averaged LET is employed (see section 2.4.3 for a formal definition). The exact radiobiological effect of protons is described by the radiobiological relative effectiveness (RBE), see section 2.4.4 for a more in depth explanation and references.

The LET is a purely physical quantity and calculations with MC simulations have shown that it increases towards the end of range of a beamlet and away from the central axis, just like the average proton energy decreases. Due to the fact that IMPT plans are formed by many individual beamlets coming from several directions, they tend to present highly inhomogeneous LET distributions [GP11; Gia+13]. Despite having a more favourable physical dose distribution over DS plans [Gia+18], areas of high LET placed near the edge of the target or at organs at risk can have an increased radiobiological effect which would impact the treatment quality. Despite the exact consequences of the increased radiobiological effect are no predictable, it would be advisable to avoid any potential complication arising from it. The high number of degrees of freedom of IMPT plans should allow the goal of preventing these elevated LET areas in organs at risk (OARs) without affecting the physical dose.

Project 2 was dedicated to achieve the goal of reducing the risk of high radiobiological effect of the dose given to OARs close to the target. Therefore, the GPU-MC package gPMC was extended to also tally dose-averaged LET. Optimization matrices were constructed from the product of dose-averaged LET and physical dose and employed in a prioritized optimization scheme to achieve the proposed goal without affecting the physical dose.

1.2.3 Respiratory motion and lung cancer

As stated in section 1.1.3.2 and explained in chapter 2.1, IMPT plans are very sensitive to geometry changes. When treating moving targets like in lung tumors, the target moves while the fraction is being delivered due to the patient respiration (respiratory cycle ~5 s, irradiation ~5 min). This intrafractional movement should be taken into account in the creation of the IMPT plan due to its impact on the plan quality [Phi+92; BD11]. There are two different

levels at which this movement has consequences [Sec+08]. On the first level, part of the dose may simply not be given to the tumor as it moved away from the position where the dose is being delivered. The direct dosimetric consequence is that the dose profiles are not as sharp as planned and more healthy tissue is irradiated. This affects all proton delivery modalities. In the second level, the interplay effect between the movement characteristic of the PBS delivery of IMPT plans (see section 1.1.3.2) and the tumor movement gives rise to under- and over-dose areas in the target and surrounding tissues.

The solution of solve the interplay effect is to allow statistics to average out the high- and low-dose regions. The simplest way of doing this is to take advantage of the multiple fractions usually delivered to the patient, which force a rescan of the patient at each fraction and eventually the fluctuations are smoothed. If hypofractionation is desired and the number of fractions are not enough to properly average out the interplay effect, active rescanning techniques can be applied. Active rescanning consists of splitting each fraction in n subfractions, each delivering $1/n$ times the planned dose in the session.

Of course, the ideal situation would be not having to deal with the respiratory motion. This could be achieved if the dose to the tumor was given fast enough, using very high dose rate of tens of Gy per second. There could be also an additional benefit from utilizing high dose rate. It has been shown in *in vivo* experiments that high dose rate electrons spare better the healthy tissue while maintaining tumor control, providing an additional beneficial biological effect [Pat+18]. Experiments with protons have yet to be conducted to assess this hypothetical biological effect [Pat+18]. However, the tumor motion can not be neglected if IMPT plans are to be delivered this way. Because PBS delivery takes time to adjust the machine parameters between a beamlet and the next, the tumor position should be tracked in order to deliver the beamlets when intended. A possible option would be to deliver the dose when the tumor is at a predefined region, in a technique called *gating*. In any case, this high dose rate irradiations have yet to be developed and therefore are not an option to manage motion.

Another possible solution to manage the respiratory motion would be to perform four-dimensional (4D) plan optimization and deliver the plan precisely to the tumor while tracking its position. However precise tracking is technically very challenging [Zha+13; Zha+14] and errors in the determination of the tumor position would systematically deliver the dose to unwanted areas. Without tracking, 4D-optimized IMPT plans taking the patient respiratory motion into account have been shown to deliver good dose distributions in each treatment fraction if active rescanning techniques are employed [ERK06; Gra17; Ber+17b]. Nevertheless, 4D optimizations are generally very time consuming as they need to take into account the PBS delivery time structure and the patient breathing pattern. Even when highly

optimized algorithms are designed to perform this task, the dose distribution delivered to the patient is very sensitive to the breathing patter of the patient, which is not predictable [Ber+17b].

Simpler approaches considering static 3D CTs modified to contain information of the movement have been reported to yield good results when used with rescanning and/or gating techniques. In these approaches, it is common to define the static CT as the average of a 4DCT and then define the target to be irradiated with an internal tumor volume (ITV). Usually an ITV contour delineates the total area the tumor has occupied during the breathing motion. Several proposals to define this contour have been published either by modifying the ITV delineation itself of altering the content the ITV delineates [EK05; Kan+07; GDB12; Kno+13; Wan+13; Gra+15]. However, these techniques had not been compared with high calculation accuracy.

Project 3 was dedicated to perform this comparison. In order to compare the approaches accurately, MC simulations were employed as they have been reported as the recommended dose calculation technique in lung cases [GLP15; Sch+15; Yep+18]. Therefore, a 4D GPU-MC framework to simulate the delivery of IMPT plans to moving patients taking the beam delivery time structure into account was developed. The different planning CT definitions proposed in [EK05; Kan+07; GDB12; Kno+13; Wan+13; Gra+15] were implemented for a set of lung patients, the cases were optimized using GPU-MC-generated optimization matrices and their performance evaluated on the 4DCTs was compared.

An important tool to evaluate the total dose given to a deforming geometry is deformable image registration (DIR). DIR is employed to create vector fields mapping the anatomy of the patient at different moments during the respiratory motion. The vector fields contain the information of the patient deformation, describing how each position of the patient is displaced as the respiration proceeds. Ultimately, these vector fields can be applied to the coordinates of the different dose distributions calculated at different moments during the respiratory cycle and therefore the dose can be *accumulated* in the corresponding positions of a reference coordinate system. The technique is described in section 3.3.

1.2.4 Patient anatomy evolution and positioning

Additionally to the intrafractional geometry changes produced by movement, patients also may undergo interfractional changes. The most notable cases concern the patient positioning (setup) and anatomy. Given the high influence of geometry on IMPT plans, if the original patient position or anatomy recorded in the planning CT is not conserved through the course of treatment the plan quality may drop drastically. A site where this is of particular importance is head and neck, where OARs are very close or overlapping the target [Ahn+14] (among

other publications). In this situation, interfractional changes may shift the high dose region to an OAR causing toxicities and not treating the target properly.

Studying only the effect of patient positioning uncertainties, Liebl et al. [Lie+14] have reported min/median/max standard deviations of proton range differences at 90% dose falloff using anatomy-based positioning, giving -12.7/0.5/12.5 mm water equivalent distances (WED). At 50% dose falloff, a more conservative measure, they were -6.3/0/6.1 mm WED, respectively. This is a large deviation that can account for up to 14% tumor control probability drop, although only for few cases [Lie+14]. Their findings, represent just an example of possible effects and are dependent on the planning strategy and delivery technique (passive scattering). The anatomy uncertainty in patients is very hard to forecast as it is very patient dependent, but its dosimetric effects can be estimated, showing the wide dosimetric implications this uncertainty may have [Alb+08].

One approach to try to alleviate the underdosage of the tumor caused by these uncertainties is to expand the area to be treated, changing the target contour. Even if this approach maintains a decent dose distribution in a given fraction, it is not a general solution in proton therapy due to the finite proton range and the steep gradients. A more advanced approach is performing robust optimization. Robust optimization consists of optimizing the plan taking into account different error scenarios so that the plan performs well if one of them occurs. This can be used for setup uncertainties, but anatomical changes are hard to forecast. Additionally, the bigger the number of positioning errors and anatomy changes scenarios taken into account, the bigger the high dose volume around the nominal target, which increases the dose to OARs [Wat+16; Dij+16; Pla+17]. Therefore, a common consequence of both strategies, target expansion and robust optimization, is to expand the volume receiving high dose levels, while not being able to guarantee high plan quality throughout the treatment. Additionally, none of these approaches guarantee coverage at any given fraction, which is a requirement in hypofractionated treatments.

The ideal approach would be to automatically adjust the plan parameters to the daily patient setup and anatomy at every fraction while the patient is at treatment position, removing the need to forecast the patient position and anatomy changes. Such a technique, called online IMPT plan adaptation, would maintain high plan quality throughout the treatment. There have been several studies proposing adaptation procedures [Kur+16; Mor+17; Jag+17; Ber+18; Jag+18] based on ADC algorithms. The presented algorithms, with variable success, address the setup and anatomical uncertainty, but using ADC algorithms the range uncertainty is not addressed.

Project 4 was dedicated to design an online adaptation algorithm capable of adjusting IMPT plans to the daily patient setup and anatomy while maintaining high dose calcula-

tion accuracy through GPU-MC simulations. This way the setup, anatomical and range uncertainties are minimized on a daily base.

1.3 Thesis structure and specific aims

Chapter 1 has given an overview of proton therapy and its uncertainties, motivating the goals of this thesis.

Chapter 2 will present the theoretical aspects of proton interactions with matter from a physical and biological perspective, within the energy range of interest in proton therapy. Quantities of interest in proton therapy will also be introduced.

Chapter 3 will briefly introduce the rationale behind the speed up of MC algorithms in GPUs in section 3.1, including the (unpublished) extensions implemented in gPMC for the development of the projects in this thesis. Afterwards, a basic overview of IMPT plans optimization and the tools employed to create IMPT plans in this thesis will be given in section 3.2. Finally, deformable image registration (DIR) and it uses will be explained in 3.3. These last two items are not a research focus in this thesis, but tools employed throughout it, therefore a very brief outline is provided. The extensions of gPMC to allow fast and flexible IMPT simulations at the Massachusetts General Hospital (MGH) were instrumental to all the other goals, but not a specific aim itself, therefore it will be explained in this methods and materials chapter.

One result chapter is dedicated to each project. The specific aims of this thesis are:

- Chapter 5: Investigate the feasibility and estimate the impact of reducing the radiobiological effect of IMPT plans with high LET$\times$D in organs at risk close to or in the target for ependymoma, meningioma and chordoma patients.

- Chapter 6: Investigate and compare definition strategies of treatment planning targets in 3D static planning CTs for the treatment of mobile lung tumors with IMPT, maintaining high dose calculation accuracy.

- Chapter 7: Minimize the impact of geometrical changes and therefore reduce the geometrical uncertainty during the course of IMPT treatments of head and neck tumors through the development of an online IMPT plan adaptation algorithm with high dose calculation accuracy.

At the beginning of each of these chapters my role in each study is explained along with comments on the adaptation of the publication to the thesis format. A reference to the original publication has been included when fit.

Chapter 8 is dedicated to the discussion of each project, focusing on the outlook. The conclusions are contained in chapter 9.

Chapter 2

Proton interactions with matter and quantities of interest

This chapter analyzes first the main proton interaction mechanisms in proton therapy and then some of the quantities of interest to proton therapy.

Within the energy range employed in proton therapy treatments (3-300 MeV), there are three important mechanisms through which protons interact with matter. All three affect protons differently and have very distinct dosimetric effects in proton beams. A very brief summary to set the ground goes as follows:

1. **Inelastic scattering with electrons:** per individual interaction the incoming proton losses very little energy, that adds up to a quasi-continuous energy loss process, removing more and more energy from the proton as it travels slower, ultimately making the proton stop. Dosimetric effect: creates the Bragg peak.

2. **Elastic scattering with nuclei:** the proton is scattered, changing its incoming direction with negligible energy loss. Many individual deflections generate a quasi-Gaussian profile. Effect: broadening of incoming beam.

3. **Nuclear reactions:** less likely than the previous two, protons undergo nuclear reactions with nuclei with several outcomes. Effect: proton beam fluence reduction, secondary protons, wide angle scattering giving dose to out-of-beam regions, secondaries such as neutrons, photons and others.

2.1 Proton stopping

Protons lose energy as they traverse a material until they have no kinetic energy left, in a process usually referred to as *stopping*. This process is studied as the energy loss per unit path length, with the *stopping power* concept. Many authors have contributed to the current knowledge of charged particle stopping. A good reference for a more in depth analysis of this process not limited to the scope of proton therapy can be found in the work by Ziegler [Zie99].

The loss of kinetic energy may be produced by collisions with the particles of the medium or by irradiation of photons in a process named Bremsstrahlung. Therefore, the total stopping power (S) is divided between the *collision* and the *radiative* terms:

$$-\frac{1}{\rho}\frac{\mathrm{d}E}{\mathrm{d}x} = \frac{S}{\rho} = \frac{S_{col}+S_{rad}}{\rho} \underbrace{\approx}_{m_p,\, T_{clin}} \frac{S_{col}}{\rho} \tag{2.1}$$

Within the clinically employed proton energy range ($T_{clin} \in 3-300$ MeV) and taking the proton mass (m_p) into account, the *radiative* contribution to the stopping power due to *Bremsstrahlung* (S_{rad}) can be neglected, leaving the so-called *collision stopping power* (S_{col}) as main contributor. Note that equation 2.1 focuses on the *mass stopping power*, dividing by the material density (ρ) because it allows for a more general framework as it will be shown later. The collision stopping power is often called *electronic stopping power*, but in this section both will be simplified to*stopping power*, as the radiative component is neglected.

The understanding of the stopping power has a long history. A simple but powerful expression without much physical insight can be employed to obtain the stopping power at a position z in an absorber [Bor97]:

$$\frac{S}{\rho} = -\frac{1}{\rho}\frac{\mathrm{d}E}{\mathrm{d}x} \approx -\frac{1}{\rho}\frac{(\alpha E^p - z)^{1/p-1}}{p\alpha^{1/p}} \tag{2.2}$$

In this equation, E is the initial energy of the proton and $p = 1.77$ and $\alpha = 2.2\times10^{-3}$ are parameters fitted to experimental data.

2.1.1 Bohr's approach

Much more physical insight than with equation 2.2 can be obtained following Bohr's approach to calculate the stopping power produced by unbound electrons [Boh15]. I will develop his estimation step by step in order to illustrate how the main dependencies of the stopping power arise. Bohr estimated the impulse given to unbound electrons by an incoming proton

with a velocity $\beta = v/c$, as a function of the impact parameter b. He started by computing the momentum gained Δp by an unbound electron in a collision with a proton with impact parameter b, as represented in figure 2.1:

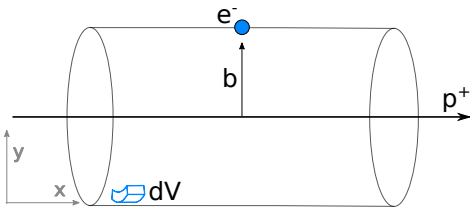

Fig. 2.1 Proton-electron collision with impact parameter b.

$$\left.\begin{aligned} \Delta p = \int F\,\mathrm{d}t = e\int E_y \mathrm{d}t = e\int E_y \frac{\mathrm{d}t}{\mathrm{d}x}\mathrm{d}x = \frac{e}{c\beta}\int E_y \mathrm{d}x \\ \int E \mathrm{d}s = \int E_y 2\pi b \mathrm{d}x = 4\pi z e \quad \Longrightarrow \quad \int E_y \mathrm{d}x = \frac{2ze}{b} \end{aligned}\right\} \quad \Longrightarrow \quad \Delta p = \frac{2ze^2}{c\beta b} \tag{2.3}$$

Where e is the electron's charge and ze is the projectile charge. Gauss' law was used to calculate the total electric field the electron is subject to: $\int E_y \mathrm{d}x$. This gives the energy gained by such electron of mass m_e as a function of the impact parameter:

$$\Delta E(b) = \frac{(\Delta p)^2}{2m_e} = \frac{2z^2e^4}{m_e c^2 \beta^2 b^2} \tag{2.4}$$

Of course, the amount energy loss by the proton is the same as the one gained by the electron. However, in a material there are more than one electron in a given volume, therefore, the total energy lost by the incoming proton is $-\mathrm{d}E\,(b) = \Delta E\,\mathrm{d}N$. Considering the electron density of the material n_e, $\mathrm{d}N$ can be rewritten as $\mathrm{d}N = n_e \mathrm{d}V = n_e \cdot 2\pi b \mathrm{d}b \mathrm{d}x$. Finally, integrating over the range of b, the stopping power in a material is obtained as a function of b_{max} and b_{min}:

$$\begin{aligned} -\mathrm{d}E(b) = \Delta E(b) n_e dV = \frac{4\pi z^2 e^4}{m_e c^2 \beta^2} n_e \frac{\mathrm{d}b}{b}\mathrm{d}x \quad \Longrightarrow \\ -\frac{\mathrm{d}E(b)}{\mathrm{d}x} = \frac{4\pi z^2 e^4}{m_e c^2 \beta^2}\, n_e\, \ln\left(\frac{b_{max}}{b_{min}}\right) \end{aligned} \tag{2.5}$$

Only b_{min} and b_{max} need to be computed now. b_{min} can be obtained considering the maximum energy given to an electron by a proton collision (not demonstrated here):

$$\Delta E_{max} = 2m_e c^2 \beta^2 \gamma^2 \left[1 + 2\gamma \frac{m_e}{m_p} + \left(\frac{m_e}{m_p} \right)^2 \right]^{-1} \underbrace{\approx}_{m_e \ll m_p} 2m_e c^2 \beta^2 \gamma^2 \tag{2.6}$$

$$\Delta E_{max} = \frac{2z^2 e^4}{m_e c^2 \beta^2 b_{min}^2} = 2m_e c^2 \beta^2 \gamma^2 \quad \Longrightarrow \quad b_{min} = \frac{ze^2}{\gamma m_e c^2 \beta^2} \tag{2.7}$$

b_{max} is obtained from the fact that the interaction is not adiabatic and therefore the interaction time must be at most the atom's average orbital period $\langle \tau \rangle$. The adiabatic limit is $\Delta t \approx \langle \tau \rangle$, thus:

$$\Delta t = \frac{b_{max}}{\gamma c \beta} = \langle \tau \rangle \quad \Longrightarrow \quad b_{max} = \gamma c \beta \langle \tau \rangle = \frac{\gamma c \beta}{\langle \nu \rangle} \tag{2.8}$$

Some last touches can be added to make the notation closer to the modern version of the equation. The electron density can be defined from the mass density, the atomic number Z, the mass number A and Avogadro's number N_A: $n_e = \rho N_A Z/A$. Plugging b_{min}, b_{max} and the definition of the electron density, Bohr's stopping power equation becomes.

$$-\frac{1}{\rho}\frac{\mathrm{d}E(b)}{\mathrm{d}x} = \frac{4\pi e^4 N_A}{m_e c^2} \frac{Z}{A} \frac{z^2}{\beta^2} \ln\left(\frac{\gamma^2 c^3 \beta^3 m_e}{\langle \nu \rangle z e^2} \right) \tag{2.9}$$

The most important features seen in equation 2.9 are the dependencies of the stopping power on projectile charge and velocity. The higher the projectile charge the more energy it looses. More importantly for proton therapy, where the charge is fixed, the slower the projectile travels, the bigger the stopping power, which creates the Bragg peak at the end of the beam's range described in the introduction (figure 1.1). The stopping power has linear dependencies on the material density and Z/A ratio. However, the Z/A ratio does not change substantially among elements. With the exception of hydrogen that has a $Z/A \approx 1$, the other elements can be found in the $0.4 \leq Z/A \leq 0.5$ region and can be estimated by a straight line $Z/A \approx 0.48 - 0.00092\, Z$. Therefore, the mass stopping power is a rather stable quantity with respect to the absorber material.

$$-\frac{\mathrm{d}E}{\mathrm{d}x} \propto \rho \frac{Z}{A} \frac{z^2}{\beta^2} \tag{2.10}$$

2.1.2 Modern description

The basis for the modern stopping power theory was laid by Bethe and Bloch in the early 1930's [BH34; Blo33] and further corrections have been developed to account for different quantum effects. Equation 2.11 shares the main dependencies with the equation calculated

by Bohr.

$$-\frac{1}{\rho}\frac{\mathrm{d}E(b)}{\mathrm{d}x} = 4\pi N_A r_e^2 m_e c^2 \frac{Z}{A}\frac{z^2}{\beta^2}\left[\ln\left(\frac{2m_e c^2\beta^2}{I(1-\beta^2)}\right) - \beta^2 - \frac{\delta}{2} - \frac{C}{Z}\right] \tag{2.11}$$

In this equation, r_e is the classical electron radius, I is the mean excitation energy of the material, $\delta/2$ is the density correction from the shielding of electrons by closer ones (reduction of energy loss for very high energies), and C is the shell correction item (important only for very low energies, close to the adiabatic limit). The other quantities have been previously defined. I is an important quantity in proton therapy and the uncertainties in its value that can be in the order of 10-15% is an importance source of possible range deviations with high clinical impact [Pag12; BPB13].

Figure 2.2 shows the electronic (collision) and nuclear stopping powers in water for protons.

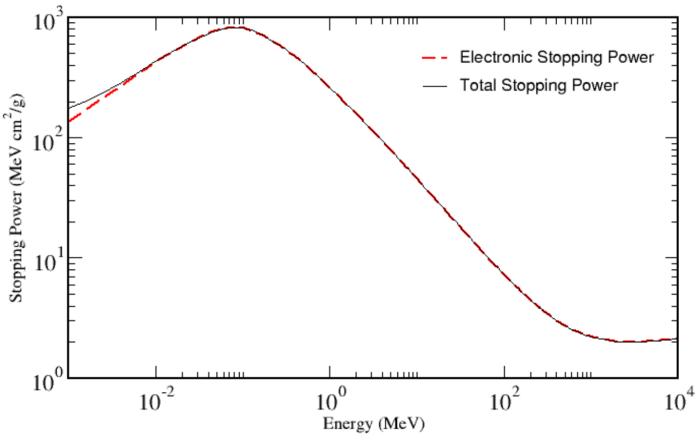

Fig. 2.2 Proton stopping power in water, obtained from NIST's PSTAR database [Ber+17a].

Due to the stochastic nature of particle interactions, after a given absorber depth or thickness, not all protons will have lost the same amount of energy due to random fluctuations in the energy loss. This phenomenon is called energy straggling and several models have been proposed to account for it. A Gaussian approximation may be employed if the absorber thickness is not very small and/or the particle's β is not close to 1 [SB64], which are the usual conditions in proton therapy. Nevertheless, Vavilov's distribution is considered more exact. The main consequence of energy straggling is the broadening of the proton energy spectrum as the beam traverses the material. This ultimately affects the Bragg peak, making it broader and with a smaller maximum (figure 1.1).

In order to compute the stopping power in mixed media, each element in the compound is taken into account weighting by the fraction of electrons belonging to it. This is called the

Bragg's additivity rule:

$$\frac{S}{\rho} = \sum_i \omega_i \frac{S_i}{\rho} \tag{2.12}$$

2.1.3 CSDA range

The kinetic energy loss in each of the proton-electron collision is limited due to the mass ratio between protons and electrons, as expressed in equation 2.6. As a consequence, the stopping process can be regarded as quasi-continuous. This approach is called the *continuous slowing down approximation* (CSDA) and it allows for a simple definition of particle range from the initial particle energy E_0 (equation 2.13). The total stopping power (electronic and nuclear) must be taken into account in this calculation. As seen in figure 2.2, the nuclear stopping power is not negligible at very low energies (< 0.01 MeV). The CSDA range (R_{CSDA}) should be interpreted as the distance traveled inside the absorber, not as the total penetration depth in it. Although protons travel almost in a straight line, the penetration depth will be smaller than the range due to scattering, however only about ~0.1% at clinical energies [Jan82].

Bragg and Kleeman [BK05] observed that an exponential equation is a good descriptor of the range.

$$R_{CSDA} = \int_0^{E_0} \left(\frac{S(E)}{\rho} \right)^{-1} \mathrm{d}E \approx \alpha E^p \tag{2.13}$$

The range of projectiles with the same kinetic energy in a material is related. Therefore, if the proton range in a material R_p is known for a given kinetic energy, the range of other projectiles with different mass and charge but with the same velocity β can be estimated, again, disregarding lateral scattering:

$$\frac{R_1}{R_2} = \frac{z_2^2 m_1}{z_1^2 m_2} \quad \Longrightarrow \quad R = \frac{1}{z^2} \frac{m}{m_\mathrm{p}} R_\mathrm{p} \tag{2.14}$$

2.1.4 Raytracing

Raytracing of protons is a practical application of the CSDA, where protons are traced in straight lines through a geometry, like a voxelized patient CT in the case of this thesis. The traces are forced to lose energy gradually until they stop following the CSDA. Raytracing is useful to predict the approximate end of range location of a set of beamlets within a patient. In homogeneous media, the positions predicted by raytracing is the depth at 80% maximum dose after the Bragg peak (R80). This position marks the 50% remaining proton fluence and is independent of the initial beam energy spread and also to energy straggling if the Gaussian approximation is valid. However, when a beam traverses different tissues, the

Bragg peak shape is distorted because some sections traverse materials different than other. In this situation R80 no longer has the same meaning and therefore the traces may represent better other dosimetric indices.

In order to take into account lateral inhomogeneities and make raytracing predict an average end of range postion for each beamlet, each trace may be assigned a Gaussian distribution dependent on depth that take the material composition of surrounding voxels into account assigning Gaussian weights. Although this improves the estimation quality, in highly heterogeneous media there is no well defined end of range position because some regions of the beam penetrate further than others.

In order to calculate the energy loss per voxel, the easiest approach consists of applying

$$\Delta E = S(E_0)\Delta l, \tag{2.15}$$

while limiting the step length Δl so that a constant $S(E_0)$ can be used at each step, that is, so that $S(E) \approx S(E_0)$.

2.2 Proton scattering

Proton beams scatter inside a medium, gradually increasing the beam profile width due to the combination of many small deflections of individual protons undergoing Coulomb interactions with the material nuclei. The scattering probability is called *scattering power*, similarly to the concept of *stopping power*. In this case, given the symmetry of the scattering angle, the average θ is 0 and therefore, the *scattering power* depends on $\langle\theta^2\rangle$:

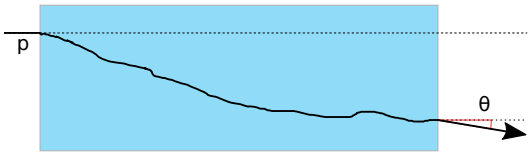

Fig. 2.3 Multiple Coulomb scattering in a material.

$$\frac{T}{\rho} = \frac{\mathrm{d}\langle\theta^2\rangle}{\mathrm{d}x} \tag{2.16}$$

The description of elastic Coulomb scattering depends on the number of scattering events (Ns) in an absorber. In the case of a single event, Rutherford's scattering theory can be applied. However, multiple Coulomb scattering (MCS; $Ns \geq 20$) has to be described with statistical approaches to calculate the net deflection angle θ shown in figure 2.3.

The solution for MCS was given by Molière [HMS47] assuming that each individual event is deflected by a small angle, which is consistent with Rutherford's theory. Molière's

theory is usually termed as "a bit too complicated" for the precision required in medical physics, so I will give a brief introduction based on the published work by Gottschalk [Got+93; Got10] and the review on proton therapy physics by Newhauser [NZ15].

Molière's theory approximates the scattering distribution $P(\theta)$ with a power series on the inverse of the *reduced target thickness* $(1/B)$

$$P(\theta) = \frac{1}{2\pi\theta_M^2}\frac{1}{2}\left[f_0(\theta') + \frac{f_1(\theta')}{B} + \frac{f_2(\theta')}{B^2}\right], \tag{2.17}$$

where θ_M is the *characteristic multiple scattering angle* for the given target and incident particle. θ_M depends on the *characteristic single scattering angle* χ_c as in

$$2\theta_M^2 = \chi_c^2 B \tag{2.18}$$

$$\chi_c^2 = 4\pi N_A e^4 \frac{zZ^2}{A}\frac{t}{(pc\beta)^2}, \tag{2.19}$$

where t is the absorber thickness, p the particle's momentum and the other variables are consistent with previous definitions in this section. B can be computed with numerical methods from 2.20, with previous calculation of c_2. $\hbar$ is the reduced Planck constant.

$$B - \ln B = \frac{c_2}{pc^2}(1.13 + 3.76\alpha^2) \tag{2.20}$$

$$c_2 \equiv \left[\frac{1}{0.885}\left(\frac{e^2}{\hbar c}\right) m_e c^2 Z^{1/3}\right]^2 \tag{2.21}$$

$$\alpha = \frac{c_1}{\beta^2} \equiv \frac{1}{\beta^2}\left[\left(\frac{e^2}{\hbar c}\right) zZ\right] \tag{2.22}$$

In equation 2.17, $f_i(\theta)$ are defined using the Bessel function $J_0(\theta y)$ as follows:

$$f_i(\theta) = \frac{1}{n!}\int_0^\infty y\mathrm{d}y\, J_0(\theta y) e^{-\frac{y^2}{4}}\left(\frac{y^2}{4}\ln\frac{y^2}{4}\right)^n \tag{2.23}$$

The evaluation of these expressions is a complex process and approximations are generally employed for practical reasons. The good news is that the most common approximation relies on limiting the scattering distribution $P(\theta)$ to the first term of the polynomial, reducing the expression to a Gaussian. In practice this means that large scattering angles might not be well represented, but for most cases this is not of crucial importance in medical physics applications because protons that are scattered with big angles after MCS are not very

energetic and do not travel far.

$$P(\theta) \approx \frac{1}{2\pi\sigma^2} \exp\left\{-\frac{\theta^2}{2\sigma^2}\right\} \tag{2.24}$$

Many parametrizations $P(\theta)$ have been proposed [Got+93], but one of the most commonly used approximations is the one proposed by Highland [Hig75]. Highland observed that the description of the target properties in MCS had similar dependencies as the *radiation length* L_R [Got+93], which can be found tabulated for different materials. He proposed expression 2.25, allowing the simple estimation of θ in situations like the one in figure 2.3. Rossi and Greisen [RG41] also proposed a parametrization of the Gaussian width, shown in equation 2.26 where E_s is a fitting parameter.

$$\sigma = \frac{13.6\,\text{MeV}}{pc\beta} z \sqrt{\frac{t}{L_R}} \left[1 + 0.038 \ln\left(\frac{t}{L_R}\right)\right] \tag{2.25}$$

$$\sigma^2 = \left(\frac{E_s}{\beta p}\right)^2 \frac{t}{L_R} \tag{2.26}$$

Using either of this widths in equation 2.24, θ can be sampled fast and so they are commonly found in many MC simulation packages. In this case, often times t is reinterpreted as the step length. Some algorithms allow the user to select the scattering model beyond the small angle approximation as a parameter. FRED [Sch+17], for example, also models MCS as a double Gaussian and a Gauss-Rutherford peak. In gPMC, the GPU-MC code employed in this thesis, the Rossi and Greisen parametrization [RG41] of the small angle approximation is employed, but two E_s values are included depending on the energy of the proton, with the changing point empirically set at 70 MeV.

2.3 Nuclear interactions

Additionally to the elastic electromagnetic interactions with nuclei, protons may also undergo nuclear reactions. The main result of these interactions is the absorption of the primary proton by the nucleus, reducing the incoming beam fluence. All protons undergo electromagnetic interactions, but only about a quarter undergo head-on collisions with the material's nuclei [Pag02] (depending on the energy). After a collision, the nucleus is left in an excited state and it usually emits the energy in excess in the form of prompt gammas, neutrons, nuclear fragments like alpha particles and secondary protons. The presence of secondary protons in part mitigates the loss of primary fluence. The final fluence reduction is ~1 $\%\,\text{cm}^{-1}$ [Pag02].

There is a minimum proton energy of about ~8 MeV because the incoming proton must overcome the Coulomb potential of the atom to interact via the strong force [Pag02].

In summary, nuclear interactions are responsible for the following:

- Fluence reduction.
- Neutron production: they deliver a small dose to the patient inside and outside the main dose region, also interacting with the treatment room. In double scattering delivery, the neutrons are mainly generated in the delivery nozzle when protons traverse the modulator, scatterers and other components, while in pencil beam scanning they are created within the patient.
- Secondary protons: they are scattered at higher angles than the primaries scattered by MCS and have a high contribution to the dose to the lateral region of the beam (up to ≈ 10 %) [GP11]. This is the most common secondary from the nuclear interactions [Pag02].
- In the case of target fragmentation heavier particles do not travel much within the patient and therefore their energy is deposited very close to their creation.
- Some subproducts of nuclear interactions offer possibilities of beam monitoring. Positrons emitted by radioactive fragments may be employed for imaging the beam path through positron emission tomography (PET). Also, nuclear de-excitation processes emit prompt gamma that can also be detected.

Often times, precise calculation of species other than secondary protons produced within a patient is not required in proton therapy [FS04]. Internal nuclear cascade models are as well not often necessary in proton therapy [FS04]. On the one hand, charged secondaries heavier than neutrons or protons (nuclear fragments) do not travel far due to their usually high charge and very low velocity (see equations 2.10 and 2.11), so the location of the energy deposition can be assigned to the location of the interaction point. Also, the usual resolution of the scoring grids employed in proton therapy is too big to accurately represent the displacement of these secondaries. On the other hand, gammas or neutrons travel far, so they provide a very low dose bath to the whole patient that can, again, be neglected [FS04]. Therefore when calculating the dose given by an IMPT plan with negligible beam contamination from other species, the MC package employed is not necessarily required to perform accurate simulations of the nuclear interactions. This means that the major implementation step of nuclear interactions in a simulation package for proton therapy is the cross section or interaction probability for each reaction. Usually, this data is employed either via look-up

tables or by evaluating fits to them. This simple approach to nuclear interactions is the one followed in gPMC, where nuclear cross sections were fitted [Jia+12].

A more involved discussion of the nuclear interaction channels in proton therapy can be found in the publications by Paganetti [Pag02] and Newhauser [NZ15].

2.4 Quantities of interest in proton therapy

2.4.1 Fluence

The particle fluence ϕ across a surface is defined as the number of particles N crossing the surface area A. The energy fluence φ is the total energy crossing such surface and can be expressed as a function of the energy spectrum ψ. It can also be easily related to ϕ for monoenergetic beams of energy E_0:

$$\phi = \frac{N}{A} \qquad \left[\mathrm{m}^{-2}\right] \tag{2.27}$$

$$\varphi = \frac{1}{A}\int \psi(E)\,\mathrm{d}E \underbrace{=}_{\psi(E)\mathrm{d}E = E_0 \mathrm{d}N} E_0\,\frac{N}{A} = E_0\,\phi \qquad \left[\mathrm{MeV\,m}^{-2}\right] \tag{2.28}$$

2.4.2 Dose

In proton therapy the treatment prescription is given in terms of the *dose*. The microscopic dose D deposited in a region with mass $\mathrm{d}m$ is given as a function of the energy $\mathrm{d}\varepsilon$:

$$D = \frac{\mathrm{d}\varepsilon}{\mathrm{d}m} \qquad \left[\mathrm{J\,kg}^{-1} = \mathrm{Gy}\right] \tag{2.29}$$

In a macroscopic region, such as a voxel in a Computed Tomography (CT) scan, the dose can be calculated from the total energy deposited E by all the interactions in the region, the volume V and density ρ:

$$D = \frac{\int \mathrm{d}\varepsilon}{\rho \int \mathrm{d}V} = \frac{E}{\rho V} \tag{2.30}$$

The dose deposited in a volume can be written in terms of the fluence by knowing the amount of energy lost while traversing the material (eq. 2.31). The stopping power is a function of the energy, but assuming the energy loss is small with respect to the stopping power change and the incoming beam is monoenergetic, the dose in a volume can be easily

computed (eq. 2.32):

$$D = \frac{1}{V}\int_{E_0}^{E} \mathrm{d}E\, \psi(E)\frac{S(E)}{\rho} \tag{2.31}$$

$$= \phi E_0 \frac{S(E_0)}{\rho V} \tag{2.32}$$

2.4.3 Linear energy transfer

The linear energy transfer (LET) is a concept similar to the electronic stopping power. While the stopping power expresses the amount of energy lost by an incoming proton, the LET describes how much of the energy lost is deposited in the vicinity of the proton particle track. This definition leaves one free parameter undefined: the concept of vicinity. Vicinity is expressed as a threshold of the secondary electrons energy. Only those interactions that produce a secondary electron with energy $E < \Delta$ are considered in the LET, as those electrons do not have enough energy to leave the track vicinity.

$$LET_\Delta = \frac{\mathrm{d}E}{\mathrm{d}l} \qquad \left[\mathrm{keV\,\mu m^{-1}}\right] \tag{2.33}$$

We speak of unrestricted LET when Δ is higher or equal to the maximum energy of the secondary electrons that can be produced. Restricted LET is used otherwise. The unrestricted LET is numerically equal to the electronic stopping power, although the concept is different as the scope in this case is focused in the medium in which the energy is deposited, not on the effect the medium has on the incoming track.

When considering the LET produced by a non-monoenergetic beam in a region, like a voxel in a CT, the LET presents a spectrum of values that arise from the stochastic nature of the energy loss and from the different energies of the incoming particles. If a single LET value per region is required, the LET spectrum can be averaged with different techniques [GS15; Gua+15]. One of the most common way of computing this average is to weight by dose deposited at each interaction in the region, yielding the *dose-averaged* LET, or LET_D.

$$LET_D = \frac{\sum_i d_i LET_{\Delta i}}{\sum_i d_i} \tag{2.34}$$

2.4.4 Biological effect of the dose

The biological dose refers to the effect of a dose deposited on a biological system. While physics is rather simple, damage to a biological system through radiation can produce a whole array of outcomes, which makes this relation hard to study. The majority of the studies

of the relation of dose versus a particular *endpoint* have been developed using X-rays. An example of such study could be to irradiate a cell population and plot the cell survival against the absorbed dose, where the endpoint would be cell survival. Such studies are the basis to prescribe the dose to treat a certain lesion, so the dose is given as if the lesion were treated with X-rays. Therefore, a way to draw endpoint equivalences between the effect of a certain X-ray dose and a proton dose is necessary.

The *relative biological effect* (RBE) is used to establish dose equivalences between the dose given by X-rays D_X and that given by protons D for a particular endpoint:

$$RBE = \frac{D}{D_X} \tag{2.35}$$

Although the concept is easily explained, in reality the RBE is a complex function of the characteristics of the irradiated medium and the dose distribution. There is an expected dependency of the RBE on LET, because it represents the energy locally absorbed in the vicinity of the track, which should be correlated via some tissue-specific parameters with the final effect. Many studies have been published on parametrizations of these RBE dependency, including [WO04; Car+12; CA12; WLH13; Pag14; MSP15] among others. However, this is not the only main parameter of RBE models that has been proposed [SS04; SS06; Ste+11; Ste+15; Fri+13; Fre+11; Car+08]. Nevertheless, the parametrization presented by McNamara et al. [MSP15] is given here to illustrate the complexity of the relation:

$$RBE[D,\ (\alpha/\beta)_X,\ LET_d] = \frac{1}{2D}\cdot \tag{2.36}$$
$$\left(\sqrt{\left(\frac{\alpha}{\beta}\right)_X^2 + 4D\left(\frac{\alpha}{\beta}\right)_X\left(p_0 + \frac{p_1}{(\alpha/\beta)_X}LET_d\right) + 4D^2\left(p_2 + p_3\sqrt{\left(\frac{\alpha}{\beta}\right)_X}LET_d\right)^2} - \left(\frac{\alpha}{\beta}\right)_X\right)$$
$$p_0 = 0.991\ (\text{SE } 0.014), \quad p_1 = 0.356\ (\text{SE } 0.015), \quad p_2 = 1.101\ (\text{SE } 0.006)$$
$$p_3 = -0.00387\ (\text{SE } 0.00091), \quad R^2 = 0.255$$

In the previous equation, D is the proton dose, $(\alpha/\beta)_X$ characterizes the biological effect of the equivalent photon dose and is tissue dependent, LET_d is the dose average LET introduced in the previous section describing the local ionization density and $p_{0\to3}$ are the fitting parameters. This parametrization was calculated on the data collected by Paganetti [Pag14], however, the high uncertainty in these data is transferred to the parametrization (see R^2 measuring the data variance explained by the model in the previous set of equations). As a

consequence, it is not possible to give values of the RBE with high precision and a constant RBE of 1.1 is usually employed as a conservative compromise.

The RBE for neutrons and ions heavier than protons is higher and if they are used as therapy projectiles, a constant value would not be a good compromise. This is nevertheless outside the scope of this thesis.

Chapter 3

Materials and methods

This chapter describes aspects and concepts used in the papers here included that are not central to the investigation and are therefore not given enough credit in the manuscripts. All tools are commonly used in medical physics and are therefore only mentioned in the manuscripts as no further description is usually necessary.

The first section is an introduction to Monte Carlo transport simulations of protons and the additional extensions implemented in gPMC in order to carry out the projects. The second section briefly discusses the creation and optimization procedure of IMPT plans. The last one deals with deformable image registration (DIR) and its uses.

3.1 Monte Carlo simulations and gPMC

Monte Carlo (MC) simulations are the gold standard for dose calculations in proton therapy, producing accurate results in highly heterogeneous patient regions where analytical dose calculation algorithms do not [GLP15; Sch+15; Yep+18].

The following gives a brief introduction to MC simulations. Next, unpublished improvements included in gPMC in order to carry out the projects here presented and others will be detailed.

3.1.1 Monte Carlo background

As briefly defined in the introduction chapter, Monte Carlo transport simulations allow the statistical estimation of macroscopic quantities arising from the evaluation of the interaction probabilities of particles with their microscopic environment and the sampling of the products of these interactions. In a more general definition, the Monte Carlo method comprises a collection of techniques that allow the estimation of the moments of probability density

functions through statistical sampling. These methods can be applied to integrate complex functions as well as to calculate the moments of complex distributions. The utilization of the Monte Carlo method for particle transport simulation dates back to the *Manhattan project* in the 1940's, where it was applied to neutron transport calculations. In principle and if all the physical models have been correctly implemented, MC simulations should converge to the exact solution of the linear Boltzmann transport equation (LBTE) due to the central limit theorem.

A Monte Carlo particle transport algorithm can be defined as a repetition of the following 3 steps:

1. Get constant context: get particle being simulated, surrounding material information, geometrical constrains and mean free path (λ) resulting from the particle type and momentum and the surroundings.

2. Get interaction and step length s by statistical sampling and constraints:

   (a) Get constraints on the step: distance to the voxel border in which the material changes (s_{geo}) or a maximum allowed step length in the algorithm (s_{max}). The rationale behind specifying a s_{max} is given below.

   (b) Sample step length to next interaction point $s_\lambda = -\ln(\eta)/\lambda$, using a random number $\eta \in [0,1]$. The sampling function follows from the probability density function (PDF) of an interaction $p(x)\,\mathrm{d}x = \lambda e^{-\lambda x}\,\mathrm{d}x$ with mean free path λ, calculating the cumulative density function (CDF) $\eta = \int_0^{s_\lambda} \lambda e^{-\lambda x}\,\mathrm{d}x$ and solving for s_λ.

   (c) Get the minimum of the three steps: $s = \min(s_{geo},\ s_{max},\ s_\lambda)$

3. Move s and sample interaction if $s = s_\lambda$ and produce secondaries if necessary.

Many adaptations of this simple recipe have been proposed, but gPMC has been designed following the published algorithm by Fippel et al. implemented in VMCpro [FS04]. A thorough description of the implementation ported to gPMC has been included in the initial code presentation by Jia et al. [Jia+12].

Item 3 of the previous enumeration is a complicated term than involves a lot of physical concepts and modeling due to the particle interactions, specially when nuclear interactions occur. Protons are charged particles and present many small interactions with the electrons in the material, as it was explained in section 2.1 (specially 2.1.3). If all the small interactions were to be explicitly simulated, the simulation would take a very long time to converge to the solution. Instead, variance reduction techniques (VRT) are applied to increase the

convergence rate. Often not classified as VRT due to its ubiquity, the *condense history method class II* (CHII), introduced by Berger [Ber63], is used in most charged particles simulations to cluster together many small interactions into single steps, while explicitly simulating important collisions. At the end of the condensed steps, the incoming proton (or charged particle) losses some energy and is deflected through MCS. This method can bias the simulation if not performed carefully, deviating the result from the LBTE. Its classification as VRT here might be polemic, but the characteristics of the method and consequences when misused are the similar to other VRT, while serving the same purpose of increasing the convergence rate (with respect to time, not to number of simulated histories).

Therefore, the concept of *moving* in item 3 may hide many small interactions in a single step in proton simulations. It is often required to set some limits on the CHII method by defining a maximum allowable step length (included in item 2 of the previous list) and a maximum allowable energy loss to maintain the simulation unbiased. In the condensed steps, the stopping power is considered constant, which means that the nominal energy loss in the step is $\varepsilon = S(E) \cdot s$ and it can not be big with respect to the particle's original energy E. In order to calculate the total energy loss ΔE, straggling has to be considered. This can be done by sampling ξ from a Gaussian distribution, as the conditions outlined in section 2.1 to employ the Gaussian model are generally met in proton therapy. Therefore, the energy loss in a proton condensed step is $\Delta E = \varepsilon + \xi$. The angular deflection of the incoming proton due to multiple Coulomb scattering can be sampled from a Gaussian expression as well, like the one proposed by Highland [Hig75] (see section 2.2). In some situations, specially when simulating electrons, the sampled step length might be too long to accurately describe the lateral displacement, so a random hinge can be used to split the step into two substeps at a random position, as introduced in PENELOPE [Bar+95]. This is not necessary with protons [FS04].

After performing the condensed step, if $s = s_\lambda$, it is decided by sampling whether the production of a high energy electron or the interaction with another proton or nucleus occurs. Any subproduct is stored in a stack to be simulated at a later moment. In proton therapy, however, due to the combination of the projectile nature, its energy and the spatial scale at which results are needed, only secondary protons have to be explicitly simulated in most cases [FS04]. Electrons and charged particles heavier than protons can be assumed to deposit all their energy in the creation point and neutral particles like gammas and neutrons travel too far to contribute a significant dose to any specific patient position. It is beyond the scope of this background introduction to define the exact interaction models employed during the simulations as they vary from code to code. For the example of gPMC, refer to chapter 4 for the updated nuclear models, mainly dealing with secondary sampling from the reactions.

Refer also to [Jia+12] for electronic interactions and general implementation and [FS04] for the algorithm rationale.

Therefore, in gPMC simulations of proton plans, millions of primary and secondary protons are simulated until they have lost all their initial kinetic energy through interactions or have left the region of interest.

It is interesting to consider the reasons why MC simulations gain such speed up factors when implemented in GPUs. First and foremost, the problem type allows the simulation of all protons as independent particles with no interactions between them. Therefore they can be calculated in parallel without any synchronization needed. Second, the combination of energy range and spatial scale employed in proton therapy allows the usage of simplified algorithms where some secondary particles do not need to be tracked [FS04], allowing easier implementation in the GPU device while maintaining memory consumption low. This last reason also allows for faster CPU implementations, of course. In gPMC, both factors are exploited to increase the simulation efficiency.

3.1.2 Further gPMC developments

Aside from the improvements presented in chapter 4, other unpublished improvements have been implemented in order to provide further capabilities, giving support for the projects presented in chapters 5–7 and others like [Gia+17; Ver+17].

The following is a non-exhaustive list of the extensions and improvements implemented. Minor features, bugs fixes and code refactoring are omitted.

1. **Physics development mode:** Extra control over parameters and additional hyper-parameters for physics benchmark and development as compilation option. Added cylindrical scorers to take advantage of the symmetric profiles often used for physics benchmark.

2. **Particle source:** The initial version of gPMC imported the primary protons from a single phase space file generated by a different code. This was not an ideal solution, not only because it was produced by a different code increasing the number of steps required to perform a simulation, but also because the other code did not take advantage of GPU parallelization. Also, this implied a disconnect between gPMC and the files defining treatments in the clinic. To solve this, a particle source was implemented that reads the treatment files and samples primaries employing a beam model selected by the user from several available options (see next item). The particle source was implemented in the GPU, causing a minor overhead to the whole simulation.

3. **PBS beam models:** Beam models to use in IMPT treatment simulations were implemented following [GLP15]. The beam model from MGH was also implemented, along others characterizing a range of beamlet widths (σ) to support studies with several *beamlet sizes* (σ). Ideal sources with zero initial σ and/or energy spread were also included. A parameter is passed to the CUDA kernel running the particle source to select the beam model to sample primaries from. All beam models present Gaussian σ and energy spread.

4. **Simulation levels:** The original version of gPMC disregarded the treatment hierarchy in fields, beamlets and individual protons. Four execution levels with parameters exposed to the user were implemented to select what level within the hierarchy should be simulated and how it should be reported:

    - Simulate all fields and output the results.
    - Simulate all fields, but output the results per field.
    - Simulate all fields, but output the results per beamlet.
    - Simulate a single field.
    - Simulate a single field, but output the results per beamlet.
    - Simulate a single beamlet.

5. **Treatment devices:** Added lucite (hardcoded) range shifters and binary apertures with automatic beamlet filtering. Automatic beamlet filtering in the aperture refers to only testing those beamlets that are likely to be cropped by the aperture, speeding up the process.

6. **Additional scored quantities:** gPMC was extended not only to score dose to medium or water per voxel, but also other quantities that can be activated by the user:

    - Energy deposited.
    - Proton dose-averaged LET: A maximum allowed LET value was included at 100 $\mathrm{keV\,\mu m^{-1}}$ to prevent LET spikes. LET spikes are an artifact created by the transportation of particles in a voxelized geometry in MC simulations. Near the border of a voxel, very short steps depositing a relatively high energy can cause these spikes. The maximum unrestricted LET in water is in the order of ~83 $\mathrm{keV\,\mu m^{-1}}$ [Ber+17a].
    - Proton end of tracks: Accumulate the number of protons stopping per voxel. This is a more stable quantity than LET and could be employed as a surrogate to take into account high RBE areas.

- Proton spectrum: The proton spectrum can be scored with a variable number of bins per voxel for the application of prompt gamma spectroscopy to range verification. The spectrum can then be utilized to evaluate prompt gamma production cross sections [Hue+18].

7. **Scoring masks:** The code accepts a set of arbitrarily shaped binary masks in a cartesian grid to define a sensitive region in the scoring grid. The mask may represent the planning target, main OARs and/or a desired sensitive region. If more than one mask are passed, they are combined. This implementation allows scoring in a single structure, paving the way to score per structure and to take the structures into account during the simulation for variance reduction techniques or uncertainty levels assessment for intelligent simulation stopping. The results are given within the scoring grid, leaving 0 outside the mask and the tallied quantities inside of it.

8. **Scoping mask mode:** Transforms a 3D scoring grid into a linear index defined by a scoping mask. The scoping mask attribute can be attached to the scoring masks. Because there is no scoring outside the scoring mask, this option removes the voxels outside the mask by linearizing the grid, drastically reducing the necessary memory space allocated in the GPU memory. The implementation of this attribute is driven by the necessity to employ more aggressive binnings on the original scoring grid, like for example creating a scoring grid per beamlet.

9. **Dose/LET matrices for optimization:** Create and fill an array of n beamlets $\times$ m voxels for optimization. A scoring grid is allocated per beamlet, multiplying the memory required in the GPU. In order to maintain the memory requirements within the capabilities of the GPU, this feature can be used while scoring in arbitrarily shaped scoped regions and simulating field by field. It is therefore a mixture between a scorer and an execution mode due to its influence in other parameters.

10. **Native scoring grid:** Transport particles in the CT grid, but score in scoring grid, as opposed to navigate and score in the CT grid and interpolate to scoring grid after the calculation. When doing this, the interaction point were quantities are recorded becomes important due to the high impact of the CT voxel borders.

11. **Random interaction point within step:** Randomly use scoring position along step, as opposed to scoring at the end of the step. Scoring at the end of step causes artifacts when scoring in grids other than the CT because a step is forced at each voxel change. Therefore many interactions are recorded at the voxel interfaces. Another option would be to split the quantity to be scored between the voxels contained in the step

(weighting by the step length per voxel). The random position was chosen over this option, because the results were satisfactory and it reduced race conditions in the GPU because a single memory location is used, as opposed to writing to multiple locations.

In some special situations the interaction point model can cause artifacts if histories are highly correlated. If most histories start from the same position, with the same momentum and are forced a given step length, then the interaction point model will create different characteristic artifact shapes when scoring energy/dose. An example of this is when transporting protons with the same starting position and momentum in air, with small voxels and large mean free path compared to the maximum step length. The voxel maximum step length will limit the steps and the dose profile within the voxel will present artifacts following a characteristic shape. The artifacts will disappear with depth as more particles present steps other than the ones forced by the voxel crossing. Figure 3.1 illustrates this issue. This artifacts were mainly present when generating data for physics development and do not affect patient simulations so a more general solution to this issue was not seeked.

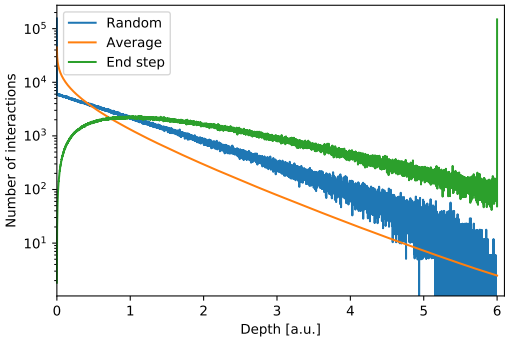

Fig. 3.1 Characteristic shape of dose deposition along the step of highly correlated histories with mean free path equal to the voxel size (1 unit of length). The dose deposition is considered proportional to the step length because all the particles have the same starting energy, therefore equation 2.32 applies. End of step, random position and averaging the total dose across voxels are compared. Scoring at the end of the step shows a peak dominating the distribution.

12. **Other improvements:** Allow user specification of density or energy scaling for range uncertainty studies, isocenter shifts and CT rotations for setup uncertainties and online adaptation algorithm (chapter 6) and user defined scoring grids.

3.2 IMPT plans creation

This section gives a brief overview of the data flow and the mathematical optimization process employed in the presented projects for the generation of IMPT plans.

3.2.1 Data flow

The flow of data to create a treatment plan in the projects here presented consisted of 6 steps:

1. The patients structures (tumor, OARs, etc.) were contoured in MiM (MiM Software Inc.).

2. The contoured patient scans were exported to *XiO* (Elekta) to define the field angles. The field angles were selected following current clinical practice, minimizing the dose given to OARs, uncertainties caused by imaging artifacts in the CT and potential anatomy changes in the patient.

3. The plans were imported into Astroid [Koo+10], the software clinically employed for IMPT planning at MGH. Astroid houses an ADC algorithm and because within the projects here presented accurate dose calculation was necessary, Astroid was used only to define the set of beamlets to be considered for plan optimization.

4. The data needed to simulate the patients with gPMC was queried from Astroid's database and transformed to the appropriate format using an upgraded version of MCAUTO [Ver+16].

5. A dose-influence optimization matrix per field was created by simulating each individual beamlet with gPMC and then combining the result into a compressed format. The compressed format employed a sparse histogram compression, neglecting voxels with dose smaller than 0.001 Gy per 10^9 initial protons. Post-processing is necessary because dose-influence matrices are big (millions of elements) and do not fit into the limited GPU memory. Newer GPU cards might challenge the previous sentence.

6. The dose-influence matrices were then fed to an external optimizer, Opt4D [Tro+05], to find the set of beamlet weights that give the best dose distribution. Further details about the optimization procedure are given in the following section.

3.2.2 Plan optimization

Many authors have contributed to the literature of IMPT plan optimization, for example and just to cite some of them [Lom+01; TB03]. Treatment planning systems employed to create IMPT plans have different types of specialized optimizers embedded, but they all perform the task of finding the minimum of a given cost function [Pfl+08]. The optimizer tries to answer the following question: having the dose per unit of fluence given to each point of the patient CT by each candidate beamlet characterized in the dose-influence matrix D, how

many units of fluence x should be delivered per beamlet so that the final dose distribution d fulfills the clinical criteria of tumor coverage and OAR sparing? This is the same as finding the vector x in equation 3.1 such that the dose d fulfills the clinical criteria at each patient position. The solution is found by minimizing a cost function f that includes all the criteria for the given plan.

$$Dx = d, \quad \text{explicitly:} \tag{3.1}$$

$$\overset{n \text{ beamlets}}{\rightarrow}\ \overset{m \text{ voxels}}{\downarrow}\begin{pmatrix} D_{11} & D_{12} & D_{13} & \dots & D_{1n} \\ D_{21} & D_{22} & D_{23} & \dots & D_{2n} \\ \vdots & \vdots & \vdots & \ddots & \vdots \\ D_{m1} & D_{m2} & D_{m3} & \dots & D_{mn} \end{pmatrix} \begin{pmatrix} x_1 \\ x_2 \\ \vdots \\ x_n \end{pmatrix} \overset{n \text{ beamlets}}{\downarrow} = \begin{pmatrix} d_1 \\ d_2 \\ \vdots \\ d_m \end{pmatrix} \overset{m \text{ voxels}}{\downarrow}$$

As it was introduced in the previous section, in the projects presented in this thesis, the optimization package Opt4D was employed to minimize f. Opt4D was initially developed for temporo-spatial studies [Tro+05] and it approximates x using an implementation of the quasi-Newtonian *L-BFGS* (Limited-memory Broyder-Fletcher-Goldfarb-Shanno) algorithm. D was generally constructed after post-processing of the dose array of each individual beamlet calculated with gPMC. However, when the problem was small enough, the extensions of gPMC explained in section 3.1.2, allowed for D to be directly generated during the simulation in the GPU.

The cost function f definition depended on the specific patient and goals. The cost function is a weighted sum of objectives $\omega_i g_i$ that depend on the dose distribution d and the region R they are applied to:

$$f = \sum_i \omega_i g_i(R, d) \tag{3.2}$$

It is common to include constraints in the cost functions that force the solution to be within a certain space, but constraints in Opt4D are objectivized so the only hard condition is for all elements in x to be positive ($x_i \geq 0$). In the included papers, the objectives employed were not explicitly defined, therefore, some are here stated along with their rationales to allow a better understanding of the optimizations. The summation index i refers to the voxels in the region:

- Enforce the minimum dose in the target as prescription dose d_p (3.3) and penalize over a certain maximum dose in the target (T), set as 105 % of the prescription dose (3.4):

$$g = \sum_{i \in T} (d_i - d^p)^2_- \tag{3.3}$$

$$g = \sum_{i \in T} (d_i - 1.05 \cdot d^p)^2_+ \tag{3.4}$$

- Penalize when the dose in a given voxel is superior or inferior (3.5 or 3.6) to a predefined variable dose map M in a given region R. Utilized for dose conformance to the target in IMPT planning and to fill the remaining dose to the target in the online adaptation algorithm:

$$g = \sum_{i \in R} (d_i - M_i)^2_+ \tag{3.5}$$

$$g = \sum_{i \in R} (d_i - M_i)^2_- \tag{3.6}$$

- Minimize the mean dose in a specific region $R \in OARs$ or outside the target $\bigcup_{R \in \text{Pat.}} R \setminus T$ (in the latter case the summation limits would change):

$$g = \frac{1}{N_R} \sum_{i \in R} d_i \tag{3.7}$$

- Minimize the generalized equivalent uniform dose (gEUD) in a region with a parameter a depending on the dose-volume characteristics of the organs represented by the region. The gEUD is a convex function and can represent the minimum, mean or maximum dose for $a = 0,\ 1$ or ∞. For OARs, $a = 5$ was generally employed.

$$g = \left(\frac{1}{N_R} \sum_{i \in R} d_i^a \right)^{1/a} \tag{3.8}$$

The subindex conditions $z_{+/-}$ used in the notation are defined as:

$$z_+ = \begin{cases} 0 & \text{if } z \leq 0 \\ 1 & \text{otherwise} \end{cases} \qquad z_- = \begin{cases} 0 & \text{if } z \geq 0 \\ 1 & \text{otherwise} \end{cases} \tag{3.9}$$

One of the main concerns in plan optimization is the consideration of uncertainties associated with dose calculations, treatment delivery and patient positioning, among others.

A solution to handle these uncertainties is to employ robust optimization [UCB07; PWO08; UP18], calculating and array of D matrices, one per each scenario, and solving equation 3.1 taking all of them into account, which can be done in different ways. The expected result with this technique is that the quality of the final plan would not suffer significantly when an error in treatment delivery occurs. In the projects here presented, robust optimization was not performed, therefore it is not explained here. However, in some early results for the continuation of the online adaptation project it has been utilized and it is dicussed in the project itself (chapter 7 and in the discussion in chapter 8).

3.3 Deformable image registration

Deformable image registration (DIR) is a technique that can be applied to establish a mapping between points in a coordinate system to points in another one. In the case of patient images, DIR the registration of each of the respiratory phases in a 4DCT to one selected as reference, as in the example given in figure 3.2. Another application is to relate a patient scan taken after a patient has lost some weight and the original patient scan. Registration in this context should be understood as the procedure to establish a relation between an image and another. The mapping resultant from this operation is usually called a *vector field* (v). Again, in the case of images of a patient during the breathing motion, the resultant v would contain the deformation of the patient anatomy during the breathing process and as the treatment progresses. If the patient geometry has not been deformed, but translated or rotated, *rigid image registration* can be applied by limiting the solution space to translations in x, y, z and rotations about x, y, z.

One of the most important applications of v is to use it to reassign the dose calculated in a given location in a certain image to a reference image. This procedure, called dose accumulation is used, for example, in 4D dose simulations using respiratory data to assess the effect of movement on the total dose or the effect of the evolving anatomy of a patient on the quality of a treatment plan. Examples of both applications are found in chapters 6 and 7, respectively.

Deformable registration is an ill-posed problem that lacks a unique solution. The mapping g is calculated such that it defines a vector field v between the coordinate system (x, y, z) in which image $I_0(x, y, z)$ is defined to the coordinate system $(x', y', z') = (x + v_x, y + v_y, z + v_z)$ by minimizing or maximizing a similarity metric between $g(I_0(x, y, z))$ and the target image $I(x', y', z')$. This procedure assumes that the imaging dataset is accurate and that the cost function can guide the optimization process to the global minimum. In equation 3.10 describing the cost function f to be minimized, the similarity metric is mean squared error

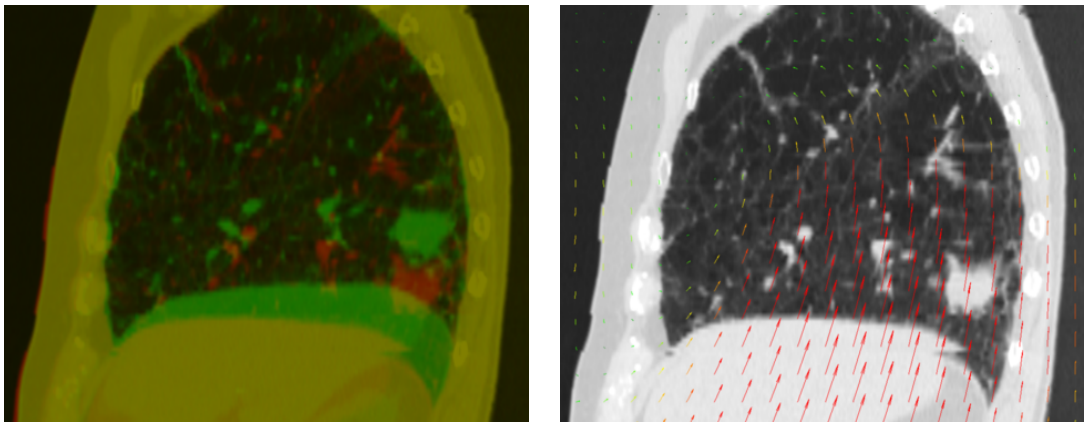

(a) (b)

Fig. 3.2 Patient deformation and DIR examples. (a) Overlay of lung cancer patient at end of inhalation (red) and expiration (green). (b) VF representing the deformation over the end of expiration.

(MSE) of the intensity between images. N can be the number of voxels or a set of points.

$$f = \frac{1}{N}\sum_{i=1}^{N}\left(I(x+v_x, y+v_y, z+v_z)_i - I_0(x,y,z)_i\right)^2 \tag{3.10}$$

Even without a unique solution, the solution space should be limited by physically unsound deformations. Therefore, penalties in the optimization process can be applied to select more physically sound transformations using regularization techniques [Sha+12].

In the studies here presented, *Plastimatch* (http://plastimatch.org), an open source software for high-performance registration with a GPU-implemented cubic B-Spline DIR algorithm [SKS10], was used for DIR. B-Splines are piece-wise polynomials that can be linearly combined to describe the mapping. Please, refer to [SKS10] for an in-depth discussion of the implementation. Several registration stages with increasingly finer B-spline grid and decreasing regularization lambda were employed for the registrations in the projects here presented. The MSE similarity metric was employed. This registration procedure was inspired by [SKS10; Sha+12].

One of the challenges of DIR is the verification of the resultant v. The simplest procedure for patient images is to have both image sets contoured and measure the overlap of corresponding structures after applying the v. If both image sets are not contoured, which was the case in the projects here introduced, visual verification can be used in the visible structures to accept the accuracy of the v. This effectively limits the applicability of DIR in automated frameworks, however, it is not a big burden for studies such as the ones here presented.

DIR is also a key step in *dose accumulation*. Dose accumulation allows to calculate the total dose given to each point of a moving geometry, such as the lung patient shown in figure 3.2. Because v relates the coordinates systems of the two images, it holds the information to relocate dose depositions in I to depositions in I_0.

Chapter 4

Results I: Further development of the GPU-MC package

In section 4.2 of this chapter, the following publication is reproduced:

Nan Qin, Pablo Botas, Drosoula Giantsoudi, Jan Schuemann, Zhen Tian, Steve B Jiang, Harald Paganetti, and Xun Jia. "Recent developments and comprehensive evaluations of a GPU-based Monte Carlo package for proton therapy". In: *Physics in Medicine & Biology* 61.20 (2016), p. 7347.

My role in the publication is clearly stated in the following subsection. Some comments on the adaptation of the publication are also given.

4.1 Role in study

This study was developed in collaboration, mainly with Dr. Qin. My role in the collaboration was: provide nuclear cross section data, simulate dose and LET distributions for benchmarking, general project discussion and manuscript discussion. All the physics data was extracted from Geant4 10.2 [Ago+03] using TOPAS [Per+12].

Comments on the adaptation of the paper: The position of figures and tables may differ from the published manuscript. The citation style and the internal figure, table and equation numbers have been altered, but the underlying meaning has been conserved.

4.2 Recent developments and comprehensive evaluations of a GPU-based MC package for proton therapy

N. Qin[1], P. Botas[2,4], D. Giantsoudi[2,3], J. Schuemann[2,3], Z. Tian[1], S. B. Jiang[1], H. Paganetti[2,3], X. Jia[1]

[1] Department of Radiation Oncology, University of Texas Southwestern Medical Center, Dallas, TX, USA

[2] Department of Radiation Oncology, Massachusetts General Hospital, Boston, MA, USA.

[3] Harvard Medical School, Boston, MA, USA.

[4] Department of Physics, University of Heidelberg, Heidelberg, Germany.

Abstract Monte Carlo (MC) simulation is commonly considered as the most accurate dose calculation method for proton therapy. Aiming at achieving fast MC dose calculations for clinical applications, we have previously developed a graphics-processing unit (GPU)-based MC tool, gPMC. In this paper, we report our recent updates on gPMC in terms of its accuracy, portability, and functionality, as well as comprehensive tests on this tool. The new version, gPMC v2.0, was developed under the OpenCL environment to enable portability across different computational platforms. Physics models of nuclear interactions were refined to improve calculation accuracy. Scoring functions of gPMC were expanded to enable tallying particle fluence, dose deposited by different particle types, and dose-averaged linear energy transfer (LETd). A multiple counter approach was employed to improve efficiency by reducing the frequency of memory writing conflict at scoring. For dose calculation, accuracy improvements over gPMC v1.0 were observed in both water phantom cases and a patient case. For a prostate cancer case planned using high-energy proton beams, dose discrepancies in beam entrance and target region seen in gPMC v1.0 with respect to the gold standard tool for proton Monte Carlo simulations (TOPAS) results were substantially reduced and gamma test passing rate (1%/1 mm) was improved from 82.7%-93.1%. The average relative difference in LETd between gPMC and TOPAS was 1.7%. The average relative differences in the dose deposited by primary, secondary, and other heavier particles were within 2.3%, 0.4%, and 0.2%. Depending on source proton energy and phantom complexity, it took 8-17 s on an AMD Radeon R9 290x GPU to simulate 107 source protons, achieving less than 1% average statistical uncertainty. As the beam size was reduced from 10×10 cm^2 to 1×1 cm^2, the time on scoring was only increased by 4.8% with eight counters, in contrast to a 40% increase using only one counter. With the OpenCL environment, the portability of gPMC v2.0 was enhanced. It was successfully executed on different CPUs and GPUs and its performance on different devices varied depending on processing power and hardware structure.

4.2.1 Introduction

The Monte Carlo (MC) method is widely regarded as the gold standard for proton therapy dose calculations [Pag+08; Sch+14; Sch+15]. Computational efficiency has been a major issue preventing its wide application in the clinic and hindering its utilization in research. Over the years, there have been tremendous efforts devoted to accelerating proton MC dose calculation [Koh+03; FS04; Li+05]. In particular, graphics-processing unit (GPU) platforms have been recently employed to speed up the computations and significant acceleration factors have been achieved [Yep+09; Jia+12; JZJ14; Ma+14; TMB15]. We have developed a

proton MC dose calculation package, gPMC v1.0 on GPU [Jia+12]. The transport physics of gPMC was mainly based on that developed by Fippel and Soukup [FS04]. GPU-friendly implementations were designed to achieve a high computational efficiency. With an NVIDIA Tesla C2050 GPU, the simulation time for 10^7 source protons ranged from 6-22 s depending on the source proton energy and the phantom or patient complexity [Jia+12].

Despite the success, the gPMC code left room for improvement regarding its acc uracy, functionality, and suitability for clinical uses. It is desirable to refine the model for nuclear interaction to improve accuracy. There existed a few approximations in the original gPMC physics model [FS04]. In a study evaluating dose calculation in 30 patients, gPMC was compared to the gold standard MC package TOPAS [Per+12; Tes+13]. Sufficient accuracy of gPMC in most cases was reported with gamma passing rate (1%/1 mm) over 94% for voxels within 10% isodose line. However, ~2% systematic overestimation of dose in the entrance region and 1-2% underestimation in the target was observed for prostate cancer cases [Gia+15]. This discrepancy was ascribed to the relatively simple model of nuclear interactions, which appeared less accurate in dose calculations for a high-energy proton beam because of the ~1% primary protons undergoing a nuclear interaction per cm water equivalent depth. Recently, another GPU-based proton MC simulation package was developed [TMB15], which utilized a more accurate nuclear interaction model. Yet the inclusion of a complex model inevitably impacted the computational efficiency. Hence, it was our aim to refine the physics model in gPMC to maintain its simplicity, while achieving a sufficient level of dose calculation accuracy for clinical applications.

Furthermore, the suitability of gPMC for clinical and research applications was previously limited by several factors. First, the use of NVidia's Compute Unified Device Architecture (CUDA) [NVI11] tied gPMC to NVidia GPU cards, hindering its portability to other GPUs and conventional CPUs. Recently, Open Computing Language (OpenCL) was introduced into the high-performance computing field. It provides a framework for developers to write programs that are executable across different platforms, including conventional CPUs, CPU clusters, and GPUs from different manufacturers. There has been an initial study regarding the use of OpenCL as the development platform for GPU-based MC dose calculation [Tia+15]. In this paper, we will present our implementations of gPMC on the OpenCL environment.

In addition, there is a great desire to use MC to compute quantities other than just the physical dose. For instance, there has been growing interest in research to consider the variation of the proton relative biological effectiveness (RBE) in treatment planning instead of using a constant value of 1.1 [Pag14]. Due to the complexity of computing tissue specific RBE values, it was proposed to use linear energy transfer (LET) as a surrogate

[Gia+13]. Enabling accurate and fast computation of LET in gPMC would greatly facilitate its application in proton biology. Hence, we have included functions in gPMC to score LET.

Our new study also includes a comprehensive evaluation of gPMC's accuracy. This evaluation yields an in-depth understanding about the capability and limitation of gPMC depending on different applications. The total physical dose has typically been the quantity of interest when establishing the accuracy of a fast MC code. To obtain a more detailed evaluation of the performance of our updated gPMC code, this paper will also compare deposited dose differentiated by particle types, LET, and particle fluence to gold standard results computed by TOPAS.

4.2.2 Methods

4.2.2.1 Updates in physics model

Protons undergo different types of interactions when propagating in a medium. For an electromagnetic interaction channel, gPMC employed a class II condensed history simulation scheme. The accuracy of transport in this channel has been previously demonstrated [Jia+12] by performing simulations with only this channel and comparisons with TOPAS.

Protons also undergo interactions with nuclei. gPMC v1.0 followed the empirical strategy developed previously by Fippel and Soukup [FS04] to model interactions in three channels: proton-proton elastic interaction, proton-oxygen elastic interaction and proton-oxygen inelastic interaction. The total cross section data in this model were obtained through an empirical fit. In gPMC v2.0, the data were extracted and tabulated from the Geant4 system (release 10.2). In addition, we employed a new model to sample the proton angular distribution after nuclear interactions. For proton-proton elastic scattering, the kinetic energy of the scattered proton was sampled from a uniform distribution in gPMC v1.0 and the scattering angle was determined via kinematics. In the new version of the code, we sample the proton scattering angle θ according to the differential cross section in the center-of-mass frame given by [Ran72]

$$\frac{\mathrm{d}\sigma_{el}}{\mathrm{d}\Omega} \approx A^{1.63} \exp\left(14.5A^{0.66}t\right) + 1.4A^{0.33} \exp\left(10t\right), \tag{4.1}$$

where A is the mass number of the target and $t \equiv -2p^2(1-\cos\theta)$ is the invariant momentum transfer (p being the momentum of the scattered proton). Sampling of the variable t is achieved via a rejection method. Specifically, we first sample t uniformly in the interval $[0, -4p^2]$. Then another random variable ξ is uniformly sampled between 0 and $A^{1.63} + 1.4A^{0.33}$ to reject the sampled t, if ξ is greater than $\frac{\mathrm{d}\sigma_{el}}{\mathrm{d}\Omega}$. Other kinematic quantities, including

the θ and recoil proton momentum, are determined and transformed to the laboratory coordinate system.

For proton-oxygen inelastic scattering, the deflection angle of secondary protons in gPMC v1.0 was sampled such that $\cos\theta$ is uniformly distributed in the interval $[2T_s/T_p - 1, 1]$, where T_s and T_p are the kinetic energies of the secondary proton and incidental primary proton, respectively. However, the proton scattering angles generated as such were not sufficiently forward peaked and the unphysical cutoff at $\cos^{-1}(2T_s/T_p - 1)$ excluded some large scattering angles. To overcome these problems, we empirically modified the sampling methods to yield a distribution of $\cos\theta$ that is forward peaked within $[0, \pi]$. The new probability density function is

$$P\{x \leq \cos\theta < x + \mathrm{d}x\} = \frac{\xi e^{\xi x}}{e^{\xi} - e^{-\xi}}\,\mathrm{d}x. \tag{4.2}$$

This is achieved by sampling $\cos\theta$ as

$$\cos\theta = \ln\left[\eta\left(e^{\xi} - e^{-\xi}\right) + e^{-\xi}\right]\frac{1}{\xi}, \tag{4.3}$$

where η is a random number uniformly distributed in $[0, 1]$ and $\xi \equiv \lambda T_s/T_p$. λ is a parameter fitted to be 6.5 according to nuclear data published by the ICRU [Mal01].

The main difference between gPMC and TOPAS lies in the simulation of nuclear interactions. By default, TOPAS uses the quark gluon string model for high-energy hadronic interactions of protons, and the binary cascade model for low energy interaction of protons and ions [Ago+03]. These models describe physics processes in detail and provide good agreement with experiments [WYD15]. Due to the sophisticated calculations involved, simulating according to these models is time consuming. On the contrary, gPMC employs simpler models, as described above, to achieve high efficiency and sufficient accuracy for dose calculations in radiation therapy. The empirical cross section for elastic collision in equation 4.1 matches with experimental data [Bel+66] and is convenient for sampling. The total cross section data for inelastic collisions are from the fitted model developed in Fippel and Soukup [FS04]. The angular distribution of secondary protons is empirically chosen to match published data.

4.2.2.2 OpenCL implementation

We have rewritten gPMC in OpenCL to improve code portability across various platforms and devices. An OpenCL program is composed of a host program and one or more kernel functions. A host program is the outer control logic that performs the configuration and

usually runs on a general purpose CPU. Kernel functions are C-based routines executed on a computing device, e.g. a GPU. In OpenCL, parallel computing is achieved by simultaneously executing kernel functions with independent elements, namely work-items (which NVIDIA refers to as "CUDA threads"). At a hardware level, each work-item corresponds to a multiple processing core. A collection of related work-items that execute on a single computing unit (composed of one or more multiple processing cores) is called a work-group. Devices such as GPUs and CPU clusters that have a large number of processing cores can thus be programed to accomplish high performance computation. This structure is essentially the same as in CUDA. Hence, we transformed gPMC from the previous CUDA platform to the OpenCL platform with the code structure remaining unchanged.

Memory management is another critical issue in parallel computing. The memory model in OpenCL defines four virtual memory regions on the computing device with different size, accessibility, read/write speed and other features. The global memory is accessible to all work-items and has the largest size but low speed. In gPMC v2.0, physics data and patient data are stored as image objects in the global memory. The image object also supports fast hardware interpolations using built-in sampler functions. The position, momentum and weight of the protons are initialized as buffer objects, which are dynamically allocated on the host side and transferred to the global memory. Because the protons frequently change position, direction and energy, it is inefficient to repeatedly visit the buffer objects in the global memory during simulation. Therefore, at the beginning of the particle transport kernel execution, the information of one particle is read by the corresponding work-item from the global memory into its individual private memory, which is small but allows fast access. The dose, LET and fluence counters, as well as the stack for secondary protons, are allocated as buffer objects in the global memory, since they require relatively large memory space and need to be accessible to all work-items.

Since there is no OpenCL-based library for random number generators, we implemented a random number generator (RNG) using the MT19937 algorithm [MN98] to generate a random sequence with a period of $2^{19937} - 1$. The random seeds in each work-item are initialized with the system clock and its unique thread ID at the code initialization stage. Therefore the random number sequences generated by different work-items are assumed to be independent.

To achieve high efficiency, single precision floating-point variables are used, because GPUs have much higher processing power on single precision than double precision (e.g. ~3.5 times higher in peak performance in GFLOPS (giga-floating-point operations per second) for NVidia TITAN GPU and ~8 times higher for AMD Radeon R9 290x GPU). In addition, the image objects and their associated fast hardware interpolation on GPU cards are only

available for single precision. However, a pitfall of using single precision floating-point variables is the potential loss of precision, particularly when two numbers with a largely different order of magnitude are added [Mag+15]. This could occur during a simulation when a large number of protons are simulated, and hence the dose deposition from an additional proton is much smaller than the total dose. To avoid such a problem, gPMC runs in a batched fashion. After each batch of simulation, the code copies data from dose counters to an additional memory buffer. This method effectively eliminates the large difference between each dose deposition and the total dose, hence avoiding the potential loss of precision [Mag+15].

4.2.2.3 Memory writing conflict

The memory conflict during dose scoring limited the overall computational efficiency in gPMC v1.0 [Jia+12]. Specifically, when more than one work-item tried to write to the same block of memory, the writing actions were serialized to avoid unpredictable results. This serialization counteracts the parallel processing efficiency achieved by GPUs. To mitigate this problem, a multi-counter technique is employed in gPMC v2.0. As such, a number of M dose counters are allocated at the code initialization stage. During particle transport simulation, when a work-item tries to update a dose counter, it randomly chooses one counter and deposits the dose to it. This approach reduces the scoring time, because the probability of two worktems updating the same counter is inversely proportional to the number of counters. However, the number of counters M, is limited by the memory size of computing devices, especially in the cases with a high-resolution phantom. gPMC v2.0 checks the memory size at its initialization stage and notifies users if the memory becomes a limitation. The use of multiple counters also leads to additional overheads, such as memory allocation, memory addressing when depositing energy to a certain counter, and combining data from different counters. The impact of these factors will be analyzed in detail later in section 4.2.3.5.

4.2.2.4 Scoring quantities

In gPMC v1.0, only the physical dose was scored. However, recent research on proton RBE suggests using LET for biological dose calculations [MSP15; Pol+15]. We thus implemented the scoring of dose-averaged LET (LETd) in gPMC v2.0. LETd in each voxel was calculated as

$$\mathrm{LETd} = \frac{\sum_i \delta E_i \times \dfrac{\delta E_i}{\delta l_i}}{\rho \sum_i \delta E_i}, \tag{4.4}$$

where ρ is the voxel density, δE_i is the energy deposition corresponding to a step δl_i plus the energy of the δ-electron that were created along the step, and the summation is over all energy deposition events in a given scoring volume. During simulation, it is possible to have a proton moving a very small step but kicking out a δ-electron with relatively large energy. In such cases $\delta E_i/\delta l_i$ can give values of several thousand MeV cm^{-1}, known as LET spikes. Given that the maximum proton LET in water is around 830 MeV cm^{-1} (ICRU 49), we applied a cutoff at 1000 MeV cm^{-1} on $\delta E_i/\delta l_i$ to avoid these spikes. In case an event is neglected by the cutoff, its energy is not taken into account when averaging the LET by dose.

gPMC v2.0 also supports scoring particle fluence defined as

$$\phi_j = \frac{\sum_i \delta l_{ij}}{V}, \tag{4.5}$$

for voxel j where $\sum_i \delta l_{ij}$ is the summation of all step lengths in that voxel and V is the voxel volume. During proton transport, secondary protons and other heavier ions are produced in nuclear interactions. To distinguish the contribution of different components, the dose of primary protons, secondary protons and other heavier ions are scored separately in gPMC v2.0.

4.2.2.5 Validation cases

A set of studies was performed to demonstrate the functionality of the new gPMC code, as well as to comprehensively validate its accuracy. Specifically, the total dose, the dose of primary protons, secondary protons and other heavier ions, fluence of primary protons and secondary protons, as well as LETd were compared to the results computed by TOPAS [Per+12]. For dose comparison, a pencil beam with zero width was simulated and the result was integrated laterally to obtain the dose distribution of a broad beam with a size of 5×5 cm^2. The choice of a pencil beam was because dose and fluence distributions on the central beam axis from this infinitesimal beam are very sensitive to discrepancies in angular deflection and the angular distribution of protons. In contrast, the broad beam is more realistic and was hence used to evaluate the accuracy in a more clinically relevant setup. For LETd comparison, 2×2 cm^2 broad beams were studied. The phantom we used was a pure water phantom of $10.1 \times 10.1 \times 30$ cm^3 in dimension with a voxel size of $0.1 \times 0.1 \times 0.1$ cm^3; 100 MeV and 200 MeV mono-energetic beams normally impinged on the phantom surface.

The second scenario studied was a prostate cancer patient. gPMC v1.0 was reported to have a systematic overestimation in the dose at the entrance region and underestimation at the target for prostate cases due to approximations in nuclear interaction models [Gia+15].

To demonstrate the improvements made in this new version, a prostate cancer patient with two laterally opposite beams was used. The dose in this patient was computed with gPMC v1.0, gPMC v2.0 and TOPAS.

The efficiency and cross-platform portability of gPMC v2.0 were tested with several different devices, including an NVidia GeForce GTX TITAN GPU card, an AMD Radeon R9 290x GPU card, an Intel i7-3770 CPU processor and an Intel Xeon E5-2640 CPU processor. We also conducted tests with different numbers of dose counters to investigate its impact on the memory conflict issue.

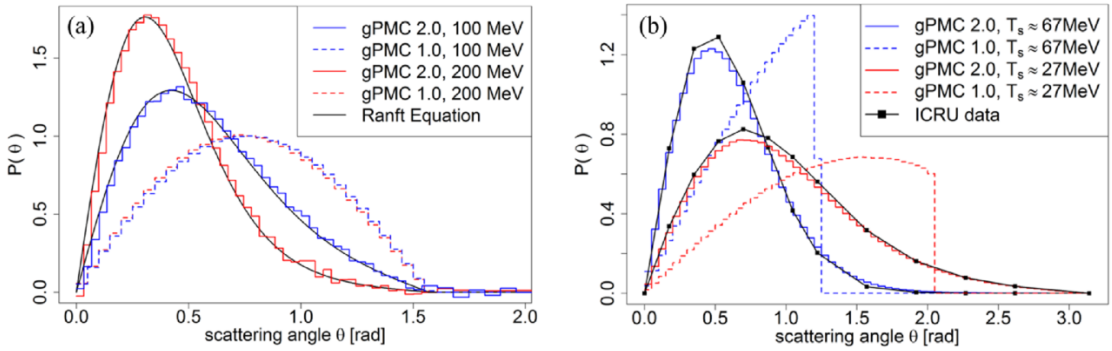

Fig. 4.1 (a) Angular distribution of scattered protons after proton-proton elastic scattering with incoming proton energies of 100 MeV and 200 MeV. (b) Angular distributions of secondary protons with kinetic energy around 67 MeV and 27 MeV after proton-oxygen inelastic scattering with incoming proton energy of 100 MeV. Adapted from [Qin+16].

4.2.3 Results

4.2.3.1 Angular distribution corrections

The physics model of proton-proton elastic scattering and proton-oxygen inelastic scattering was modified in gPMC v2.0. The total cross section data was updated as well. The improvement of proton-proton elastic scattering is illustrated in figure 4.1(a). In gPMC v1.0, distributions of the scattering angle are almost identical among different incoming proton energies. On the contrary, the distributions are energy dependent and are more forward-peaked in gPMC v2.0, according to equation 4.1. The improvement of scattering angle distributions in the proton-oxygen inelastic interaction channel shown in figure 4.1(b) demonstrates a better agreement of scattering angles with the ICRU data in gPMC v2.0 as compared to gPMC v1.0. The inaccurately modeled scatter angle in gPMC v1.0 does not cause a large dose discrepancy in broad beam cases. However, the problem will appear in pencil beam cases that are more sensitive to proton scattering angles, as will be shown later.

4.2.3.2 Dose and fluence distributions in a water phantom

Figures 4.2 and 4.3 present the dose calculations in comparison with the TOPAS results. The dose distributions of pencil beams were computed and the results were integrated laterally to obtain the corresponding result of broad beams. The uncertainty σ in each voxel is estimated by the dose results in all multi-counters in our simulation. All the figures below the error bars for the gPMC v2.0 results correspond to 2σ values after simulating 1×10^7 primary protons. Those for the TOPAS results are not drawn for clarity. We have also calculated average uncertainty $\overline{\sigma/D}$, over a high dose region where the local dose exceeds 10% of D_{max} inside the entire phantom. For all the cases $\overline{\sigma/D}$ is less than 1%.

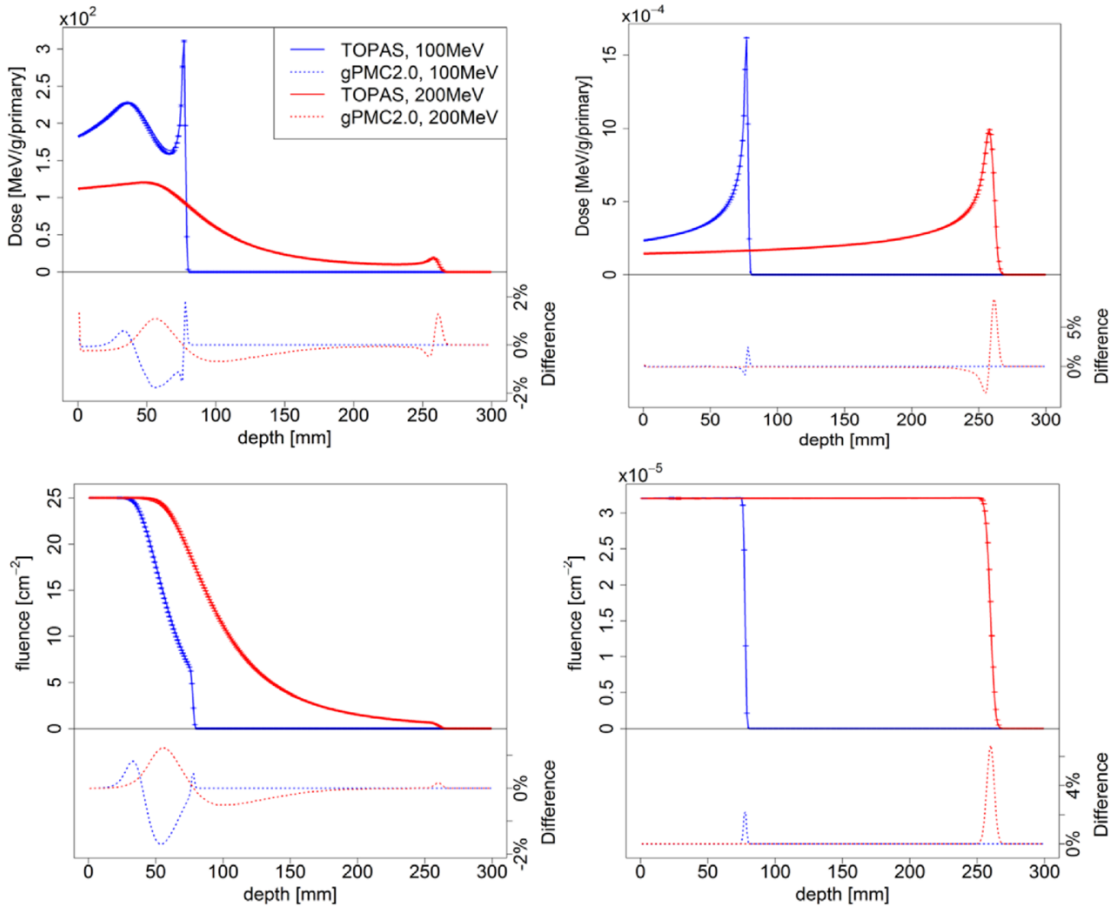

Fig. 4.2 Depth dose (top row) and fluence (bottom row) curves of 100 MeV (blue) and 200 MeV (red) proton pencil beams (left column) and broad beams (right column) in a homogeneous water phantom considering only electromagnetic interactions.

Electromagnetic interactions We first present the simulation results in the water phantom with only electromagnetic interactions, because protons deposit energy mainly through this

channel. Figure 4.2 shows the depth dose and fluence curves of 100 MeV and 200 MeV protons. The broad beam doses and fluences match very well with the TOPAS simulation results, except at the gradient Bragg peak region. The accuracy of broad beam dose calculations has been demonstrated previously. For the pencil beam cases considered in this paper, small dose differences (within 2%) are observed and can be ascribed to the difference in the modeling of multiple scattering. Because pencil beams are the most sensitive cases, these simulations are where discrepancies in multiple scattering become apparent. In contrast, differences are smeared out rapidly with increasing beam width leading to a negligible difference for broad beams. The relatively large discrepancy at the beam's end of range was due to a sub-mm difference in the beam ranges.

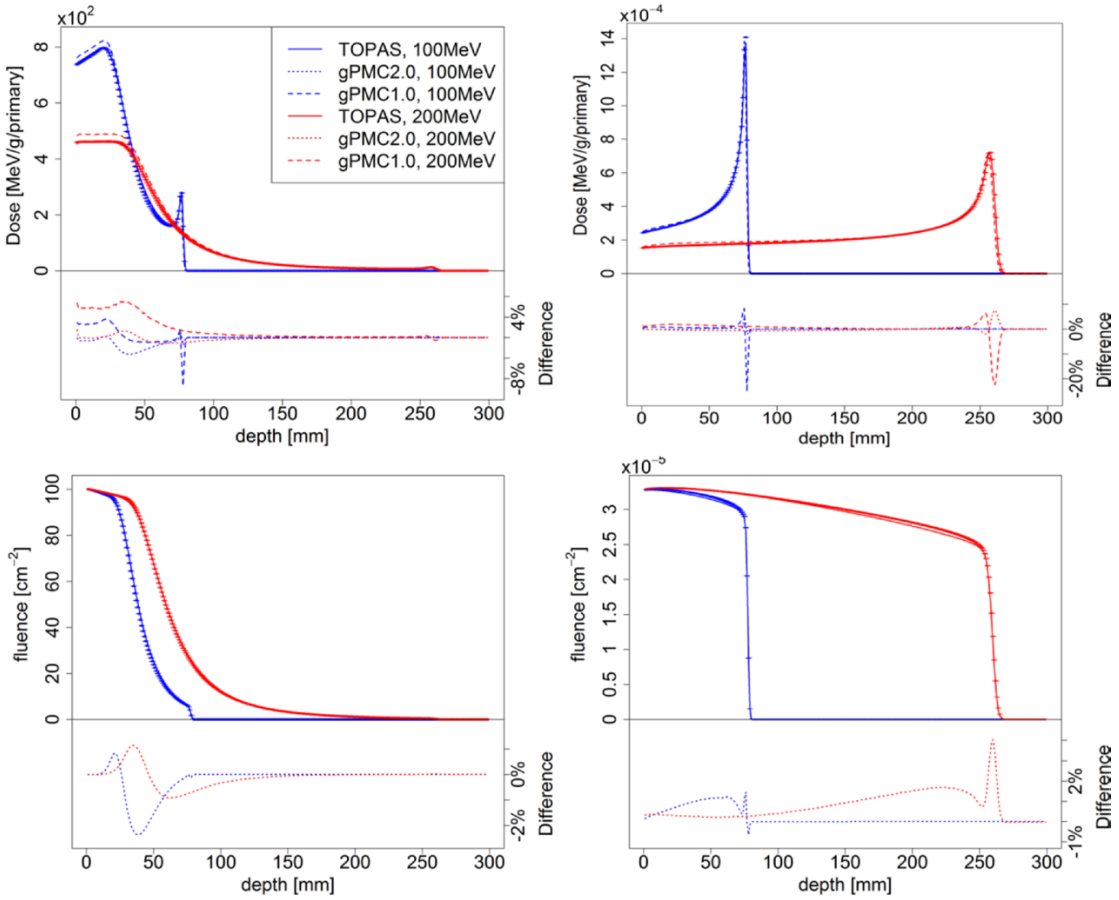

Fig. 4.3 Depth dose (top row) and fluence (bottom row) curves of 100 MeV (blue) and 200 MeV (red) proton pencil beams (left column) and broad beams (right column) in a homogeneous water phantom with all interactions considered. Adapted from [Qin+16].

Nuclear interactions Figure 4.3 illustrates the depth dose and fluence curves of 100 MeV and 200 MeV protons transport in water when switching on the feature of simulating nuclear

interactions. For comparison, dose distributions calculated with gPMC v1.0 are also presented. The most significant improvement is in the entrance region, where the dose overestimation from gPMC v1.0 was removed in gPMC v2.0 as a result of the improved nuclear interaction models. Dose discrepancies around the Bragg peak region are also significantly reduced. For gPMC v2.0, the dose distributions of broad beams match well with TOPAS, but for pencil beams, a relative difference up to 3% were observed. The relatively large dose discrepancy at the end of the beam due to a small range difference was also observed.

In figure 4.4, we present the dose contributions from different particle components for both 100 MeV and 200 MeV broad beams. The dose from primary protons is the major component and matches well with TOPAS. However, discrepancies in the secondary proton dose and other heavier particle doses can be identified for two reasons. First, gPMC and TOPAS use different physics models for nuclear interactions. Second, in gPMC, secondary ions (heavier than protons) are assumed to have ranges smaller than a voxel and hence their energies are locally deposited instead of tracking.

To quantitatively evaluate the agreement, the relative dose difference was computed for each component, defined as $\left|d^i_{\text{gPMC}} - d^i_{\text{TOPAS}}\right| / d^t_{\text{max}}$. Here $|\cdot|$ is the standard L2 vector norm, d^i is a vector consisting of the dose for the ith component (i = 1, 2, 3 for primary protons, secondary protons, and heavy particles) in voxels with doses greater than 10% of the maximum dose (within 10% isodose line), and d^t_{max} is the maximal value of the total dose computed by TOPAS. The results are 1.1%, 0.1%, and 0.2% for the 100 MeV beam and 2.3%, 0.4%, and 0.2% for the 200 MeV beam, respectively.

4.2.3.3 LETd distributions

Figure 4.5 illustrates the LETd distributions in water for 100 MeV and 200 MeV mono--energetic broad beams. The physical dose calculated by gPMC is also presented for reference. The LETd spikes are observed laterally outside the beam width and beyond the Bragg peak region due to secondary protons in low dose regions. This artifact needs to be corrected for biological dose computations (this is done within TOPAS by evoking different user-defined scoring techniques). The low proton numbers in these regions resulted in LETd values with a large uncertainty. Quantitatively, we computed the relative difference between the two LETd results as $\left|\text{LETd}_{\text{gPMC}} - \text{LETd}_{\text{TOPAS}}\right| / \text{LETd}_{\text{max}}$, where LETd is a vector consisting of calculated results in voxels within the 10% isodose line. This difference was found to be 0.7% and 1.1% for 100 MeV and 200 MeV beams respectively, indicating a good agreement.

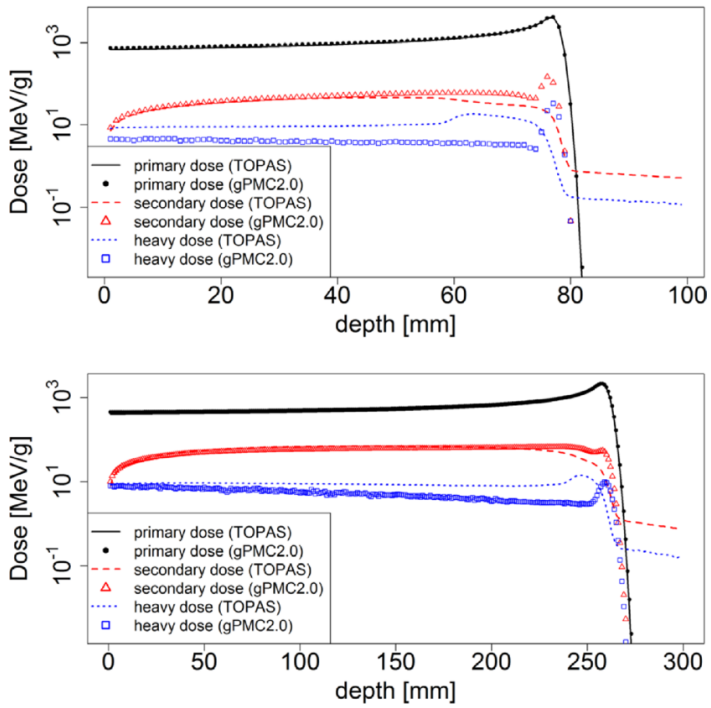

Fig. 4.4 Dose from different components including primary protons, secondary protons and heavy ions after 100 MeV (top) and 200 MeV (bottom) broad proton beams impinging on a homogeneous water phantom. Adapted from [Qin+16].

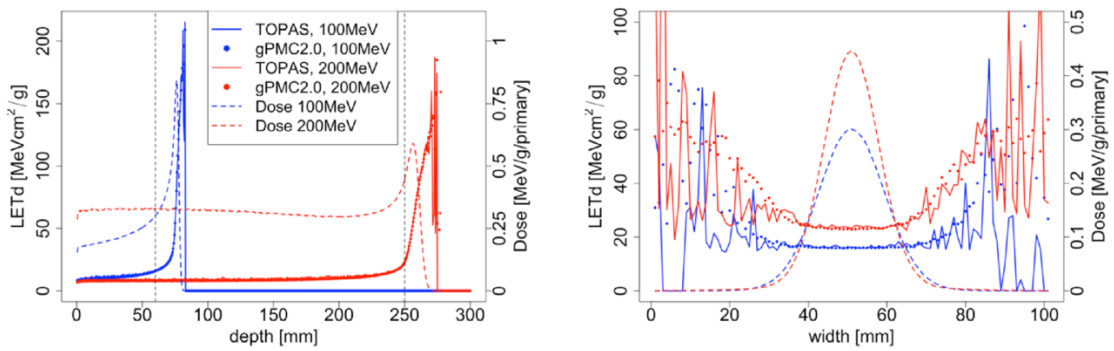

Fig. 4.5 Left: LETd depth curves of 100 MeV (blue) and 200 MeV (red) proton beams; right: lateral profile of 100 MeV beam at 60 mm depth and 200 MeV beam at 250 mm depth as indicated by dashed vertical lines in left. Adapted from [Qin+16].

4.2.3.4 Patient case

One of the motivations to improve physics modeling was to resolve the dose discrepancies observed between gPMC v1.0 and TOPAS calculations for prostate cancer cases. The main reason was the inaccuracy of the nuclear interaction model and data. After the model refinement in this study, significant improvements are observed, as illustrated in figure 4.6.

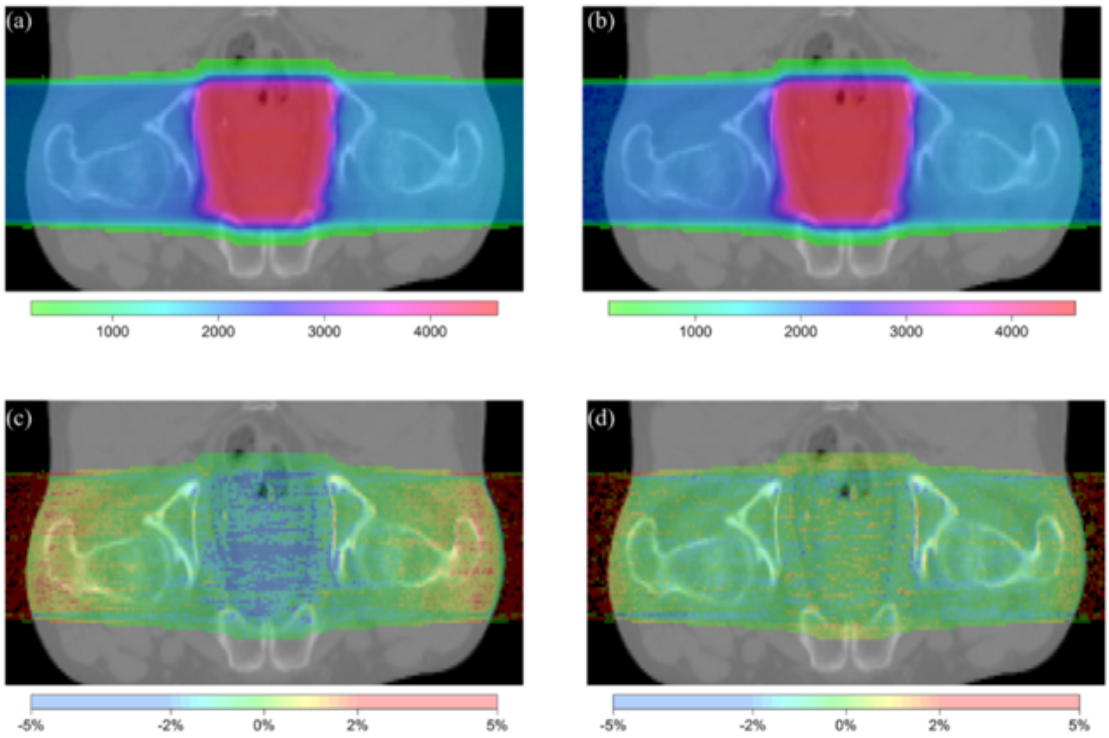

Fig. 4.6 2D comparison between gPMC v2.0 and TOPAS for doses in a prostate cancer patient. (a) TOPAS-calculated dose distribution. (b) gPMC v2.0-calculated dose distribution. (c) Relative dose difference of gPMC v1.0 as ((gPMC v1.0-TOPAS)/prescribed dose). (d) Relative dose difference of gPMC v2.0 as ((gPMC v2.0-TOPAS)/prescribed dose). Adapted from [Qin+16].

Both the overestimation in the entrance region and the underestimation in the target region seen in gPMC v1.0 are largely reduced. To further investigate the accuracy, we calculated the gamma index with a GPU-based gamma index computational tool [GJJ11]. The passing rate for the 1%/1 mm criterion improved from 82.7%-93.1% in the region with doses greater than 10% of the maximum dose.

4.2.3.5 Efficiency and portability evaluations

We first compared the computational efficiency of gPMC v2.0 with a different number of dose counters to study the impact of the memory writing conflict. Table 4.1 illustrates the simulation time of different beams on two GPUs with 1, 4, 8 and 16 dose counters. As expected, memory conflicts are more severe for pencil beams because most protons are not scattered beyond the central axis voxels, and hence almost all the threads simultaneously update the same memory address when scoring the dose. With multiple dose counters, the speed of simulating pencil beams is significantly improved, especially for low energy protons,

Table 4.1 Simulation time in seconds for cases with a different number of dose counters on NVidia and AMD GPUs. Adapted from [Qin+16].

		Number of dose counters			
Beam	Device	1	4	8	16
100 MeV pencil beam	NVidia GeForce GTX TITAN	50.35	8.36	7.73	7.77
	AMD Radeon R9 290x	23.07	8.27	7.99	10.44
100 MeV 10×10 cm^2 beam	NVidia GeForce GTX TITAN	5.63	6.32	6.89	7.71
	AMD Radeon R9 290x	4.85	6.44	7.77	10.72
200 MeV pencil beam	NVidia GeForce GTX TITAN	35.51	20.59	20.03	20.39
	AMD Radeon R9 290x	27.92	16.26	16.57	18.95
200 MeV 10×10 cm^2 beam	NVidia GeForce GTX TITAN	16.77	19.05	20.21	21.19
	AMD Radeon R9 290x	13.46	15.93	17.41	20.67

Note: For each case 1×10^7 primary protons in water were simulated.

since most of them still remain in the central axis voxels at the end of their range where energy deposition events and consequent memory writing happens more frequently. On the other hand, the memory writing conflict was not a significant problem for broad beams and hence a single dose counter worked well. To further understand this effect, we recorded the dose deposition time as a function of field size and number of dose counters. The results are plotted in figure 4.7. As the beam size was reduced from 10×10 cm^2 to 1×1 cm^2, the time on scoring was only increased by 4.8% with eight counters, in contrast to a ~40.0% increase of the scoring time when using only one counter.

Table 4.2 Simulation time in seconds of gPMC v2.0 on different devices. Adapted from [Qin+16].

Beam	NVidia GeForce GTX TITAN GPU	AMD Radeon R9 290x GPU	Intel i7-3770 CPU	Intel Xeon E5-2640 CPU
100 MeV pencil beam	7.73	7.99	187.06	24.29
200 MeV pencil beam	20.03	16.57	554.13	67.68

Note: For each case we used 8 dose counters to simulate 1×10^7 primary protons in water.

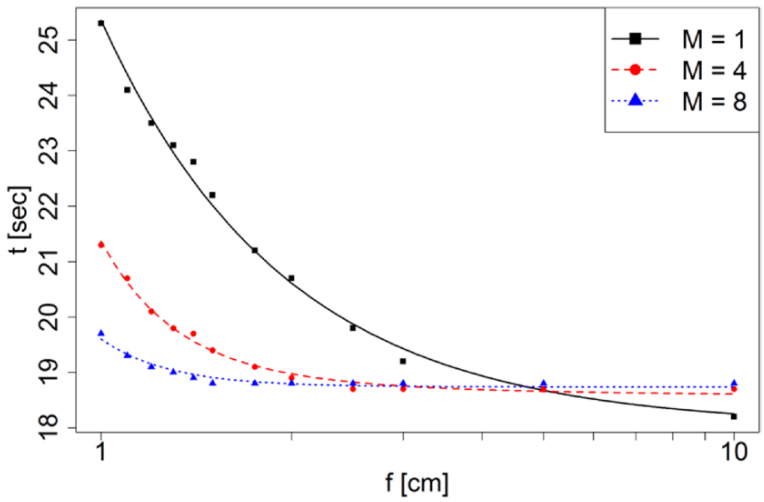

Fig. 4.7 Dose deposition time as a function of field size f and number of dose counters M. Adapted from [Qin+16].

To further understand the factors of scoring time, let us denote the number of dose deposition events in a simulation as N and the probability of memory conflict as p. The total dose deposition time can be expressed as the sum of three terms $t = t_{\text{Non-conflict}} + t_{\text{Conflict}} + t_{\text{Counter}}$. The first term is the time for deposition events executed in parallel by all GPU threads without encountering the memory conflict issue. Hence $t_{\text{Non-conflict}} = N(1-p)\Delta t/N_t$, where Δt is the dose deposition time per event and N_t is the total number of threads. The second term t_{Conflict} is the time for dose deposition events with memory conflict. Suppose these events occurred in N_v voxels. Since events at different voxels do not encounter any memory conflict, $t_{\text{Conflict}} = Np\Delta t/N_v$. Furthermore, let us denote the field size as f^2. N_v is then proportional to f^2, namely $N_v = \beta f^2$. The probability of memory conflict p is inversely proportional to f^2 and the number of dose counters M, namely $p = \alpha/(Mf^2)$. The third term corresponds to the overhead due to the use of multiple dose counters, which is proportional to M, namely $t_{\text{Counter}} = \lambda M$. Putting everything together, we can write the total dose deposition time as

$$t = \frac{N\Delta t}{N_t}\left(1 - \frac{\alpha}{Mf^2}\right) + \frac{\alpha N\Delta t}{\beta M f^4} + \lambda M \tag{4.6}$$

With this model, we fitted our experimental data as a function of M and f and the results are shown in figure 4.7. The successful data fitting confirms our model. Note that multiple dose counters also require a larger memory space, so one should be careful when running the code on computing devices which have limited memory. gPMC v2.0 allows users to specify the number of dose counters.

To test the portability of gPMC v2.0, we ran it on two Intel CPUs and two GPUs manufactured by NVidia and AMD, respectively. Simulation times are presented in table 4.2. The performances of the two GPUs were of the same order, as the two cards have similar computation power. For high energy beams, the performance of the AMD card was slightly better than the NVidia card. This was also observed in a previous article of an OpenCL MC dose engine for photon radiation therapy, in which it was attributed to the superiority of the AMD card over the NVidia card at the hardware level. The speed of the CPUs was lower than the GPUs since CPUs have much fewer cores. Between the two CPUs, the 32-core Intel Xeon E5-2640 CPU performed much better compared to the Intel i7-3770 CPU that has only eight cores.

4.2.4 Conclusion and discussion

Our recent updates on the GPU-based MC dose calculation package, gPMC, are reported in this paper. The new version, gPMC v2.0, was developed under the OpenCL environment to enable portability across different platforms. Physics models of nuclear interactions were refined to improve calculation accuracy. Scoring functions of gPMC were expanded to enable tallying particle fluence and LET in addition to absorbed dose. A multiple counter approach was employed to mitigate memory writing conflict problems. Comprehensive evaluations on accuracy, efficiency and portability of gPMC v2.0 were also performed. Accuracy improvements over gPMC v1.0 were observed for both homogeneous water phantoms as well as a prostate patient case. In particular, for a prostate cancer treatment requiring high-energy beams, dose discrepancy in beam entrance and target regions seen in gPMC v1.0 with respect to the gold standard TOPAS calculations has been substantially reduced as a consequence of refined nuclear interaction models. Besides the total dose, particle fluence, LETd, and dose contributed by different particle components were also compared with TOPAS results, showing reasonable agreements.

The computation time of gPMC v2.0 was found comparable to the previous 1.0 version. The multi-counter approach was also found to be effective. As the beam size was reduced from 10×10 cm^2 to 1×1 cm^2 , the time for scoring only increased by 4.8% with eight counters in contrast to a 40.0% increase of the scoring time when using only one counter. With the OpenCL environment, the portability of gPMC was enhanced. It was successfully executed on different CPUs and GPUs, and its performance on different devices was found to vary depending on hardware processing power and structure. Meanwhile, the OpenCL code is not always the best option for a specific GPU type in terms of performance. For instance, CUDA has a higher efficiency than OpenCL on NVidia's GPU. Hence, we have

also maintained the CUDA version of gPMC. The physics refinement, LETd scoring and multi-counter approach reported in this manuscript were also included in the CUDA version.

Scoring of LET is a new and useful feature in gPMC v2.0 that could facilitate a number of studies regarding proton radiobiological effects. It has been proposed in recent studies to use LET as a surrogate for RBE in order to evaluate plan quality from a biological perspective. It can be incorporated into treatment planning to develop treatment plans, not only optimal in terms of physical dose, but also in terms of LET [Gia+13; Pag14; Wan+16]. For plan optimization studies, the new gPMC version is expected to be beneficial compared to Monte Carlo codes, such as TOPAS, because of its capability for rapid LET calculation. Especially for LET-based inverse treatment planning, the fast computation will be critical to ensure clinical applicability of this method.

The validity of using gPMC does depend on specific problems of interest. For clinical studies on dose calculation, the overall agreement between gPMC and TOPAS is acceptable. There is a discrepancy between the two MC engines in terms of secondary proton and heavier particle doses, as illustrated in figure 4.4. This is mainly due to the fact that different nuclear interaction models are employed in gPMC and TOPAS. Because these components account for only a small fraction of primary proton dose (2-3 orders of magnitude less), this discrepancy does not significantly impact the total dose distribution. Yet, one should be cautious when using gPMC to study the effects sensitive to secondary protons or other heavier particles in proton therapy.

The RNG used in gPMC was implemented in a straightforward fashion. Each GPU thread kept its own random number state, which was updated each time a random number was produced. It is noted that efficient RNG SFMT19937 under the single instruction multiple data (SIMD) scheme has been previously developed [SM08]. This method stores a global state array of 128 bit integers of length 156. The block generation approach can efficiently produce a group of random numbers employing the SIMD scheme. However, it may be difficult to incorporate this method in our MC simulation. If only one global state array is allocated, since different GPU threads perform particle transport simulation in a random fashion, they will need to access and modify the state array randomly, which will cause memory-writing conflict. On the other hand, if each GPU thread holds its own global state array, due to the large number of GPU threads, GPU memory size would become a limiting factor. The solution to incorporate the SFMT19937 in our MC simulation problem is to develop novel schemes to coordinate transport simulations among GPU threads. Investigations along this direction will be in our future study.

Acknowledgments

This work is supported in part by an NIH grant (P20CA183639-01A1) and the Federal Share of program income earned by Massachusetts General Hospital on C06 CA059267.

References

[Ago+03] S. Agostinelli et al. "Geant4: a simulation toolkit". In: *Nuclear Instruments and Methods in Physics Research Section A: Accelerators, Spectrometers, Detectors and Associated Equipment* 506.3 (2003), pp. 250–303. ISSN: 0168-9002. DOI: https://doi.org/10.1016/S0168-9002(03)01368-8. URL: http://www.sciencedirect.com/science/article/pii/S0168900203013688.

[Bel+66] G. Bellettini, G. Coccon, A.N. Diddens, E. Lillethun, G. Matthiae, J.P. Scanlon, and A.M. Wetherell. "Proton-nuclei cross sections at 20 GeV". In: *Nuclear Physics* 79.3 (May 1, 1966), pp. 609–624. ISSN: 0029-5582. DOI: 10.1016/0029-5582(66)90267-7. URL: https://www.sciencedirect.com/science/article/pii/0029558266902677 (visited on 08/22/2018).

[FS04] Matthias Fippel and Martin Soukup. "A Monte Carlo dose calculation algorithm for proton therapy". In: *Medical Physics* 31.8 (Aug. 1, 2004), pp. 2263–2273. ISSN: 0094-2405. DOI: 10.1118/1.1769631. URL: http://scitation.aip.org.ezp-prod1.hul.harvard.edu/content/aapm/journal/medphys/31/8/10.1118/1.1769631 (visited on 04/19/2016).

[Gia+13] Drosoula Giantsoudi, Clemens Grassberger, David Craft, Andrzej Niemierko, Alexei Trofimov, and Harald Paganetti. "Linear Energy Transfer-Guided Optimization in Intensity Modulated Proton Therapy: Feasibility Study and Clinical Potential". In: *International Journal of Radiation Oncology*Biology*Physics* 87.1 (Sept. 1, 2013), pp. 216–222. ISSN: 0360-3016. DOI: 10.1016/j.ijrobp.2013.05.013. URL: http://www.sciencedirect.com/science/article/pii/S0360301613005452 (visited on 08/13/2018).

[Gia+15] Drosoula Giantsoudi, Jan Schuemann, Xun Jia, Stephen Dowdell, Steve Jiang, and Harald Paganetti. "Validation of a GPU-based Monte Carlo code (gPMC) for proton radiation therapy: clinical cases study". In: *Physics in Medicine & Biology* 60.6 (2015), p. 2257. ISSN: 0031-9155. DOI: 10.1088/0031-9155/60/6/2257. URL: http://stacks.iop.org/0031-9155/60/i=6/a=2257 (visited on 08/13/2018).

[GJJ11] Xuejun Gu, Xun Jia, and Steve B. Jiang. "GPU-based fast gamma index calculation". In: *Physics in Medicine & Biology* 56.5 (2011), p. 1431. ISSN: 0031-9155. DOI: 10.1088/0031-9155/56/5/014. URL: http://stacks.iop.org/0031-9155/56/i=5/a=014 (visited on 08/22/2018).

[Jia+12] Xun Jia, Jan Schümann, Harald Paganetti, and Steve B. Jiang. "GPU-based fast Monte Carlo dose calculation for proton therapy". In: *Physics in Medicine & Biology* 57.23 (2012), p. 7783. ISSN: 0031-9155. DOI: 10.1088/0031-9155/57/23/7783. URL: http://stacks.iop.org/0031-9155/57/i=23/a=7783 (visited on 08/22/2018).

[JZJ14] Xun Jia, Peter Ziegenhein, and Steve B. Jiang. "GPU-based high-performance computing for radiation therapy". In: *Physics in Medicine & Biology* 59.4 (2014), R151. ISSN: 0031-9155. DOI: 10.1088/0031-9155/59/4/R151. URL: http://stacks.iop.org/0031-9155/59/i=4/a=R151 (visited on 08/22/2018).

[Koh+03] Ryosuke Kohno, Yoshihisa Takada, Takeji Sakae, Toshiyuki Terunuma, Keiji Matsumoto, Akihiro Nohtomi, and Hiroyuki Matsuda. "Experimental evaluation of validity of simplified Monte Carlo method in proton dose calculations". In: *Physics in Medicine & Biology* 48.10 (2003), p. 1277. ISSN: 0031-9155. DOI: 10.1088/0031-9155/48/10/303. URL: http://stacks.iop.org/0031-9155/48/i=10/a=303 (visited on 08/22/2018).

[Li+05] J. S. Li, B. Shahine, E. Fourkal, and C.-M. Ma. "A particle track-repeating algorithm for proton beam dose calculation". In: *Physics in Medicine & Biology* 50.5 (2005), p. 1001. ISSN: 0031-9155. DOI: 10.1088/0031-9155/50/5/022. URL: http://stacks.iop.org/0031-9155/50/i=5/a=022 (visited on 08/22/2018).

[Ma+14] Jiasen Ma, Chris Beltran, Hok Seum Wan Chan Tseung, and Michael G. Herman. "A GPU-accelerated and Monte Carlo-based intensity modulated proton therapy optimization system". In: *Medical Physics* 41.12 (Dec. 1, 2014), p. 121707. ISSN: 2473-4209. DOI: 10.1118/1.4901522. URL: https://aapm.onlinelibrary.wiley.com/doi/abs/10.1118/1.4901522 (visited on 08/22/2018).

[Mag+15] Vincent Magnoux, Benoît Ozell, Éric Bonenfant, and Philippe Després. "A study of potential numerical pitfalls in GPU-based Monte Carlo dose calculation". In: *Physics in Medicine & Biology* 60.13 (2015), p. 5007. ISSN: 0031-9155. DOI: 10.1088/0031-9155/60/13/5007. URL: http://stacks.iop.org/0031-9155/60/i=13/a=5007 (visited on 08/22/2018).

[Mal01] Cynthia J. Malmer. "ICRU Report 63. Nuclear Data for Neutron and Proton Radiotherapy and for Radiation Protection". In: *Medical Physics* 28.5 (May 1, 2001), pp. 861–861. ISSN: 2473-4209. DOI: 10.1118/1.1369116. URL: https://aapm.onlinelibrary.wiley.com/doi/abs/10.1118/1.1369116 (visited on 08/22/2018).

[MN98] Makoto Matsumoto and Takuji Nishimura. "Mersenne Twister: A 623-dimensionally Equidistributed Uniform Pseudo-random Number Generator". In: *ACM Trans. Model. Comput. Simul.* 8.1 (Jan. 1998), pp. 3–30. ISSN: 1049-3301. DOI: 10.1145/272991.272995. URL: http://doi.acm.org/10.1145/272991.272995 (visited on 08/22/2018).

[MSP15] Aimee L. McNamara, Jan Schuemann, and Harald Paganetti. "A phenomenological relative biological effectiveness (RBE) model for proton therapy based on all published in vitro cell survival data". In: *Physics in medicine and biology* 60.21 (Nov. 7, 2015), pp. 8399–8416. ISSN: 0031-9155. DOI: 10.1088/0031-9155/60/21/8399. URL: https://www.ncbi.nlm.nih.gov/pmc/articles/PMC4634882/ (visited on 08/13/2018).

[NVI11] NVIDIA. *NVIDIA CUDA Compute Unified Device Architecture, Programming Guide, 4.0*. 2011. URL: http://developer.download.nvidia.com/compute/DevZone/docs/html/C/doc/CUDA_C_Programming_%20Guide.pdf.

[Pag+08] Harald Paganetti, Hongyu Jiang, Katia Parodi, Roelf Slopsema, and Martijn Engelsman. "Clinical implementation of full Monte Carlo dose calculation in proton beam therapy". In: *Physics in Medicine and Biology* 53.17 (Sept. 7, 2008), p. 4825. ISSN: 0031-9155. DOI: 10.1088/0031-9155/53/17/023. URL: http://iopscience.iop.org.ubproxy.ub.uni-heidelberg.de/0031-9155/53/17/023 (visited on 03/10/2015).

[Pag14] Harald Paganetti. "Relative biological effectiveness (RBE) values for proton beam therapy. Variations as a function of biological endpoint, dose, and linear energy transfer". In: *Physics in Medicine and Biology* 59.22 (Nov. 21, 2014), R419–472. ISSN: 1361-6560. DOI: 10.1088/0031-9155/59/22/R419.

[Per+12] J. Perl, J. Shin, J. Schümann, B. Faddegon, and H. Paganetti. "TOPAS: An innovative proton Monte Carlo platform for research and clinical applications". In: *Medical Physics* 39.11 (Nov. 1, 2012), pp. 6818–6837. ISSN: 2473-4209. DOI: 10.1118/1.4758060. URL: https://aapm.onlinelibrary.wiley.com/doi/abs/10.1118/1.4758060 (visited on 08/22/2018).

[Pol+15] Lisa Polster et al. "Extension of TOPAS for the simulation of proton radiation effects considering molecular and cellular endpoints". In: *Physics in Medicine & Biology* 60.13 (2015), p. 5053. ISSN: 0031-9155. DOI: 10.1088/0031-9155/60/13/5053. URL: http://stacks.iop.org/0031-9155/60/i=13/a=5053 (visited on 08/22/2018).

[Qin+16] Nan Qin, Pablo Botas, Drosoula Giantsoudi, Jan Schuemann, Zhen Tian, Steve B. Jiang, Harald Paganetti, and Xun Jia. "Recent developments and comprehensive evaluations of a GPU-based Monte Carlo package for proton therapy". In: *Physics in Medicine & Biology* 61.20 (2016), p. 7347. ISSN: 0031-9155. DOI: 10.1088/0031-9155/61/20/7347. URL: http://stacks.iop.org/0031-9155/61/i=20/a=7347 (visited on 08/20/2018).

[Ran72] J. Ranft. "Estimation of radiation problems around high-energy accelerators using calculations of the hadronic cascade in matter". In: (1972). URL: https://core.ac.uk/display/25433561 (visited on 08/22/2018).

[Sch+14] J. Schuemann, S. Dowdell, C. Grassberger, C. H. Min, and H. Paganetti. "Site-specific range uncertainties caused by dose calculation algorithms for proton therapy". In: *Physics in medicine and biology* 59.15 (Aug. 7, 2014), pp. 4007–4031. ISSN: 0031-9155. DOI: 10.1088/0031-9155/59/15/4007. URL: https://www.ncbi.nlm.nih.gov/pmc/articles/PMC4136435/ (visited on 06/28/2018).

[Sch+15] Jan Schuemann, Drosoula Giantsoudi, Clemens Grassberger, Maryam Moteabbed, Chul Hee Min, and Harald Paganetti. "Assessing the Clinical Impact of Approximations in Analytical Dose Calculations for Proton Therapy". In: *International Journal of Radiation Oncology • Biology • Physics* 92.5 (Aug. 1, 2015), pp. 1157–1164. ISSN: 0360-3016. DOI: 10.1016/j.ijrobp.2015.04.006. URL: https://www.redjournal.org/article/S0360-3016(15)00379-X/fulltext (visited on 08/22/2018).

[SM08] Mutsuo Saito and Makoto Matsumoto. "SIMD-Oriented Fast Mersenne Twister: a 128-bit Pseudorandom Number Generator". In: *Monte Carlo and Quasi-Monte Carlo Methods 2006*. Ed. by Alexander Keller, Stefan Heinrich, and Harald Niederreiter. Berlin Heidelberg: Springer-Verlag, 2008. ISBN: 978-3-540-74495-5. URL: //www.springer.com/us/book/9783540744955 (visited on 08/22/2018).

[Tes+13] M. Testa, J. Schümann, H.-M. Lu, J. Shin, B. Faddegon, J. Perl, and H. Paganetti. "Experimental validation of the TOPAS Monte Carlo system for passive scattering proton therapy". In: *Medical Physics* 40.12 (Dec. 1, 2013), p. 121719. ISSN: 2473-4209. DOI: 10.1118/1.4828781. URL: https://aapm.onlinelibrary.wiley.com/doi/abs/10.1118/1.4828781 (visited on 08/22/2018).

[Tia+15] Zhen Tian, Feng Shi, Michael Folkerts, Nan Qin, Steve B. Jiang, and Xun Jia. "A GPU OpenCL based cross-platform Monte Carlo dose calculation engine (goMC)". In: *Physics in Medicine & Biology* 60.19 (2015), p. 7419. ISSN: 0031-9155. DOI: 10.1088/0031-9155/60/19/7419. URL: http://stacks.iop.org/0031-9155/60/i=19/a=7419 (visited on 08/22/2018).

[TMB15] H. Wan Chan Tseung, J. Ma, and C. Beltran. "A fast GPU-based Monte Carlo simulation of proton transport with detailed modeling of nonelastic interactions". In: *Medical Physics* 42.6 (June 1, 2015), pp. 2967–2978. ISSN: 0094-2405. DOI: 10.1118/1.4921046. URL: http://scitation.aip.org.ezp-prod1.hul.harvard.edu/content/aapm/journal/medphys/42/6/10.1118/1.4921046 (visited on 03/23/2016).

[Wan+16] Hok Seum Wan Chan Tseung, Jiasen Ma, Cole R. Kreofsky, Daniel J. Ma, and Chris Beltran. "Clinically Applicable Monte Carlo–based Biological Dose Optimization for the Treatment of Head and Neck Cancers With Spot-Scanning Proton Therapy". In: *International Journal of Radiation Oncology*Biology*Physics* 95.5 (Aug. 1, 2016), pp. 1535–1543. ISSN: 0360-3016. DOI: 10.1016/j.ijrobp.2016.03.041. URL: http://www.sciencedirect.com/science/article/pii/S0360301616300311 (visited on 08/13/2018).

[WYD15] H. Wenzel, J. Yarba, and A. Dotti. "The Geant4 physics validation repository". In: *Journal of Physics: Conference Series* 664.6 (2015), p. 062066. ISSN: 1742-6596. DOI: 10.1088/1742-6596/664/6/062066. URL: http://stacks.iop.org/1742-6596/664/i=6/a=062066 (visited on 08/22/2018).

[Yep+09] Pablo Yepes, Sharmalee Randeniya, Phillip J. Taddei, and Wayne D. Newhauser. "Monte Carlo fast dose calculator for proton radiotherapy: application to a voxelized geometry representing a patient with prostate cancer". In: *Physics in Medicine & Biology* 54.1 (2009), N21. ISSN: 0031-9155. DOI: 10.1088/0031-9155/54/1/N03. URL: http://stacks.iop.org/0031-9155/54/i=1/a=N03 (visited on 08/22/2018).

Chapter 5

Results II: Radiobiological optimization

In section 5.2 of this chapter, the following publication is reproduced:

Jan Unkelbach, Pablo Botas, Drosoula Giantsoudi, Bram L Gorissen, and Harald Paganetti. "Reoptimization of intensity modulated proton therapy plans based on linear energy transfer". In: *International Journal of Radiation Oncology* Biology* Physics* 96.5 (2016), pp. 1097-1106.

My role in the publication is clearly stated in the following subsection. Some comments on the adaptation of the publication are also given.

5.1 Role in study

This study was developed in collaboration, mainly with Dr. Unkelbach. My role in the collaboration was general project discussion, provide the tools to generate dose-influence and LET$\times$D-influence matrices for optimization and create the matrices, writing parts of the manuscript and discussing it.

In order to generate the optimization matrices, gPMC needed to be connected to the patient data systems in MGH. Once the connectionw as developed, for each patient case, each beamlet was simulated in the patient's planning CT and the optimization matrices were generated post-processing the resultant dose distributions. Each beamlets was simulated using 10^6 protons. A beam model that represents a modern proton beam line with spot sizes ranging from 5.6 to 2.2 mm sigma and energy spreads from 0.56 to 0.82 MeV for nominal proton energies between 60 and 230 MeV was implemented and used for this study. Pencil beams were placed at 1 sigma lateral distance within an energy layer. Energy layers were separated by 0.7 times the Bragg peak width at 80%. Bragg peaks were placed within the

target volume plus a 1-2 cm margin surrounding the target, depending on the case. The large margin for spot placement was applied to provide sufficient degrees of freedom for the reoptimization step and not restrict the ability to redistribute LET×D by spot placement. On average, approximately 2000 pencil beams per field were used. The average calculation time per pencil beam was 3-4 s on a NVIDIA Tesla C2075, corresponding to 2 hours computation time per field. Routines to produce other data files required by Opt4D were also created (structure masks, dose map for conformity to target ...).

For this study, the particle source and beam models were implemented as CPU subroutines, creating a sequence of particle buffers that were transferred to the GPU for simulation (previous gPMC versions relied on external phase space files). The code's execution was made more flexible to permit the treatmet simulation at different levels of the hierarchy, allowing the simulation of individual fields and/or beamlets. Finally, a maximum threshold was implemented into the dose-averaged LET scorer after observing LET spikes. The maximum was defaulted to 100 keV µm^{-1} after studying dose-averaged LET spectra in patients. From the list of specific developments of gPMC in section 3.1.2, items 2–5 were created and the dose-averaged LET scorer was tuned, item 6.

Comments on the adaptation of the paper: Minor changes were made on the published manuscript. In this reproduction, the short form of IMPT and LET were employed in the title to keep it shorter. The distribution of subfigures in figs. 5.1–5.3 was adjusted, which affects the appreciation of the colorbar scales. Comments in *italics* were included in the captions of the affected figure to explain the changes and clarify the color scales. The position of figures and tables may differ from the published manuscript. The citation style and the internal figure, table and equation numbers have been altered, but the underlying meaning has been conserved.

5.2 Reoptimization of IMPT Plans based on LET

J. Unkelbach[1,2], P. Botas[1,3], D. Giantsoudi[1,2], B. L. Gorissen[1,2] and H. Paganetti[1,2]

[1] Department of Radiation Oncology, Massachusetts General Hospital, Boston, MA, USA.

[2] Harvard Medical School, Boston, MA, USA.

[3] Department of Physics, University of Heidelberg, Heidelberg, Germany.

Abstract Purpose: We describe a treatment plan optimization method for intensity modulated proton therapy (IMPT) that avoids high values of linear energy transfer (LET) in critical structures located within or near the target volume while limiting degradation of the best possible physical dose distribution.

Methods and Materials: To allow fast optimization based on dose and LET, a GPU- based Monte Carlo code was extended to provide dose-averaged LET in addition to dose for all pencil beams. After optimizing an initial IMPT plan based on physical dose, a prioritized optimization scheme is used to modify the LET distribution while constraining the physical dose objectives to values close to the initial plan. The LET optimization step is performed based on objective functions evaluated for the product of LET and physical dose (LET$\times$D). To first approximation, LET$\times$D represents a measure of the additional biological dose that is caused by high LET.
Results: The method is effective for treatments where serial critical structures with maximum dose constraints are located within or near the target. We report on 5 patients with intracranial tumors (high-grade meningiomas, base-of-skull chordomas, ependymomas) in whom the target volume overlaps with the brainstem and optic structures. In all cases, high LET$\times$D in critical structures could be avoided while minimally compromising physical dose planning objectives.
Conclusion: LET-based reoptimization of IMPT plans represents a pragmatic approach to bridge the gap between purely physical dose-based and relative biological effectiveness (RBE)-based planning. The method makes IMPT treatments safer by mitigating a potentially increased risk of side effects resulting from elevated RBE of proton beams near the end of range.

5.2.1 Introduction

In vitro cell survival experiments suggest an increase in proton relative biological effectiveness (RBE) toward the end of range. Although the data from in vitro experiments vary substantially, they suggest that, depending on the dose and the tissue parameters, the RBE might increase from values between 1.0 and 1.1 in the entrance region to values around 1.3 at the Bragg peak and 1.6 in the falloff region [Pag14]. It is typically assumed that this RBE increase is explained by an increase of linear energy transfer (LET) toward the end of range. By contrast, proton treatment planning and dose reporting have been based on physical dose and a constant RBE of 1.1.

This creates a dilemma for proton therapy planning, especially for intensity modulated proton therapy (IMPT). Underestimation of RBE may lead to underestimation of normal tissue complication probabilities. IMPT treatments with highly modulated fields may deliver highly inhomogeneous LET distributions. This may result in LET hot spots in critical structures within or near the target volume, with LET values higher than those observed for passive scattering or single field uniform dose (SFUD) treatments. By contrast, large uncertainties in endpoint-specific RBE values, and the fact that dose reporting has historically been based on physical dose, discourage RBE-based IMPT planning approaches that lead to drastic changes compared with current practice.

Previous works have investigated IMPT optimization based on biological dose instead of physical dose [WO04; Fre+11]. However, such approaches are yet to be adopted clinically. If treatment planning objectives for target coverage are evaluated only in terms of biological dose, such methods typically lead to lower physical doses in parts of the target, based on

the assumption that the RBE is larger than 1.1 in areas of high LET. There is a danger that this could lead to underdosage to the target if the RBE is overestimated. Other authors have redressed this issue by combining physical dose optimization with the goal of additionally influencing the LET distribution [Wan+16; Fag+15; Bas+10; Gia+13; Gra+11]. Most works [Wan+16; Fag+15; Bas+10] focus on increasing LET in radioresistant tumors to achieve a higher biological effect.

Unlike previous studies, our work is primarily concerned with the risk of normal tissue complications. We introduce a hybrid method between physical dose and LET-based IMPT planning. In contrast to previous works, our method does not assume knowledge of RBE to perform biological IMPT planning. Instead, it is designed to facilitate IMPT planning in the absence of reliable normal tissue RBE values. We first determine an IMPT plan based on physical dose objectives, as is current clinical practice. In a second step, we modify the LET distribution to avoid high LET in critical structures. This is done using a prioritized optimization scheme [Wil+07; JMF07] in which LET-based objectives are optimized while limiting the degradation of the physical dose distribution. In that sense, IMPT treatment plans

5.2.2 Methods and Materials

5.2.2.1 Patients

We reviewed patients with intracranial tumors that were treated with passively scattered proton beams at our institution. For this study, we selected patients in whom the clinical target volume was directly adjacent to, or overlapping, with serial organs at risk (OARs) (i.e., structures where the risk of side effects mainly depends on the maximum dose). We discuss 3 selected patients in detail: 1 patient with an atypical meningioma in whom the target volume overlapped the brainstem, optic nerve, chiasm, and pituitary gland (Fig. 5.1a), 1 patient with an ependymoma in whom the target volume involved parts of the brainstem (Fig. 5.2a), 1 patient with a base-of-skull chordoma in whom the target abutted the brainstem (Fig. 5.3a). The results for 2 additional patients (1 ependymoma, 1 base-of-skull chordoma) are presented in Appendix D (available online at www.redjournal.org). For the current study, these patients were replanned for IMPT using the beam directions from the clinically delivered treatment. The pencil beam sizes used represent the latest generation of proton machines (2.2-5.6 mm sigma at isocenter in air for energies of 230-60 MeV). For all patients, the gross tumor volume (GTV) and clinical target volume (CTV) were taken from the clinical treatment plan. An isotropic 2-mm margin was added to the CTV to obtain a planning target volume (PTV) for IMPT planning.

5.2.2.2 Parameterization of biological effects

We consider the exponential cell survival model:

$$S = \exp(-\alpha d) \tag{5.1}$$

where d is the physical dose and S is the surviving fraction of cells. To a first approximation, it is assumed [WO04; Car+10; MSP15; WLH13] that the radiosensitivity parameter α increases linearly with dose-averaged LET, which we denote by L:

$$\alpha = \alpha_0(1 + cL) \tag{5.2}$$

In analogy to the biologically effective dose (BED) model, the total biological dose b can be defined as:

$$b = -\frac{\log(S)}{\alpha_0} = (1 + cL)d = d + cLd \tag{5.3}$$

Hence, the product of LET and dose, scaled by a parameter c, can be interpreted as the additional biological dose due to the LET effect, which is added to the physical dose to obtain the total biological dose b. Alternatively, $(1 + cL)$ can be interpreted as the RBE, so that b represents the RBE-weighted dose (see discussion in Appendix A; available online at www.redjournal.org).

For IMPT planning, the biological dose model is extended to multiple pencil beams. Let $D_{ij}x_j$ denote the physical dose that pencil beam j delivers to voxel i. Here, D_{ij} denotes the dose contribution of pencil beam j to voxel i for unit fluence, and x_j denotes the fluence of pencil beam j. The total cell survival in voxel i is given by:

$$S_i = \prod_j \exp\left(\alpha_0 \left(1 + cL_{ij}\right) D_{ij}x_j\right) \tag{5.4}$$

where L_{ij} is the dose-averaged LET of pencil beam j in voxel i. The RBE-weighted dose is thus given by:

$$b_i = -\frac{\log(S_i)}{\alpha_0} = \sum_j (1 + cL_{ij}) D_{ij}x_j = d_i + c\sum_j L_{ij}D_{ij}x_j \tag{5.5}$$

where d_i is physical dose in voxel i. By defining the dose-averaged LET over all pencil beam contributions as:

$$\overline{L}_i = \frac{\sum_j L_{ij}D_{ij}x_j}{d_i} \tag{5.6}$$

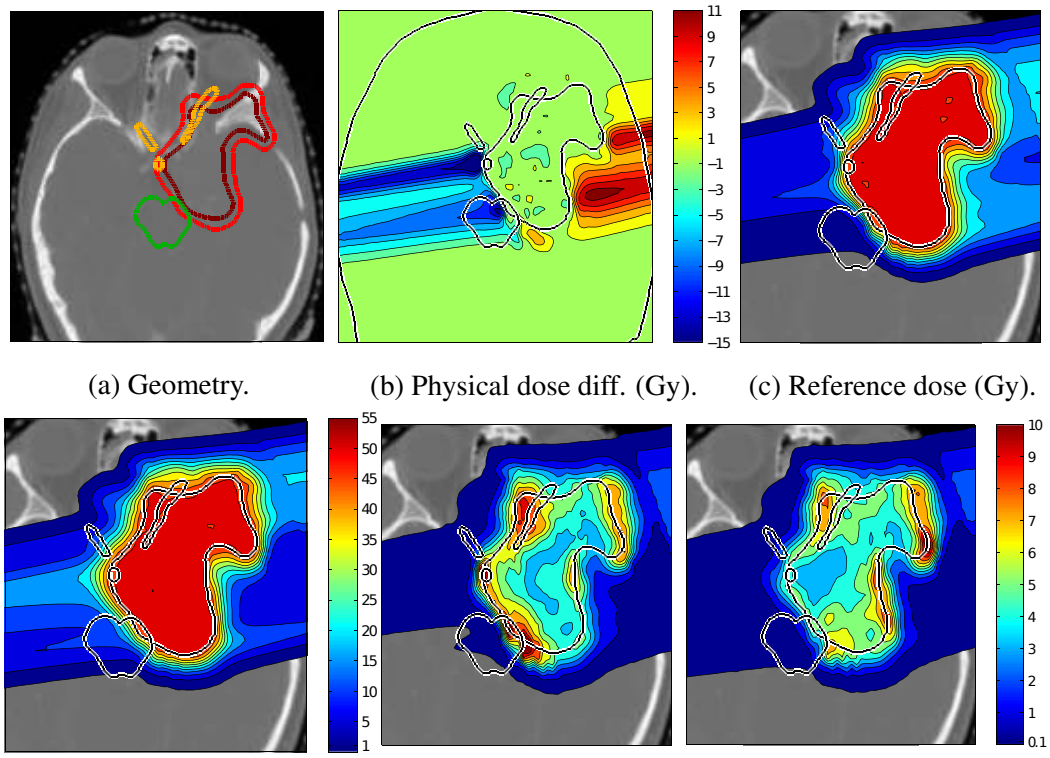

(a) Geometry. (b) Physical dose diff. (Gy). (c) Reference dose (Gy).

(d) Reoptimized dose (Gy). (e) Ref. $cLET \times D$ (Gy). (f) Reopt. $cLET \times D$ (Gy).

Fig. 5.1 Plan comparison for the atypical meningioma (patient 1). (a) Contours for target volume (red), GTV (brown), brainstem (green), and optic structures and pituitary gland (yellow). (c and e) Physical dose and LET×D for the reference plan. (d and f) Physical dose and LET×D for the reoptimized plan. (b) Difference in physical dose. Positive values indicate higher doses in the reference plan. (A color version of this figure is available at www.redjournal.org). Adapted from [Unk+16]. *Note: The distribution of subfigures has been edited from the original publication. The colorbar in (d) also applies to figure (c) and the one in figure (f) also to (e). "Reference" and "Reoptimized" have also been shortened in (e) and (f) to "Ref." and "Reopt.", respectively.*

the biological extra dose due to the LET effect is given by the product of physical dose and dose-averaged LET, $c\overline{L}_i d_i$. The calculation of dose and LET contributions, D_{ij} and L_{ij}, is performed using a fast GPU-based Monte Carlo code [Jia+12; Gia+15] as detailed in Appendix B (available online at www.redjournal.org). Given the dose coefficients D_{ij} and LET coefficients L_{ij}, the additional biological dose due to elevated LET is a linear function of the optimization variables x_j. Hence, the same mathematical optimization techniques as in physical dose optimization can be applied.

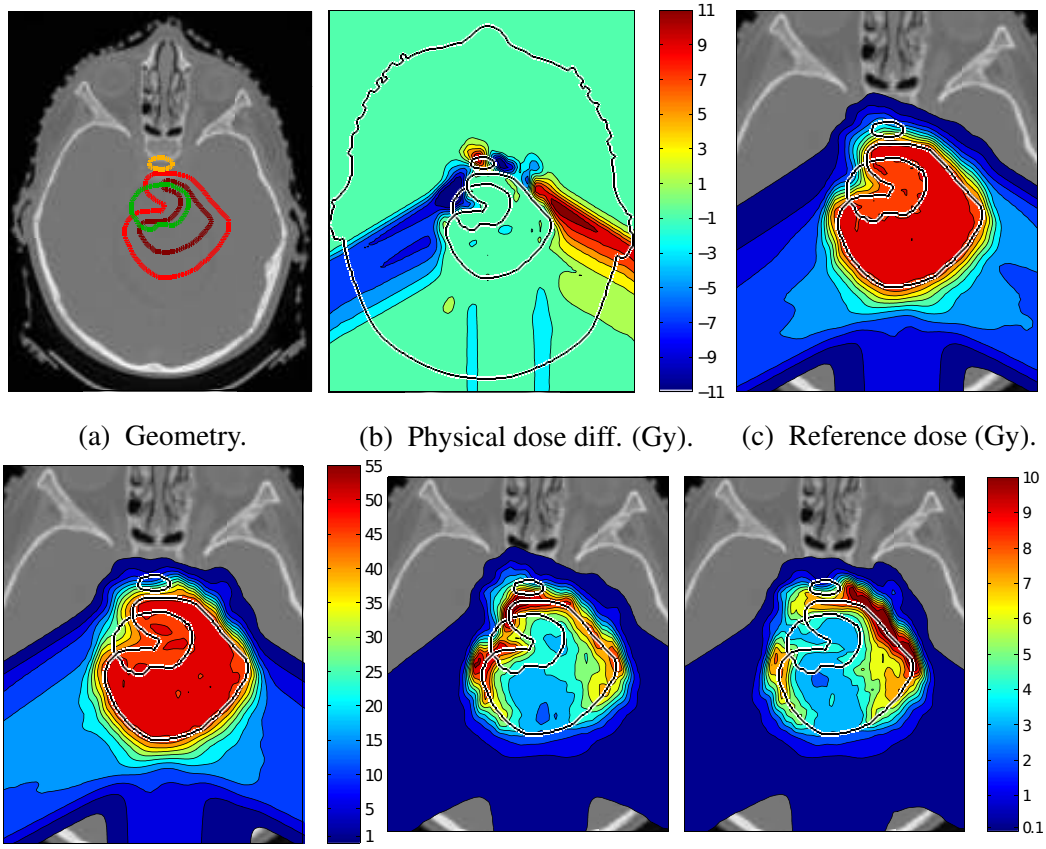

(a) Geometry. (b) Physical dose diff. (Gy). (c) Reference dose (Gy).

(d) Reoptimized dose (Gy). (e) Ref. $cLET \times D$ (Gy). (f) Reopt. $cLET \times D$ (Gy).

Fig. 5.2 Plan comparison for the ependymoma (patient 2). (a) Contours for target volume (red), GTV (brown), brainstem (green), and optic structures and pituitary gland (yellow). (c and e) Physical dose and LET×D for the reference plan. (d and f) Physical dose and LET×D for the reoptimized plan. (b) Difference in physical dose. Positive values indicate higher doses in the reference plan. (A color version of this figure is available at www.redjournal.org). Adapted from [Unk+16]. *Note: The distribution of subfigures has been edited from the original publication. The colorbar in (d) also applies to figure (c) and the one in figure (f) also to (e). "Reference" and "Reoptimized" have also been shortened in (e) and (f) to "Ref." and "Reopt.", respectively.*

5.2.2.3 Treatment plan optimization

To perform treatment planning in a manner consistent with current clinical practice, we first optimize an IMPT plan based on physical dose. We used the following objectives:

1. Deliver a prescribed physical dose of 50 Gy to the target volume, and penalize dose above 52.5 Gy (implemented by quadratic penalty functions).

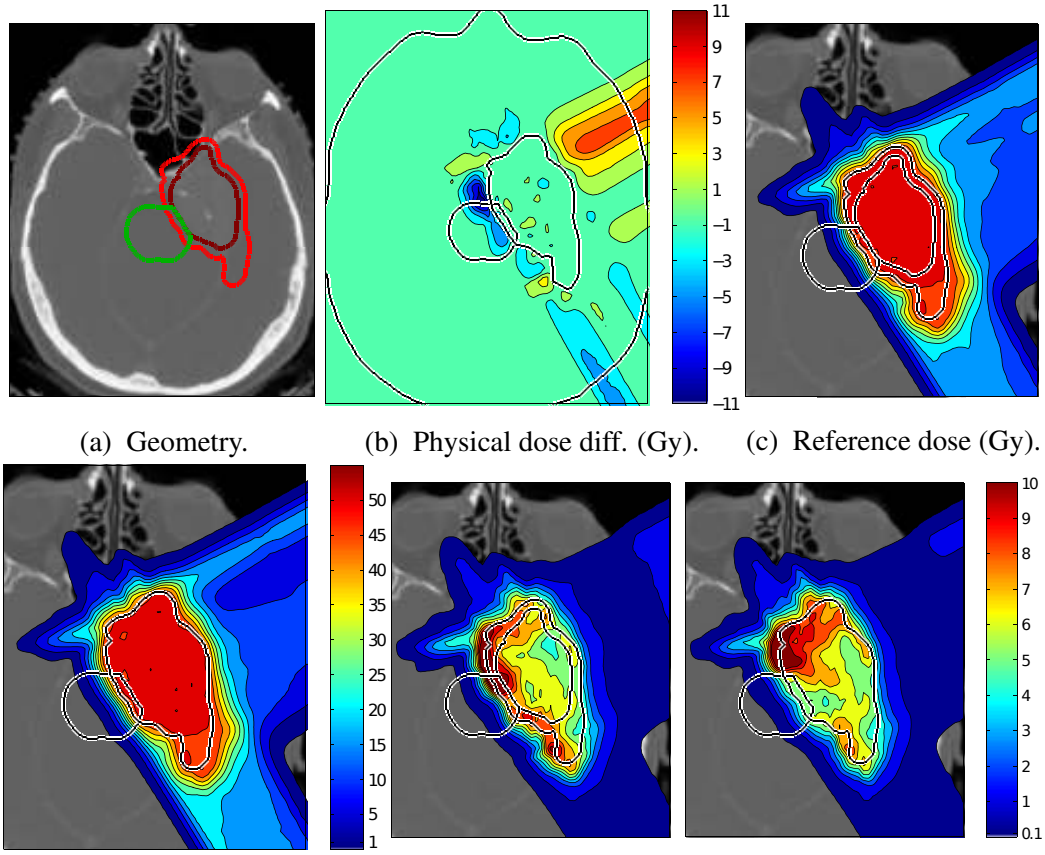

(a) Geometry. (b) Physical dose diff. (Gy). (c) Reference dose (Gy).

(d) Reoptimized dose (Gy). (e) Ref. $cLET \times D$ (Gy). (f) Reopt. $cLET \times D$ (Gy).

Fig. 5.3 Plan comparison for the base-of-skull chordoma (patient 3). (a) Contours for target volume (red), GTV (brown), brainstem (green), and optic structures and pituitary gland (yellow). (c and e) Physical dose and LET×D for the reference plan. (d and f) Physical dose and LET×D for the reoptimized plan. (b) Difference in physical dose. Positive values indicate higher doses in the reference plan. (A color version of this figure is available at www.redjournal.org). Adapted from [Unk+16]. *Note: The distribution of subfigures has been edited from the original publication. The colorbar in (d) also applies to figure (c) and the one in figure (f) also to (e). "Reference" and "Reoptimized" have also been shortened in (e) and (f) to "Ref." and "Reopt.", respectively.*

2. Penalize dose above 50 Gy in OARs (optic structures, brainstem, pituitary gland) (implemented by quadratic penalty functions).

3. Conformity (implemented by quadratic penalty functions with a maximum dose that depends linearly on the distance from the target).

4. Minimize the generalized equivalent uniform dose (gEUD) in the brainstem.

5. Minimize the mean dose in the brain.

The details of treatment plan optimization can be found in Appendix C.1 (available online at www.redjournal.org). This initial step yields a plan that is optimal in terms of the chosen physical dose objectives, which we refer to as the reference plan below.

In the second step, the plan is adjusted to avoid high values of $\overline{L}_i d_i$ in the brainstem and other OARs. This is performed with a prioritized optimization scheme [Wil+07; JMF07] (i.e., a second IMPT optimization problem is solved where all physical dose planning goals are handled through constraints). In our application, target coverage should not be compromised. Also, the physical dose in OARs should not increase above 50 Gy, and conformity should not deteriorate. Hence, the values of objectives 1, 2, and 3 are constrained to the optimal value in the reference plan. However, it is expected that plan modifications will lead to small increases in integral dose and the brainstem gEUD. We therefore allow a 3% increase for objectives 4 and 5.

The only objective in the second IMPT optimization problem is to reduce $\overline{L}_i d_i$ in the OARs (brainstem, optic structures, pituitary gland). This can be done using quadratic penalty functions that penalize $\overline{L}_i d_i$ values that are higher than the minimum value that can realistically be achieved for the given prescription dose. To obtain such a minimum value, we consider the histogram of $\overline{L}_i d_i$ values in the target volume for the reference plan. We determine a threshold value Ld^{ref} such that 95% of the target volume receives $\overline{L}_i d_i$ values higher than Ld^{ref}. We then introduce the objective function:

$$f_L = \sum_{i \in OARs} \left(\overline{L}_i d_i - Ld^{ref} \right)_+^2 \tag{5.7}$$

which is minimized to obtain the final treatment plan (see Appendix C.2; available online at www.redjournal.org, for details).

5.2.2.4 Visualizing LET$\times$ distributions

The treatment planning approach as described above does not require any quantification of RBE effects (ie, the parameter c that scales the biological dose contribution $\overline{L}_i d_i$ does not have to be known). However, for visualization and estimating the potential benefit of LET redistribution, it is useful to select the parameter c so that $d_i + c\overline{L}_i d_i$ reflects an estimate of the RBE-weighted dose. For this work, we set $c = 0.04$ µm/keV, which yields an RBE of 1.1 in the center of a spread-out Bragg peak of 5 cm modulation and 10 cm range where the dose-averaged LET is approximately $L \approx 2.5$ keV/µm. For a pristine Bragg peak, this corresponds to an RBE of approximately 1.3 at the Bragg peak (see Appendix A available online at www.redjournal.org).

Although difficult to verify for clinically relevant endpoints in normal tissues, it has been hypothesized that the RBE increase with LET is steeper for normal tissues with low α/β values than for tumors with higher α/β values. Therefore, the RBE-weighted dose resulting from $c = 0.04$ µm/keV can be considered a reference point, but the RBE may be higher by an unknown amount. For example, at a dose of 1.67 Gy per fraction (50 Gy in 30 fractions), the RBE model by McNamara et al. [MSP15] predicts an approximately linear increase of RBE with LET corresponding to $c \approx 0.02$ µm/keV for $\alpha/\beta = 10$ and $c \approx 0.05$ µm/keV for $\alpha/\beta = 2$.

5.2.3 Results

5.2.3.1 Atypical meningioma (patient 1)

We first illustrate the method for the meningioma patient shown in Figure 5.1a. Figure 5.1c shows the physical dose distribution of the reference plan, and Figure 5.1e the corresponding LET×D distribution reflecting the extra biological dose due to elevated LET. The average value of $c\overline{L}_i d_i$ in the target volume is 5.8 Gy (for $c = 0.04$ µm/keV). However, in the high-dose region of the brainstem, the pituitary gland, the chiasm, and the optic nerve, $c\overline{L}_i d_i$ reaches values of approximately 12 Gy, corresponding to RBE-weighted doses exceeding 60 Gy. If the value $c = 0.04$ µm/keV underestimates the LET effect on RBE in these critical structures, the RBE-weighted dose will be even higher.

Figures 5.1d and 5.1f show the reoptimized treatment plan that penalizes $c\overline{L}_i d_i$ values in critical structures exceeding $Ld^{ref} = 3.8$ Gy. Figure 5.1f demonstrates that LET×D hot spots in OARs are avoided; LET×D is reduced to values close to the mean target LET×D of 5.8 Gy. Corresponding dose-volume histograms (DVH) evaluated for LET×D confirm the reduction in LET×D in OARs (Fig. 5.4b). Table 1 quantifies the LET×D reductions in the brainstem for specific DVH points. Figures 5.1d and 5.4a confirm that the physical dose distribution in the vicinity of the target is close to the reference plan as enforced by the constraints.

It is clear that, to modify the LET×D distribution in critical structures, the dose to these regions must be delivered by different pencil beams. This is illustrated in Figure 5.1b, which shows the difference between the physical dose distributions (the reoptimized plan is subtracted from the reference plan). The fluence of pencil beams incident from the patient's left (right side of the image) that stop in the OARs is reduced. Instead, more dose is delivered by pencil beams incident from the patient's right (left side of the image).

Table 5.1 LET×D values (scaled with $c = 0.04$ µm/keV) in the brainstem for the reference and reoptimized plans. Adapted from [Unk+16].

Plan	Patient				
	1: Meningioma	2: Ependymoma	3: Chordoma	4: Chordoma	5: Ependymoma
Tumor volume, cc	92	69	51	62	53
Beam directions	3 (2 coplanar)	3 coplanar	3 (2 coplanar)	6 coplanar	3 coplanar
Reference plan					
LET×D max (Gy)	12.0	11.5	14.8	13.4	13.1
LET×D 0.1 cc (Gy)	11.2	10.3	13.0	10.2	11.6
LET×D 0.5 cc (Gy)	9.9	9.2	10.6	7.7	9.3
Ld^{ref} (Gy)	3.8	3.1	5.0	4.4	3.5
Mean PTV LET×D (Gy)	5.8	5.0	7.1	6.8	5.2
Reoptimized plan					
LET×D max (Gy)	7.4	8.5	8.5	8.9	8.7
LET×D 0.1 cc (Gy)	5.9	6.7	6.9	6.5	6.6
LET×D 0.5 cc (Gy)	5.2	5.4	6.2	5.3	5.6

Abbreviations: LET×D = product of linear energy transfer × physical dose; PTV = planning target volume.
The maximum LET×D value in the brainstem is reported, as is the LET×D value that is exceeded in 0.1 cc and 0.5 cc. For comparison, Ld^{ref} (see equation 7) and the mean LET×D value in the target are reported.

5.2.3.2 Ependymoma (patient 2)

Figure 5.2 shows results for a patient with ependymoma in whom the target volume includes parts of the brainstem. In the reference treatment plan, elevated LET×D values are observed in the brainstem (Fig. 5.2e). After reoptimization, LET×D hot spots in the brainstem can be avoided (Fig. 5.2f). Figure 5.2b illustrates how the LET×D distribution is modified. The reference plan heavily uses pencil beams from the left-posterior beam (right side of the image) that stop within the brainstem. The reoptimized plan increases the fluence of pencil beams in the right-posterior beam (left side of the image), which traverse the brainstem and deliver low-LET irradiation to the region where target and brainstem overlap.

5.2.3.3 Base-of-skull chordoma (patient 3)

Figure 5.3 shows a base-of-skull chordoma where the target volume abuts the brainstem. The patient is treated with 2 coplanar beams and a superior oblique beam. Similar to patients 1 and 2, treatment planning based on physical dose alone leads to high LET×D values in the brainstem as a result of pencil beams incident from the patient's left (right side of the image) that stop in front of the brainstem (Fig. 5.3e). LET×D values can be reduced (Fig. 5.3f) by using pencil beams in the posterior beam that avoid the brainstem laterally (Fig. 5.3b).

5.2.3.4 Summary of results

Table 1 summarizes the results for LET×D reductions after reoptimization for the brainstem, which is the OAR common to all 5 patients. For all cases, LET×D hot spots exceeding twice the mean target LET×D value were observed in OARs in the reference plan. After reoptimization, LET×D in OARs was reduced to values close to the mean value in the target. DVH comparisons for patients 2 to 5 are shown in Appendix F (available online at www.redjournal.org).

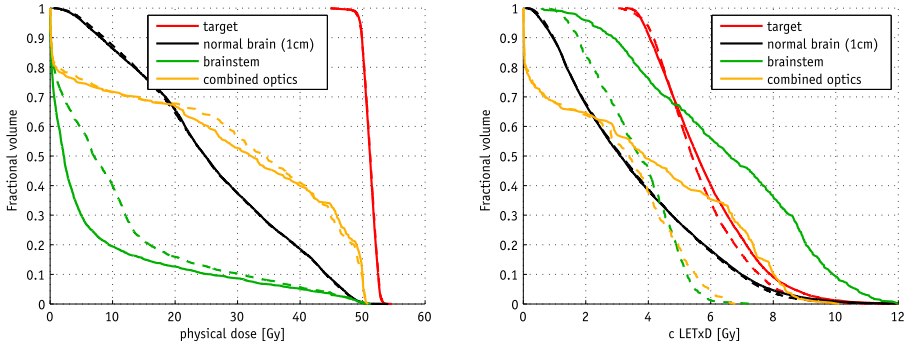

(a) (b)

Fig. 5.4 Dose-volume histogram (DVH) comparison for the atypical meningioma (patient 1) between reference plan (solid lines) and reoptimized plan (dashed lines). (a) Physical dose DVHs, showing identical target coverage for both plans. (b) DVHs evaluated for LET×D (scaled with $c = 0.04$ µm/keV). In the LET×D DVH of the brainstem, voxels that receive less than 10 Gy physical dose in the reference plan were removed for better visualization. The black lines correspond to all normal tissue voxels in a 1-cm margin around the target volume. (A color version of this figure is available at www.redjournal.org). Adapted from [Unk+16].

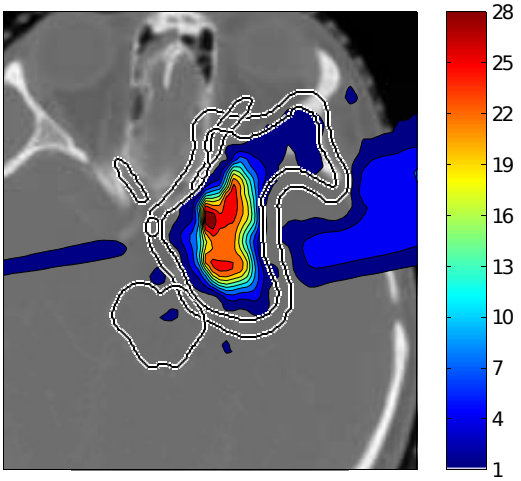

Fig. 5.5 Difference in physical dose (Gy) between the dose-escalated plan and Fig. 5.1e (ie, the figure shows the additional physical dose on top of 50 Gy, which can be delivered to the gross tumor volume without worsening any normal tissue dose objective). The corresponding LET×D distribution is shown in Appendix E.2 (available online at www.redjournal.org). Adapted from [Unk+16].

5.2.4 Discussion

Compared with passive scattering and SFUD techniques, IMPT has the potential to improve conformity and reduce the integral normal tissue dose. However, as a consequence of highly modulated fields, IMPT plans may yield highly inhomogeneous LET distributions, even for homogeneous physical dose distributions. In particular, IMPT may yield high LET values in serial critical structures within or near the target volume that exceed the values observed in passive scattering or SFUD. This could lead to an increased rate of adverse events, but this concern is yet to be underpinned by clinical evidence.

We suggest a method based on prioritized optimization that reoptimizes IMPT plans for their LET distribution while limiting degradations of the physical dose distribution. We applied the method to intracranial tumors where the brainstem or optic structures overlapped with the target volume. For the cases studied here, high LET values in these structures could be avoided at little cost: degradations to the optimal physical dose distributions were minor. However, in general the method's degree of success depends on the patient's geometry and beam arrangement (see also patient 5 in Fig. 8 of Appendix D; available online at www.redjournal.org). For example, high LET in a critical structure overlapping the target can be avoided only if that structure falls within the entrance region of some pencil beams (ie, the structure can not only receive dose from Bragg peaks placed at its location). If this is not fulfilled, changing the incident beam directions may be necessary to reduce LET hot spots.

5.2.4.1 LET$\times$ redistribution beyond OARs

The objective in the above examples was to reduce potential areas of high RBE in OARs. As seen in Figures 5.1, 5.2 and 5.3, this is achieved mostly by shifting LET hot spots to other regions at the periphery of the target, which may still contain functioning brain tissue. Hence, it is implicitly assumed here that OARs are contoured to represent structures that are more important to spare than the remaining normal brain. Additional iterations of prioritized optimization can be applied to reduce LET$\times$D in all of the normal brain inside and outside of the PTV, and to concentrate high LET exclusively in the GTV. However, these modifications are typically associated with more substantial degradation of the physical dose distribution. The treatment plan that minimizes the healthy tissue dose in the beam entrance regions preferentially uses Bragg peaks placed at the distal edge of the target because these pencil beams deposit additional dose for free while traversing the target. Unfortunately, this leads to high LET$\times$D values in the periphery of the GTV and to low values in the center of the GTV (Figs. 5.1d, 5.2d, and 5.3d). By contrast, high LET in the GTV is achieved if as many protons as possible stop within the GTV. In terms of physical dose, this corresponds to an

inefficient use of protons, which conflicts with the goal of minimizing dose to healthy tissue in the entrance region.

At first glance, it appears plausible to maximize LET×D in the GTV as a means to increase the RBE-weighted dose. However, the alternative strategy is to allow higher physical dose in the GTV. Hence, to assess the potential benefit of LET×D escalation in the GTV, such treatment plans should be compared with what physical dose escalation can achieve. In this context, we point out that higher doses in parts of the GTV can often be achieved without increasing normal tissue dose. This effect is also referred to as the price of uniformity, a term that alludes to the mathematical certainty that adding an IMPT optimization objective that penalizes hot spots in the GTV will worsen the combined remaining planning objectives.

To illustrate this, we consider the atypical meningioma patient (Fig. 5.1). We apply an additional prioritized optimization step to the treatment plan in Figures 5.1e and 5.1f. The only objective is to maximize the mean physical dose in the GTV. The physical dose constraints are the same as for the plan in Figures 5.1e and 5.1f, except that the penalty for overdosing the GTV has been removed (while keeping the overdose penalty for the part of the PTV that is not GTV). The exact formulation is provided in Appendix E.1 (available online at www.redjournal.org). Figure 5.5 shows the difference in physical dose between the dose-escalated plan and Figure 5.1e. By construction, the normal tissue receives approximately the same dose, but much higher doses of up to 100 Gy can be achieved in the center of the GTV. The mean physical GTV dose is increased from 51 Gy to 58 Gy without compromising conformity or increasing integral dose to the healthy tissue. Hence, if dose escalation in the GTV is the goal, physical dose and LET×D should be considered jointly, rather than reoptimizing the LET×D distribution alone while constraining the physical dose.

5.2.4.2 RBE- versus LET-based IMPT planning

Whereas this report suggests an IMPT planning method based on LET, other authors have proposed IMPT planning based on RBE-weighted dose [WO05; Fre+11; Wan+16; Fag+15]. Whether LET-guided or RBE-based planning is appropriate depends on the application and the goals of treatment planning. Both methods may coexist. The approach in this report is motivated by the following scenario:

1. We are concerned about serial OARs with maximum dose constraints that are located within/near the target. We would like to avoid LET hot spots in these OARs because they may increase the risk of adverse events by an unknown amount.

2. We do not want to lower the physical dose in the target volume in comparison with current practice. Multiple reasons support this practice, such as skepticism regarding

the accuracy of RBE models for the tumor and the necessity to comply with clinical trial protocols that specify the physical prescription dose.

3. While reducing LET hot spots in OARs, we want to assess and control physical dose increases in normal tissues compared with the treatment plan that is optimal in terms of physical dose alone. This is because the tradeoff between the clinical value of LET reduction versus physical dose increase is unknown.

These goals are achieved with the proposed combination of physical dose and LET-guided planning using prioritized optimization. However, in other situations, IMPT optimization based on RBE-weighted dose may be appropriate. For example, if dose escalation in the GTV is the goal, as described above and similarly by Tseung et al. [Wan+16] and by Fager et al. [Fag+15], this can be achieved by objective functions evaluated for RBE-weighted dose.

Potentially, plan improvements can be achieved by lowering the physical dose in the target in areas of high LET, based on the assumption that RBE is larger than 1.1. The reduced target dose may in turn lead to lower doses in normal tissue. Such treatment plans can be created by evaluating target coverage objectives for RBE-weighted dose rather than physical dose [WO05; Fre+11]. Currently, practitioners are hesitant to pursue this approach because it risks under-dosing the tumor if the RBE is overestimated. However, advances in RBE measurements [Gua+15] may facilitate such approaches in the future.

5.2.5 Conclusion

We describe a prioritized optimization method to reoptimize IMPT plans in terms of their LET distributions while limiting the degradation of the best possible physical dose distribution. The method does not depend on tissue or patient-specific RBE, which currently is associated with large uncertainties. It can be applied to patients in whom serial critical structures are located within or adjacent to the target volume, to avoid high LET values in these structures. This makes the use of IMPT safer, considering that the risk of side effects associated with high LET is largely unknown.

References

[Bas+10] Niels Bassler, Oliver Jäkel, Christian Skou Søndergaard, and Jørgen B. Petersen. “Dose- and LET-painting with particle therapy”. In: *Acta Oncologica* 49.7 (Oct. 1, 2010), pp. 1170–1176. ISSN: 0284-186X. DOI: 10.3109/0284186X.2010.510640. URL: https://doi.org/10.3109/0284186X.2010.510640 (visited on 08/13/2018).

[Car+10] A. Carabe-Fernandez, R. G. Dale, J. W. Hopewell, B. Jones, and H. Paganetti. "Fractionation effects in particle radiotherapy: implications for hypofractionation regimes". In: *Physics in Medicine & Biology* 55.19 (2010), p. 5685. ISSN: 0031-9155. DOI: 10.1088/0031-9155/55/19/005. URL: http://stacks.iop.org/0031-9155/55/i=19/a=005 (visited on 08/13/2018).

[Fag+15] Marcus Fager, Iuliana Toma-Dasu, Maura Kirk, Derek Dolney, Eric S. Diffenderfer, Neha Vapiwala, and Alejandro Carabe. "Linear Energy Transfer Painting With Proton Therapy: A Means of Reducing Radiation Doses With Equivalent Clinical Effectiveness". In: *International Journal of Radiation Oncology*Biology*Physics* 91.5 (Apr. 1, 2015), pp. 1057–1064. ISSN: 0360-3016. DOI: 10.1016/j.ijrobp.2014.12.049. URL: http://www.sciencedirect.com/science/article/pii/S0360301614045635 (visited on 08/13/2018).

[Fre+11] Malte C. Frese, Jan J. Wilkens, Peter E. Huber, Alexandra D. Jensen, Uwe Oelfke, and Zahra Taheri-Kadkhoda. "Application of constant vs. variable relative biological effectiveness in treatment planning of intensity-modulated proton therapy". In: *International Journal of Radiation Oncology, Biology, Physics* 79.1 (Jan. 1, 2011), pp. 80–88. ISSN: 1879-355X. DOI: 10.1016/j.ijrobp.2009.10.022.

[Gia+13] Drosoula Giantsoudi, Clemens Grassberger, David Craft, Andrzej Niemierko, Alexei Trofimov, and Harald Paganetti. "Linear Energy Transfer-Guided Optimization in Intensity Modulated Proton Therapy: Feasibility Study and Clinical Potential". In: *International Journal of Radiation Oncology*Biology*Physics* 87.1 (Sept. 1, 2013), pp. 216–222. ISSN: 0360-3016. DOI: 10.1016/j.ijrobp.2013.05.013. URL: http://www.sciencedirect.com/science/article/pii/S0360301613005452 (visited on 08/13/2018).

[Gia+15] Drosoula Giantsoudi, Jan Schuemann, Xun Jia, Stephen Dowdell, Steve Jiang, and Harald Paganetti. "Validation of a GPU-based Monte Carlo code (gPMC) for proton radiation therapy: clinical cases study". In: *Physics in Medicine & Biology* 60.6 (2015), p. 2257. ISSN: 0031-9155. DOI: 10.1088/0031-9155/60/6/2257. URL: http://stacks.iop.org/0031-9155/60/i=6/a=2257 (visited on 08/13/2018).

[Gra+11] Clemens Grassberger, Alexei Trofimov, Anthony Lomax, and Harald Paganetti. "Variations in Linear Energy Transfer Within Clinical Proton Therapy Fields and the Potential for Biological Treatment Planning". In: *International Journal of Radiation Oncology*Biology*Physics* 80.5 (Aug. 1, 2011), pp. 1559–1566. ISSN: 0360-3016. DOI: 10.1016/j.ijrobp.2010.10.027. URL: http://www.sciencedirect.com/science/article/pii/S0360301610034486 (visited on 08/13/2018).

[Gua+15] Fada Guan et al. "Spatial mapping of the biologic effectiveness of scanned particle beams: towards biologically optimized particle therapy". In: *Scientific Reports* 5 (May 18, 2015), p. 9850. ISSN: 2045-2322. DOI: 10.1038/srep09850. URL: https://www.nature.com/articles/srep09850 (visited on 08/13/2018).

[Jia+12] Xun Jia, Jan Schümann, Harald Paganetti, and Steve B. Jiang. "GPU-based fast Monte Carlo dose calculation for proton therapy". In: *Physics in Medicine & Biology* 57.23 (2012), p. 7783. ISSN: 0031-9155. DOI: 10.1088/0031-

9155/57/23/7783. URL: http://stacks.iop.org/0031-9155/57/i=23/a=7783 (visited on 08/22/2018).

[JMF07] Kyung-Wook Jee, Daniel L. McShan, and Benedick A. Fraass. "Lexicographic ordering: intuitive multicriteria optimization for IMRT". In: *Physics in Medicine & Biology* 52.7 (2007), p. 1845. ISSN: 0031-9155. DOI: 10.1088/0031-9155/52/7/006. URL: http://stacks.iop.org/0031-9155/52/i=7/a=006 (visited on 08/13/2018).

[MSP15] Aimee L. McNamara, Jan Schuemann, and Harald Paganetti. "A phenomenological relative biological effectiveness (RBE) model for proton therapy based on all published in vitro cell survival data". In: *Physics in medicine and biology* 60.21 (Nov. 7, 2015), pp. 8399–8416. ISSN: 0031-9155. DOI: 10.1088/0031-9155/60/21/8399. URL: https://www.ncbi.nlm.nih.gov/pmc/articles/PMC4634882/ (visited on 08/13/2018).

[Pag14] Harald Paganetti. "Relative biological effectiveness (RBE) values for proton beam therapy. Variations as a function of biological endpoint, dose, and linear energy transfer". In: *Physics in Medicine and Biology* 59.22 (Nov. 21, 2014), R419–472. ISSN: 1361-6560. DOI: 10.1088/0031-9155/59/22/R419.

[Unk+16] Jan Unkelbach, Pablo Botas, Drosoula Giantsoudi, Bram L. Gorissen, and Harald Paganetti. "Reoptimization of Intensity Modulated Proton Therapy Plans Based on Linear Energy Transfer". In: *International Journal of Radiation Oncology*Biology*Physics* 96.5 (Dec. 1, 2016), pp. 1097–1106. ISSN: 0360-3016. DOI: 10.1016/j.ijrobp.2016.08.038. URL: http://www.sciencedirect.com/science/article/pii/S0360301616331534.

[Wan+16] Hok Seum Wan Chan Tseung, Jiasen Ma, Cole R. Kreofsky, Daniel J. Ma, and Chris Beltran. "Clinically Applicable Monte Carlo–based Biological Dose Optimization for the Treatment of Head and Neck Cancers With Spot-Scanning Proton Therapy". In: *International Journal of Radiation Oncology*Biology*Physics* 95.5 (Aug. 1, 2016), pp. 1535–1543. ISSN: 0360-3016. DOI: 10.1016/j.ijrobp.2016.03.041. URL: http://www.sciencedirect.com/science/article/pii/S0360301616300311 (visited on 08/13/2018).

[Wil+07] Jan J. Wilkens, James R. Alaly, Konstantin Zakarian, Wade L. Thorstad, and Joseph O. Deasy. "IMRT treatment planning based on prioritizing prescription goals". In: *Physics in Medicine & Biology* 52.6 (2007), p. 1675. ISSN: 0031-9155. DOI: 10.1088/0031-9155/52/6/009. URL: http://stacks.iop.org/0031-9155/52/i=6/a=009 (visited on 08/13/2018).

[WLH13] Minna Wedenberg, Bengt K. Lind, and Björn Hårdemark. "A model for the relative biological effectiveness of protons: the tissue specific parameter α/β of photons is a predictor for the sensitivity to LET changes". In: *Acta Oncologica (Stockholm, Sweden)* 52.3 (Apr. 2013), pp. 580–588. ISSN: 1651-226X. DOI: 10.3109/0284186X.2012.705892.

[WO04] J. J. Wilkens and U. Oelfke. "A phenomenological model for the relative biological effectiveness in therapeutic proton beams". In: *Physics in Medicine and Biology* 49.13 (July 7, 2004), pp. 2811–2825. ISSN: 0031-9155.

[WO05] Jan J. Wilkens and Uwe Oelfke. "Optimization of radiobiological effects in intensity modulated proton therapy". In: *Medical Physics* 32.2 (Feb. 2005), pp. 455–465. ISSN: 0094-2405. DOI: 10.1118/1.1851925.

Chapter 6

Results III: Lung planning

In section 6.2 of this chapter, the following publication is reproduced:

P Botas, C Grassberger, G Sharp, and H Paganetti. "Density overwrites of internal tumor volumes in intensity modulated proton therapy plans for mobile lung tumors". In: *Physics in Medicine & Biology* 63.3 (2018), p. 035023.

My role in the publication is clearly stated in the following subsection. Some comments on the adaptation of the publication are also given.

6.1 Role in study

I was the main author in this study, writing all required software and performing the analysis. This includes:

- Creation of the patient's planning CTs with the ITV density overwrites.
- Implementation of the dose delivery time structure from the cyclotron.
- Development of the 4D framework to connect the DIR software, Plastimatch [Sha12], with the dose delivery time structure model and gPMC.
- Plastimatch development to support multiplication and maximum image filters from ITK (Insight Segmentation and Registration Toolkit).
- Results analysis scripts, mainly written in R using the *tidyverse* libraries (https://www.tidyverse.org/).
- Manuscript writing.

Discussions were held with all the authors, providing key insights.

Comments on the adaptation of the paper: The position of figures and tables may differ from the published manuscript. The citation style and the internal figure, table and equation numbers have been altered, but the underlying meaning has been conserved.

6.2 Density overwrites of ITV in IMPT plans for mobile lung tumors

P. Botas[1,2], C. Grassberger[1,3], G. Sharp[1,3] and H. Paganetti[1,3]
[1] Department of Radiation Oncology, Massachusetts General Hospital, Boston, MA, USA.
[2] Department of Physics, University of Heidelberg, Heidelberg, Germany.
[3] Harvard Medical School, Boston, MA, USA.

Abstract The purpose of this study was to investigate internal tumor volume density overwrite strategies to minimize intensity modulated proton therapy (IMPT) plan degradation of mobile lung tumors.
Four planning paradigms were compared for nine lung cancer patients. Internal gross tumor volume (IGTV) and internal clinical target volume (ICTV) structures were defined encompassing their respective volumes in every 4DCT phase. The paradigms use different planning CT (pCT) created from the average intensity projection (AIP) of the 4DCT, overwriting the density within the IGTV to account for movement. The density overwrites were: (a) constant filling with 100 HU (C100) or (b) 50 HU (C50), (c) maximum intensity projection (MIP) across phases, and (d) water equivalent path length (WEPL) consideration from beam's-eye-view. Plans were created optimizing dose-influence matrices calculated with fast GPU Monte Carlo (MC) simulations in each pCT. Plans were evaluated with MC on the 4DCTs using a model of the beam delivery time structure. Dose accumulation was performed using deformable image registration. Interplay effect was addressed applying 10 times rescanning.
Significantly less DVH metrics degradation occurred when using MIP and WEPL approaches. Target coverage (D99 *geq* 70 Gy(RBE)) was fulfilled in most cases with MIP and WEPL (D99WEPL = 69.2 $\pm$ 4.0 Gy (RBE)), keeping dose heterogeneity low (D5 - D95WEPL = 3.9 $\pm$ 2.0 Gy(RBE)). The mean lung dose was kept lowest by the WEPL strategy, as well as the maximum dose to organs at risk (OARs). The impact on dose levels in the heart, spinal cord and esophagus were patient specific.
Overall, the WEPL strategy gives the best performance and should be preferred when using a 3D static geometry for lung cancer IMPT treatment planning. Newly available fast MC methods make it possible to handle long simulations based on 4D data sets to perform studies with high accuracy and efficiency, even prior to individual treatment planning.

6.2.1 Introduction

Radiation therapy is the mainstay of treatment for inoperable non-small-cell lung cancer (NSCLC). However, NSCLC tumors usually show significant respiratory motion, to which particle therapy is especially sensitive due to the resulting range variations [KL13]. Additionally, the tumor often moves in an orthogonal direction from beam's-eye-view, which may exacerbate the effect. There are techniques to reduce the dosimetric effects of motion

during delivery of a certain plan. Gated therapy can be employed to deliver the plan only when the tumor is within a predefined region; rescanning of IMPT can be employed to give a more homogeneous dose by reducing the interplay effect between the pencil beam scanning delivery pattern of the IMPT plan and the tumor movement; or even delivering the treatment without limitations with the free breathing technique. Regardless of the delivery approach, the tumor motion must be taken into account during the planning stage. It is common practice to define an internal tumor volume (ITV) extracted from a 4-dimensional CT (4DCT), representing the patient geometry and the variations the field would encounter during delivery. By planning in such contour, the plan is more robust towards dosimetric effects caused by geometry changes.

Protons have the potential to offer a dosimetric advantage over photons because they stop within the patient releasing most of their energy at a certain position. This adds an extra degree of freedom for treatment optimization [Lom99; Lom+04] but also introduces additional uncertainties due to the need to precisely predict the range in patients [Lom08b; Lom08a; Unk+09; Pag12]. The range uncertainty is particularly important in lung due to the low density of lung tissue and high-density areas in the beam path such as ribs. For this site it has been shown that analytical dose calculation algorithms as available in proton planning systems are significantly less accurate than Monte Carlo (MC) simulations [Yam+12; Gra+14; Sch+15; Zhe+16; Zvo+17]. Precise dose calculations and plan evaluation with MC methods is therefore important for proton therapy for NSCLC.

The low convergence rate of MC methods has prevented researchers from studying 4D treatment planning approaches with high accuracy, thus focusing mainly on retrospective data analysis. In 4D treatment planning, each plan should be evaluated on each phase of the 4DCT, which, due to the MC simulation times, is often unpractical. However, recent developments in computing architectures, such as graphics processing units (GPU), offer the possibility to exploit the parallelizable nature of MC methods while keeping high accuracy [Jia+12; TMB15]. Another tool necessary to study the effect of patient movement on the delivered dose distribution is deformable image registration (DIR). DIR allows the registration of the different 4DCT phases to a reference phase. The cubic B-spline algorithm has been reported to have sufficient accuracy for dose accumulation in the thorax region [Mur+11]. Implementation of this algorithm for GPUs allows fast registration of the 4DCT phases [SKS10]. As a consequence of these GPU based developments, it is now possible to perform prospective planning studies in 4D based on MC dose calculations.

The efforts found in the literature towards 4D treatment planning can be clustered in two main directions. One is to perform plan optimization on the 4DCT using time-resolved optimization matrices [ERK06; Gra17]. A simpler and more clinically efficient approach

that has been reported to yield good results is to perform plan optimization on one or more static 3D planning CT constructed from the 4DCT that represent the moving geometry [EK05; Kan+07; GDB12; Kno+13; Wan+13; Gra+15]. The goal of this work was to perform a comparison of 4DCT-based IMPT planning strategies using ITV density overwrites for NSCLC cases. Additionally, it was intended to demonstrate that such studies are feasible with high accuracy dose calculation using state of the art dose calculations techniques to improve accuracy. To this end we have developed a GPU-based framework to study 4D treatment planning approaches in IMPT for NSCLC.

In particular we studied 4 strategies for the definition of ITVs. For all strategies, the intensities of the planning CT outside the internal gross tumor volume (IGTV) were defined by the average image projection (AIP) across the 4DCT. Within the IGTV, intensities were set according to four different intensity fillings: constant intensity fillings of 100 HU (C100) and 50 HU (C50), maximum image projection (MIP) filling, and water equivalent path length (WEPL) dependent filling. The reason behind choosing these strategies was that they have been already proposed in the literature as potentially working solutions, but they had not been compared consistently. Kang et al. [Kan+07] have compared AIP CT, free breathing CT, MIP CT and C100 filling of the IGTV within AIP CT, demonstrating that the latter gave the best results. Graeff et al. [GDB12] has reported that a WEPL strategy similar to the concept introduced here yields better results than a purely geometric definition of the ITV. Knopf et al. [Kno+13] also compared a geometrical definition of the ITV contour with a WEPL-adapted definition, proving the latter to be superior; Grassberger et al. [Gra+15] used a C50 filling within AIP CT. Wang et al. [Wan+13] reported the MIP approach presented in their study to be the best when compared with AIP and end-exhale images. All four techniques, although some with different implementations, have been included in our study.

6.2.2 Methods and materials

The steps followed in this study were as follow: first, targets were defined for each patient; next, for each patient, the CT intensities within the IGTV were filled following four different strategies and the intensities outside the IGTV were set to the average of the 4DCT; next, treatment plans were optimized for each strategy with the beamlets data calculated with GPU MC; finally, a 4D evaluation was performed applying GPU MC.

6.2.2.1 Patient cohort and contour definition

A set of nine NSCLC patients with a representative range of tumor volumes and movement amplitudes was used for this retrospective study under IRB-approved protocol. For each

Table 6.1 Patient characteristics. Amplitude is peak-to-peak motion amplitude. The Dice coefficient is a measure of the minimum overlap between GTVs as defined in two phases of the 4DCT. Previously included in [Bot+18].

Patient number	GTV vol. (cm^3)	Amplitude (mm)	Min. GTV Dice coefficient	Number of fields: angles
1	21.1	30.6	0.70	4: 150, 180, 220, 270
2	64.9	3.5	0.87	2: 180, 270
3	26.0	10.7	0.92	2: 90, 180
4	4.0	14.6	0.64	2: 60, 140
5	21.7	10.0	0.84	2: 100, 210
6	2.6	5.1	0.82	2: 240, 310
7	15.4	15.1	0.74	2: 50, 120
8	24.5	9.1	0.87	3: 0, 40, 270
9	100.0	6.5	0.93	2: 250, 330
Average:	31.1 ± 31.5	11.7 ± 8.1	0.8 ± 0.1	–

patient, the gross tumor volume (GTV) was manually contoured at end-of-expiration phase of the 4DCT (50 % or p50). The clinical target volume (CTV) was defined as an isotropic 8 mm expansion of the GTV to account for microscopic disease. The IGTV and internal CTV (ICTV) were defined in the MIP CT, encompassing the GTV and CTV in every phase of the 4DCT. Both were validated in the 4DCT by examining the entire respiratory cycle. The liver and the tumor overlapped in the MIP in one case, for which the IGTV was created as the union of the GTV in all phases. The planning target volume (PTV) was defined as a 5 mm expansion of the ICTV, accounting for patient setup and DIR uncertainties. Normal lung was defined in the planning CT as the combination of both lungs minus the IGTV and at the reference phase as the combination of both lungs minus the GTV.

Table 6.1 summarizes the patient cohort. Tumor volumes ranged from 2.6 to 100.0 cm^3, tumor movement amplitude was between 4.5 and 30.6 mm. The dice coefficient, measuring the overlap between the tumor positions during the respiratory cycle, ranged between 0.64 and 0.93, meaning that at any respiratory phase at least 64 % of the tumor volume overlaps with the volume at a different phase.

6.2.2.2 Strategies to define planning CTs

Treatment plans were designed for each patient in four different planning CTs. Each of the planning CTs was defined following a different strategy to mitigate the effect of patient movement and limit plan degradation. For all planning CTs we defined two components: the AIP of the 4DCT outside the IGTV and the intensity filling overwrite inside the IGTV. For all strategies, the intensities of the planning CT outside the IGTV were defined by the AIP. Within the IGTV, intensities were set according to four different strategies: constant intensity

fillings of 100 HU (C100) and 50 HU (C50), MIP filling, and WEPL dependent filling. Choosing the AIP around the target was a measure to balance under- and overestimations of the range to the proximal end of the target. Underestimations would then be taken into account by selecting conservative fillings of the IGTV.

In C100 and C50, the intensity values in the IGTV were set to 100 and 50 HU, respectively (expression 6.1). The values chosen for the constant fillings were inspired by literature, from previous studies on 4D planning [Kan+07; Gra+13] and studies of tissue changes after treatment, where values of 50-100 HU are shown to represent tumor intensities [May+98; Aki+15]. From the cohort here included, the chosen values have been observed to be close representations of the 99 and 70 percentiles of intensity distribution of the GTV of all patients on all phases combined. Specifically for our patients, these values correspond to 99 and 48 HU. Therefore, the two selected values represent two conservative measures of GTV intensities (figure 6.2a). Both referenced 4D studies have reported the constant fillings to maintain tumor coverage at acceptable dose to normal tissue. C100 is more conservative than C50 in terms of maintaining target dose levels to plan quality, but with potentially higher OAR doses.

$$I_i = 100 \quad \text{or} \quad I_i = 50 \quad \forall i \in \text{IGTV} \tag{6.1}$$

The MIP filling sets each voxel in the IGTV to its maximum intensity across the 4DCT phases (expression 6.2). Due to the tumor densities observed across the patients, the MIP filled IGTV usually presents lower intensities than the constant fillings, although in some points it may have higher intensities. The MIP essentially selects the most conservative intensity value across the phases. The scope of the technique is therefore limited to changes in the IGTV.

$$I_i = \max\left(I_{i,p}\right) \quad \forall i \in \text{IGTV},\ p \in \text{4DCT} \tag{6.2}$$

The WEPL adjusted target sets the intensity of each voxel in the IGTV to the intensity it has in the 4DCT phase presenting the biggest WEPL at the voxel position (expression 6.2). The procedure is as follows: first, the WEPL is calculated per each voxel in each phase, secondly the WEPLs are compared and lastly the voxel is set to the intensity corresponding to the biggest WEPL. This method considers CT intensities outside of IGTV region on a phase by phase basis, because the WEPL is integrated along the beam path. Consequently, this strategy defines a planning CT per treatment field. The resultant intensity values in the IGTV are, by definition, equal or smaller than the intensity values set with the MIP method.

$$I_i = I_{i,p} \quad \text{where} \quad I_{i,p} = \underset{I_{i,p}}{\arg\max}\ \text{WEPL}(I_{i,p}) \quad \forall i \in \text{IGTV},\ p \in \text{4DCT} \tag{6.3}$$

Figure 6.1 illustrates the strategies differences.

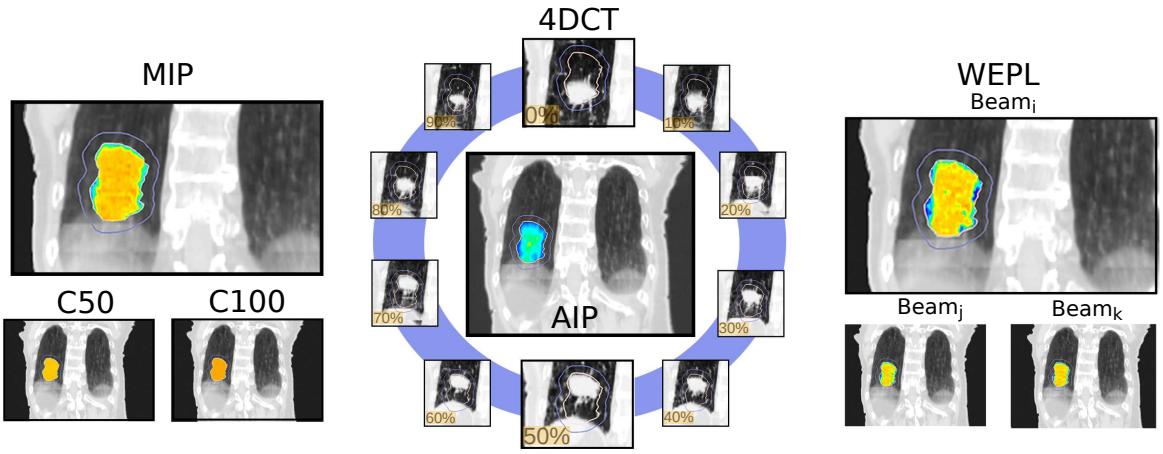

Fig. 6.1 Illustration of planning strategies: each planning CT (C50, C100, MIP, WEPL) was created from the 4DCT (blue circle) and its average image projection (AIP, center). The AIP was applied outside the IGTV, while the IGTV filling depends on the strategy. A color scale was added in the IGTV to help the reader, representing low intensities with blue and higher with red. Images extracted from patient 1. Previously included in [Bot+18].

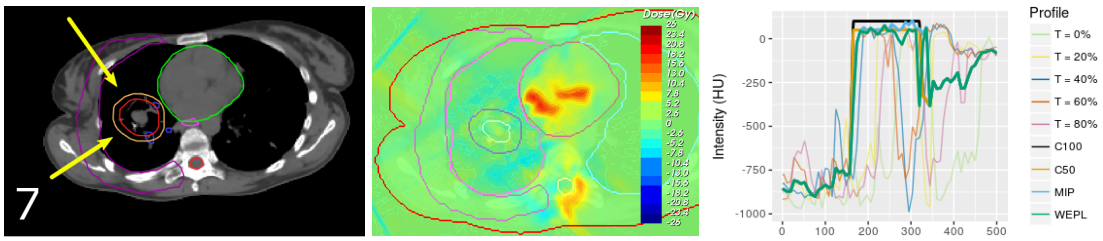

(a) (b) (c)

Fig. 6.2 (a) Structures and field arrangements for patient 6. (b) Dose difference between the planned and the 4D evaluated dose for the MIP strategy. (c) Intensity profiles on a line across the phases of the 4DCT. Previously included in [Bot+18].

6.2.2.3 Treatment planning

For each patient, 4 IMPT plans were created using the different planning CTs described above. The prescription dose was 70 Gy(RBE), delivered to at least 99 % of the ICTV and 95 % of the PTV. Dose was limited in both target structures to V110 $\leq$ 20 %. Normal tissue constraints [Mar+10] were satisfied in all plans. Specifically for the lung, the mean dose was kept below 20 Gy(RBE) and V20 < 30 %. Hotspots were avoided in the esophagus and spinal cord. The beams were chosen as orthogonal to the main motion direction (superior-inferior).

Most cases consisted of two coplanar fields. Gantry angles were chosen to minimize normal tissue dose and to avoid placing a critical structure at the distal end of the beam. A constant RBE of 1.1 was used.

Table 6.1 shows the field angles for each patient. Figure 6.2a shows patient 6 structures and fields arrangement. Figure 6.2b shows the dose difference between the plan and the 4D evaluation using the results from the same patient. Figure 6.2c shows the intensity profiles across the 4DCT phases and the intensity profiles assigned by each strategy.

All dose calculations were performed with gPMC, a previously validated fast MC for GPUs [Qin+16]. gPMC was employed to generate the dose-influence matrix (d_{ij}) of each field in each planning CT. IMPT optimization of the d_{ij}s was performed with Opt4D, an in-house optimization tool originally developed for temporo-spatial studies [Tro+05].

6.2.2.4 Evaluation

For evaluation, each plan was split into 10 subplans, one for each 4DCT phase. Dose for each subplan was computed on the corresponding phase, and finally the total dose was accumulated. The subplans were generated using a model of the beam delivery time structure at our institution and assuming a fixed duration per 4DCT phase of 0.5 s. To avoid a bias in the results caused by the interplay effect, we performed 10 times rescanning by setting the initial respiratory phase during the assignment to the subplans at every 4DCT phase and averaging the subplan dose. This corresponds to 10× phase-averaged rescanning and has been shown to eliminate the effect [Sec+09; Gra+13]. The dose delivered by each subplan was then accumulated into the reference phase. The dose was warped with vector fields generated by DIR between each phase and the reference. The DIR and the dose warping were performed in Plastimatch, an open source suite for radiotherapy and medical imaging, using its GPU parallelized B-spline algorithm [Sha12; SKS10]. The correctness of the registrations was visually verified.

Target coverage was evaluated in the CTV of the reference phase after 4D simulation and dose accumulation. The metrics analyzed were D99, V110 and D5-D95. Normal lung was evaluated with mean lung dose (MLD), maximum dose and V20Gy(RBE). Maximum dose was used for the spinal cord and esophagus. Strategy comparison was performed after 4D evaluation. Because the same set of objectives and constrains are applied for all the strategies, the final 4D-evaluated dose distribution is the only measure of the goodness of each strategy.

Specific comparisons between strategies were performed. The patient-by-patient difference between strategies for a given quantity X was calculated and one-tailed paired *t-tests* to compare the resultant distribution were applied (H_0 : mean$\left(x_j - x_i\right) > 0$ or mean$\left(x_j - x_i\right) < 0$, depending on the case). This approach is discussed in detail in the following section.

6.2.3 Results and discussion

Assessing the performance of the different strategies can be approached in two ways, either with the study of the relative changes between the plan and the 4D accumulated dose or the absolute plan performance at 4D evaluation.

When studying plan changes, there is an inconsistency in the plan baseline. Because each strategy is designed with different densities in the target, different spots will be selected by the optimizer to deliver the most optimal dose. This causes the plan dose distribution to be different for different strategies within the same patient. As such, accidental differences in plan quality arise between strategies, yielding no well-defined baseline per patient to study plan changes. Additionally, the facts that proton dose distribution is very sensitive to patient density heterogeneities [Sch+14] and that the planning CTs are somewhat an artificial construct, suggest that the planned dose distribution is as well an artificial construct. Hence, studying its change might not be meaningful. Therefore, as introduced in the previous section, strategy comparisons we performed after 4D evaluation. The results are summarized in table 6.2.

The boxplots in this section show the 1st (Q_1), 2nd (Q_2) and 3rd (Q_3) quartiles with the colored box, the lower fence is the smallest observation bigger than $Q_1 - 1.5 \cdot IQR$ and the upper fence is the largest observation smaller than $Q_3 + 1.5 \cdot IQR$. The IQR is the inter-quartile range ($Q_3 - Q_1$). The two fences are shown with the vertical lines. Data points beyond the fences are outliers. Individual patient points have been plotted over the boxplots to allow outlier identification.

6.2.3.1 Framework performance

4D plan simulation with GPU MC takes an average of 5 min per patient on one GPU unit (NVIDIA Tesla K40C). The total process, including DIR of the 4DCT phases to the reference phase takes place in 10 min if serial calculations are performed. Parallel calculations in a cluster could speed up the process considerably. Both, MC and DIR could be parallelized on multiple CPUs to perform the 4D plan evaluation in less than 1 min.

6.2.3.2 Target coverage

Figure 6.3 shows the target coverage metrics for each strategy after 4D dose simulation. In all metrics C100 and C50 have been observed to perform more poorly than the MIP and WEPL strategies.

The delivered D99 meets at least the prescription dose in 7 out of 9 cases (77.7 %) planned with the MIP and WEPL strategy. The average D99 with the MIP and WEPL strategies were

Table 6.2 Strategy averages across patients per contour and dose metric. WEPL in absolute values, others as a difference with respect to WEPL values. One tailed paired t-tests were performed to assess the significance of the difference between strategies, with null hypothesis H_0 : mean$(x_i - x_{WEPL}) > 0$. Previously included in [Bot+18].

		Strategy						
Structure	Metric Gy(RBE), unless specified	WEPL (Absolute)	MIP (Average absolute difference w.r.t. WEPL and p-value)		C50		C100	
CTV	D99	69.2 ± 4.0	-0.3 ± 0.9	0.92	-3.3 ± 2.8	> 0.99	-3.3 ± 2.8	> 0.99
	V110 (%)	2.7 ± 6.1	2.1 ± 3.1	0.04	6.9 ± 9.8	0.03	8.9 ± 13.6	0.04
	D5-D95	3.9 ± 2.0	1.1 ± 1.7	0.05	4.9 ± 3.7	< 0.01	5.2 ± 4.0	< 0.01
Lung	$\overline{D}$	6.9 ± 2.6	0.1 ± 0.1	0.09	0.2 ± 0.4	0.06	0.3 ± 0.5	0.06
	V20Gy(RBE) (%)	11.9 ± 4.6	0.2 ± 0.3	0.08	0.8 ± 1.3	0.04	1.0 ± 1.4	0.04
	D_{max}	76.7 ± 3.0	1.1 ± 1.3	0.02	5.3 ± 5.2	0.01	5.2 ± 4.5	< 0.01
Spinal Cord	D_{max}	7.8 ± 13.5	1.4 ± 2.8	0.08	3.5 ± 7.0	0.09	3.9 ± 7.1	0.07
Heart	V25Gy (%)	6.3 ± 10.4	-0.2 ± 1.1	0.64	0.2 ± 0.5	0.12	0.5 ± 0.4	0.01
	(without Pat. 6)	2.6 ± 3.6	0.2 ± 0.4	0.13	0.4 ± 0.4	0.03	0.5 ± 0.5	0.02
Esophagus	D_{max}	15.1 ± 18.0	1.5 ± 1.7	0.02	2.1 ± 8.0	0.24	1.8 ± 7.5	0.26

68.9 ± 3.8 and 69.2 ± 4.0 Gy(RBE), respectively. The 2 patients not fulfilling the prescribed dose present an average D99 = 63.4 Gy(RBE), 9.4 % below prescription. Performing the MIP and WEPL comparison as described at the beginning of this section shows that the WEPL strategy consistently yields a higher D99 ($p = 0.08$).

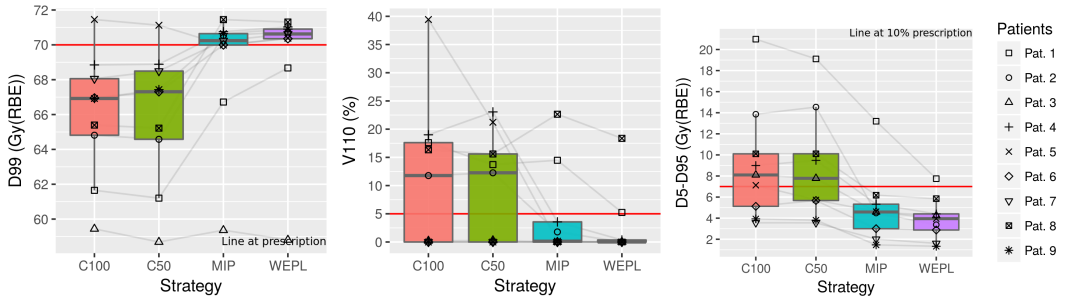

(a) (b) (c)

Fig. 6.3 Target (CTV) coverage metrics. From left to right: D99, V110 and D5-D95. C100 and C50 provide inappropriate coverage. MIP and WEPL provide coverage, having WEPL a higher D99 index and lower V110 and D5-D95. Previously included in [Bot+18].

V110 was also similar for the MIP and WEPL strategies. Their average V110 were 4.7 ± 8.2 and 2.7 ± 6.1 %, respectively. Most cases show a V110 below 5 % of prescription dose. The WEPL strategy produces less hotspots than the MIP strategy ($p = 0.04$), which results in a higher average D5-D95 for the MIP strategy than for the WEPL, with 5.0 ± 3.4

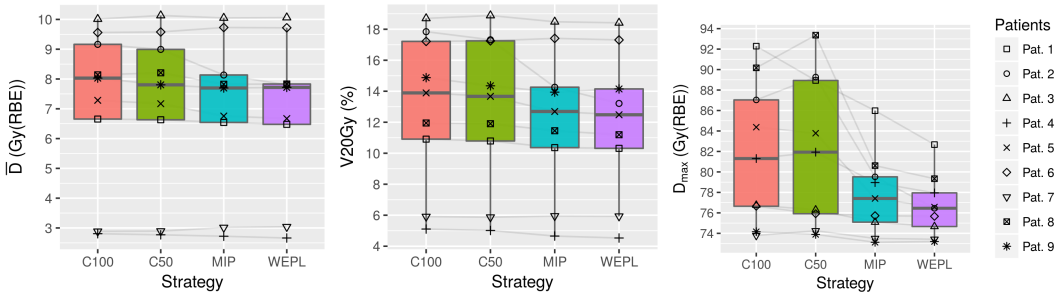

(a) (b) (c)

Fig. 6.4 Lung dose metrics. From left to right: mean dose, V20Gy(RBE) and Max dose. Lower dose levels are given by the WEPL strategy. Previously included in [Bot+18].

and 3.9 ± 2.0 Gy(RBE). The WEPL strategy produces more homogeneous dose than the MIP ($p = 0.05$).

Patient 1 was the only outlier in all three target metrics with the MIP and WEPL strategies. As shown in table 6.1, this case presents the biggest amplitude in the patient cohort with 30.6 mm, which may explain the observed behavior. In this case, the WEPL strategy has a higher V99 than the MIP, with 95.3 % and 82.1 %, respectively, but is insufficient to provide target coverage.

6.2.3.3 Lung dose

Figures 6.4a shows the mean lung dose, V20Gy(RBE) (6.4b) and maximum dose (6.4c) for each strategy after 4D dose simulation and accumulation. The difference between strategies is not as clear as in the target dose levels (figure 6.3). Still, C100 and C50 are seen to perform poorer than the MIP and WEPL strategies, giving higher MLD, V20Gy(RBE) and maximum dose. The maximum lung dose is not a clinical constraint but it serves to estimate the magnitude of hotspots that could arise in normal tissue close to the target, where other critical structures such as esophagus might be located in certain patients.

The MLD is kept by all strategies below 20 Gy(RBE) and V20Gy(RBE) is also below 30 %, fulfilling the plan constrains. The average MLD for C100, C50, MIP and WEPL are 7.2 ± 2.7, 7.1 ± 2.7, 6.9 ± 2.6 and 6.9 ± 2.6 Gy. The MLD ranges from 2.7 to 10.1 Gy(RBE).

Hotspots are present in normal lung when employing C100 and C50 (figure 6.4c). MIP and WEPL reduce the hotspots. Comparing MIP and WEPL, the latter produces lower MLD, V20Gy(RBE) and maximum dose ($p = 0.09$, $p = 0.09$ and $p = 0.02$, respectively).

6.2.3.4 Impact on other OARs

Dose to OARs downstream the target, mainly the heart, esophagus and spinal cord, depends on the specific combination of tumor movement, spot maps and beam angles. As such, the dose per patient in these OARs presented a wide range. This can be seen in figure 6.5.

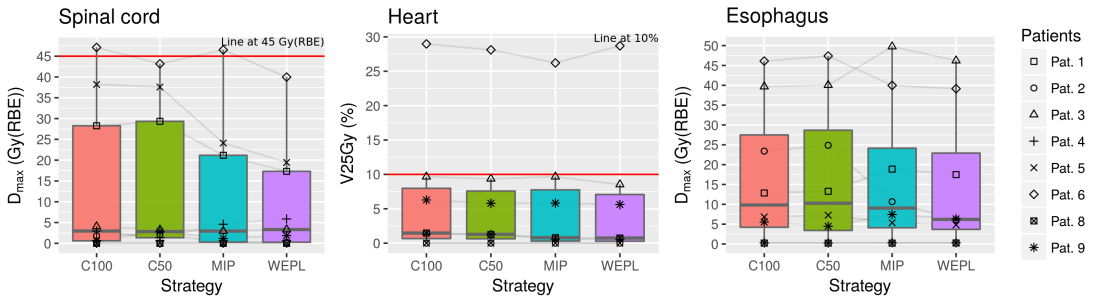

(a) (b) (c)

Fig. 6.5 Dose metrics for spinal cord, heart and esophagus. From left to right: max dose to spinal cord, V25Gy(RBE) in the heart and max dose to esophagus. Lower dose levels are given by the WEPL strategy. Previously included in [Bot+18].

The maximum dose to the spinal cord is kept within the constraints for all patients by C50 and WEPL, as shown in figure 6.5a. The average maximum dose is, however, significantly lower in the WEPL case than in C50: 9.8 ± 13.5 and 13.3 ± 17.9 Gy(RBE). MIP and WEPL are the strategies with lowest average maximum doses. The dose level for MIP is 11.2 ± 16.2 Gy(RBE). The patient-by-patient comparison shows the WEPL gives smaller maximum dose to the spinal cord ($p = 0.08$).

As shown in figures 6.5b and 6.2a, patient 6 presents hotspots in the heart, spinal cord and esophagus as a result of tumor movement. However, it is only in the case of the heart that patient 6 can be considered an outlier. The fact that the WEPL strategy has a higher V25Gy(RBE) for this patient increases its average, thus making it higher than with the MIP strategy. Removing this patient from the analysis shows that the WEPL strategy consistently produces lower V25Gy(RBE) in the heart than the MIP ($p = 0.13$). In summary, the WEPL strategy usually delivers less dose (V25Gy(RBE)) to the heart than the other strategies. The WEPL strategy also limits the average maximum dose in the esophagus.

6.2.3.5 Discussion

As shown in figures 6.3-6.5 and table 6.2, the WEPL strategy is superior to the MIP, C50 and C100 strategies in the current study. Target coverage is provided by the WEPL and MIP strategies, with less overdose given by the WEPL. The dose to OARs was kept lower by the

WEPL strategy as well. OARs other than the lung show big differences between patients, but, with some outliers, the WEPL strategy consistently showed better dose metrics.

The fundamental idea behind the WEPL strategy here studied has already been introduced previously [GDB12; Kno+13]. In any WEPL-dependent approach, field specific information has to be included in the planning process, either before or after the creation of the d_{ij} for optimization. In the approach by Knopf et al. [Kno+13] field specific ITVs as a function of the WEPL are generated making the d_{ij} agnostic of the movement information. However, the lack of a common or generalized target contour implies a limitation for IMPT planning as it can only be jointly optimized using single field uniform dose (SFUD) conditions or by joining the ITVs, considerably augmenting the target volume. On the other hand, the methods by Graeff et al. [GDB12] and the one introduced in our work include the movement information in the optimization matrix itself, providing a well-defined target for full IMPT optimization. The only difference between the two approaches is that, contrary to our approach, Graeff et al. define adapted intensity-WEPL conversion curves for each beamlet in each field. These curves scale the WEPL seen inside the target by the dose calculation algorithm to cover the minimum and maximum WEPL found along the beamlet across the phases of the 4DCT. After being calculated with this curve, each beamlet is included in the d_{ij} for optimization. This method, depending on the specific implementation, should yield similar results to the WEPL method presented in this manuscript, although out approach is simpler. Note that, if the plans are done with the SFUD method, all three WEPL dependent methods will yield very similar results.

In order to apply the WEPL method here discussed, the treatment planning system has to be able to deal with as many CTs as fields in the plan during the d_{ij} calculations.

One main caveat in this study is the assumption that the 4DCT is a good representation of the breathing pattern of the patient at treatment time. Some studies have reported significant changes in the tumor baseline and tumor motion pattern as the treatment progresses [Yi+11; Zha+13; Phi+15; Tak+16]. Some deformation of the tumor may also occur during this time [Yi+11]. These effects are not captured in the current study design, which relies on the 4DCT. Nevertheless, from the data presented in this study it can be hypothesized that the MIP and WEPL strategies are the most robust towards these changes as well. As shown in figure 6.2c, strategies C100 and C50 are the most conservative because they force the optimizer to employ beamlets with higher energy due to the higher density overwrite. Therefore, they could be expected to be more robust than MIP and WEPL against patient geometry changes not captured in the 4DCT that involve an increase in patient water-equivalent thickness from beam's eye view. Nevertheless, even in this case, being C100 and C50 more robust does not mean that their plan quality would be superior to the MIP and WEPL strategies because the

performance baseline, as studied in this manuscript, is better in the latter strategies. More importantly, in lung cancer, especially during a prolonged treatment regimen with concurrent chemotherapy, tumor shrinkage is usually more likely, which would lead to more beamlets being placed behind the target in the constant overwrite strategies (C50/100). The same argument could potentially be employed with other patient-specific constant fillings. Any constant filling strategy would be deduced mainly from the study of the tumor intensity spectra across the 4DCT, ultimately simplifying it to a single point. On the contrary, non-constant fillings do not show this limitation, hence including more information. In summary, the robustness of these strategies towards patient changes should be compared, although the authors do not expect differences in plan degradation to overcome the plan quality baseline differences seen in this study. Other constant filling strategies remain to be investigated; however, the authors do not expect an improvement on the MIP or WEPL strategies analyzed herein.

6.2.4 Conclusions

Respiratory motion degrades the planned IMPT dose distribution. Four strategies to limit the plan degradation produced by the patient's respiratory motion were studied using state of the art Monte Carlo simulations. A fast GPU-framework was developed for treatment planning and 4D dose evaluation. Of the four considered strategies, the AIP of the 4DCT along with the WEPL-dependent IGTV filling best capture different patient geometries represented in the 4DCT in one planning CT. This strategy keeps prescription dose levels to the target, while maintaining low dose to OARs. The WEPL strategy is accordingly recommended as a good approach in any case involving collapsing different patient geometries, such as respiratory phases, into a representative construct. Concerning its applicability, the treatment planning system has to be able to handle as many CT volumes as fields in the plan for the generation of the optimization matrices. No other special requirements are necessary for the IMPT optimization.

Additionally, we show that it is possible to assess the quality of a treatment plan on 4D geometries on a patient-per-patient basis with high accuracy calculations. Assuming the 4DCT is a representative geometry of the patient's breathing cycle during delivery, the developed GPU MC framework could be implemented as a treatment plan validation of NSCLC proton therapy.

Acknowledgments

We thank Jan Unkelbach for helping with the application of the optimizer ”Opt4D“. This work was supported by NCI U19 CA-21239 ”Proton Therapy Research“.

References

[Aki+15] H. Akimoto, M. Aoki, Y. Takai, K. Hirose, M. Sato, H. Kawaguchi, S. Ono, and H. Miura. “Correlation Between Tumor Size and Blood Volume in Lung Tumors: A Prospective Study on Dual-Energy Gemstone Spectral CT Imaging”. In: *International Journal of Radiation Oncology • Biology • Physics* 93.3 (Nov. 1, 2015), E435. ISSN: 0360-3016. DOI: 10.1016/j.ijrobp.2015.07.1656. URL: https://www.redjournal.org/article/S0360-3016(15)02387-1/fulltext (visited on 08/13/2018).

[Bot+18] Pablo Botas, Clemens Grassberger, Gregory Sharp, and Harald Paganetti. “Density overwrites of internal tumor volumes in intensity modulated proton therapy plans for mobile lung tumors”. In: *Physics in Medicine & Biology* 63.3 (2018), p. 035023. ISSN: 0031-9155. DOI: 10.1088/1361-6560/aaa035. URL: http://stacks.iop.org/0031-9155/63/i=3/a=035023 (visited on 08/09/2018).

[EK05] Martijn Engelsman and Hanne M. Kooy. “Target volume dose considerations in proton beam treatment planning for lung tumors”. In: *Medical Physics* 32.12 (Dec. 1, 2005), pp. 3549–3557. ISSN: 2473-4209. DOI: 10.1118/1.2126187. URL: https://aapm.onlinelibrary.wiley.com/doi/abs/10.1118/1.2126187 (visited on 08/13/2018).

[ERK06] Martijn Engelsman, Eike Rietzel, and Hanne M. Kooy. “Four-dimensional proton treatment planning for lung tumors”. In: *International Journal of Radiation Oncology • Biology • Physics* 64.5 (Apr. 1, 2006), pp. 1589–1595. ISSN: 0360-3016. DOI: 10.1016/j.ijrobp.2005.12.026. URL: https://www.redjournal.org/article/S0360-3016(05)03095-6/fulltext (visited on 08/13/2018).

[GDB12] Christian Graeff, Marco Durante, and Christoph Bert. “Motion mitigation in intensity modulated particle therapy by internal target volumes covering range changes”. In: *Medical Physics* 39.10 (Oct. 1, 2012), pp. 6004–6013. ISSN: 2473-4209. DOI: 10.1118/1.4749964. URL: https://aapm.onlinelibrary.wiley.com/doi/abs/10.1118/1.4749964 (visited on 08/13/2018).

[Gra+13] Clemens Grassberger, Stephen Dowdell, Antony Lomax, Greg Sharp, James Shackleford, Noah Choi, Henning Willers, and Harald Paganetti. “Motion Interplay as a Function of Patient Parameters and Spot Size in Spot Scanning Proton Therapy for Lung Cancer”. In: *International Journal of Radiation Oncology • Biology • Physics* 86.2 (June 1, 2013), pp. 380–386. ISSN: 0360-3016. DOI: 10.1016/j.ijrobp.2013.01.024. URL: https://www.redjournal.org/article/S0360-3016(13)00088-6/fulltext (visited on 08/13/2018).

[Gra+14] Clemens Grassberger, Juliane Daartz, Stephen Dowdell, Thomas Ruggieri, Greg Sharp, and Harald Paganetti. "Quantification of Proton Dose Calculation Accuracy in the Lung". In: *International Journal of Radiation Oncology • Biology • Physics* 89.2 (June 1, 2014), pp. 424–430. ISSN: 0360-3016. DOI: 10.1016/j.ijrobp.2014.02.023. URL: https://www.redjournal.org/article/S0360-3016(14)00208-9/fulltext (visited on 08/13/2018).

[Gra+15] Clemens Grassberger, Stephen Dowdell, Greg Sharp, and Harald Paganetti. "Motion mitigation for lung cancer patients treated with active scanning proton therapy". In: *Medical Physics* 42.5 (May 1, 2015), pp. 2462–2469. ISSN: 2473-4209. DOI: 10.1118/1.4916662. URL: https://aapm.onlinelibrary.wiley.com/doi/abs/10.1118/1.4916662 (visited on 08/13/2018).

[Gra17] Christian Graeff. "Robustness of 4D-optimized scanned carbon ion beam therapy against interfractional changes in lung cancer". In: *Radiotherapy and Oncology* 122.3 (Mar. 1, 2017), pp. 387–392. ISSN: 0167-8140, 1879-0887. DOI: 10.1016/j.radonc.2016.12.017. URL: https://www.thegreenjournal.com/article/S0167-8140(16)34458-9/fulltext (visited on 08/13/2018).

[Jia+12] Xun Jia, Jan Schümann, Harald Paganetti, and Steve B. Jiang. "GPU-based fast Monte Carlo dose calculation for proton therapy". In: *Physics in Medicine & Biology* 57.23 (2012), p. 7783. ISSN: 0031-9155. DOI: 10.1088/0031-9155/57/23/7783. URL: http://stacks.iop.org/0031-9155/57/i=23/a=7783 (visited on 08/22/2018).

[Kan+07] Yixiu Kang et al. "4D Proton treatment planning strategy for mobile lung tumors". In: *International Journal of Radiation Oncology • Biology • Physics* 67.3 (Mar. 1, 2007), pp. 906–914. ISSN: 0360-3016. DOI: 10.1016/j.ijrobp.2006.10.045. URL: https://www.redjournal.org/article/S0360-3016(06)03385-2/fulltext (visited on 08/13/2018).

[KL13] Antje-Christin Knopf and Antony Lomax. "In vivo proton range verification: a review". In: *Physics in Medicine & Biology* 58.15 (2013), R131. ISSN: 0031-9155. DOI: 10.1088/0031-9155/58/15/R131. URL: http://stacks.iop.org/0031-9155/58/i=15/a=R131.

[Kno+13] Antje-Christin Knopf, Dirk Boye, Antony Lomax, and Shininchiro Mori. "Adequate margin definition for scanned particle therapy in the incidence of intrafractional motion". In: *Physics in Medicine and Biology* 58.17 (2013), p. 6079. ISSN: 0031-9155. DOI: 10.1088/0031-9155/58/17/6079. URL: http://stacks.iop.org/0031-9155/58/i=17/a=6079 (visited on 04/03/2017).

[Lom+04] Antony J. Lomax, Eros Pedroni, Hanspeter Rutz, and Gudrun Goitein. "The clinical potential of intensity modulated proton therapy". In: *Zeitschrift Für Medizinische Physik* 14.3 (2004), pp. 147–152. ISSN: 0939-3889.

[Lom08a] A. J. Lomax. "Intensity modulated proton therapy and its sensitivity to treatment uncertainties 1: the potential effects of calculational uncertainties". In: *Physics in Medicine and Biology* 53.4 (Feb. 21, 2008), p. 1027. ISSN: 0031-9155. DOI: 10.1088/0031-9155/53/4/014. URL: http://iopscience.iop.org.ubproxy.ub.uni-heidelberg.de/0031-9155/53/4/014 (visited on 03/10/2015).

[Lom08b] A. J. Lomax. "Intensity modulated proton therapy and its sensitivity to treatment uncertainties 2: the potential effects of inter-fraction and inter-field motions". In: *Physics in Medicine and Biology* 53.4 (Feb. 21, 2008), p. 1043. ISSN: 0031-9155. DOI: 10.1088/0031-9155/53/4/015. URL: http://iopscience.iop.org.ubproxy.ub.uni-heidelberg.de/0031-9155/53/4/015 (visited on 03/10/2015).

[Lom99] A. Lomax. "Intensity modulation methods for proton radiotherapy". In: *Physics in Medicine and Biology* 44.1 (Jan. 1, 1999), p. 185. ISSN: 0031-9155. DOI: 10.1088/0031-9155/44/1/014. URL: http://iopscience.iop.org.ubproxy.ub.uni-heidelberg.de/0031-9155/44/1/014 (visited on 03/10/2015).

[Mar+10] Lawrence B. Marks et al. "Radiation Dose–Volume Effects in the Lung". In: *International Journal of Radiation Oncology • Biology • Physics* 76.3 (Mar. 1, 2010), S70–S76. ISSN: 0360-3016. DOI: 10.1016/j.ijrobp.2009.06.091. URL: https://www.redjournal.org/article/S0360-3016(09)03293-3/fulltext (visited on 08/13/2018).

[May+98] Rulon Mayer, Kristi Stanton, Larry Kleinberg, Anuradha Chakravarthy, and Elliot Fishman. "CT number distribution and its association with local control and as a marker of lung tumor response to radiation". In: *Radiation Oncology Investigations* 6.6 (Jan. 1, 1998), pp. 281–288. ISSN: 1520-6823. DOI: 10.1002/(SICI)1520-6823(1998)6:6<281::AID-ROI6>3.0.CO;2-H. URL: https://onlinelibrary.wiley.com/doi/abs/10.1002/%28SICI%291520-6823%281998%296%3A6%3C281%3A%3AAID-ROI6%3E3.0.CO%3B2-H (visited on 08/13/2018).

[Mur+11] K. Murphy et al. "Evaluation of Registration Methods on Thoracic CT: The EMPIRE10 Challenge". In: *IEEE Transactions on Medical Imaging* 30.11 (Nov. 2011), pp. 1901–1920. ISSN: 0278-0062. DOI: 10.1109/TMI.2011.2158349.

[Pag12] Harald Paganetti. "Range uncertainties in proton therapy and the role of Monte Carlo simulations". In: *Physics in Medicine and Biology* 57.11 (June 7, 2012), R99–R117. ISSN: 0031-9155. DOI: 10.1088/0031-9155/57/11/R99. URL: https://www.ncbi.nlm.nih.gov/pmc/articles/PMC3374500/ (visited on 06/28/2018).

[Phi+15] J. Phillips, G. Gueorguiev, C. Grassberger, N. C. Choi, H. Paganetti, and G. C. Sharp. "Effects of Excess Breathing Motion on Proton Dose Coverage". In: *International Journal of Radiation Oncology • Biology • Physics* 93.3 (Nov. 1, 2015), E435. ISSN: 0360-3016. DOI: 10.1016/j.ijrobp.2015.07.1655. URL: https://www.redjournal.org/article/S0360-3016(15)02386-X/fulltext (visited on 08/13/2018).

[Qin+16] Nan Qin, Pablo Botas, Drosoula Giantsoudi, Jan Schuemann, Zhen Tian, Steve B. Jiang, Harald Paganetti, and Xun Jia. "Recent developments and comprehensive evaluations of a GPU-based Monte Carlo package for proton therapy". In: *Physics in Medicine & Biology* 61.20 (2016), p. 7347. ISSN: 0031-9155. DOI: 10.1088/0031-9155/61/20/7347. URL: http://stacks.iop.org/0031-9155/61/i=20/a=7347 (visited on 08/20/2018).

[Sch+14] J. Schuemann, S. Dowdell, C. Grassberger, C. H. Min, and H. Paganetti. "Site-specific range uncertainties caused by dose calculation algorithms for proton therapy". In: *Physics in medicine and biology* 59.15 (Aug. 7, 2014), pp. 4007–4031. ISSN: 0031-9155. DOI: 10.1088/0031-9155/59/15/4007. URL: https://www.ncbi.nlm.nih.gov/pmc/articles/PMC4136435/ (visited on 06/28/2018).

[Sch+15] Jan Schuemann, Drosoula Giantsoudi, Clemens Grassberger, Maryam Moteabbed, Chul Hee Min, and Harald Paganetti. "Assessing the Clinical Impact of Approximations in Analytical Dose Calculations for Proton Therapy". In: *International Journal of Radiation Oncology • Biology • Physics* 92.5 (Aug. 1, 2015), pp. 1157–1164. ISSN: 0360-3016. DOI: 10.1016/j.ijrobp.2015.04.006. URL: https://www.redjournal.org/article/S0360-3016(15)00379-X/fulltext (visited on 08/22/2018).

[Sec+09] Joao Seco, Daniel Robertson, Alexei Trofimov, and Harald Paganetti. "Breathing interplay effects during proton beam scanning: simulation and statistical analysis". In: *Physics in Medicine & Biology* 54.14 (2009), N283. ISSN: 0031-9155. DOI: 10.1088/0031-9155/54/14/N01. URL: http://stacks.iop.org/0031-9155/54/i=14/a=N01.

[Sha12] James A. Shackleford. "Plastimatch 1.6 - Current Capabilities and Future Directions". In: *INt Cong Med Image Comput Comput Assist Interv*. INt Cong Med Image Comput Comput Assist Interv. Vol. 15. Int Conf Med Image Comput Comput Assist Interv. MICCAI 2012, Oct. 15, 2012. URL: http://igtpg.spl.harvard.edu/publications/item/view/2371 (visited on 04/04/2017).

[SKS10] J. A. Shackleford, N. Kandasamy, and G. C. Sharp. "On developing B-spline registration algorithms for multi-core processors". In: *Physics in Medicine and Biology* 55.21 (2010), p. 6329. ISSN: 0031-9155. DOI: 10.1088/0031-9155/55/21/001. URL: http://stacks.iop.org/0031-9155/55/i=21/a=001 (visited on 04/04/2017).

[Tak+16] Seishin Takao et al. "Intrafractional Baseline Shift or Drift of Lung Tumor Motion During Gated Radiation Therapy With a Real-Time Tumor-Tracking System". In: *International Journal of Radiation Oncology • Biology • Physics* 94.1 (Jan. 1, 2016), pp. 172–180. ISSN: 0360-3016. DOI: 10.1016/j.ijrobp.2015.09.024. URL: https://www.redjournal.org/article/S0360-3016(15)26480-2/fulltext (visited on 08/13/2018).

[TMB15] H. Wan Chan Tseung, J. Ma, and C. Beltran. "A fast GPU-based Monte Carlo simulation of proton transport with detailed modeling of nonelastic interactions". In: *Medical Physics* 42.6 (June 1, 2015), pp. 2967–2978. ISSN: 0094-2405. DOI: 10.1118/1.4921046. URL: http://scitation.aip.org.ezp-prod1.hul.harvard.edu/content/aapm/journal/medphys/42/6/10.1118/1.4921046 (visited on 03/23/2016).

[Tro+05] Alexei Trofimov, Eike Rietzel, Hsiao-Ming Lu, Benjamin Martin, Steve Jiang, George T. Y. Chen, and Thomas Bortfeld. "Temporo-spatial IMRT optimization: concepts, implementation and initial results". In: *Physics in Medicine and Biology* 50.12 (2005), p. 2779. ISSN: 0031-9155. DOI: 10.1088/0031-9155/50/12/004. URL: http://stacks.iop.org/0031-9155/50/i=12/a=004 (visited on 04/03/2017).

[Unk+09] Jan Unkelbach, Thomas Bortfeld, Benjamin C. Martin, and Martin Soukup. "Reducing the sensitivity of IMPT treatment plans to setup errors and range uncertainties via probabilistic treatment planning". In: *Medical Physics* 36.1 (Jan. 1, 2009), pp. 149–163. ISSN: 2473-4209. DOI: 10.1118/1.3021139. URL: https://aapm.onlinelibrary.wiley.com/doi/abs/10.1118/1.3021139 (visited on 08/13/2018).

[Wan+13] Ning Wang, Baldev Patyal, Abiel Ghebremedhin, and David Bush. "Evaluation and comparison of New 4DCT based strategies for proton treatment planning for lung tumors". In: *Radiation Oncology* 8.1 (Mar. 25, 2013), p. 73. ISSN: 1748-717X. DOI: 10.1186/1748-717X-8-73. URL: https://doi.org/10.1186/1748-717X-8-73 (visited on 08/13/2018).

[Yam+12] T. Yamashita, T. Akagi, T. Aso, A. Kimura, and T. Sasaki. "Effect of inhomogeneity in a patient's body on the accuracy of the pencil beam algorithm in comparison to Monte Carlo". In: *Physics in Medicine and Biology* 57.22 (Nov. 21, 2012), pp. 7673–7688. ISSN: 1361-6560. DOI: 10.1088/0031-9155/57/22/7673.

[Yi+11] B. S. K. Yi, J. Perks, R. Houston, R. Stern, J. A. Purdy, and A. M. Chen. "Changes in Position and Volume of Lung Cancer Target Volumes during Stereotactic Body Radiotherapy (SBRT): Is Image Guidance Necessary?:" in: *Technology in Cancer Research & Treatment* (Oct. 1, 2011). DOI: 10.7785/tcrt.2012.500226. URL: http://journals.sagepub.com/doi/10.7785/tcrt.2012.500226 (visited on 08/13/2018).

[Zha+13] Ye Zhang, A. Knopf, C. Tanner, D. Boye, and A. J. Lomax. "Deformable motion reconstruction for scanned proton beam therapy using on-line x-ray imaging". In: *Physics in Medicine and Biology* 58.24 (2013), p. 8621. ISSN: 0031-9155. DOI: 10.1088/0031-9155/58/24/8621. URL: http://stacks.iop.org/0031-9155/58/i=24/a=8621 (visited on 02/15/2016).

[Zhe+16] Dandan Zheng, Qinghui Zhang, Xiaoying Liang, Xiaofeng Zhu, Vivek Verma, Shuo Wang, and Sumin Zhou. "Effect of the normalized prescription isodose line on the magnitude of Monte Carlo vs. pencil beam target dose differences for lung stereotactic body radiotherapy". In: *Journal of Applied Clinical Medical Physics* 17.4 (July 1, 2016), pp. 48–58. ISSN: 1526-9914. DOI: 10.1120/jacmp.v17i4.5965. URL: https://aapm.onlinelibrary.wiley.com/doi/abs/10.1120/jacmp.v17i4.5965 (visited on 08/13/2018).

[Zvo+17] Kristina Zvolanek et al. "Still equivalent for dose calculation in the Monte Carlo era? A comparison of free breathing and average intensity projection CT datasets for lung SBRT using three generations of dose calculation algorithms". In: *Medical Physics* 44.5 (May 1, 2017), pp. 1939–1947. ISSN: 2473-4209. DOI: 10.1002/mp.12193. URL: https://aapm.onlinelibrary.wiley.com/doi/abs/10.1002/mp.12193 (visited on 08/13/2018).

Chapter 7

Results IV: Online adaptation of IMPT plans

The contents of this chapter, section 7.2, have been submitted for publication to *Physics in Medicine and Biology*. The contents are currently being reviewed for publication. The final published version is expected to differ from the one here contained after receiving the input from the reviewers.

7.1 Role in study

I was the main author in this study, developing the software and analysis. This includes:

- Conceptualization and creation of the online adaptation algorithm and creation of a *single button* software with several adaptation modes and automatic dashboard reporting based on Python data analysis and plotting libraries (Pandas, Matplotlib, Seaborn). See manuscript for details.
- Conceptualization and implementation in gPMC of the masked scorer and scoping mode, items 7 and 8 in the enumeration in section 3.1.2.
- Conceptualization and implementation in gPMC of the dose matrices for optimization scorer, item 9 in the enumeration in section 3.1.2.
- Results analysis scripts, mainly written in R using the *tidyverse* libraries (https://www.tidyverse.org/).
- Manuscript writing.

Discussions were held with all the authors.

7.2 Online adaption approaches for intensity modulated proton therapy for head and neck patients based on cone beam CTs and Monte Carlo simulations

P. Botas[1,2], J. Kim[1,3], B. Winey[1,3] and H. Paganetti[1,3]
[1] Department of Radiation Oncology, Massachusetts General Hospital, Boston, MA, USA.
[2] Department of Physics, University of Heidelberg, Heidelberg, Germany.
[3] Harvard Medical School, Boston, MA, USA.

Abstract Purpose: To develop an online plan adaptation algorithm for intensity modulated proton therapy (IMPT) based on fast Monte Carlo dose calculation and cone beam CT (CBCT) imaging.
Methods: A cohort of 10 head and neck cancer patients with an average of 6 CBCT scans were studied. To adapt the treatment plan to the new patient geometry, contours were propagated to the CBCTs with a vector field (VF) calculated with deformable image registration between the CT and the CBCTs. Within the adaptive planning algorithm, beamlets were shifted following the VF at their distal falloff and raytraced in the CBCT to adjust their energies, creating a geometrically adapted plan. Four geometric adaptation modes were studied: unconstrained geometric shifts (Free), isocenter shift (Iso), a range shifter (RS), or isocenter shift and range shifter (Iso RS). After evaluation of the geometrical adaptation, the weights of a selected subset of beamlets were automatically tuned using MC generated influence matrices to fulfill the original plan requirements. All beamlet calculations were done with a fast Monte Carlo running on a GPU (Graphics Processing Unit).
Results: Geometrical adaptation alone only worked with small anatomy changes. The weight tuned adaptation worked for every fraction, with the Free and Iso modes performing similarly and being superior than the two range shifters modes. The mean V95 and V107 were 99.4 $\pm$ 0.9 and 6.4 $\pm$ 4.7 % in the Free mode with weight tuning. The calculation time per fraction was ~5 min, but further task parallelization could reduce it to ~1-2 min for delivery adaptation right after patient setup.
Conclusions: An online adaptation algorithm was developed that significantly improved the treatment quality for inter fractional geometry changes. Clinical implementation of the algorithm would allow delivery adaptation right before treatment and thus allow planning margin reductions for IMPT.

7.2.1 Introduction

Head and neck (H&N) tumors are often very close to organs at risk (OARs) such as the parotids, larynx, submandibular glands, or others. Due to the proximity of CTVs to OARs, H&N cases benefit from steep dose gradients in the planned dose distribution to better spare the OARs while giving therapeutic doses to the target. Intensity modulated proton therapy (IMPT) is capable of producing such steep gradients while also reducing dose to OARs and integral dose, thus offering dosimetric benefits over photon treatments [Ahn+14; Bla+16; McK+16; Sio+16; Lee+17]. However, proton plans, and in particular IMPT plans, can be very sensitive to geometrical changes that may distort the planned dose distribution impacting the treatment quality [Ahn+14; Alb+08; Art+17; Lie+14; Lom08b; Pag12; Stü+17; Sze+16]. There are several reasons why the patient's geometry might be different from the one used

for the planned dose distribution, including uncertainties in patient setup or interfractional anatomy changes. The setup uncertainty arises from the patient location on the treatment couch being different to the one recorded in the planning CT. The anatomy changes arises from the patient anatomy evolution throughout the course of treatment, not only due to loss of weight modifying subcutaneous tissue and/or structure locations, but also due to the posture on the treatment couch. Both uncertainty sources might modify the radiological pathway, by introducing high/low density materials in the beamlet's path, affecting the planned dose distribution and affecting the planned target coverage and OAR sparing. This is particularly true in proton therapy due to the impact of uncertainties and geometrical changes on the predicted range of each beamlet.

These uncertainty sources are usually taken into account during the planning procedure with the creation of margins (PTV plus range margin) around the target in an attempt to guarantee treatment quality throughout the treatment course. As a consequence, the high dose volume in the patient is enlarged and organs at risk (OARs) may receive higher doses. It is therefore desirable to shrink the margin to improve IMPT plan quality. More importantly,this method does not guarantee target coverage and OAR sparing throughout the treatment. An alternative to the target expansion is to perform robust IMPT optimization, which entails optimizing the plan considering different scenarios derived from uncertainty models. With this approach, the resultant plan provides target coverage within OAR constraints at delivery, as long as the current situation was included as a scenario during the optimization [Liu+13; Stu+13; Dij+16]. As it is shown in the cited studies, robust optimization is generally able to maintain the original plan target coverage and OAR sparing better than the margin approach. However, robust planning usually softens dose gradients, which, again, results in enlarged high dose volumes and higher dose to OARs compared to a plan performed in a single scenario [Wat+16]. Uncertainties can also be minimized by careful selection of beam angles, but this does not offer a general solution to account for setup and anatomy uncertainties while simultaneously shrinking margins.

Two solutions that might fulfill both requirements are to either perform online IMPT plan adaptation at every fraction or to perform offline treatment re-planning in scenarios when the robust IMPT plan does not fulfill treatment constraints and prescriptions. Online adaptation has the advantages that the treatment delivery is not delayed and that it accounts for the current setup and anatomy, potentially allowing margin reduction.

Online plan adaptation requires an imaging system capable of providing the patient anatomy at treatment position and an updated set of contours localizing the target and OARs. There are currently three options to provide the patient anatomy information: performing a new CT in the treatment position, using the information of a cone beam CT (CBCT) to

deform the original CT or using a CBCT directly [Kur+15; Kur+16b; Lan+15; Oli+18]. However, an adaptation algorithm should be agnostic of the image source. With the new image, an algorithm would then generate an appropriate set of new or modified beamlets for the new geometry. All these steps should occur in a few minutes to fit into the clinical workflow.

Several studies have reported on online and offline IMPT adaptation. Automatic offline full plan reoptimization for H&N cases on deformed planning CT and contours was reported by [Kur+16a], where new beamlet maps were created and optimized. In 2017 Jagt et al. published an online dose restoration procedure [Jag+17] and recently an adaptation algorithm [Jag+18] capable of tailoring the daily dose distribution to the original plan in prostate cases by adding new beamlets to the plan after correcting the beamlet energies. Also recently, Bernatowicz et al. [Ber+18] extended the work presented by Jagt et at. to allow other reoptimization strategies in the dose restoration, applying them to nasopharynx, H&N and lung (1 case each). Except Jagt et al. (2018) [Jag+18], these approaches rely on full plan reoptimization, which, in turn, requires the costly calculation of full dose-influence matrices. A different approach was presented by Moriya et at. [Mor+17] in a different context. In this study the range shifter thickness was adapted in passive scattering plans for lung cancer. This methodology could be expected to have limited success if non-uniform energy shifts are needed, but it is an example of possible adaptation approaches that do not require full plan reoptimization. Although these studies have shown many advances towards online adaptation, none of the proposed methods include Monte Carlo simulations (MC) as dose calculation engine.

It has been shown that MC dose calculation significantly increases accuracy in proton therapy. Specifically for H&N analytical dose calculations accuracy is compromised due to tissue heterogeneities [Lom08a; Pag12; Sch+14; Gra+14; Sch+15; Gen+17]. Using MC calculations for online adaptation imposes time constrains on the design and applicability of the adaptation framework, as they are typically slower than analytical algorithms. Employing graphics processing units (GPU) for MC simulations could potentially allow online IMPT plan adaptation at acceptable efficiency.

The main goal of this work was to demonstrate the feasibility of online adaptation of IMPT plans on daily acquired cone beam CT (CBCT) scans of H&N patients, with automatically propagated deformed contours and using a GPU MC code gPMC [Jia+12; Gia+15; Qin+16], as dose calculation engine. The adaptation would be applied while the patient is on the couch and could potentially allow margins reduction and reduction of the number of re-planning steps, increasing workflow efficiency. An immediate challenge of this goal was to design an algorithm that minimized the calculation burden to allow its online

application. As a secondary goal, different adaptation approaches were studied. Some plan adaptation procedures may modify individual beamlet's energy, drastically increasing the number of energy layers and possibly rendering the new plan undeliverable. Other approaches could be successful, yet simpler than using the delivery system to modify the energy and position of individual beamlets independently. Therefore, the utilization of range shifters and isocenter shifts was compared against the independent adaptation of individual beamlet's energies and positions.

7.2.2 Methods and materials

In this section, first, an adaptive delivery workflow is introduced to explain the adaptation algorithm. Next, based on patient data, different approaches applying the algorithm's operation modes are explained along with the quantities selected to assess their performance.

7.2.2.1 Patient cohort and treatment planning

A representative set of 10 H&N patients with 5-7 CBCT each was studied, for a total of 60 scenarios. The CBCTs were taken weekly as opposed to daily but serve as proof of principle for our daily adaptation workflow. The set is summarized in table 7.1. All patients were treated with photons (IMRT) and new plans were created for IMPT. The plans were designed as 60 Gy(RBE) to the clinical target volume (CTV) delivered with no PTV or range uncertainty margin considered in as many fractions as the number of available CBCTs per patient. A single homogeneous dose level was prescribed for the CTV, creating a more challenging scenario for the plan adaptation, as allowing higher dose in the innermost part of the CTV potentially reduces the number and relevance of cold spots in the periphery of the structure. A specifically demanding situation for the adaptation algorithm was created on purpose by assuming that all the uncertainties not directly addressed by the online adaptation, i.e. all except for setup and patient anatomy, are considered by the original planning technique. Hence, no robust optimization was employed on the original plans, effectively sharpening the dose gradients around the target. The minimum and maximum doses in the CTV were 60 and 63 Gy(RBE), weighting the under/over-dose by 20 and 10, respectively. The dose conformity was enforced by a voxel dependent gradient from the prescription dose at the edge of the CTV to 15 Gy(RBE) at 1 cm from the CTV (overdose weight = 3). The generalized uniform dose (gEUD) to the main OARs was minimized (exponent = 5, weight = 1). In cases this approach did not provide appropriate sparing to specific OARs, additional objectives were created to minimize the dose. The maximum and mean dose to the healthy tissue were minimized (weight = 1).

Table 7.1 Patient cohort.

Pat. No.	Tumor location	N fields	N CBCTs	Plan CTV volume (cm^3)	Average CTV vol. ratio change (min, max)	Average CTV dice (min, max)
1	Oropharynx	4	6	22.3	1.00 (0.97, 1.05)	0.58 (0.50, 0.67)
2	Tonsil	2	6	9.0	1.02 (0.94, 1.12)	0.87 (0.83, 0.90)
3	Oropharynx	3	7	30.7	0.93 (0.90, 1.00)	0.82 (0.77, 0.88)
4	R. Neck	4	6	81.3	1.03 (0.98, 1.06)	0.79 (0.75, 0.84)
5	Hypopharynx	3	5	59.6	0.97 (0.95, 0.98)	0.89 (0.87, 0.91)
6	Mouth	3	7	116.5	0.78 (0.75, 0.82)	0.87 (0.83, 0.90)
7	Larynx	3	6	25.0	1.21 (1.08, 1.34)	0.84 (0.77, 0.88)
8	Tongue	4	5	79.9	1.06 (1.04, 1.11)	0.87 (0.82, 0.91)
9	Tonsil	2	6	12.0	0.98 (0.95, 1.00)	0.87 (0.83, 0.93)
10	Oropharynx	3	7	95.9	0.96 (0.91, 1.02)	0.89 (0.85, 0.92)
	Summary:		60	53.2 ± 38.4	0.99 ± 0.11	0.83 ± 0.09

The tumor locations included larynx, oropharynx, mouth, tonsil, tongue and hypopharynx. Tumor volumes ranged from 9.0 to 116.5 cm^3, with an average of 53.2 ± 38.4 cm^3. Deformable image registration between the CT and the CBCTs was performed to obtain vector fields (VF) representing the patient evolution (see details in section 2.3).

The gPMC GPU based MC code [Jia+12; Gia+15; Qin+16] was utilized as dose calculation engine to create the IMPT plans. This approach provided high accuracy at this step and a consistent framework throughout the study, avoiding systematic differences between the adapted plan evaluations also performed with gPMC and a treatment planning system (TPS). To create the IMPT plans, all the necessary information was extracted from the TPS, including non-optimized fluence maps. Dose-influence matrices (D matrices) were created with gPMC and optimized with Opt4D, an in-house optimization tool originally developed for temporo-spatial studies [Tro+05]. The optimization was performed with an implementation of the L-BFGS algorithm (Limited-memory Broyden-Fletcher-Goldfarb-Shanno). Beam angles were selected to spare OARs and avoid artifact regions in the CT or CBCT.

7.2.2.2 Adaptation workflow

The current planning-delivery workflow shown in figure 7.1(left side) is sensitive to the uncertainties of the patient positioning and anatomy, as explained in the introduction (uncertainties are represented by the red arrows). This may be solved by employing an adaptive workflow, shown in figure 1(right side).

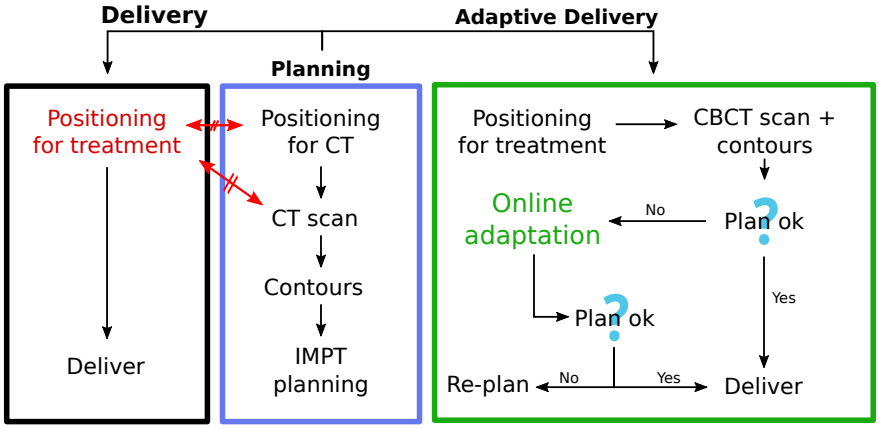

Fig. 7.1 The current (left) and adaptive (right) planning delivery workflows. The red arrows indicate that the patient anatomy and setup might differ between the delivery and the planning stage.

The first step of such an adaptive workflow would be to acquire information about the patient geometry immediately before treatment, including a possible automatic generation of contours. Then the original IMPT plan would be evaluated on the new patient geometry with a GPU MC simulation. If the clinical requirements specified in the initial plan constraints in target and OARs were still met, then the plan would be delivered. If the clinical requirements were not met, the patient information would be used as input into an online adaptation algorithm. If the adaptation was successful, the patient would be treated, else, a re-planning and re-scheduling of treatment would be necessary. Our goal was to maintain high dose calculation accuracy at every step by using GPU MC simulations, therefore, gPMC was employed as dose calculation engine at the initial IMPT planning step, at the plan evaluation on the individual CBCTs and within the adaptation algorithm.

7.2.2.3 Imaging inputs: CBCTs, vector field maps and contours

The adaptation decision is based on the patient geometry as obtained by CBCT, the VF mapping the original planning CT to the CBCT, and a set of new contours localizing the structures on the CBCT.

CBCTs are known to provide limited accuracy for dose calculation, but strategies have been developed to reduce uncertainties [Ara+17; Kim+17; Kur+16a; Niu+10; NAZ12; Par+15]. We applied an a priori planning CT-based scatter-correction algorithm developed in-house [Par+15; Kim+17]. Park et al. have reported average accumulated WEPL errors across different locations of 2.3 $\pm$ 1.9%. The CT and CBCTs were aligned at the plan isocenter, which better maintains the target coverage of the original plan at every evaluation,

as opposed to aligning to a given OAR. While we employed this method, our algorithm does not depend on it and would be applicable if a given OAR needs to be prioritized.

The contours defined in the planning CT were propagated onto the CBCTs applying a VF. The VF map was calculated between the planning CT and the CBCT with deformable image registration (DIR) using the GPU parallelized B-spline algorithm in Plastimatch, an open source suite for radiotherapy and medical imaging [SKS10; Sha12]. The correctness of the structures on the CBCTs had to be visually verified because there is no automatic and reliable procedure to validate the structure contours for H&N cases [Li+17; Per+12]. The deformed contours represented well the visible structures, while the others were required to present smooth deformations (i.e. the VF nominal values and Jacobian did not present steep gradients) to be accepted. The target volume was observed to evolve throughout the CBCT sets. The dice similarity coefficient, measuring the overlap between the original target contour and the contour propagated to each CBCT, was on average 0.83 ± 0.09 (see table 7.1). The small dice coefficient value in patient 1 was due to the fact that this oropharynx case had a thin target and a small displacement.

The accuracy of the CBCTs and the VFs employed does not affect the evaluation of the adaptation algorithm. The latter in the main goal of this manuscript. Even though the CBCTs and VFs may not perfectly represent the current patient geometry and deformation, they represent plausible and consistent geometries and deformations of the patient as well as the propagated contours. Improvement of CBCT accuracy and automatic propagation/generation of structure sets would be necessary to clinically apply the workflow here employed to test the adaptation algorithm and is an active field of research [Li+17]. Several approaches have been followed regarding the imaging modality best suited to perform online adaptation. An alternative option to the one utilized here is to register and warp the planning CT to the CBCT creating a virtual CV (vCT) [Vei+14; Vei+16]. However, this method, for instance employed by Kurz et al. [Kur+16b], depends on the accuracy of the VF to physically displace tissues, which may introduce artifacts if the VF did not capture the real patient deformation. Therefore, any error in the VF will be transferred to the patient anatomy contained in the vCT and that would imply range errors. Employing the CBCT circumvents this potential issue, although its accuracy might have to be improved as previously pointed out.

7.2.2.4 Adaptation algorithm

The adaptation algorithm was designed as two consecutive methods connected by a GPU based MC validation. First, the geometrical method adjusted the beamlets positions and energies, creating a geometrically adapted plan. The geometrically adapted plan was verified on the CBCT. If the result was satisfactory, the plan would be delivered, if not, the second

adaptation method would be applied, performing the weight tuning of the beamlets of the geometrically adapted plan. The algorithm performed the following steps:

1. Geometrical adaptation method
2. Verification with GPU-MC on CBCT
3. Weights tuning (if necessary)

The algorithm was implemented in C++/OpenMP with the raytracing parallelized for NVIDIA GPUs with CUDA. The GPU MC code, gPMC, and the IMPT optimizer, Opt4D, were spawned as subprocesses, automatically providing the required inputs.

Geometrical adaptation The geometrical adaptation method adjusted the position and energy of the beamlets to the new geometry as depicted in figure 7.2(left). Each beamlet was raytraced along its central axis until the end of range in the planning CT (step 1 in figure 7.2(left)). The locations resulting from the raytracing are called endpoints. Each beamlet has a lateral profile, causing different protons in it to traverse different voxels in a CT. Therefore, in heterogeneous media there is no well defined range in a beamlet. To capture the heterogeneity of the patient's tissue and the subsequent deformation of the Bragg peak in the raytracing algorithm, the density of each voxel along the central axis was averaged with its surroundings. The averaging procedure consisted of adding a set of 8 radial probes defined as an octagon on the orthogonal plane around the central axis, which contained the central probe. The radius of the octagon was equal to the σ of the beamlet profile (Gaussian) in water at the equivalent radiological depth. The radial probes weights were set from the same Gaussian profile. The angular position of the first radial probe was randomized. Because the patient deformation was captured in the VF, the set of original endpoints defined in the CT was warped by applying the VF, yielding the position that should be occupied in the new geometry by each endpoint, and, therefore, by the high dose region of each beamlet (step 2 in figure 7.2(left)). This was the same deformation previously applied to the contours propagation. Next, the new position of each warped beamlet in the particle source plane was calculated (step 3 in figure 7.2(left)). Then, the shifted beamlets were raytraced in the CBCT applying the averaging procedure (step 4 in figure 7.2(left)). Finally, the energies were adjusted to match the end of ranges in the CBCT with the warped endpoints (step 5 in figure 7.2(left)).

In some situations, the endpoints calculated in the original CT (step 1 in figure 7.2(left)) were located far from the CTV. This could happen for example, if during the definition of the set of useful beamlets, prior to the optimization, large margins around the CTV were

employed and the optimizer used the dose from beamlets that contribute to the CTV but are relatively far from it. In these situation, the VF would have been probed far from the CTV and the beamlets potentially moved a distance and a direction not representing the CTV deformation. To avoid this issue, the endpoints were forced to be within successive expanded CTVs called shells: CTV + 1.0, 1.5, 2.0 and 3.0 cm. Figure 7.2(right) exemplifies this procedure. The shells are ordered by importance, being the innermost the most important. The endpoint of a beamlet was taken as the last position within the shell of the highest importance its central axis traversed. This assures that the deformation of the CTV, or at least its vicinity, is applied to the beamlets.

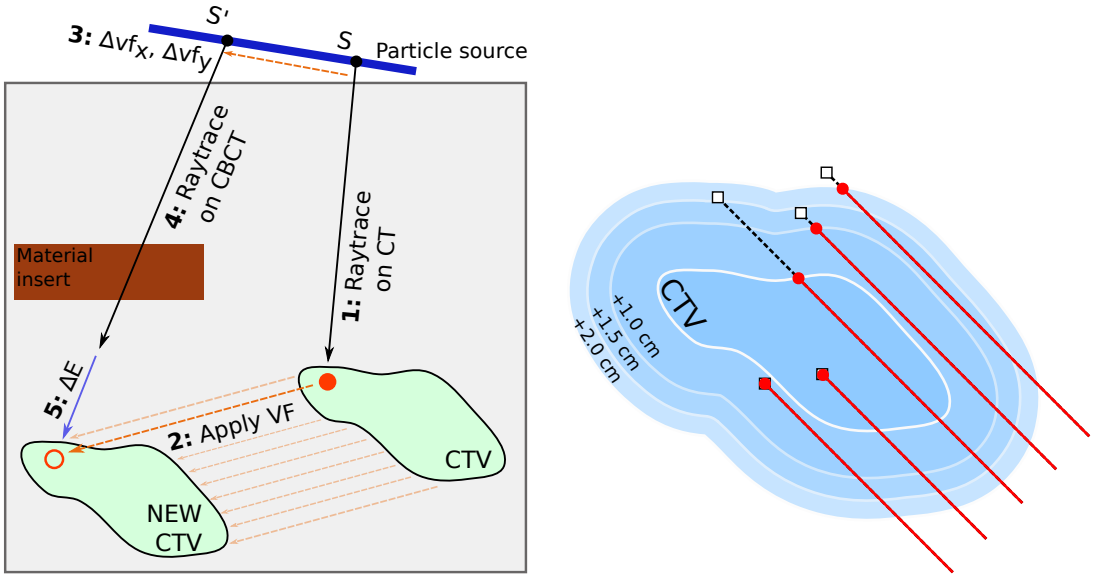

Fig. 7.2 Left: Geometrical adaptation method. (see text for explanation). Right: Beamlets endpoint selection following the expanded CTV shells. The endpoints are represented with the red dots and the end of range position of each beamlet with the rhomboid.

After the geometrical adaptation, the adjusted plan was simulated with gPMC on the CBCT. If the dose distribution fulfilled the clinical requirements, the plan would be delivered. If not, the weight tuning method would be applied.

Weight tuning The IMPT optimization solves an expression of the form of equation 7.1, with some objectives and constraints to the final dose distribution d. In equation 7.1, D is the dose-influence matrix containing the dose distribution given at each voxel by each beamlet and unit of fluence. ω represents the beamlets weights to be optimized. Therefore, D provides all the information required.

$$D\omega = d \tag{7.1}$$

However, calculating a D matrix with GPU MC with similar uncertainty per beamlet to solve such a problem is computationally demanding and generally not suitable for online applications. In order to comply with the requirements of an online application, a solution to extract enough information to define a smaller D matrix from the geometrically adapted plan validation was found. We found that a minority of the beamlets in an IMPT plan carried the majority of the weight and, therefore, deliver the majority of the dose to the patient. In MC simulations the simulation uncertainty decreases as the number of simulated protons increase. As a consequence, this implies that there was a subset of beamlets simulated at the verification step with enough precision to be used for the weight tuning. Additionally, this subset has the biggest influence on the plan performance.

$$d = d_0 + d_s = d_0 + (\omega_{s0} D_s)\omega_s \tag{7.2}$$

Consequently, the dose distribution calculated as verification after the geometrical adaptation was stored in the GPU beamlet by beamlet, forming a weighted matrix containing all the beamlets ($\omega_{0F} D_F$, where ω_0 are the original IMPT weights and F stands for full). Accumulating the dose of each beamlet, the total dose per voxel given by the geometrically adapted plan was retrieved. The smallest set of beamlets carrying at least 50% of the total weight was extracted from $\omega_{0F} D_F$, obtaining the matrix representing the subset s $\omega_{0s} D_s$. The number of selected beamlets was enforced to be at least 10% of the total to provide more flexibility to the weight tuning process. The dose provided by the non-selected beamlets d_0 was accumulated as baseline dose for each voxel, represented in figure 7.3 for a hypothetical target with the dose baseline curve. The prescription dose in the target minus the baseline d_0 was the dose that the selected beamlets should provide, d_s in equation 7.2 and green shaded area in figure 7.3. The weights of the selected beamlets were then tuned to complement the baseline and give the dose prescription in the target while sparing the OARs with the same set of objectives and constraints as in the original plan. Equation 7.1 was therefore changed to equation 7.2, where ω_s are scaling factors of the initial plan weights of the beamlets in s ω_{0s}. Figure 7.3 illustrates the role of the beamlet subset.

The same optimizer, Opt4D, from the original IMPT plan was used (see section 7.2.2.1). The same target and OAR objective values from the original plans were enforced. Because the dose baseline provided by the non-selected beamlets was not homogeneous, the prescription dose in the target was given to the optimizer as a voxel-dependent objective complementing the baseline. The same was done to set the maximum acceptable overdose in the target. After the weight tuning, another verification with GPU MC would not be required, as the new plan dose is simply $d = d_0 + d_s$.

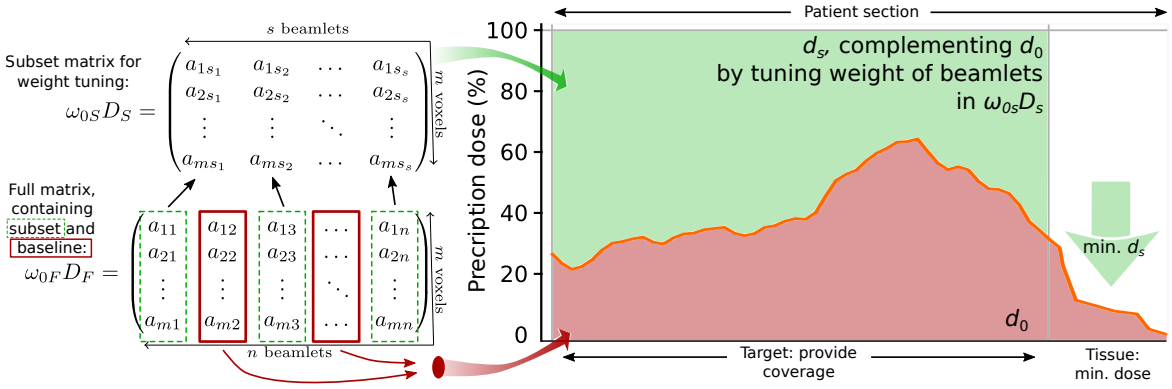

Fig. 7.3 Role of beamlet subset to provide target coverage and spare healthy tissues. Starting from the left: all the beamlets are contained in $\omega_{0F}D_F$ and some are selected for the subset matrix $\omega_{0s}D_s$ used for weight tuning (green dashed boxes). The non-selected beamlets (red solid boxes) provide the dose baseline d_0 (red filling in the graph). The beamlets in $\omega_{0s}D_s$ are optimized to complement the baseline in the target to provide coverage by giving dose d_s (green filling, above the baseline), while attempting to minimize d_s in healthy tissues. The graph represents the baseline dose (%) along a line crossing the target and some healthy tissue.

The D matrices can be large files that could cause an overflow in the GPU memory during simulations. Usually, to facilitate storage and speed up the optimization, D matrices are compressed. However, this approach cannot be used while D is being constructed in the GPU because that information is only available after all the protons have been simulated. Therefore, to fit the D matrices in the GPU, gPMC was extended to score dose in arbitrarily-shaped regions of interest defined by voxelized masks, allowing a significant reduction of the D matrices size. The region of interest defined by the masks covered the dose bath.

The conditions to select the subset of beamlets (the minimum weight of 50% they had to provide, being at least 10% of the total plan spots) were chosen empirically by observing the shape of the cumulative weight distribution and early adaptation results. Different optimizers produce different weight distributions, some giving more weight to individual beamlets and others producing more balanced plans. The L-BFGS algorithm, implemented in Opt4D and utilized here, produces individual beamlets with high weights. The performance of our method would for sure depend on the individual optimizer. Additionally, selecting the beamlets with higher weights may bias the selection towards the beamlets with higher energies. However, when employing several fields this situation should be alleviated.

7.2.2.5 Studied approaches and evaluation metrics

The geometrical adaptation method and geometrical+weights adaptation methods were studied separately. The geometrical adaptation method was applied in four modes:

1. Free: Allowing free beamlet position and energy changes by the delivery system.
2. Iso: Changing the plan isocenter with an isocenter shift, calculated from the average probed VF at the beamlet's endpoints. The energies were changed as in the Free mode.
3. RS: Changing the energy with range shifters, calculated from the average energy shift per field. The positions were changed as in the Free mode.
4. Iso-RS: Constraining the position and energy changes with a isocenter and constant range shift.

The geometrical adaptation method is the basis of the weight tuning method, therefore each of these modes was studied with and without weight tuning. Thus, forming 8 adaptation approaches that were compared against the original plans and the original plans delivered to the CBCTs without adaptation.

Dosimetric comparisons in the target were performed based on V95, V98, V107, V110, D2 and D98 (all in % of structure volume or prescription dose). The dose to OARs was analyzed in terms of mean and maximum dose. The performance was analyzed based on the cumulative dose at the end of treatment (cum.) and also on the individual CBCT scans, extrapolating the values per scan to full treatment for easier comparison. Although the cumulative dose is more clinically meaningful, this is a procedure to be used at each fraction, so its performance was judged on this basis as well. Also, if hypofractionation schemes are employed, good performance at every fraction is desired. A constant RBE = 1.1 was applied throughout the study. Boxplots were utilized to summarize the results, with the median, the lower/upper hinges corresponding to the first and third quartiles (the 25th and 75th percentiles), the lower/upper whisker extending from the hinge to the smallest/largest value no further than 1.5 times the inter-quartile range from the hinge, and observations beyond the whiskers plotted individually as outliers.

7.2.3 Results and discussion

In this section, the performance of the original plans on the CBCT scans was analyzed first. Afterwards, the adaptation performance was investigated and compared, first using only the geometrical adaptation and secondly using also the weight tuning. Furthermore, the time it took the algorithm to produce the adaptations was recorded. Additional results were included,

in appendix 1, showing the example of 2 patients' VFs as probed by the adaptation procedure and the beamlet's energy, positions and weights change.

7.2.3.1 Original plans on changing geometries

The performance of the original plans on the new geometries defined the corrections the adaptation algorithms must achieve. This was expected to be challenging because the plans were performed without margins around the CTV for the purpose of this study. The scans were taken weekly, which may increase the observed anatomy evolution, but not the setup errors.

Figure 7.4(left) shows $V95_{unadapt}$ - $V95_{plan}$ in the CTV for the cumulative (cum.) dose and the dose in the individual CBCTs, per patient. The cumulative distribution was the result of delivering the whole treatment to the successive CBCTs. The results per patient were also plotted with boxplots to better represent the plan evolution trend. A gradual descent on the value of this parameter was observed as treatment progressed from scan 1 to scan 7. All the patients, except for 2 and 5, presented a 5% drop in at least one scan. Half the patients showed a drop of the accumulated dose of at least 5% in V95, which was 100% in the plans (see figure 7.5). If V95 = 95% were employed as re-planning criteria for the target coverage, half the cases would have been re-planned. Few evaluations on the scans had a V100 > 90% and, although not shown explicitly for brevity, only patient 5 presented a cumulative V100 > 90% (V100 = 91.0%), which might have triggered re-planning for all cases, depending on the institution protocol. The average D98, mean and D2 dose percentage in the target changed from 98.9, 103.3 and 106.9% at the original plans to 90.2, 101.8 and 108.4% in the cumulative distributions. If maintaining target coverage in the target is the main goal, the parameters measuring target overdose should be judged having the coverage in mind, as a D2 value similar or better than the plan is only relevant if coverage is provided as well.

Some cases, such as patient 5, did not show large CTV coverage degradation (figure 7.4(top-right)), but the dose levels to OARs increased due to the geometry changes and the loss of conformality. On the other hand, patients such as 4, 7 and 8 showed drastic drops in plan quality. The original plan and cumulative dose DVHs for patient 7 are shown in figure 7.4(bottom-right).

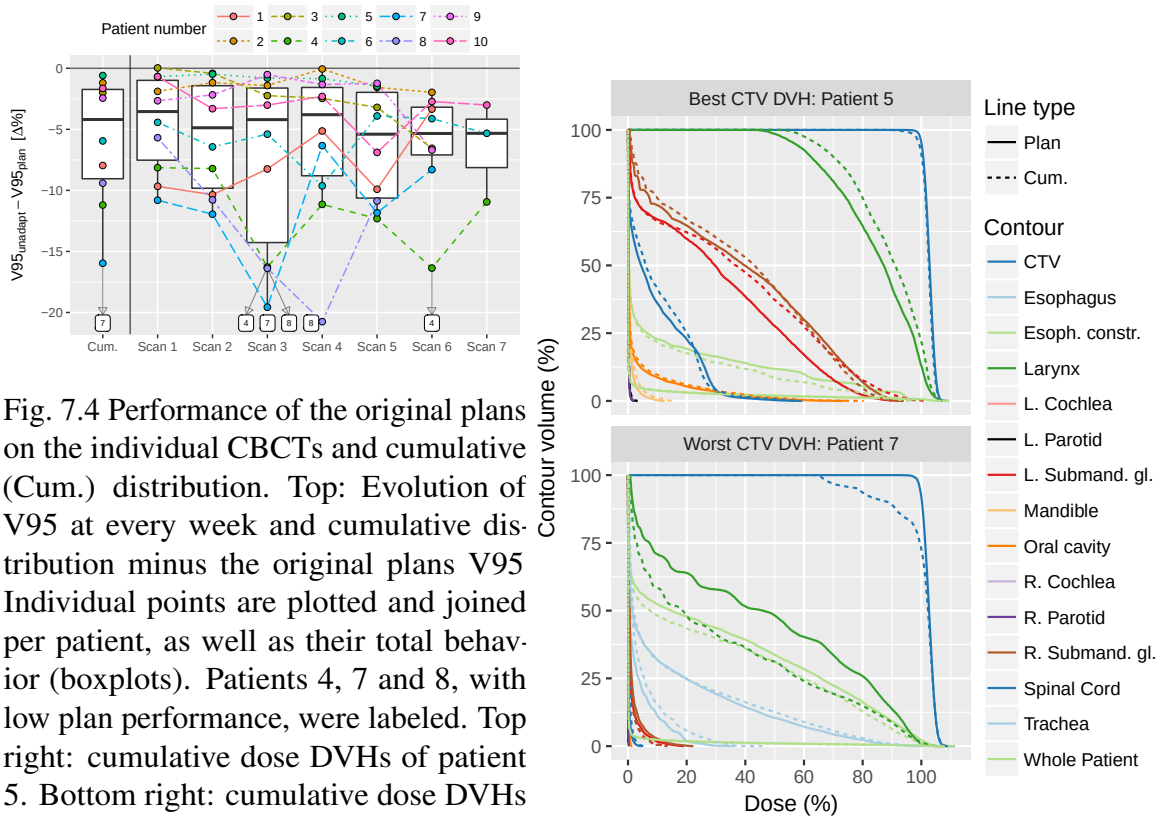

Fig. 7.4 Performance of the original plans on the individual CBCTs and cumulative (Cum.) distribution. Top: Evolution of V95 at every week and cumulative distribution minus the original plans V95 Individual points are plotted and joined per patient, as well as their total behavior (boxplots). Patients 4, 7 and 8, with low plan performance, were labeled. Top right: cumulative dose DVHs of patient 5. Bottom right: cumulative dose DVHs of patient 7, showing big changes in the CTV.

In general, the studied conditions produced a decrease in parameters measuring target coverage with respect to the original plan, while parameters measuring target overdose increased, smoothing the target DVH. Dose to OARs was increased on average. The evolution of additional CTV DVH points was included in figure 7.5 and are explained in the next subsection.

7.2.3.2 Geometrical adaptation method

Figure 7.5 shows V95, V98, V107, V110, D2 and D98 (%) for the 10 patients. Boxplots for the original plans and the cumulative plan delivered to the CBCTs with and without geometrical adaptation were included and separated by color, allowing the comparison of several CTV DVH bands. Each boxplot illustrate the variations amongst the 10 patients. Boxplots were included for the original plans in the planning CTs (Plan), the plans delivered to the CBCT scans with no adaptation (None) and the 4 geometrical adaptation modes described in the methods: free energy and position changes (Free), isocenter shifts (Iso), range shifters (RS) and the last two combined (Iso-RS).

The plot shows the original plan delivered 95 and 98% of the prescription dose to the whole CTV volume (orange, leftmost boxplots). The volume percentage decreased as the dose increased until it was ~5% for V107 and close to 0% at V110. The average D98 and D2 doses were 99.0 and 107.0% for the original plans. However, this behavior was not reproduced when the original plans were delivered to the CBCTs without adaptation (None method, yellow, second boxplot from the left), as explained in the previous subsection.

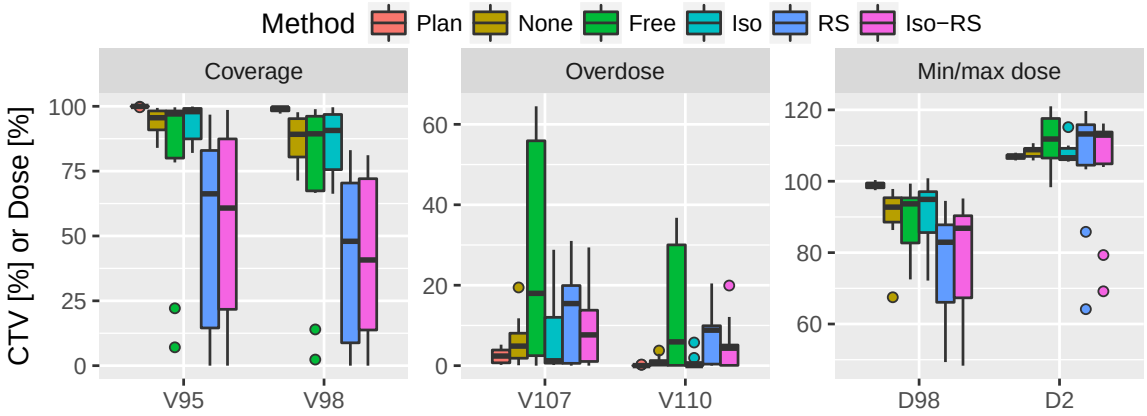

Fig. 7.5 Performance of the cumulative dose of the geometrical adaptation method compared to the original plan and the original plan (Plan) delivered to the CBCTs (None). The geometrical adaptation methods are split into the implemented modes: free energy and positon changes (Free), isocenter shifs (Iso), range shifers (RS) and the last two combined (Iso RS). The modes fail to reproduce the original plans values.

As shown in figure 7.5, the geometrical adaptation method failed to recover the original plans' prescriptions for all 4 modes. The Free and Iso modes improved in some cases the performance with respect to not adapting the plan, according to V95 and V98, but in others they performed worse. The beamlets movement created hot-spots in the CTV as show by V107, V110 and D2. Both modes adapting with range shifters (RS, Iso-RS) worsened the CTV coverage as shown with V95 and V98.

In general, the geometrical adaptation method did not recover target coverage. There are several reasons, individually or in combination. Although theses methods relocated the beamlets' end-of-range position in the target according to the deformation, the change of shape of the dose distribution of each beamlet after adaptation produced by the new patient geometry could generate cold/hot spots in the target that impacted the plan quality. Not only the materials traversed may have affected the adapted beamlets, but also the beamlet energy may have changed, which would have changed the beamlet width and energy spread. Additionally, the relative positions between endpoints may be different if the VF contained non-parallel deformations, creating potential cold/hot-spots. Because the VFs

were probed at certain individual positions, there was an underlying assumption that the VFs behaved smoothly. Any non-smooth regions of the VFs might not be captured by the probing procedure, but they would certainly be used to warp the original contours, potentially creating deformations that the adaptation algorithm did not take into account. However, non-smooth regions of the VFs, specially in low contrast tissue, might be an artifact of the DIR and not actually represent the anatomy deformation.

7.2.3.3 Geometrical adaptation and weight tuning methods

The weight tuning algorithm was applied after simulating the geometrical adaptations in a per-beamlet fashion.

Target coverage As shown in figure 7.6, the weight tuning was able to recover good plan quality in terms of the CTV DVH parameters. Again, the boxplots represent the distribution of values for the given parameter evaluated at every patient's cumulative dose distribution. The Free and Iso modes represented better the results by the initial plan boxplots for all dosimetric indices, except for V107, where the modes showed higher values. These higher values were not reflected in V110 indicating that the DVHs had high slopes in the V107-V110 region. Comparing against the non-adapted and the geometrical adaptation method in figure 7.5, all modes with weight tuning represented an improvement. The modes utilizing range shifters necessitated higher dose levels to achieve similar coverage, as shown in V107, V110 and D2. Figure 7.6 provides information about the general distribution of DVH parameters values in the same or similar scale as in figure 7.5, but it does not provide information about what values each patient presents, specifically about the difference between the adaptation and the original plan per patient.

Figure 7.7 shows the difference of each adaptation mode minus the original plan per patient (mode - plan, $\Delta\%$). The modes utilizing range shifters were not included in this figure for clarity and because the previous plot showed they had worse performance than the Free and Iso modes. The previous plots focused on the cumulative dose as it was recognized as having more clinical relevance. In this plot, however, the performance of the adaptations on the individual CBCTs was included. Table 7.2 shows the results for the selected dosimetric indices for the original plan, its performance on the CBCTs and the weight adaptation modes.

As shown in figure 7.7, the difference between the original plan and the Free and Iso modes was small in the CTV. The Free mode showed slightly improved nominal values with respect to the Iso mode, but the difference was not statistically significant. The average difference across patients between the adaptations and the original plan for V95 was less than 1% as shown in the figure and in table 7.2 (99.4 - 99.9 for the free mode). For V98

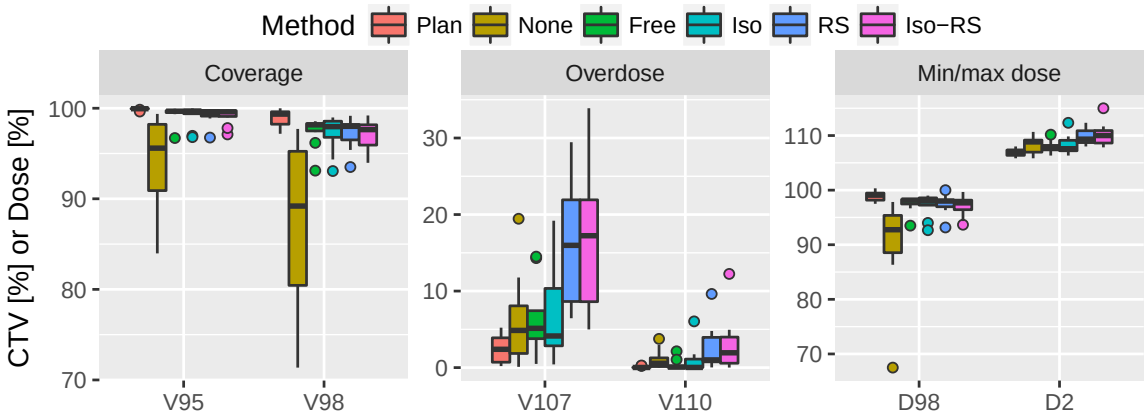

Fig. 7.6 Performance of the cumulative dose of the weight tuned adaptation modes compared to the original plan and the original plan (Plan) delivered to the CBCTs (None). The Free and Iso modes closely reproduce the original plans values. RS and Iso RS present lower V95 and V98 and higher V107 and V110. The plot scale may have hidden the boxplot color, the order is the same as in the legend. Please, note that the plotted range in this figure differs from the one in figure 7.5.

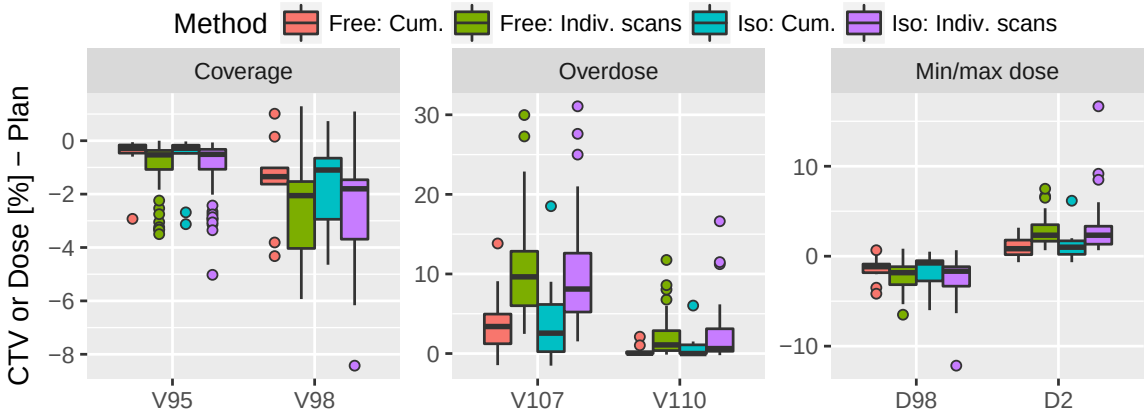

Fig. 7.7 Distribution of the difference between the adaptations and the original plans. The difference was taken patient by patient, either using the cumulative dose distribution or using the dose distributions on the individual scans. Both adaptation modes here included behaved similarly. Target coverage was well maintained in the cumulative distribution. The distributions on the individual CBCTs presented bigger fluctuations.

it was less than 2% (97.4 - 98.9 for the free mode). In order to deliver such coverage, the adaptations increased V107 by ~4% on average, from 2.4 to 6.4%, however it impacted V110 by less than 1%. The minimum and maximum dose were also well maintained with average differences smaller than 2%. These small differences contrast with the values shown by the original plan without the adaptation algorithm.

Table 7.2 Dosimetric values from the cumulative dose distributions and the dose distributions on the individual CBCTs.

		Cumulative				Individual CBCTs			
All in %		Min	Mean ± sd	Median (IQR)	Max	Min	Mean ± sd	Median (IQR)	Max
V95	Plan	99.6	99.9 ± 0.1	99.9 (0.0)	100.0	99.6	99.9 ± 0.1	99.9 (0.0)	100.0
	Free	96.7	99.4 ± 0.9	99.7 (0.2)	99.9	96.1	99.0 ± 1.0	99.4 (0.6)	100.0
	Iso	96.8	99.1 ± 1.2	99.7 (0.4)	100.0	94.9	98.9 ± 1.1	99.4 (0.7)	99.9
	None	84.0	94.1 ± 5.2	95.6 (7.3)	99.4	79.2	93.9 ± 5.2	95.2 (8.0)	100.0
V98	Plan	97.2	98.9 ± 1.0	99.4 (1.4)	100.0	97.2	98.9 ± 1.0	99.4 (1.4)	100.0
	Free	93.1	97.4 ± 1.7	98.2 (0.8)	98.6	92.1	96.4 ± 1.8	97.2 (2.6)	98.5
	Iso	93.1	97.2 ± 2.0	98.0 (1.8)	99.0	90.6	96.5 ± 1.9	97.4 (2.0)	98.4
	None	71.4	87.3 ± 9.4	89.2 (14.8)	97.7	63.7	86.0 ± 9.0	87.5 (13.4)	99.5
V107	Plan	0.2	2.4 ± 1.9	2.4 (3.2)	5.2	0.2	2.4 ± 1.9	2.4 (3.2)	5.2
	Free	0.5	6.4 ± 4.7	5.1 (3.7)	14.5	5.2	12.8 ± 5.8	12.0 (8.4)	30.6
	Iso	0.4	6.6 ± 6.2	4.1 (7.5)	19.2	4.6	12.3 ± 6.4	9.8 (9.9)	31.7
	None	0.1	6.3 ± 5.9	4.9 (6.2)	19.5	0.8	9.0 ± 5.0	8.3 (5.3)	26.1
V110	Plan	0.0	0.1 ± 0.1	0.0 (0.0)	0.3	0.0	0.1 ± 0.1	0.0 (0.0)	0.3
	Free	0.0	0.4 ± 0.7	0.1 (0.2)	2.1	0.0	2.1 ± 2.4	1.1 (2.5)	11.8
	Iso	0.0	0.9 ± 1.9	0.0 (1.1)	6.0	0.1	2.1 ± 3.1	0.6 (2.9)	16.6
	None	0.0	1.1 ± 1.3	0.6 (1.1)	3.8	0.0	2.2 ± 2.4	1.8 (1.6)	15.2
D98	Plan	97.5	98.9 ± 1.0	99.1 (1.3)	100.3	97.5	98.9 ± 1.0	99.1 (1.3)	100.3
	Free	93.5	97.5 ± 1.5	98.2 (0.8)	98.5	91.2	96.7 ± 1.7	97.3 (1.3)	98.3
	Iso	92.7	97.2 ± 2.1	98.0 (1.3)	99.0	86.5	96.6 ± 2.2	97.5 (1.5)	98.3
	None	67.5	90.2 ± 8.9	92.8 (6.8)	97.8	40.5	89.5 ± 9.0	91.3 (8.8)	99.0
D2	Plan	105.8	106.9 ± 0.7	107.1 (1.0)	108.0	105.8	106.9 ± 0.7	107.1 (1.0)	108.0
	Free	106.3	108.0 ± 1.1	107.9 (0.8)	110.2	107.8	109.7 ± 1.4	109.3 (2.0)	113.7
	Iso	106.3	108.2 ± 1.8	107.6 (1.9)	112.3	107.7	109.8 ± 2.4	108.8 (2.3)	122.8
	None	105.8	108.4 ± 1.7	108.8 (2.2)	110.7	106.3	109.8 ± 1.9	109.8 (1.5)	117.5

The results based on single CBCT images showed a wider distribution than the cumulative doses and thus tended to be worse than the cumulative results. Fluctuations occurred at every fraction that compensated each other when summing the total dose. In this case the Free mode also performed slightly better than the Iso. The average V95 and V98 of the adaptations on the individual CBCTs and Free mode were 99.0 and 96.4, i.e. a 0.9 and 2.3% drop from the original plan, respectively. The bigger impact of the fluctuations in the individual CBCTs were seen at V107, where differences of up to ~30% were observed, with an average increase from 2.4 to 12.8 between the plan and the Free mode.

To better compare the adaptation modes, the Free mode was taken as reference and dosimetric indices differences were calculated per patient (Iso/RS/Iso-RS - Free). The results were plotted in figure 7.8, also including the OARs, which are analyzed in the next subsection. The mean V95, V98, V107 and V110 difference were -0.23 ± 0.83, -0.23 ± 1.05, 0.21 ± 3.17 and 0.57 ± 1.66% in the cumulative doses, respectively. All the values indicate the Free strategy had a better performance, but they did not reach a level of significance. The modes

using range shifters delivered higher dose than the Free mode to the CTV. For the RS mode, the mean difference in V107 and V110 were 9.55 ± 5.98 and 2.17 ± 2.70%, respectively. For Iso-RS they were 10.49 ± 7.68 and 2.66 ± 3.40%. In both modes with range shifters V107 was significantly worse than the Free strategy, with p = 0.0003 for the RS mode and p = 0.0010 for the Iso-RS, at a 95% confidence level. The comparisons performed on the individual scans' dose distributions showed similar behavior as the cumulative distributions, but with higher variance.

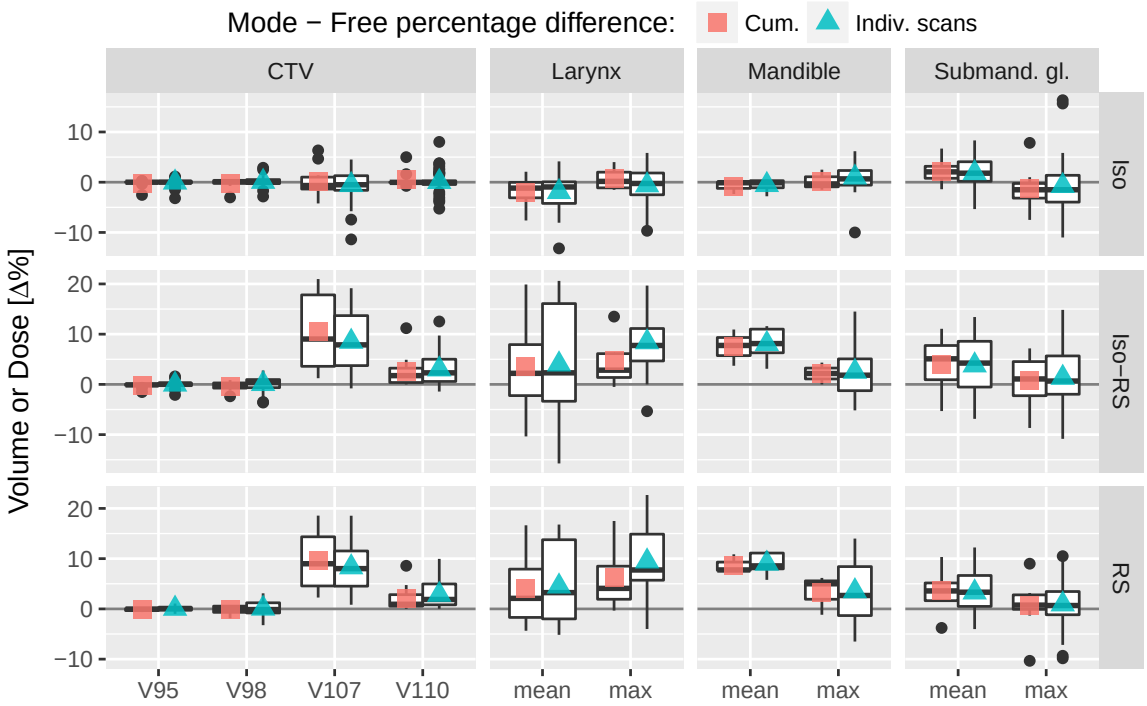

Fig. 7.8 Comparison of weight tuned adaptation modes with respect to the Free mode. Each of the adaptation modes in a row (labels on the right) and each contour in a column (labels on top). The values show the difference between the given mode and the Free mode. The Iso mode was seen to perform similarly to the Free mode, as most values are close to 0 or symmetrical around it, but the Iso RS and RS performed worse. The mean differences were plotted over the boxplots for the cumulative dose distributions and the dose distributions at each individual scan.

OAR sparing Although the adaptation workflow focused on recovering tumor coverage, OAR dose constraints need to be met. The difference in mean and max dose between the weight tuned adaptations minus the original plans is shown in figure 7.9 for all adaptation modes. Only the larynx, mandible and submandible glands had high enough dose levels across patients to allow the comparison, so the analysis was focused on these structures. The

OAR dose levels were kept similar to the original plan by the Free and Iso modes, as the distribution of differences is close to 0. The modes with range shifters displayed increased dose to the larynx and mandible. Because the patient anatomy changed, in some situations the weight adaptation algorithm was able to find better sparing than the original plan in the original patient geometry, confirming that the original plan dose distribution might not the optimal for every patient geometry. This is expected to be very patient- and anatomy-specific. In general, the adaptations gave similar dose levels as the original plans.

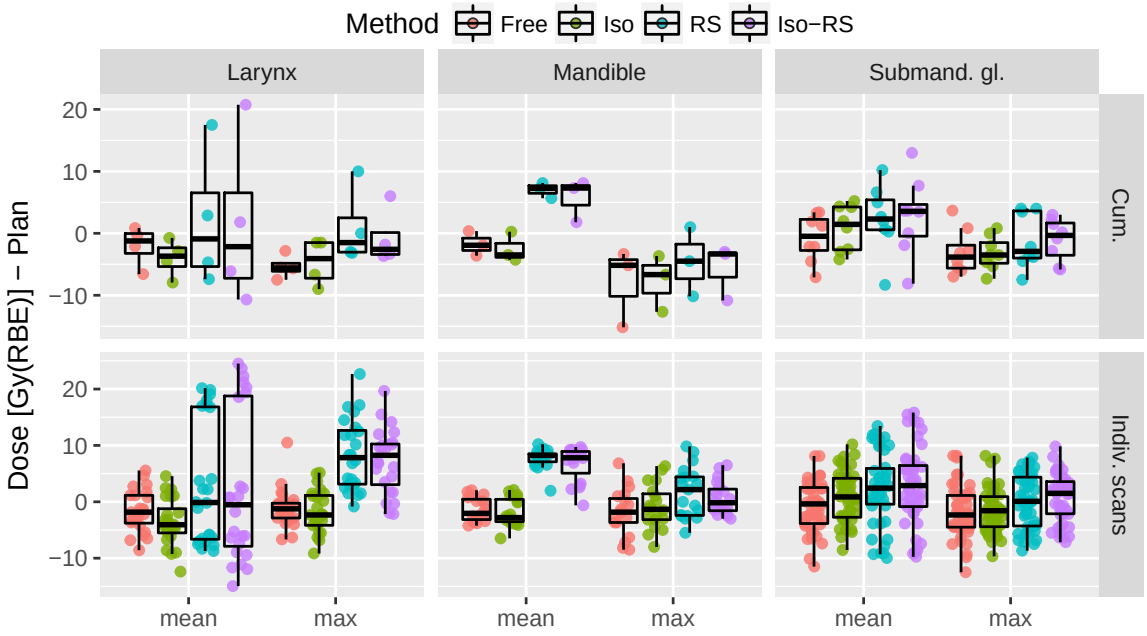

Fig. 7.9 Dose difference given to OARs by the adaptations with respect to the plans. The dose levels were well maintained by the adaptations, specially the Free and Iso modes.

The modes comparison in figure 7.8 showed that the Iso mode had lower dose to the larynx, but higher to the submandibular glands w.r.t. the Free mode The modes with range shifter had higher dose to OARs. However, the dose to OARs had a high dependency on the specific case so that no conclusion could be drawn regarding the differences as to whether the Free mode was better than the Iso. As in the CTV, the comparisons performed on the individual scans' dose distributions showed similar behavior as the cumulative distributions, but with higher variance.

Patients DVHs Figure 7.10 shows DVHs of four patients with big plan degradation in the CBCTs and the performance of the Free adaptation mode with weight tuning. The adaptations restored the plan to a quality comparable to the original plan, both in the CTV

and in the OARs. The CTV coverage and OAR sparing were similar as in the original plans, as analyzed in detail in the previous sections.

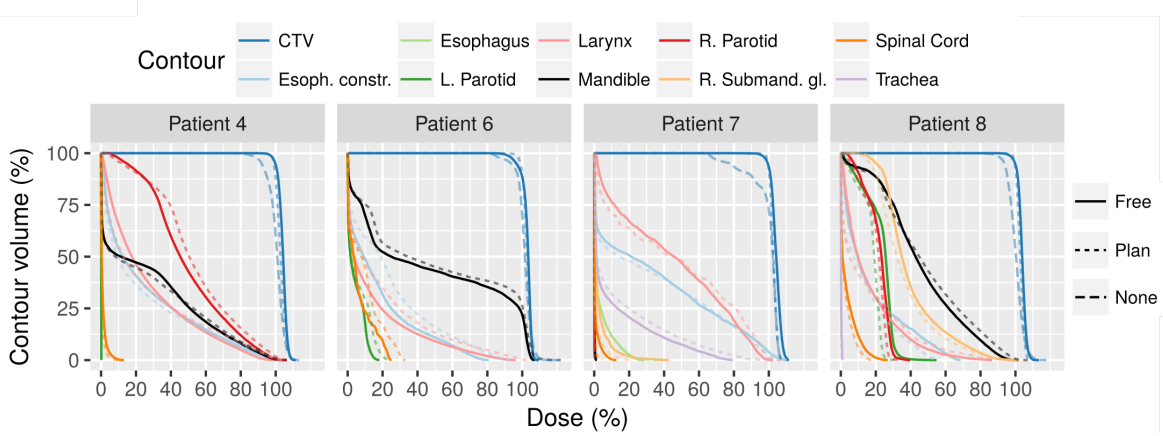

Fig. 7.10 Patient DVHs of the original plan (doted line), the cumulative unadapted plan (dashed line) and the cumulative plan adapted with Free geometrical adaptation and weight tuning (solid line).

7.2.3.4 Time performance

The framework time is reported in table 7.3 without considering the time required for CBCT imaging and the DIR. All calculations were performed on a Dell Precision 7600 workstation (two Intel Xenon CPUs, 8 cores total at 2.4 GHz) with a NVIDIA Tesla K40 GPU obtained from NVIDIA's GPU Grant Program[1].

The geometrical adaptation method times include all data transfers between the host and the GPU, the VF probing and geometry changes to adapt to internal code coordinates. It took an average of 16.9 seconds. Improvements could be implemented to minimize data conversions and transfers, reducing the overhead of operations and increasing algorithm speed. A CPU parallelization might improve the efficiency for this step. In the current GPU implementation of the geometrical adaptation method, a beamlet is processed per thread, but the number of beamlets might not be high enough so that the acceleration in the GPU compensates the data transfer time. On the other hand, more modern connection ports between the GPU and the host allow faster data transfer.

The simulation with gPMC took between 115.6 and 419.2 seconds. These values can be drastically reduced by launching the calculation in a multi-GPU system. Newer GPUs and motherboard-GPU connections would also improve the performance, although it is hard to predict what the expected improvement would be. In system with 10 GPU of the ones

[1]NVIDIA GPU Grant Program: https://developer.nvidia.com/academic_gpu_seeding

Table 7.3 Time needed with the available hardware and software. To the right, expected time with the improvements explained in the text.

(All in s)	Minimum	Average	Maximum	Expected
Geometrical adapt.	11.7	16.9	26.6	1-5
gPMC simulation	115.6	261.9	419.2	10-60
Weight tuning	12.0	44.8	198.0	5-120
Total	-	322.7	-	~60-120

here utilized, the calculation time would be in the order of 10-60 s for any of the cases here included.

The weight tuning with Opt4D presented a wide range of calculation times, from 12 to 198 s. All dose calculations were performed on the CT grid. Should this grid be resampled to a coarser one, the optimization time would decrease as the problem size decreases. Another factor impacting the weight tuning time was the number of beamlets to consider. Currently, the beamlet selection criteria does not take into account the position of the problematic areas. Including that information might reduce the number of beamlets to be considered, reducing the total tuning time. Lastly, a multithreaded implementation of Opt4D would also have an impact. Reducing the dose calculation grid and increasing the parallelization is expected to reduce the duration of the optimization step to the range of 5-120 s.

7.2.4 Conclusions and outlook

An algorithm was presented that is capable of yielding adapted plans of similar quality as the original treatment plans. Adaptation of beamlet positions and energies alone (geometrical adaptation) was shown to be insufficient. However, tuning the weight of a subset of beamlets after this geometrical adaptation was successful. Several geometrical adaptation modes were individually tested and compared. It was shown that allowing the change of individual beamlets position and energy (the Free mode) yielded the best results, although using an isocenter shift with free energy changes yielded results very close to it. Using range shifters for the energy adaptation gave higher doses to the CTV and OARs.

A consequence of these adaptation modes without range shifter is the creation of many energy layers that might deem the plan undeliverable due to time limitations. This could be alleviated by clustering them in a number of layers considered deliverable and will be investigated in future projects. Furthermore, it is expected that future proton therapy delivery systems might employ multi-energy extraction allowing faster energy switching [MDL17], which would also alleviate the issue.

The efficiency of our online adaptation workflow makes the method applicable for on-line adaptation while the patient is set up for treatment. Parallelization and hardware upgrade might improve the framework even further. The full adaptation workflow would need to perform the CBCT acquisition and processing, the DIR calculation and the contour propagation and verification. As indicated in the previous sections, a precise evaluation of the accuracy of CBCT scans should be performed before any clinical implementation. Additionally, an automated procedure to define the daily contours and evaluate the uncertainty should also be investigated. Dose accumulation using DIR presents uncertainties as well [Vei+15]. All these remaining uncertainties could be handled with daily robust optimization, which may put more pressure on the adaptation algorithm computational efficiency. Once all these uncertainties are properly taken into account, a quantitative evaluation of the adaptation algorithm should be performed against robust optimization.

A final unresolved issue is the quality assurance test of the adapted plan. It comes down to the definition of a new plan versus a corrected plan. A possible option would be to address this issue by performing independent MC simulations of the plan or using the treatment delivery log files.

Nevertheless, the algorithm here introduced may allow margin reduction due to setup, anatomy and dose calculation uncertainties, with the consequential plan quality improvement. It may also reduce the number of required re-plans for H&N cancer treatments, having a positive impact on the quality of life of patients by reducing the number of visits and on total treatment cost.

References

[Ahn+14] Peter H. Ahn, J. Nicholas Lukens, Boon-Keng Kevin Teo, Maura Kirk, and Alexander Lin. “The use of proton therapy in the treatment of head and neck cancers”. In: *Cancer Journal (Sudbury, Mass.)* 20.6 (Dec. 2014), pp. 421–426. ISSN: 1540-336X. DOI: 10.1097/PPO.0000000000000077.

[Alb+08] Francesca Albertini, Alessandra Bolsi, Antony J. Lomax, Hans Peter Rutz, Beate Timmerman, and Gudrun Goitein. “Sensitivity of intensity modulated proton therapy plans to changes in patient weight”. In: *Radiotherapy and Oncology: Journal of the European Society for Therapeutic Radiology and Oncology* 86.2 (Feb. 2008), pp. 187–194. ISSN: 0167-8140. DOI: 10.1016/j.radonc.2007.11.032.

[Ara+17] Kazuhiro Arai et al. “Feasibility of CBCT-based proton dose calculation using a histogram-matching algorithm in proton beam therapy”. In: *Physica medica: PM: an international journal devoted to the applications of physics to medicine and biology: official journal of the Italian Association of Biomedical Physics (AIFB)* 33 (Jan. 2017), pp. 68–76. ISSN: 1724-191X. DOI: 10.1016/j.ejmp.2016.12.006.

[Art+17] Tine Arts et al. “The impact of treatment accuracy on proton therapy patient selection for oropharyngeal cancer patients”. In: *Radiotherapy and Oncology: Journal of the European Society for Therapeutic Radiology and Oncology* 125.3 (Dec. 2017), pp. 520–525. ISSN: 1879-0887. DOI: 10.1016/j.radonc.2017.09.028.

[Ber+18] Kinga Bernatowicz, Xavier Geets, Ana Barragan, Guillaume Janssens, Kevin Souris, and Edmond Sterpin. “Feasibility of online IMPT adaptation using fast, automatic and robust dose restoration”. In: *Physics in Medicine and Biology* (2018). ISSN: 1361-6560. DOI: 10.1088/1361-6560/aaba8c. URL: http://iopscience.iop.org/10.1088/1361-6560/aaba8c (visited on 04/03/2018).

[Bla+16] Pierre Blanchard et al. “Intensity-modulated proton beam therapy (IMPT) versus intensity-modulated photon therapy (IMRT) for patients with oropharynx cancer - A case matched analysis”. In: *Radiotherapy and Oncology: Journal of the European Society for Therapeutic Radiology and Oncology* 120.1 (2016), pp. 48–55. ISSN: 1879-0887. DOI: 10.1016/j.radonc.2016.05.022.

[Dij+16] Lisanne V. van Dijk, Roel J. H. M. Steenbakkers, Bennie ten Haken, Hans Paul van der Laan, Aart A. van ’t Veld, Johannes A. Langendijk, and Erik W. Korevaar. “Robust Intensity Modulated Proton Therapy (IMPT) Increases Estimated Clinical Benefit in Head and Neck Cancer Patients”. In: *PloS One* 11.3 (2016), e0152477. ISSN: 1932-6203. DOI: 10.1371/journal.pone.0152477.

[Gen+17] Changran Geng, Juliane Daartz, Kimberley Lam-Tin-Cheung, Marc Bussiere, Helen A. Shih, Harald Paganetti, and Jan Schuemann. “Limitations of analytical dose calculations for small field proton radiosurgery”. In: *Physics in Medicine and Biology* 62.1 (2017), pp. 246–257. ISSN: 1361-6560. DOI: 10.1088/1361-6560/62/1/246.

[Gia+15] Drosoula Giantsoudi, Jan Schuemann, Xun Jia, Stephen Dowdell, Steve Jiang, and Harald Paganetti. “Validation of a GPU-based Monte Carlo code (gPMC) for proton radiation therapy: clinical cases study”. In: *Physics in Medicine & Biology* 60.6 (2015), p. 2257. ISSN: 0031-9155. DOI: 10.1088/0031-9155/60/6/2257. URL: http://stacks.iop.org/0031-9155/60/i=6/a=2257 (visited on 08/13/2018).

[Gra+14] Clemens Grassberger, Juliane Daartz, Stephen Dowdell, Thomas Ruggieri, Greg Sharp, and Harald Paganetti. “Quantification of Proton Dose Calculation Accuracy in the Lung”. In: *International Journal of Radiation Oncology • Biology • Physics* 89.2 (June 1, 2014), pp. 424–430. ISSN: 0360-3016. DOI: 10.1016/j.ijrobp.2014.02.023. URL: https://www.redjournal.org/article/S0360-3016(14)00208-9/fulltext (visited on 08/13/2018).

[Jag+17] Thyrza Jagt, Sebastiaan Breedveld, Steven van de Water, Ben Heijmen, and Mischa Hoogeman. “Near real-time automated dose restoration in IMPT to compensate for daily tissue density variations in prostate cancer”. In: *Physics in Medicine & Biology* 62.11 (2017), p. 4254. ISSN: 0031-9155. DOI: 10.1088/1361-6560/aa5c12. URL: http://stacks.iop.org/0031-9155/62/i=11/a=4254 (visited on 08/08/2018).

[Jag+18] Thyrza Jagt, Sebastiaan Breedveld, Rens van Haveren, Ben Heijmen, and Mischa Hoogeman. "An automated planning strategy for near real-time adaptive proton therapy in prostate cancer". In: *Physics in Medicine & Biology* 63.13 (2018), p. 135017. ISSN: 0031-9155. DOI: 10.1088/1361-6560/aacaa7. URL: http://stacks.iop.org/0031-9155/63/i=13/a=135017 (visited on 07/12/2018).

[Jia+12] Xun Jia, Jan Schümann, Harald Paganetti, and Steve B. Jiang. "GPU-based fast Monte Carlo dose calculation for proton therapy". In: *Physics in Medicine & Biology* 57.23 (2012), p. 7783. ISSN: 0031-9155. DOI: 10.1088/0031-9155/57/23/7783. URL: http://stacks.iop.org/0031-9155/57/i=23/a=7783 (visited on 08/22/2018).

[Kim+17] Jihun Kim, Yang-Kyun Park, Gregory Sharp, Paul Busse, and Brian Winey. "Water equivalent path length calculations using scatter-corrected head and neck CBCT images to evaluate patients for adaptive proton therapy". In: *Physics in Medicine and Biology* 62.1 (2017), pp. 59–72. ISSN: 1361-6560. DOI: 10.1088/1361-6560/62/1/59.

[Kur+15] Christopher Kurz et al. "Comparing cone-beam CT intensity correction methods for dose recalculation in adaptive intensity-modulated photon and proton therapy for head and neck cancer". In: *Acta Oncologica* 54.9 (Oct. 21, 2015), pp. 1651–1657. ISSN: 0284-186X. DOI: 10.3109/0284186X.2015.1061206. URL: http://www-tandfonline-com.ezp-prod1.hul.harvard.edu/doi/abs/10.3109/0284186X.2015.1061206 (visited on 03/23/2016).

[Kur+16a] Christopher Kurz, Reinoud Nijhuis, Michael Reiner, Ute Ganswindt, Christian Thieke, Claus Belka, Katia Parodi, and Guillaume Landry. "Feasibility of automated proton therapy plan adaptation for head and neck tumors using cone beam CT images". In: *Radiation Oncology (London, England)* 11 (Apr. 30, 2016). ISSN: 1748-717X. DOI: 10.1186/s13014-016-0641-7. URL: https://www.ncbi.nlm.nih.gov/pmc/articles/PMC4851791/ (visited on 03/30/2018).

[Kur+16b] Christopher Kurz et al. "Investigating deformable image registration and scatter correction for CBCT-based dose calculation in adaptive IMPT". In: *Medical Physics* 43.10 (Oct. 2016), p. 5635. ISSN: 2473-4209. DOI: 10.1118/1.4962933.

[Lan+15] Guillaume Landry et al. "Investigating CT to CBCT image registration for head and neck proton therapy as a tool for daily dose recalculation". In: *Medical Physics* 42.3 (Mar. 1, 2015), pp. 1354–1366. ISSN: 0094-2405. DOI: 10.1118/1.4908223. URL: http://scitation.aip.org/content/aapm/journal/medphys/42/3/10.1118/1.4908223 (visited on 06/23/2016).

[Lee+17] Jonathan E. Leeman et al. "Proton therapy for head and neck cancer: expanding the therapeutic window". In: *The Lancet. Oncology* 18.5 (2017), e254–e265. ISSN: 1474-5488. DOI: 10.1016/S1470-2045(17)30179-1.

[Li+17] Xin Li, Yuyu Zhang, Yinghua Shi, Shuyu Wu, Yang Xiao, Xuejun Gu, Xin Zhen, and Linghong Zhou. "Comprehensive evaluation of ten deformable image registration algorithms for contour propagation between CT and cone-beam CT images in adaptive head & neck radiotherapy". In: *PloS One* 12.4 (2017), e0175906. ISSN: 1932-6203. DOI: 10.1371/journal.pone.0175906.

[Lie+14] Jakob Liebl, Harald Paganetti, Mingyao Zhu, and Brian A. Winey. "The influence of patient positioning uncertainties in proton radiotherapy on proton range and dose distributions". In: *Medical Physics* 41.9 (Sept. 1, 2014), p. 091711. ISSN: 2473-4209. DOI: 10.1118/1.4892601. URL: https://aapm.onlinelibrary.wiley.com/doi/abs/10.1118/1.4892601 (visited on 09/10/2018).

[Liu+13] Wei Liu, Steven J. Frank, Xiaoqiang Li, Yupeng Li, Peter C. Park, Lei Dong, X. Ronald Zhu, and Radhe Mohan. "Effectiveness of robust optimization in intensity-modulated proton therapy planning for head and neck cancers". In: *Medical Physics* 40.5 (May 2013), p. 051711. ISSN: 2473-4209. DOI: 10.1118/1.4801899.

[Lom08a] A. J. Lomax. "Intensity modulated proton therapy and its sensitivity to treatment uncertainties 1: the potential effects of calculational uncertainties". In: *Physics in Medicine and Biology* 53.4 (Feb. 21, 2008), p. 1027. ISSN: 0031-9155. DOI: 10.1088/0031-9155/53/4/014. URL: http://iopscience.iop.org.ubproxy.ub.uni-heidelberg.de/0031-9155/53/4/014 (visited on 03/10/2015).

[Lom08b] A. J. Lomax. "Intensity modulated proton therapy and its sensitivity to treatment uncertainties 2: the potential effects of inter-fraction and inter-field motions". In: *Physics in Medicine and Biology* 53.4 (Feb. 21, 2008), p. 1043. ISSN: 0031-9155. DOI: 10.1088/0031-9155/53/4/015. URL: http://iopscience.iop.org.ubproxy.ub.uni-heidelberg.de/0031-9155/53/4/015 (visited on 03/10/2015).

[McK+16] Matthew R. McKeever, Terence T. Sio, G. Brandon Gunn, Emma B. Holliday, Pierre Blanchard, Merrill S. Kies, Randal S. Weber, and Steven J. Frank. "Reduced acute toxicity and improved efficacy from intensity-modulated proton therapy (IMPT) for the management of head and neck cancer". In: *Chinese Clinical Oncology* 5.4 (Aug. 2016), p. 54. ISSN: 2304-3873. DOI: 10.21037/cco.2016.07.03.

[MDL17] Radhe Mohan, Indra J. Das, and Clifton C. Ling. "Empowering Intensity Modulated Proton Therapy Through Physics and Technology: An Overview". In: *International Journal of Radiation Oncology • Biology • Physics* 99.2 (Oct. 1, 2017), pp. 304–316. ISSN: 0360-3016. DOI: 10.1016/j.ijrobp.2017.05.005. URL: https://www.redjournal.org/article/S0360-3016(17)30902-1/fulltext (visited on 10/09/2018).

[Mor+17] Shunsuke Moriya, Hidenobu Tachibana, Kenji Hotta, Naoki Nakamura, Takeji Sakae, and Tetsuo Akimoto. "Feasibility of dynamic adaptive passive scattering proton therapy with computed tomography image guidance in the lung". In: *Medical Physics* 44.9 (Sept. 2017), pp. 4474–4481. ISSN: 2473-4209. DOI: 10.1002/mp.12444.

[NAZ12] Tianye Niu, Ahmad Al-Basheer, and Lei Zhu. "Quantitative cone-beam CT imaging in radiation therapy using planning CT as a prior: First patient studies". In: *Medical Physics* 39.4 (Apr. 1, 2012), pp. 1991–2000. ISSN: 0094-2405. DOI: 10.1118/1.3693050. URL: http://scitation.aip.org.ezp-prod1.hul.harvard.edu/content/aapm/journal/medphys/39/4/10.1118/1.3693050 (visited on 03/23/2016).

[Niu+10] Tianye Niu, Mingshan Sun, Josh Star-Lack, Hewei Gao, Qiyong Fan, and Lei Zhu. "Shading correction for on-board cone-beam CT in radiation therapy using planning MDCT images". In: *Medical Physics* 37.10 (Oct. 1, 2010), pp. 5395–5406. ISSN: 0094-2405. DOI: 10.1118/1.3483260. URL: http://scitation.aip.org.ezp-prod1.hul.harvard.edu/content/aapm/journal/medphys/37/10/10.1118/1.3483260 (visited on 03/23/2016).

[Oli+18] Jasmine A. Oliver, Omar Zeidan, Sanford L. Meeks, Amish P. Shah, Jason Pukala, Patrick Kelly, Naren R. Ramakrishna, and Twyla R. Willoughby. "Commissioning an in-room mobile CT for adaptive proton therapy with a compact proton system". In: *Journal of Applied Clinical Medical Physics* 19.3 (May 2018), pp. 149–158. ISSN: 1526-9914. DOI: 10.1002/acm2.12319.

[Pag12] Harald Paganetti. "Range uncertainties in proton therapy and the role of Monte Carlo simulations". In: *Physics in Medicine and Biology* 57.11 (June 7, 2012), R99–R117. ISSN: 0031-9155. DOI: 10.1088/0031-9155/57/11/R99. URL: https://www.ncbi.nlm.nih.gov/pmc/articles/PMC3374500/ (visited on 06/28/2018).

[Par+15] Yang-Kyun Park, Gregory C. Sharp, Justin Phillips, and Brian A. Winey. "Proton dose calculation on scatter-corrected CBCT image: Feasibility study for adaptive proton therapy". In: *Medical Physics* 42.8 (Aug. 1, 2015), pp. 4449–4459. ISSN: 0094-2405. DOI: 10.1118/1.4923179. URL: http://scitation.aip.org.ezp-prod1.hul.harvard.edu/content/aapm/journal/medphys/42/8/10.1118/1.4923179 (visited on 03/23/2016).

[Per+12] Marta Peroni, Delia Ciardo, Maria Francesca Spadea, Marco Riboldi, Stefania Comi, Daniela Alterio, Guido Baroni, and Roberto Orecchia. "Automatic Segmentation and Online virtualCT in Head-and-Neck Adaptive Radiation Therapy". In: *International Journal of Radiation Oncology*Biology*Physics* 84.3 (Nov. 1, 2012), e427–e433. ISSN: 0360-3016. DOI: 10.1016/j.ijrobp.2012.04.003. URL: http://www.sciencedirect.com/science/article/pii/S0360301612005160 (visited on 07/06/2016).

[Qin+16] Nan Qin, Pablo Botas, Drosoula Giantsoudi, Jan Schuemann, Zhen Tian, Steve B. Jiang, Harald Paganetti, and Xun Jia. "Recent developments and comprehensive evaluations of a GPU-based Monte Carlo package for proton therapy". In: *Physics in Medicine & Biology* 61.20 (2016), p. 7347. ISSN: 0031-9155. DOI: 10.1088/0031-9155/61/20/7347. URL: http://stacks.iop.org/0031-9155/61/i=20/a=7347 (visited on 08/20/2018).

[Sch+14] J. Schuemann, S. Dowdell, C. Grassberger, C. H. Min, and H. Paganetti. "Site-specific range uncertainties caused by dose calculation algorithms for proton therapy". In: *Physics in medicine and biology* 59.15 (Aug. 7, 2014), pp. 4007–4031. ISSN: 0031-9155. DOI: 10.1088/0031-9155/59/15/4007. URL: https://www.ncbi.nlm.nih.gov/pmc/articles/PMC4136435/ (visited on 06/28/2018).

[Sch+15] Jan Schuemann, Drosoula Giantsoudi, Clemens Grassberger, Maryam Moteabbed, Chul Hee Min, and Harald Paganetti. "Assessing the Clinical Impact of Approximations in Analytical Dose Calculations for Proton Therapy". In: *International Journal of Radiation Oncology • Biology • Physics* 92.5 (Aug. 1, 2015), pp. 1157–1164. ISSN: 0360-3016. DOI: 10.1016/j.ijrobp.2015.04.006.

URL: https://www.redjournal.org/article/S0360-3016(15)00379-X/fulltext (visited on 08/22/2018).

[Sha12] James A. Shackleford. "Plastimatch 1.6 - Current Capabilities and Future Directions". In: *INt Cong Med Image Comput Comput Assist Interv*. INt Cong Med Image Comput Comput Assist Interv. Vol. 15. Int Conf Med Image Comput Comput Assist Interv. MICCAI 2012, Oct. 15, 2012. URL: http://igtpg.spl.harvard.edu/publications/item/view/2371 (visited on 04/04/2017).

[Sio+16] Terence T. Sio et al. "Intensity Modulated Proton Therapy Versus Intensity Modulated Photon Radiation Therapy for Oropharyngeal Cancer: First Comparative Results of Patient-Reported Outcomes". In: *International Journal of Radiation Oncology, Biology, Physics* 95.4 (2016), pp. 1107–1114. ISSN: 1879-355X. DOI: 10.1016/j.ijrobp.2016.02.044.

[SKS10] J. A. Shackleford, N. Kandasamy, and G. C. Sharp. "On developing B-spline registration algorithms for multi-core processors". In: *Physics in Medicine and Biology* 55.21 (2010), p. 6329. ISSN: 0031-9155. DOI: 10.1088/0031-9155/55/21/001. URL: http://stacks.iop.org/0031-9155/55/i=21/a=001 (visited on 04/04/2017).

[Stu+13] Martin Stuschke, Andreas Kaiser, Jehad Abu Jawad, Christoph Pöttgen, Sabine Levegrün, and Jonathan Farr. "Multi-scenario based robust intensity-modulated proton therapy (IMPT) plans can account for set-up errors more effectively in terms of normal tissue sparing than planning target volume (PTV) based intensity-modulated photon plans in the head and neck region". In: *Radiation Oncology (London, England)* 8 (June 18, 2013), p. 145. ISSN: 1748-717X. DOI: 10.1186/1748-717X-8-145.

[Stü+17] Kristin Stützer, Annika Jakobi, Anna Bandurska-Luque, Steffen Barczyk, Carolin Arnsmeyer, Steffen Löck, and Christian Richter. "Potential proton and photon dose degradation in advanced head and neck cancer patients by intratherapy changes". In: *Journal of Applied Clinical Medical Physics* 18.6 (Nov. 2017), pp. 104–113. ISSN: 1526-9914. DOI: 10.1002/acm2.12189.

[Sze+16] Yenny Z. Szeto, Marnix G. Witte, Simon R. van Kranen, Jan-Jakob Sonke, José Belderbos, and Marcel van Herk. "Effects of anatomical changes on pencil beam scanning proton plans in locally advanced NSCLC patients". In: *Radiotherapy and Oncology: Journal of the European Society for Therapeutic Radiology and Oncology* 120.2 (2016), pp. 286–292. ISSN: 1879-0887. DOI: 10.1016/j.radonc.2016.04.002.

[Tro+05] Alexei Trofimov, Eike Rietzel, Hsiao-Ming Lu, Benjamin Martin, Steve Jiang, George T. Y. Chen, and Thomas Bortfeld. "Temporo-spatial IMRT optimization: concepts, implementation and initial results". In: *Physics in Medicine and Biology* 50.12 (2005), p. 2779. ISSN: 0031-9155. DOI: 10.1088/0031-9155/50/12/004. URL: http://stacks.iop.org/0031-9155/50/i=12/a=004 (visited on 04/03/2017).

[Vei+14] Catarina Veiga et al. "Toward adaptive radiotherapy for head and neck patients: Feasibility study on using CT-to-CBCT deformable registration for "dose of the day" calculations". In: *Medical Physics* 41.3 (Mar. 1, 2014), p. 031703. ISSN: 0094-2405. DOI: 10.1118/1.4864240. URL: http://scitation.aip.org.ezp-prod1.

hul.harvard.edu/content/aapm/journal/medphys/41/3/10.1118/1.4864240 (visited on 03/24/2016).

[Vei+15] Catarina Veiga, Ana Mónica Lourenço, Syed Mouinuddin, Marcel van Herk, Marc Modat, Sébastien Ourselin, Gary Royle, and Jamie R. McClelland. "Toward adaptive radiotherapy for head and neck patients: Uncertainties in dose warping due to the choice of deformable registration algorithm". In: *Medical Physics* 42.2 (Feb. 1, 2015), pp. 760–769. ISSN: 0094-2405. DOI: 10.1118/1.4905050. URL: http://scitation.aip.org/content/aapm/journal/medphys/42/2/10.1118/1.4905050 (visited on 06/23/2016).

[Vei+16] Catarina Veiga et al. "First clinical investigation of CBCT and deformable registration for adaptive proton therapy of lung cancer". In: *International Journal of Radiation Oncology • Biology • Physics* 0.0 (Feb. 3, 2016). ISSN: 0360-3016. DOI: 10.1016/j.ijrobp.2016.01.055. URL: http://www.redjournal.org/article/S0360301616001085/abstract (visited on 03/23/2016).

[Wat+16] Steven van de Water, Iris van Dam, Dennis R. Schaart, Abrahim Al-Mamgani, Ben J. M. Heijmen, and Mischa S. Hoogeman. "The price of robustness; impact of worst-case optimization on organ-at-risk dose and complication probability in intensity-modulated proton therapy for oropharyngeal cancer patients". In: *Radiotherapy and Oncology: Journal of the European Society for Therapeutic Radiology and Oncology* 120.1 (2016), pp. 56–62. ISSN: 1879-0887. DOI: 10.1016/j.radonc.2016.04.038.

Appendix I

This appendix illustrates the change in energy, position and weight for patients 4 and 9 during the adaptation process. The adaptations consisted of the geometrical method in Free mode and the weight tuning. The plots were automatically generated by the adaptation algorithm.

Figures 7.11 and 7.12 show the vector field (VF) at the probed positions for patient 4 and 9 from the first CBCT scan anatomy for each patient respectively. Please, see the captions for the interpretation of each element in the figure.

Figure 7.11 shows a VF that resembles a shift in a single direction, with variable size. The VF was well aligned with the Y axis, almost orthogonal with the X axis, had a median modulus of ~3 mm and no probe presented a vector of 0 modulus. There were no noticeable convergent/divergent regions, which indicated that the beamlets were moved in a similar direction and only small cold/hot spots in the target would be expected.

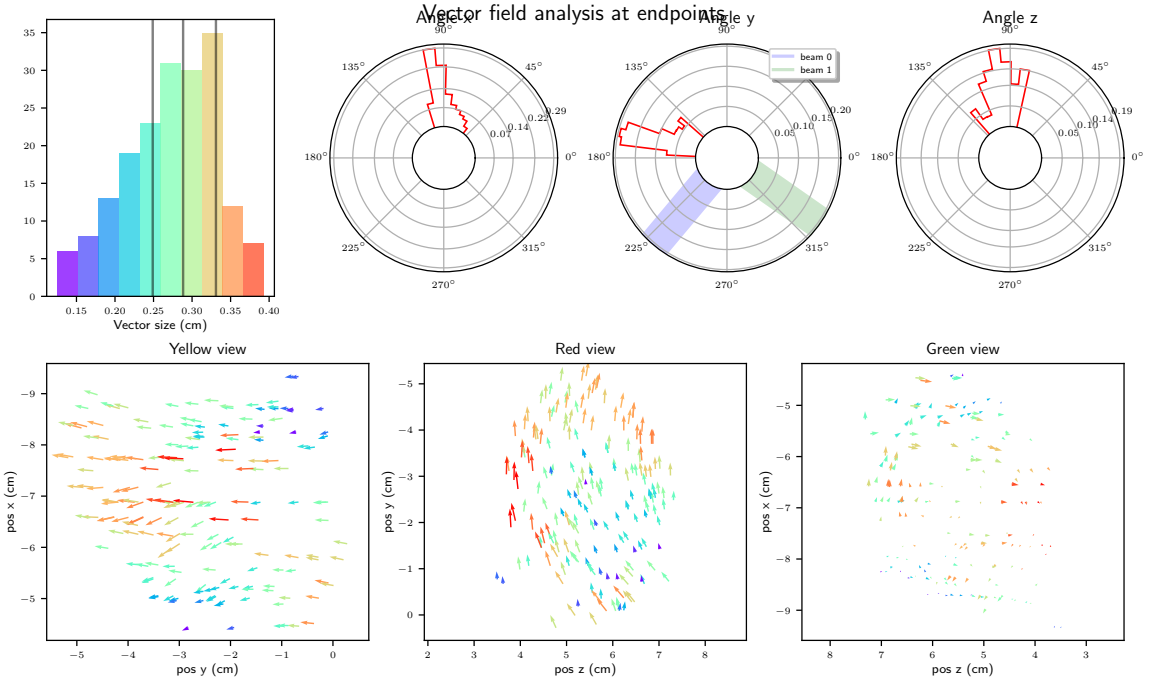

Fig. 7.11 Analysis of the patient 9 vector field at scan 1. Top-left: Histogram of the vector modulus, the lines show the 1st, 2nd (median) and 3rd quartiles. Top-center: Histogram of the angle subtended by the probed vectors with the X axis, weighted by the vector lengths. Top-right: Same as the top-center, but with the Y axis. Bottom-left: Vector field in the XY plane at the probed positions, with collapsed Z dimension. Bottom-right: Same as bottom-left, but in the YZ plane. The colors in the top-left panel are the same as in the bottom panels.

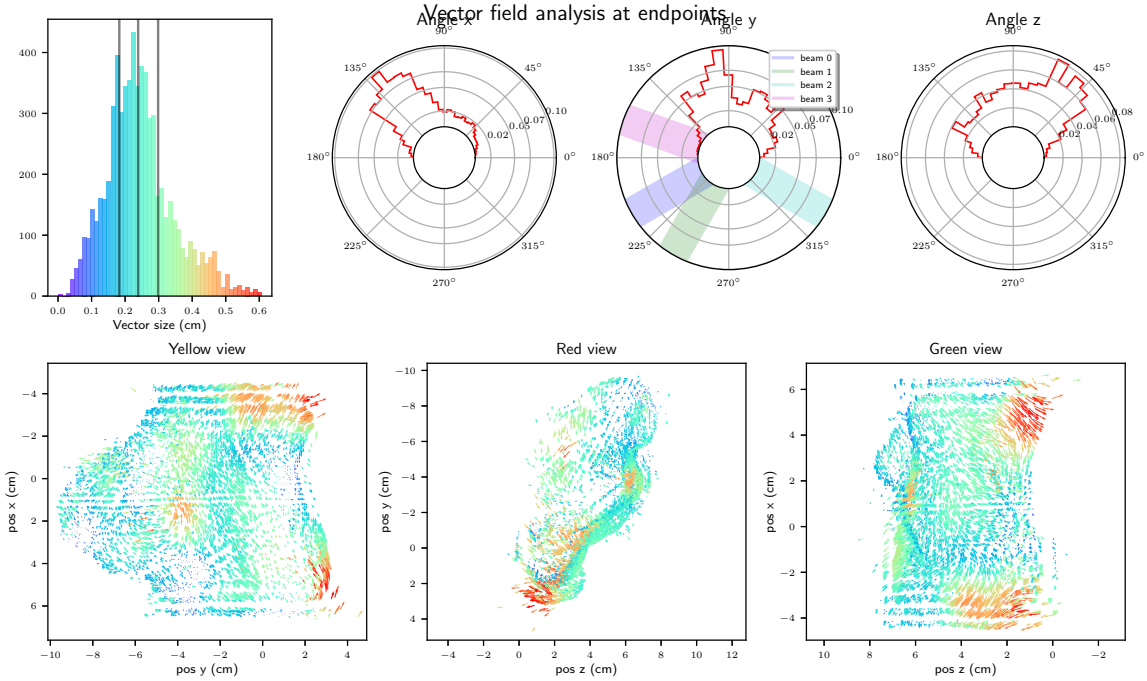

Fig. 7.12 Analysis of the patient 4 vector field at scan 1. Top-left: Histogram of the vector modulus, the lines show the 1st, 2nd (median) and 3rd quartiles. Top-center: Histogram of the angle subtended by the probed vectors with the X axis, weighted by the vector lengths. Top-right: Same as the top-center, but with the Y axis. Bottom-left: Vector field in the XY plane at the probed positions, with collapsed Z dimension. Bottom-right: Same as bottom-left, but in the YZ plane. The colors in the top-left panel are the same as in the bottom panels.

The VF in figure 7.12 showed a more complex behavior. The target in this case was bigger (see table 7.1 or plotting scale difference in bottom-left/right panels between figures 7.11 and 7.12), which increased the probability of having a non-uniform displacement. The median modulus was smaller than in the previous case (~2.5 mm), but the modulus histogram presented a wider range (from 0 to ~6 mm). The angular histogram showed a lot of variation and this can also be seen in the bottom panels. This situation indicated that the deformation would bring some beamlets closer together and some further apart, creating hot/cold spots after the geometrical adaptation method that would be solved by the weight tuning method.

Figures 7.13 and 7.14 show the effect of the deformations of patient 9 and 4 (scan 1) on the energy of the beamlets (top panels) and the beamlet's weight correction performed by the weight tuning method (bottom panels). Please, see the captions for the interpretation of each element in the figure.

The beamlet's energy changes of patient 9 in this scan were approximately between -6 and 0 MeV, with an average energy loss per layer of about 3%, which indicated a decrease in

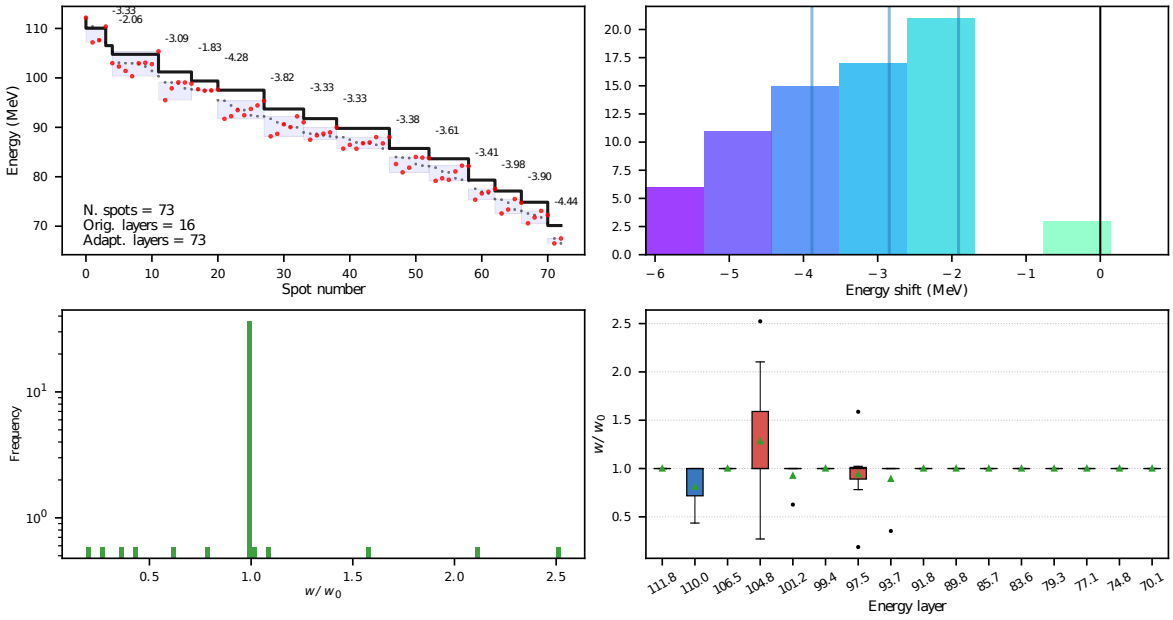

Fig. 7.13 Beamlet's energy and weight changes of patient 9 at CBCT 1. Top-left: Energy of each beamlet (spot). The original plan in black, showing the 9 energy layers, in red the new energies after the geometrical method, in light gray, the new energies in descendant order, the numbers represent the % change of the new average energies of the beamlets previously forming a layer. Top-right: Histogram of the energy change, the lines show the 1st, 2nd (median) and 3rd quartiles. Bottom-left: Histogram of the weight scaling factor after the weight tuning (most beamlets are unchanged). Bottom-right: Boxplots of the weight scaling factors as a function of the original energy layers. The boxplots follow the explanation given at the end of the methodology section, the top-bottom hinge distance might be 0, the mean is shown by the triangle.

the radiological depth of the patient. The small cold/hot spots in the target created by the beamlet displacements (seen in figure 7.11) and the effects of the energy changes (seen in the top panels of figure 7.13) were solved by the weight tuning method, while minimizing the dose to OARs. The weight changes were plotted in the bottom panels of figure 7.13. Most beamlet's weight change ratios were kept at 1, by definition of the method, since it only tuned the weights of a subset (bottom-left panel). The tuning method mostly changed the weights of the most energetic layers (bottom-right), also by definition, since it selected the higher weighted beamlets, which are usually among the most energetic.

On the other hand, figure 7.14 shows the plan for patient 4 with bigger changes at scan 1. The beamlet's energies changed from -15 to 25 MeV, approximately. On the top-left panel, it can be seen that at the beginning of the layers, the spots tended to lose energy, while they gained energy towards the end of the layers. The beginning and ends of the layers correspond to specific regions of the target, which means that some lost radiological depth,

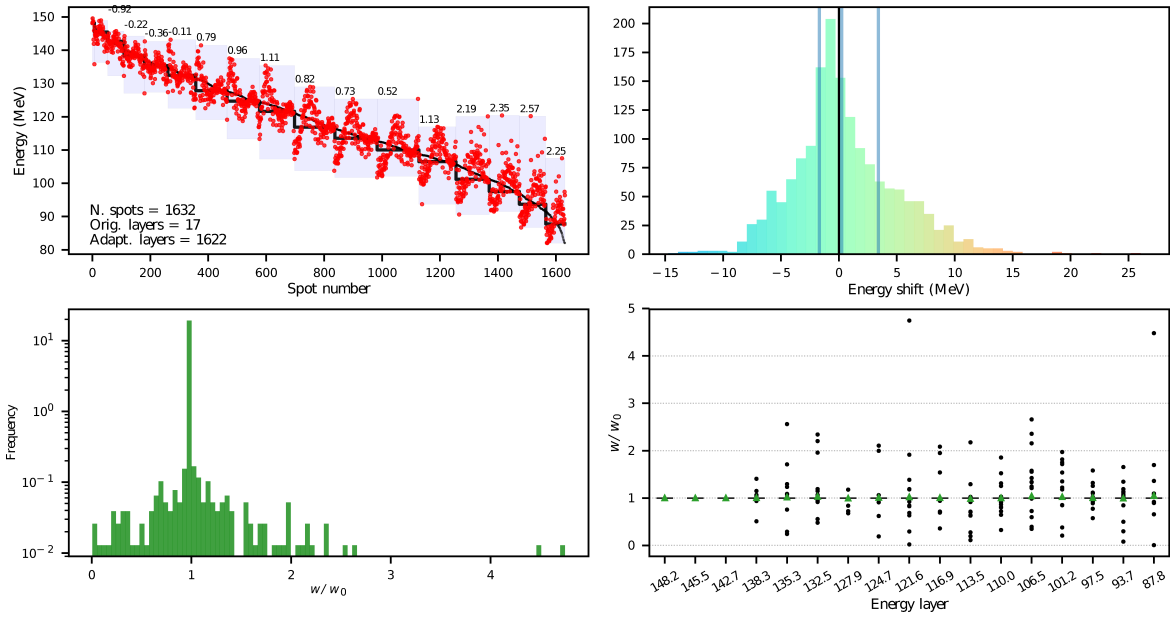

Fig. 7.14 Same as figure 7.13, but for patient 4 at CBCT 1.

while others gained. The median energy change was, however, close to 0. Most beamlets did not experience weight tuning, so the ratio was 1 for the majority. Some beamlets were rejected, while others were given ~4.5-5 times the number of initial protons (bottom panels). Contrary to the previous case, the weight tuning was applied to beamlets belonging to less energetic layers.

Chapter 8

Discussion and outlook

The projects included in this thesis have presented advances in four areas, namely: fast and accurate dose calculation, consideration of the biological effect of proton treatments through an approximation of the RBE, computationally efficient planning of moving targets and automatic adaptation of IMPT plans to different patient setups and anatomies. The fast and accurate dose calculation set the computational basis in order to perform the other projects. In the following items, each project will be discussed, with the outlook as focusing point.

8.1 Project 1: GPU-MC

The ultimate goal of using GPU Monte Carlo in the clinic is to improve the dose calculation accuracy in daily calculations and allow planning margin reductions. The code upgrades presented in chapter 4 improving the nuclear interaction models, providing the dose-averaged LET distribution and employing a programming language with broader usability brought this goal one step closer for gPMC. Yet they do not mean that a system based on the current version of gPMC can be applied in the clinic in any situation. There is an ubiquitous mantra in Monte Carlo simulations reading *garbage in, garbage out*, which means that the results obtained will be as good as the models utilized to calculate them. In the case of gPMC, the main limiting factor is that the nuclear models there implemented are based on hydrogen and oxygen only and it is assumed that the interactions with other nuclei (mainly carbon and nitrogen) will be well represented on average [FS04; Qin+16]. The contribution of these secondaries is small in comparison to the primaries, which makes the assumption true in most cases in human tissues within the accuracy required for proton treatments. However, in the presence of high Z materials in the patient, such as titanium implants, this assumption may not hold in the vicinity of these implants and might have consequences downstream. More importantly than implants, the assumption would not hold in cases were high Z materials are

systematically placed in the beam path, for example when employing apertures [Dow+12; Mot+16; Yas+18] or multi-leaf collimators [Moi+16b; Moi+16a] to sharpen the IMPT plan penumbra for sites like prostate or when the facility spot size is large compared to the tumor size [Mot+16]. Nevertheless, the expected deviations caused in these cases by the nuclear models should appear at the entrance region of the field and the calculation accuracy might be acceptable there. Other approximations in the code, such as not tracking electrons or photons (see accuracy of the electromagnetic channel in [Jia+12; Qin+16]) or disregarding species other than protons [GLP15] in the beam models should not cause major issues. Therefore, awareness of the limitations of the code is required before the code implementation in daily calculations to profit from its advantages, which are plenty.

In order to take full advantage of MC accuracy in the clinic, GPU-MC systems should be employed for IMPT treatment planning and not only for plan verification. When employing ADC algorithms for this task, the dose to the target in sites with high lateral and longitudinal heterogeneity like head and neck, breast and lung can be overestimated in the calculation by up to ~10% [Yep+18]. Subsequently the target receives less dose than planned in reality and OARs may receive up to 10 Gy more, although the median difference has been reported to be smaller than 2 Gy [Yep+18] (the prescription dose is not reported, which makes the interpretation of the absolute difference complicated). Assessing the range uncertainty analysis performed with passive scattering delivery by Schuemann et al. [Sch+15], the resultant recommended dose calculation based range margin is ~5.8% in the previous heterogeneous sites. This margin is transformed into a generic range margin of $6.3\% + 1.2$ mm. It should be noted that these values might be too high because range is defined at 90% of SOBP, which is a very sensitive point and it assumes that every field from every fraction must give full target coverage. Having said this, coupling gPMC with a treatment planning system would improve the quality of the treatments, setting the generic range margin in around $2.4\% + 1.2$ mm, as reported by Paganetti [Pag12]. For a 10 cm range field, the amount of healthy tissue spared by using Monte Carlo simulations is 3.9 mm. These values were extracted from the analysis of passive scattering proton treatment and can be directly employed for IMPT plans with single field uniform dose.

In order to employ gPMC for routine IMPT optimizations, it might be necessary to find solutions to decrease the computation time needed to calculate the optimization matrices. gPMC is capable of simulating 10^6 primaries in ~1.4 s (see table 4.2), which means that an optimization matrix for a plan with 3 fields and 1500 beamlets per field requires 6300 s, or 1.75 hours on a single NVidia GTX TITAN. If robust optimization is intended, the number of optimization matrices required increases with the number of included scenarios, being 5 a common number of scenarios for a total of 8.75 hours. One option to alleviate this is to

establish a dependency between the usage of a proton beamlet and the accuracy with which it is simulated. This can be achieved, for example, by creating an iterative system that calculates the optimization matrices without full accuracy, then optimizes the plan and keeps adding more histories to the beamlets depending on their assigned weight until the intended accuracy in a given region is reached. Such a system has already been proposed by Ma et al. [Ma+14]. A different option that has not yet been proposed to my best knowledge is to realize a hybrid ADC-MC system. In such a system, heterogeneity indices could be employed to select the beamlets in which ADC would perform well and only simulate the others with GPU-MC. In this case, the margin employed for range uncertainty would be position dependent as it would depend on which beamlets were calculated with ADC and which with GPU-MC. If robust optimization is intended with the hybrid system, dose-influence matrices could be generated forcing the beamlets generated with ADC to be recalculated in wider error scenarios than the ones calculated with GPU-MC. Such system would be beneficial in sites like head and neck, where some beamlets traverse fairly homogeneous tissues, while others do not. Of course, the most effective solution to improve the computational efficiency is to simply employ more GPUs.

In summary, gPMC is a good and flexible candidate to increase dose calculation accuracy routinely in the clinic.

8.2 Project 2: LET-based optimization

The clinical application of the LET-based biological optimization presented in chapter 5 is intimately dependent on the clinical translation of GPU-MC for IMPT planning. In this case GPU-MC simulations are again encouraged mainly by the higher calculation accuracy, however, this is more important for LET because only recently analytical calculation algorithms have modeled the lateral LET distribution [Mar+16; San+16; Hir+18]. In this project a method to cope with the large biological uncertainties present in proton therapy was proposed, leveraging the well established proportionality[1] between the biological effect of a radiation field in a given location and the quantity LET$\times$D to reduce the potential impact of the field in OARs. This method does not reduce the biological uncertainty globally, but it does reduce its potential effects locally, where they might matter the most.

The ultimate goal however, would be to exactly predict the biological impact of the field through the RBE. Until that goal is achievable (if ever), employing surrogates to take the impact into account in a conservative manner can improve clinical outcomes, reducing toxicities in OARs. The advantages of employing LET$\times$D as surrogate are that (1) it is a

[1] The proportionality is established, not its exact value.

linear function of the fluence, allowing the application of well-known optimization algorithms, (2) it is readily available from MC simulations and recently from analytical calculations [Hir+18] and (3) it can be interpreted as the biological extra effect produced by elevated LET, to first approximation.

Robust optimization with range uncertainties has similar consequences for the final plan as LET×D-based optimization. The LET×D distribution is dominated by the Bragg peak present in the dose distribution, but the product with LET makes the peak position sit at slightly deeper depth. Because the high LET×D is slightly beyond the Bragg peak, the prioritized optimization penalizes beamlets that aim directly to an OAR, favoring those that deliver the dose to the target borders with the lateral profile in sensitive regions. This is also what robust optimization with range uncertainties does, as the lateral profiles are not sensitive to small shifts in the Bragg peak depth. This realization was confirmed in [Gia+17], observing that robust optimization with range uncertainty significantly lowered the median LET in OARs, although not as efficiently as a dedicated term dependent on LET×D in the objective function. A more involved analysis by Unkelbach and Paganetti on robust treatment planning with physical and biological uncertainties can be found in a recent publication [UP18].

The expected dependency on LET is not the only base of RBE models that have been proposed, as cited in section 2.4.4 [SS04; SS06; Ste+11; Ste+15; Fri+13; Fre+11; Car+08]. However, the same expected dependency of RBE on high ionization areas might be parameterizable on other quantities. An alternative surrogate to LET is to employ the proton stop positions as this distribution should be correlated to the LET. This tally is also supported in gPMC (as reported in 6 in section 3.1.2). No studies have been published so far on this topic to my best knowledge, but it could be used to drive high LET areas out of OARs. The theoretical advantage of this quantity is that it does not suffer the spikes the LET distribution presents when scored with MC methods in a voxelized geometry. Nevertheless, the quantity LET×D employed in this project is more robust to those spikes as the low dose value in the spikes regions lowers their impact.

In any case, GPU-MC would offers the necessary flexibility to score multiple quantities in a realistic manner without having to develop a dedicated algorithm for it, allowing systematic comparisons of different candidates. Ultimately, it would allow clinical translation of such techniques.

8.3 Project 3: Lung planning

The impact of range uncertainties arising from patient movement in lung is hard to minimize, as studied in chapter 6. In the study there presented, the WEPL-dependent overwrite in the ITV showed the highest performance among the studied strategies. This strategy should be preferred over MIP or constant HU filling of the IGTV when ITVs are necessary.

Additionally, the presented 4D framework allows the systematic evaluation and comparison of planning strategies with high dose calculation accuracy. This framework can be applied to other sites and techniques, such as gating for cardiac soft tissue sarcoma and arrhythmia ablation [Lee+18][2]. The 4D simulation framework is an important software that can inform clinicians about the safety of a certain plan in movement conditions. However, a dedicated package should be developed to ease this procedure, fully connecting it to the clinical databases and allowing the flexibility to perform different studies. An aspect that could be improved in the current form of the package is the dose accumulation strategy. So far the dose is accumulated by warping a dose map, but this does not necessarily conserve energy. There is currently not a definitive agreement on how to perform dose accumulation. The mass and energy warping method conserves energy and is also commonly employed, however, it has also been seen to create artifacts near density interfaces [SZ08; ZS09; Li+14; MWU14]. Experiments should be performed to measure the exact dose in a moving heterogeneous geometry to validate the most optimal method.

8.4 Project 4: Online IMPT plan adaptation

The dosimetric effects of the anatomical changes convolved with the setup uncertainty effects have been reported in chapter 7. It was seen that they can degrade the quality of IMPT plans significantly when narrow margins are intended. Higher dose to OARs and lower dose to target than initially planned were observed, increasing the toxicities and decreasing the tumor coverage and therefore the tumor control probability. The algorithm presented in chapter 7 has shown that the plan quality can be recovered well by performing online plan adaptation, minimizing the effect of the anatomical and setup uncertainties.

After applying the online adaptation algorithm, the target coverage is only slightly decreased. The average initial plan V98 of 98.9 ± 1.0 becomes 97.4 ± 1.4 in the cumulative dose to the patient and 96.4 ± 1.8 in the daily doses. Although V98 is a rather unstable value that tends to exaggerate the actual discrepancies, it shows very good coverage. V95, a more

[2]The reference cites a preliminary study using double scattering, not pencil beam scanning, presented at 2018 annual meeting of the AAPM in Nashville (TN, USA). The reference is given to cite the main researchers in this project and avoid taking credit by citing the idea.

stable value, shows 99.9 ± 0.1 at initial plan, 99.4 ± 0.9 at cumulative and 99.0 ± 1.0 at daily evaluations. For reference, the effect of setup and anatomy dropped the V98 and V95 from the plan values given before to 87.3 ± 9.4 and 94.1 ± 5.2 in the cumulative and 86.0 ± 9.0 and 93.9 ± 5.2 in the daily. This shows that the online adaptation is capable of maintaining a high degree of coverage in the target.

The idea of online IMPT plan adaptation is not new to the field as others have already studied this procedure [Kur+16; Jag+17; Jag+18; Ber+18], but this has been the first study proving online IMPT plan adaptation while limiting range uncertainty with MC simulations. This fact should allow further shrinking of planning margins. It is important to note that the comparisons against the dosimetric results of the original plans are only fair if daily replanning with full quality is feasible. In reality, one would perform the original plan taking uncertainties into account. A fair comparison of the performance of the daily plan adaptations would then be against a robust plan against setup and anatomy uncertainties, which will be the focus of future research. In such scenario, common uncertainties could be assumed to not influence the study. Some preliminary results are included here.

Patient number 1, a complex oropharynx case planned with 4 fields (see table 7.1) was replanned with robust optimization against setup and anatomy variations. Usually, in order to perform the robust optimization, a set of plausible error scenarios is considered in which the plan is intended to perform well. This is fairly straight forward for the setup uncertainty because the patient anatomy can be shifted and rotated following a Gaussian uncertainty model, but the anatomy evolution uncertainty is much more complicated to handle. In these preliminary results, an ideal situation is studied in which the future setup errors and anatomy evolution are known before the robust optimization is performed. This corresponds to generating dose-influence matrices in the daily CBCTs, as opposed to generating them in hypothetical error scenarios. This is why the first sentence reads *robust optimization against variations*, instead of *robust optimization against uncertainties*. Of course, in such perfect forecast situation one could generate as many plans as daily scans, but the point of the study is to compare the online adaptation procedure against what could be understood as the ceiling of a robustly optimized plan assuming error scenarios. It must also be understood that there are several flavors of robust optimizations, with the strategy to bring together the n different scenarios being the most important factor. The choice of approach would produce different *ceilings*. Because this optimization is performed with perfect scenario forecast with equal importance, the expected value-based optimization was employed with equal weight for each scenario. The expected value optimization is expected to perform better than the worst case scenario in this special case, specially in OAR sparing, based on the publication by Fredriksson were the worst case scenario was seen to overestimate the dose to OARs [Fre12].

Generalizations of these two approaches might yield better results [Fre12], although in this special case it is not clear if a significant improvement would be obtained. Finally, the term *robust* might be misplaced here as there are no real uncertainties, but it serves the purpose of illustrating the comparison here performed.

When comparing the robust plan against the daily adaptations for this single case, it can be seen that the daily adaptations provided similar target coverage, while reducing the dose to OARs. This is due to the fact that high dose volume is smaller when performing plan adaptation. This can be observed in the dose levels received by the two submandible glands and the CTV in figure 8.1. Given the special situation studied here, there is indication that the online plan adaptation procedure could be an improvement over robustly optimized plans. Specially when considering that the robustly optimized plan was performed on an ideal situation. It is unclear how ideal this situation is and further investigation is required before any definitive conclusion can be reached.

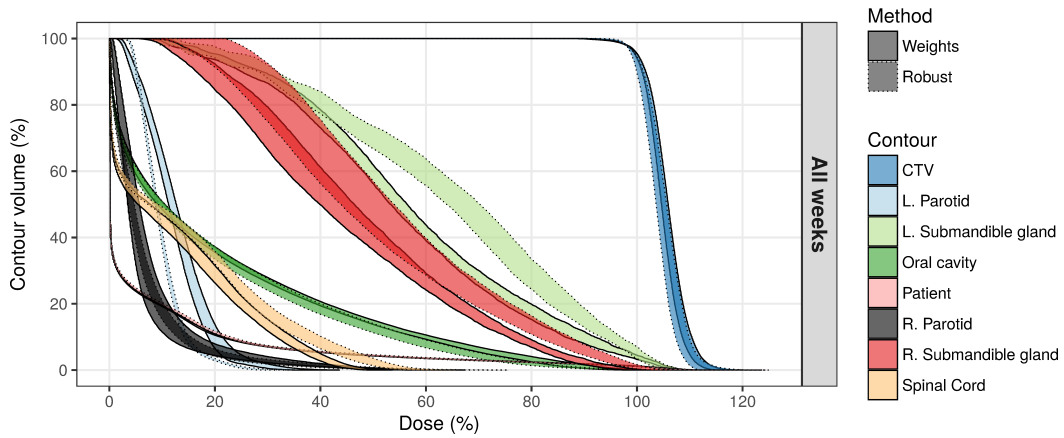

Fig. 8.1 "Robust" optimization on the daily scans *vs* daily adaptation (weights) on patient 1 on table 7.1. The bands contain the values obtained in the daily scans.

The proposed algorithm is mainly a proof of concept and there remain several improvements that should increase the computational efficiency and maybe allow better techniques to be employed. One major improvement would come from defining MC simulation-stopping sensitive regions. These regions would record the simulation uncertainty and stop it whenever a certain threshold is reached. Currently, all simulations were performed with a conservative number of particles in order to be able to automatize the adaptation process for every case studied. However this has an impact on the time needed for the adaptation that has not been assessed yet. The reason this was not assessed in the publication in chapter 7 is that a general recipe for the required number of protons to be simulated is not feasible as the uncertainty is dependent on the specific plan and geometry studied. Therefore, the only possible general

solution is to define regions to evaluate the uncertainty and stop the simulation when a certain criterion is met. Another major improvement would be to tailor the optimizer to the particular problem at hand. Currently, the same optimizer employed for the original IMPT plan was used, which runs on CPUs in single-thread mode. Different algorithms should also be investigated that could leverage the starting point of the objective function and might be better suited to optimizing for variable dose maps. The two previous points should in principle improve the computation efficiency, but they are not expected to have a great impact on the final plan quality. In order to improve this, a better selection of spots to tune should be performed. Currently they are selected based on the accuracy they have been simulated with, but that is not necessarily the best approach. An iterative process could be implemented to simulate/evaluate the beamlets' effect on under-/over-dose areas and select the one with the highest impact on them for the weight tuning. The same iterative process could be employed to evaluate the uncertainty of the simulation.

Judging from the uncertainty levels, the MC-based algorithm should be superior to ADC-based algorithms. However, it might be the case that the lower efficiency of MC simulations becomes a computational bottleneck to implement more sophisticated optimization procedures for the remaining uncertainties, such as robust optimization, having a detrimental effect on the final adapted plan quality. It remains to be seen what the best approach is when online adaptation algorithms are mature enough to allow a meaningful comparison. Publicly available packages would greatly help improve this comparison.

Independently of what the ideal algorithm is, there remains an underlying issue with any of the options given as references and the one here presented: the automatic definition of the patient contours. There is yet no accepted solution to handle the contours in an adaptive manner. The contours describe the position of each important organ and structure in the patient. As such, they are used to drive the optimization and to evaluate the radiation field, both physically and biologically. Any clinical implementation of the algorithm here presented should first solve the automatic definition of the contours. Automatic contours definition is a very active area of research without a generally accepted solution, see for reference the review article by Sharp et al. [Sha+14]. Nevertheless, the particular case of online plan adaptation may be a more forgiving situation than the general automatic contour definition because there is a previous delineation of the patient to drive the automatic procedure. There is, however, a remaining niche of investigation regarding how to handle the uncertainty of the contours definition. It would be ideal to handle this as another source of uncertainty, which in turn may ease the acceptance of automatically generated contours, since comparison of non-binary distributions yield more robust results.

In any case, online adaptation of proton plans based on MC simulation may drastically improve the quality of IMPT plans and their reproducibility by minimizing setup, anatomy and range uncertainty. Hopefully it can some day be safely implemented in routine treatments and have a positive impact on patient outcomes.

Chapter 9

Conclusions

In this thesis 4 uncertainty sources present in proton therapy were studied and solutions within specific approaches were proposed.

First, in order to reduce the dose calculation uncertainty an existing GPU Monte Carlo code, gPMC, was improved with better nuclear interaction models, bringing the goal of improving the dose routine calculation accuracy in the clinic one step closer. Additionally, these improvements pave the way to perform many different studies with high calculation accuracy, such as the ones that follow.

Second, other improvements included in gPMC, such as the LET scorer, were employed to study the reduction of the potential harm of high biological impact radiation areas in organs at risk (OARs) through an optimization method. This was done with a prioritized optimization scheme of IMPT plans that maintained high quality physical dose plan, while removing high LET$\times$D areas from OARs as a first order approximation of the unknown biological dose distribution, minimizing the potential effect of its uncertainties.

Third, computationally efficient planning strategies for lung tumors based on internal tumor volume (ITV) density overwrites were compared. The results showed that overwriting the internal GTV (IGTV) using the voxel intensity in the planning CT with the intensity that voxel has in the 4DCT phase with higher WEPL gave the best performance. Outside the IGTV, the average 4DCT image projection was used. This approach is applicable to other sites with patient movement. Additionally, a 4D framework to simulate IMPT plans in the presence of movement was developed that can be employed to accurately evaluate the degradation due to the movement for any given plan.

Lastly, the patient setup and anatomy uncertainties were tackled and an online IMPT plan adaptation algorithm was developed to adjust the original plan to the daily geometry, demonstrating it in head and neck patients. This algorithm only employs GPU-MC simulations as dose calculation engine, which also reduces the range uncertainty, which can be big due to

tissue heterogeneity and interfaces in the studied site. The clinical application of such tool would allow the reduction of planning margins, shrinking the volume receiving high dose levels and potentially improving patient outcomes.

Peer-reviewed publications during thesis

[Bot+18a] P Botas, C Grassberger, G Sharp, and H Paganetti. "Density overwrites of internal tumor volumes in intensity modulated proton therapy plans for mobile lung tumors". In: *Physics in Medicine & Biology* 63.3 (2018), p. 035023.

[Bot+ew] P Botas, J Kim, B Winey, and H Paganetti. "Online adaption approaches for intensity modulated proton therapy for head and neck patients based on cone beam CTs and Monte Carlo simulations". In: *Physics in Medicine & Biology* (**Under review**).

[Qin+16b] Nan Qin, Pablo Botas, Drosoula Giantsoudi, Jan Schuemann, Zhen Tian, Steve B Jiang, Harald Paganetti, and Xun Jia. "Recent developments and comprehensive evaluations of a GPU-based Monte Carlo package for proton therapy". In: *Physics in Medicine & Biology* 61.20 (2016), p. 7347.

[Unk+16c] Jan Unkelbach, Pablo Botas, Drosoula Giantsoudi, Bram L Gorissen, and Harald Paganetti. "Reoptimization of intensity modulated proton therapy plans based on linear energy transfer". In: *International Journal of Radiation Oncology* Biology* Physics* 96.5 (2016), pp. 1097–1106.

Chapters 4–7 correspond to [Qin+16b; Unk+16c; Bot+18a; Bot+ew], respectively.

Conference publications

[Bot+16] P Botas, C Grassberger, G Sharp, N Qin, X Jia, S Jiang, and H Paganetti. "SU-G-TeP1-06: Fast GPU Framework for Four-Dimensional Monte Carlo in Adaptive Intensity Modulated Proton Therapy (IMPT) for Mobile Tumors". In: vol. 43. 6Part26. Wiley Online Library, 2016, pp. 3653–3653.

[Bot+17a] P Botas, C Grassberger, GC Sharp, and H Paganetti. "Comparison of Internal Tumor Volume Definition Strategies to Reduce Plan Degradation of Intensity Modulated Proton Therapy Plans for Mobile Lung Tumor". In: *International Journal of Radiation Oncology• Biology• Physics*. Vol. 99. 2. Elsevier. 2017, E641.

[Bot+17b] P Botas, J Kim, C Grassberger, B Winey, and H Paganetti. "TH-AB-605-02: Assessing the Need and Feasibility for Online Plan Adaptation Based On Daily CBCT of Head and Neck Proton Therapy Treatments". In: *Medical Physics*. Vol. 44. 6. Medical Physics. 2017, p. 3276.

[Bot+18b] P Botas, J Kim, B Winey, and H Paganetti. "Online Plan Adaptation of Head and Neck IMPT Treatments Based On Cone Beam CT Imaging and GPU Monte Carlo Simulations". In: *Medical Physics*. Vol. 45. 6. Wiley 111 River st, Hoboken 07030-5774, NJ USA. 2018, E642–E642.

[Gia+17b] D Giantsoudi, J Unkelbach, P Botas, C Grassberger, and H Paganetti. "Can Robust Optimization for Range Uncertainty in Proton Therapy Act as a Surrogate for Biological Optimization?" In: vol. 99. 2. Elsevier, 2017, S106–S107.

[Unk+16a] J Unkelbach, P Botas, N Qin, X Jia, D Giantsoudi, and H Paganetti. "TH-CD-209-06: LET-Based Adjustment of IMPT Plans Using Prioritized Optimization". In: vol. 43. 6Part46. American Association of Physicists in Medicine, 2016, pp. 3887–3887.

[Ver+17a] J Verburg, T Ruggieri, P Botas, E Cascio, F Hueso-gonzalez, M Rabe, and T Bortfeld. "SU-F-601-02: Clinical Translation of Prompt Gamma-ray Spectroscopy for In Vivo Proton Range Verification". In: *Medical Physics*. Vol. 44. 6. Medical Physics. 2017, p. 2755.

References

References of the included papers are found at the end of their respective chapters, corresponding to chapters 4–7.

[Ago+03] S. Agostinelli et al. "Geant4: a simulation toolkit". In: *Nuclear Instruments and Methods in Physics Research Section A: Accelerators, Spectrometers, Detectors and Associated Equipment* 506.3 (2003), pp. 250–303. ISSN: 0168-9002. DOI: https://doi.org/10.1016/S0168-9002(03)01368-8. URL: http://www.sciencedirect.com/science/article/pii/S0168900203013688.

[Ahn+14] Peter H. Ahn, J. Nicholas Lukens, Boon-Keng Kevin Teo, Maura Kirk, and Alexander Lin. "The use of proton therapy in the treatment of head and neck cancers". In: *Cancer Journal (Sudbury, Mass.)* 20.6 (Dec. 2014), pp. 421–426. ISSN: 1540-336X. DOI: 10.1097/PPO.0000000000000077.

[Alb+08] Francesca Albertini, Alessandra Bolsi, Antony J. Lomax, Hans Peter Rutz, Beate Timmerman, and Gudrun Goitein. "Sensitivity of intensity modulated proton therapy plans to changes in patient weight". In: *Radiotherapy and Oncology: Journal of the European Society for Therapeutic Radiology and Oncology* 86.2 (Feb. 2008), pp. 187–194. ISSN: 0167-8140. DOI: 10.1016/j.radonc.2007.11.032.

[Bar+95] J. Baró, J. Sempau, J. M. Fernández-Varea, and F. Salvat. "PENELOPE: An algorithm for Monte Carlo simulation of the penetration and energy loss of electrons and positrons in matter". In: *Nuclear Instruments and Methods in Physics Research Section B: Beam Interactions with Materials and Atoms* 100.1 (May 1, 1995), pp. 31–46. ISSN: 0168-583X. DOI: 10.1016/0168-583X(95)00349-5. URL: http://www.sciencedirect.com/science/article/pii/0168583X95003495 (visited on 09/25/2018).

[BD11] C. Bert and M. Durante. "Motion in radiotherapy: particle therapy". In: *Physics in Medicine & Biology* 56.16 (2011), R113. ISSN: 0031-9155. DOI: 10.1088/0031-9155/56/16/R01. URL: http://stacks.iop.org/0031-9155/56/i=16/a=R01 (visited on 09/02/2018).

[Ber+17a] M.J. Berger, J.S. Coursey, M.A. Zucker, and J. Chang. *Stopping-Power & Range Tables for Electrons, Protons, and Helium Ions*. July 2017. URL: https://www.nist.gov/pml/stopping-power-range-tables-electrons-protons-and-helium-ions (visited on 07/19/2018).

[Ber+17b] Kinga Bernatowicz, Ye Zhang, Rosalind Perrin, Damien C. Weber, and Antony J. Lomax. "Advanced treatment planning using direct 4D optimisation for pencil-beam scanned particle therapy". In: *Physics in Medicine & Biology* 62.16 (2017), p. 6595. ISSN: 0031-9155. DOI: 10.1088/1361-6560/aa7ab8. URL: http://stacks.iop.org/0031-9155/62/i=16/a=6595 (visited on 09/02/2018).

[Ber+18] Kinga Bernatowicz, Xavier Geets, Ana Barragan, Guillaume Janssens, Kevin Souris, and Edmond Sterpin. "Feasibility of online IMPT adaptation using fast, automatic and robust dose restoration". In: *Physics in Medicine and Biology* (2018). ISSN: 1361-6560. DOI: 10.1088/1361-6560/aaba8c. URL: http://iopscience.iop.org/10.1088/1361-6560/aaba8c (visited on 04/03/2018).

[Ber63] Martin J. Berger. "Monte Carlo calculation of the penetration and diffusion of fast charged particles". In: (1963).

[BH34] H. Bethe and W. Heitler. "On the stopping of fast particles and on the creation of positive electrons". In: *Proc. R. Soc. Lond. A* 146.856 (Aug. 1, 1934), pp. 83–112. ISSN: 0950-1207, 2053-9150. DOI: 10.1098/rspa.1934.0140. URL: http://rspa.royalsocietypublishing.org/content/146/856/83 (visited on 07/19/2018).

[BK05] W. H. Bragg and R. Kleeman. "On the alpha particles of radium, and their loss of range in passing through various atoms and molecules". In: *The London, Edinburgh, and Dublin Philosophical Magazine and Journal of Science* 10.57 (Sept. 1, 1905), pp. 318–340. ISSN: 1941-5982. DOI: 10.1080/14786440509463378. URL: https://doi.org/10.1080/14786440509463378 (visited on 07/19/2018).

[Blo33] F. Bloch. "Zur Bremsung rasch bewegter Teilchen beim Durchgang durch Materie". In: *Annalen der Physik* 408.3 (1933), pp. 285–320. ISSN: 1521-3889. DOI: 10.1002/andp.19334080303. URL: https://onlinelibrary.wiley.com/doi/abs/10.1002/andp.19334080303 (visited on 07/19/2018).

[Boh15] Niels Bohr. "On the decrease of velocity of swiftly moving electrified particles in passing through matter". In: *The London, Edinburgh, and Dublin Philosophical Magazine and Journal of Science* 30.178 (Oct. 1, 1915), pp. 581–612. ISSN: 1941-5982. DOI: 10.1080/14786441008635432. URL: https://doi.org/10.1080/14786441008635432 (visited on 07/18/2018).

[Bor97] Thomas Bortfeld. "An analytical approximation of the Bragg curve for therapeutic proton beams". In: *Medical Physics* 24.12 (Dec. 1, 1997), pp. 2024–2033. ISSN: 0094-2405. DOI: 10.1118/1.598116. URL: http://scitation.aip.org.ubproxy.ub.uni-heidelberg.de/content/aapm/journal/medphys/24/12/10.1118/1.598116 (visited on 04/01/2015).

[BPB13] Abigail Besemer, Harald Paganetti, and Bryan Bednarz. "The clinical impact of uncertainties in the mean excitation energy of human tissues during proton therapy". In: *Physics in Medicine and Biology* 58.4 (Feb. 21, 2013), pp. 887–902. ISSN: 1361-6560. DOI: 10.1088/0031-9155/58/4/887.

[BTD17] Linus C. Benjamin, Alison C. Tree, and David P. Dearnaley. “The Role of Hypofractionated Radiotherapy in Prostate Cancer”. In: *Current Oncology Reports* 19.4 (2017). ISSN: 1523-3790. DOI: 10.1007/s11912-017-0584-7. URL: https://www.ncbi.nlm.nih.gov/pmc/articles/PMC5366169/ (visited on 09/24/2018).

[Bus+11] David A. Bush, Zeid Kayali, Roger Grove, and Jerry D. Slater. “The safety and efficacy of high-dose proton beam radiotherapy for hepatocellular carcinoma: a phase 2 prospective trial”. In: *Cancer* 117.13 (July 1, 2011), pp. 3053–3059. ISSN: 1097-0142. DOI: 10.1002/cncr.25809.

[Bus+13] David A. Bush, Gregory Cheek, Salman Zaheer, Jason Wallen, Hamid Mirshahidi, Ari Katerelos, Roger Grove, and Jerry D. Slater. “High-dose hypofractionated proton beam radiation therapy is safe and effective for central and peripheral early-stage non-small cell lung cancer: results of a 12-year experience at Loma Linda University Medical Center”. In: *International Journal of Radiation Oncology, Biology, Physics* 86.5 (Aug. 1, 2013), pp. 964–968. ISSN: 1879-355X. DOI: 10.1016/j.ijrobp.2013.05.002.

[CA12] Y. Chen and S. Ahmad. “Empirical model estimation of relative biological effectiveness for proton beam therapy”. In: *Radiation Protection Dosimetry* 149.2 (Apr. 2012), pp. 116–123. ISSN: 1742-3406. DOI: 10.1093/rpd/ncr218.

[Car+08] David J. Carlson, Robert D. Stewart, Vladimir A. Semenenko, and George A. Sandison. “Combined use of Monte Carlo DNA damage simulations and deterministic repair models to examine putative mechanisms of cell killing”. In: *Radiation Research* 169.4 (Apr. 2008), pp. 447–459. ISSN: 0033-7587. DOI: 10.1667/RR1046.1.

[Car+12] Alejandro Carabe, Maryam Moteabbed, Nicolas Depauw, Jan Schuemann, and Harald Paganetti. “Range uncertainty in proton therapy due to variable biological effectiveness”. In: *Physics in Medicine and Biology* 57.5 (Mar. 7, 2012), pp. 1159–1172. ISSN: 1361-6560. DOI: 10.1088/0031-9155/57/5/1159.

[Chi+05] Toshiya Chiba et al. “Proton beam therapy for hepatocellular carcinoma: a retrospective review of 162 patients”. In: *Clinical Cancer Research: An Official Journal of the American Association for Cancer Research* 11.10 (May 15, 2005), pp. 3799–3805. ISSN: 1078-0432. DOI: 10.1158/1078-0432.CCR-04-1350.

[Dij+16] Lisanne V. van Dijk, Roel J. H. M. Steenbakkers, Bennie ten Haken, Hans Paul van der Laan, Aart A. van ’t Veld, Johannes A. Langendijk, and Erik W. Korevaar. “Robust Intensity Modulated Proton Therapy (IMPT) Increases Estimated Clinical Benefit in Head and Neck Cancer Patients”. In: *PloS One* 11.3 (2016), e0152477. ISSN: 1932-6203. DOI: 10.1371/journal.pone.0152477.

[Dow+12] Stephen J. Dowdell, Benjamin Clasie, Nicolas Depauw, Peter Metcalfe, Anatoly B. Rosenfeld, Hanne M. Kooy, Jacob B. Flanz, and Harald Paganetti. “Monte Carlo study of the potential reduction in out-of-field dose using a patient-specific aperture in pencil beam scanning proton therapy”. In: *Physics in Medicine and Biology* 57.10 (May 21, 2012), pp. 2829–2842. ISSN: 1361-6560. DOI: 10.1088/0031-9155/57/10/2829.

[DP99] G. M. Duchesne and L. J. Peters. "What is the alpha/beta ratio for prostate cancer? Rationale for hypofractionated high-dose-rate brachytherapy". In: *International Journal of Radiation Oncology, Biology, Physics* 44.4 (July 1, 1999), pp. 747–748. ISSN: 0360-3016.

[EK05] Martijn Engelsman and Hanne M. Kooy. "Target volume dose considerations in proton beam treatment planning for lung tumors". In: *Medical Physics* 32.12 (Dec. 1, 2005), pp. 3549–3557. ISSN: 2473-4209. DOI: 10.1118/1.2126187. URL: https://aapm.onlinelibrary.wiley.com/doi/abs/10.1118/1.2126187 (visited on 08/13/2018).

[ERK06] Martijn Engelsman, Eike Rietzel, and Hanne M. Kooy. "Four-dimensional proton treatment planning for lung tumors". In: *International Journal of Radiation Oncology • Biology • Physics* 64.5 (Apr. 1, 2006), pp. 1589–1595. ISSN: 0360-3016. DOI: 10.1016/j.ijrobp.2005.12.026. URL: https://www.redjournal.org/article/S0360-3016(05)03095-6/fulltext (visited on 08/13/2018).

[Fre+11] Malte C. Frese, Jan J. Wilkens, Peter E. Huber, Alexandra D. Jensen, Uwe Oelfke, and Zahra Taheri-Kadkhoda. "Application of constant vs. variable relative biological effectiveness in treatment planning of intensity-modulated proton therapy". In: *International Journal of Radiation Oncology, Biology, Physics* 79.1 (Jan. 1, 2011), pp. 80–88. ISSN: 1879-355X. DOI: 10.1016/j.ijrobp.2009.10.022.

[Fre12] Albin Fredriksson. "A characterization of robust radiation therapy treatment planning methods-from expected value to worst case optimization". In: *Medical Physics* 39.8 (Aug. 2012), pp. 5169–5181. ISSN: 0094-2405. DOI: 10.1118/1.4737113.

[Fri+13] Thomas Friedrich, Uwe Scholz, Thilo Elsässer, Marco Durante, and Michael Scholz. "Systematic analysis of RBE and related quantities using a database of cell survival experiments with ion beam irradiation". In: *Journal of Radiation Research* 54.3 (May 2013), pp. 494–514. ISSN: 1349-9157. DOI: 10.1093/jrr/rrs114.

[FS04] Matthias Fippel and Martin Soukup. "A Monte Carlo dose calculation algorithm for proton therapy". In: *Medical Physics* 31.8 (Aug. 1, 2004), pp. 2263–2273. ISSN: 0094-2405. DOI: 10.1118/1.1769631. URL: http://scitation.aip.org.ezp-prod1.hul.harvard.edu/content/aapm/journal/medphys/31/8/10.1118/1.1769631 (visited on 04/19/2016).

[Fuk+09] Nobuyoshi Fukumitsu et al. "A prospective study of hypofractionated proton beam therapy for patients with hepatocellular carcinoma". In: *International Journal of Radiation Oncology, Biology, Physics* 74.3 (July 1, 2009), pp. 831–836. ISSN: 1879-355X. DOI: 10.1016/j.ijrobp.2008.10.073.

[GDB12] Christian Graeff, Marco Durante, and Christoph Bert. "Motion mitigation in intensity modulated particle therapy by internal target volumes covering range changes". In: *Medical Physics* 39.10 (Oct. 1, 2012), pp. 6004–6013. ISSN: 2473-4209. DOI: 10.1118/1.4749964. URL: https://aapm.onlinelibrary.wiley.com/doi/abs/10.1118/1.4749964 (visited on 08/13/2018).

[Gia+13] Drosoula Giantsoudi, Clemens Grassberger, David Craft, Andrzej Niemierko, Alexei Trofimov, and Harald Paganetti. "Linear Energy Transfer-Guided Optimization in Intensity Modulated Proton Therapy: Feasibility Study and Clinical Potential". In: *International Journal of Radiation Oncology*Biology*Physics* 87.1 (Sept. 1, 2013), pp. 216–222. ISSN: 0360-3016. DOI: 10.1016/j.ijrobp.2013.05.013. URL: http://www.sciencedirect.com/science/article/pii/S0360301613005452 (visited on 08/13/2018).

[Gia+15] Drosoula Giantsoudi, Jan Schuemann, Xun Jia, Stephen Dowdell, Steve Jiang, and Harald Paganetti. "Validation of a GPU-based Monte Carlo code (gPMC) for proton radiation therapy: clinical cases study". In: *Physics in Medicine & Biology* 60.6 (2015), p. 2257. ISSN: 0031-9155. DOI: 10.1088/0031-9155/60/6/2257. URL: http://stacks.iop.org/0031-9155/60/i=6/a=2257 (visited on 08/13/2018).

[Gia+17] D. Giantsoudi, J. Unkelbach, P. Botas, C. Grassberger, and H. Paganetti. "Can Robust Optimization for Range Uncertainty in Proton Therapy Act as a Surrogate for Biological Optimization?" In: *International Journal of Radiation Oncology • Biology • Physics* 99.2 (Oct. 1, 2017), S106–S107. ISSN: 0360-3016. DOI: 10.1016/j.ijrobp.2017.06.253. URL: https://www.redjournal.org/article/S0360-3016(17)31303-2/fulltext (visited on 09/06/2018).

[Gia+18] Drosoula Giantsoudi, Judith Adams, Shannon MacDonald, and Harald Paganetti. "Can differences in linear energy transfer and thus relative biological effectiveness compromise the dosimetric advantage of intensity-modulated proton therapy as compared to passively scattered proton therapy?" In: *Acta Oncologica* 0.0 (May 4, 2018), pp. 1–6. ISSN: 0284-186X. DOI: 10.1080/0284186X.2018.1468090. URL: https://doi.org/10.1080/0284186X.2018.1468090 (visited on 08/20/2018).

[GLP15] C. Grassberger, Anthony Lomax, and H. Paganetti. "Characterizing a proton beam scanning system for Monte Carlo dose calculation in patients". In: *Physics in Medicine & Biology* 60.2 (2015), p. 633. ISSN: 0031-9155. DOI: 10.1088/0031-9155/60/2/633. URL: http://stacks.iop.org/0031-9155/60/i=2/a=633 (visited on 08/20/2018).

[Got+93] B. Gottschalk, A. M. Koehler, R. J. Schneider, J. M. Sisterson, and M. S. Wagner. "Multiple Coulomb scattering of 160 MeV protons". In: *Nuclear Instruments and Methods in Physics Research Section B: Beam Interactions with Materials and Atoms* 74.4 (June 1, 1993), pp. 467–490. ISSN: 0168-583X. DOI: 10.1016/0168-583X(93)95944-Z. URL: http://www.sciencedirect.com/science/article/pii/0168583X9395944Z (visited on 07/15/2018).

[Got10] Bernard Gottschalk. "On the scattering power of radiotherapy protons". In: *Medical Physics* 37.1 (Jan. 2010), pp. 352–367. ISSN: 0094-2405. DOI: 10.1118/1.3264177.

[GP11] C. Grassberger and H. Paganetti. "Elevated LET components in clinical proton beams". In: *Physics in Medicine and Biology* 56.20 (Oct. 21, 2011), p. 6677. ISSN: 0031-9155. DOI: 10.1088/0031-9155/56/20/011. URL: http://iopscience.iop.org/0031-9155/56/20/011 (visited on 04/15/2015).

[Gra+14] Clemens Grassberger, Juliane Daartz, Stephen Dowdell, Thomas Ruggieri, Greg Sharp, and Harald Paganetti. "Quantification of Proton Dose Calculation Accuracy in the Lung". In: *International Journal of Radiation Oncology • Biology • Physics* 89.2 (June 1, 2014), pp. 424–430. ISSN: 0360-3016. DOI: 10.1016/j.ijrobp.2014.02.023. URL: https://www.redjournal.org/article/S0360-3016(14)00208-9/fulltext (visited on 08/13/2018).

[Gra+15] Clemens Grassberger, Stephen Dowdell, Greg Sharp, and Harald Paganetti. "Motion mitigation for lung cancer patients treated with active scanning proton therapy". In: *Medical Physics* 42.5 (May 1, 2015), pp. 2462–2469. ISSN: 2473-4209. DOI: 10.1118/1.4916662. URL: https://aapm.onlinelibrary.wiley.com/doi/abs/10.1118/1.4916662 (visited on 08/13/2018).

[Gra17] Christian Graeff. "Robustness of 4D-optimized scanned carbon ion beam therapy against interfractional changes in lung cancer". In: *Radiotherapy and Oncology* 122.3 (Mar. 1, 2017), pp. 387–392. ISSN: 0167-8140, 1879-0887. DOI: 10.1016/j.radonc.2016.12.017. URL: https://www.thegreenjournal.com/article/S0167-8140(16)34458-9/fulltext (visited on 08/13/2018).

[Gru+94] E. Grusell, A. Montelius, A. Brahme, G. Rikner, and K. Russell. "A general solution to charged particle beam flattening using an optimized dual-scattering-foil technique, with application to proton therapy beams". In: *Physics in Medicine and Biology* 39.12 (Dec. 1994), pp. 2201–2216. ISSN: 0031-9155.

[GS15] Dal A. Granville and Gabriel O. Sawakuchi. "Comparison of linear energy transfer scoring techniques in Monte Carlo simulations of proton beams". In: *Physics in Medicine and Biology* 60.14 (July 21, 2015), N283–291. ISSN: 1361-6560. DOI: 10.1088/0031-9155/60/14/N283.

[Gua+15] Fada Guan et al. "Analysis of the track- and dose-averaged LET and LET spectra in proton therapy using the geant4 Monte Carlo code". In: *Medical Physics* 42.11 (Nov. 2015), pp. 6234–6247. ISSN: 2473-4209. DOI: 10.1118/1.4932217.

[Hat+07] Masaharu Hata et al. "Hypofractionated high-dose proton beam therapy for stage I non-small-cell lung cancer: preliminary results of a phase I/II clinical study". In: *International Journal of Radiation Oncology, Biology, Physics* 68.3 (July 1, 2007), pp. 786–793. ISSN: 0360-3016. DOI: 10.1016/j.ijrobp.2006.12.063.

[Hig75] Virgil L. Highland. "Some practical remarks on multiple scattering". In: *Nuclear Instruments and Methods* 129.2 (Nov. 15, 1975), pp. 497–499. ISSN: 0029-554X. DOI: 10.1016/0029-554X(75)90743-0. URL: http://www.sciencedirect.com/science/article/pii/0029554X75907430 (visited on 09/26/2018).

[Hir+18] Shusuke Hirayama et al. "An analytical dose-averaged LET calculation algorithm considering the off-axis LET enhancement by secondary protons for spot-scanning proton therapy". In: *Medical Physics* 45.7 (July 1, 2018), pp. 3404–3416. ISSN: 2473-4209. DOI: 10.1002/mp.12991. URL: https://aapm.onlinelibrary.wiley.com/doi/abs/10.1002/mp.12991 (visited on 09/05/2018).

[HMS47] B. Honigmann, K. Molière, and I. N. Stranski. "Über den Gültigkeitsbereich der Thomson-Gibbs'schen Gleichung". In: *Annalen der Physik* 436.4 (1947), pp. 181–189. ISSN: 1521-3889. DOI: 10.1002/andp.19474360406. URL: https://onlinelibrary.wiley.com/doi/abs/10.1002/andp.19474360406 (visited on 07/19/2018).

[Hue+18] Fernando Hueso-González, Moritz Rabe, Thomas A. Ruggieri, Thomas Bortfeld, and Joost M. Verburg. "A full-scale clinical prototype for proton range verification using prompt gamma-ray spectroscopy". In: *Physics in Medicine and Biology* 63.18 (Sept. 17, 2018), p. 185019. ISSN: 1361-6560. DOI: 10.1088/1361-6560/aad513.

[Ino+14] Hiroshi K Inoue et al. "Optimal hypofractionated conformal radiotherapy for large brain metastases in patients with high risk factors: a single-institutional prospective study". In: *Radiation Oncology (London, England)* 9 (Oct. 17, 2014). ISSN: 1748-717X. DOI: 10.1186/s13014-014-0231-5. URL: https://www.ncbi.nlm.nih.gov/pmc/articles/PMC4203932/ (visited on 09/24/2018).

[Jag+17] Thyrza Jagt, Sebastiaan Breedveld, Steven van de Water, Ben Heijmen, and Mischa Hoogeman. "Near real-time automated dose restoration in IMPT to compensate for daily tissue density variations in prostate cancer". In: *Physics in Medicine & Biology* 62.11 (2017), p. 4254. ISSN: 0031-9155. DOI: 10.1088/1361-6560/aa5c12. URL: http://stacks.iop.org/0031-9155/62/i=11/a=4254 (visited on 08/08/2018).

[Jag+18] Thyrza Jagt, Sebastiaan Breedveld, Rens van Haveren, Ben Heijmen, and Mischa Hoogeman. "An automated planning strategy for near real-time adaptive proton therapy in prostate cancer". In: *Physics in Medicine & Biology* 63.13 (2018), p. 135017. ISSN: 0031-9155. DOI: 10.1088/1361-6560/aacaa7. URL: http://stacks.iop.org/0031-9155/63/i=13/a=135017 (visited on 07/12/2018).

[Jan82] Joseph F. Janni. "Energy loss, range, path length, time-of-flight, straggling, multiple scattering, and nuclear interaction probability: In two parts. Part 1. For 63 compounds Part 2. For elements 1 <= Z <= 92". In: *Atomic Data and Nuclear Data Tables* 27.2 (Mar. 1, 1982), pp. 147–339. ISSN: 0092-640X. DOI: 10.1016/0092-640X(82)90004-3. URL: http://www.sciencedirect.com/science/article/pii/0092640X82900043 (visited on 07/19/2018).

[Jia+12] Xun Jia, Jan Schümann, Harald Paganetti, and Steve B. Jiang. "GPU-based fast Monte Carlo dose calculation for proton therapy". In: *Physics in Medicine & Biology* 57.23 (2012), p. 7783. ISSN: 0031-9155. DOI: 10.1088/0031-9155/57/23/7783. URL: http://stacks.iop.org/0031-9155/57/i=23/a=7783 (visited on 08/22/2018).

[Kan+07] Yixiu Kang et al. "4D Proton treatment planning strategy for mobile lung tumors". In: *International Journal of Radiation Oncology • Biology • Physics* 67.3 (Mar. 1, 2007), pp. 906–914. ISSN: 0360-3016. DOI: 10.1016/j.ijrobp.2006.10.045. URL: https://www.redjournal.org/article/S0360-3016(06)03385-2/fulltext (visited on 08/13/2018).

[Kar+14] Kumiko Karasawa et al. "Comparison of hypofractionated and conventionally fractionated whole-breast irradiation for early breast cancer patients: a single-institute study of 1,098 patients". In: *Breast Cancer (Tokyo, Japan)* 21.4 (July 2014), pp. 402–408. ISSN: 1880-4233. DOI: 10.1007/s12282-012-0406-6.

[Kim+18] Tae Wan Kim et al. "Clinical Outcomes of Proton Beam Therapy for Choroidal Melanoma at a Single Institute in Korea". In: *Cancer Research and Treatment : Official Journal of Korean Cancer Association* 50.2 (Apr. 2018), pp. 335–344. ISSN: 1598-2998. DOI: 10.4143/crt.2017.070. URL: https://www.ncbi.nlm.nih.gov/pmc/articles/PMC5912133/ (visited on 09/19/2018).

[Kno+13] Antje-Christin Knopf, Dirk Boye, Antony Lomax, and Shininchiro Mori. "Adequate margin definition for scanned particle therapy in the incidence of intrafractional motion". In: *Physics in Medicine and Biology* 58.17 (2013), p. 6079. ISSN: 0031-9155. DOI: 10.1088/0031-9155/58/17/6079. URL: http://stacks.iop.org/0031-9155/58/i=17/a=6079 (visited on 04/03/2017).

[Kom+11] Shohei Komatsu et al. "Clinical results and risk factors of proton and carbon ion therapy for hepatocellular carcinoma". In: *Cancer* 117.21 (Nov. 1, 2011), pp. 4890–4904. ISSN: 1097-0142. DOI: 10.1002/cncr.26134.

[Koo+10] Hanne M. Kooy et al. "A Case Study in Proton Pencil-Beam Scanning Delivery". In: *International Journal of Radiation Oncology*Biology*Physics* 76.2 (Feb. 1, 2010), pp. 624–630. ISSN: 0360-3016. DOI: 10.1016/j.ijrobp.2009.06.065. URL: http://www.sciencedirect.com/science/article/pii/S0360301609010116 (visited on 08/20/2018).

[KSS77] A. M. Koehler, R. J. Schneider, and J. M. Sisterson. "Flattening of proton dose distributions for large-field radiotherapy". In: *Medical Physics* 4.4 (July 1, 1977), pp. 297–301. ISSN: 2473-4209. DOI: 10.1118/1.594317. URL: https://aapm.onlinelibrary.wiley.com/doi/abs/10.1118/1.594317 (visited on 08/07/2018).

[Kur+16] Christopher Kurz, Reinoud Nijhuis, Michael Reiner, Ute Ganswindt, Christian Thieke, Claus Belka, Katia Parodi, and Guillaume Landry. "Feasibility of automated proton therapy plan adaptation for head and neck tumors using cone beam CT images". In: *Radiation Oncology (London, England)* 11 (Apr. 30, 2016). ISSN: 1748-717X. DOI: 10.1186/s13014-016-0641-7. URL: https://www.ncbi.nlm.nih.gov/pmc/articles/PMC4851791/ (visited on 03/30/2018).

[Lai+16] Aaron Michael Laine, Arnold Pompos, Robert Timmerman, Steve Jiang, Michael D. Story, David Pistenmaa, and Hak Choy. "The Role of Hypofractionated Radiation Therapy with Photons, Protons, and Heavy Ions for Treating Extracranial Lesions". In: *Frontiers in Oncology* 5 (Jan. 11, 2016). ISSN: 2234-943X. DOI: 10.3389/fonc.2015.00302. URL: https://www.ncbi.nlm.nih.gov/pmc/articles/PMC4707221/ (visited on 09/24/2018).

[Lee+18] H Lee, YL Chen, J Pursley, Hsiao-Ming Lu, and Kyung-Wook Jee. "Investigation of ECG-Gated Non-Invasive Cardiac Arrhythmia Ablation using Double Scattering Proton beams". In: AAPM. Nashville, Aug. 2018.

[Li+14] Haisen S. Li, Hualiang Zhong, Jinkoo Kim, Carri Glide-Hurst, Misbah Gulam, Teamour S. Nurushev, and Indrin J. Chetty. "Direct dose mapping versus energy/mass transfer mapping for 4D dose accumulation: fundamental differences and dosimetric consequences". In: *Physics in Medicine and Biology* 59.1 (Jan. 6, 2014), pp. 173–188. ISSN: 1361-6560. DOI: 10.1088/0031-9155/59/1/173.

[Lie+14] Jakob Liebl, Harald Paganetti, Mingyao Zhu, and Brian A. Winey. "The influence of patient positioning uncertainties in proton radiotherapy on proton range and dose distributions". In: *Medical Physics* 41.9 (Sept. 1, 2014), p. 091711. ISSN: 2473-4209. DOI: 10.1118/1.4892601. URL: https://aapm.onlinelibrary.wiley.com/doi/abs/10.1118/1.4892601 (visited on 09/10/2018).

[Lom+01] A. J. Lomax et al. "Intensity modulated proton therapy: a clinical example". In: *Medical Physics* 28.3 (Mar. 2001), pp. 317–324. ISSN: 0094-2405. DOI: 10.1118/1.1350587.

[Ma+14] Jiasen Ma, Chris Beltran, Hok Seum Wan Chan Tseung, and Michael G. Herman. "A GPU-accelerated and Monte Carlo-based intensity modulated proton therapy optimization system". In: *Medical Physics* 41.12 (Dec. 1, 2014), p. 121707. ISSN: 2473-4209. DOI: 10.1118/1.4901522. URL: https://aapm.onlinelibrary.wiley.com/doi/abs/10.1118/1.4901522 (visited on 08/22/2018).

[Mar+16] F. Marsolat, L. De Marzi, F. Pouzoulet, and A. Mazal. "Analytical linear energy transfer model including secondary particles: calculations along the central axis of the proton pencil beam". In: *Physics in Medicine & Biology* 61.2 (2016), p. 740. ISSN: 0031-9155. DOI: 10.1088/0031-9155/61/2/740. URL: http://stacks.iop.org/0031-9155/61/i=2/a=740 (visited on 09/05/2018).

[Moi+16a] Alexandra Moignier et al. "Theoretical Benefits of Dynamic Collimation in Pencil Beam Scanning Proton Therapy for Brain Tumors: Dosimetric and Radiobiological Metrics". In: *International Journal of Radiation Oncology, Biology, Physics* 95.1 (May 1, 2016), pp. 171–180. ISSN: 1879-355X. DOI: 10.1016/j.ijrobp.2015.08.030.

[Moi+16b] Alexandra Moignier et al. "Toward improved target conformity for two spot scanning proton therapy delivery systems using dynamic collimation". In: *Medical Physics* 43.3 (Mar. 2016), pp. 1421–1427. ISSN: 2473-4209. DOI: 10.1118/1.4942375.

[Mor+17] Shunsuke Moriya, Hidenobu Tachibana, Kenji Hotta, Naoki Nakamura, Takeji Sakae, and Tetsuo Akimoto. "Feasibility of dynamic adaptive passive scattering proton therapy with computed tomography image guidance in the lung". In: *Medical Physics* 44.9 (Sept. 2017), pp. 4474–4481. ISSN: 2473-4209. DOI: 10.1002/mp.12444.

[Mot+16] Maryam Moteabbed, Torunn I. Yock, Nicolas Depauw, Thomas M. Madden, Hanne M. Kooy, and Harald Paganetti. "Impact of Spot Size and Beam-Shaping Devices on the Treatment Plan Quality for Pencil Beam Scanning Proton Therapy". In: *International Journal of Radiation Oncology, Biology, Physics* 95.1 (May 1, 2016), pp. 190–198. ISSN: 1879-355X. DOI: 10.1016/j.ijrobp.2015.12.368.

[MSP15] Aimee L. McNamara, Jan Schuemann, and Harald Paganetti. "A phenomenological relative biological effectiveness (RBE) model for proton therapy based on all published in vitro cell survival data". In: *Physics in medicine and biology* 60.21 (Nov. 7, 2015), pp. 8399–8416. ISSN: 0031-9155. DOI: 10.1088/0031-9155/60/21/8399. URL: https://www.ncbi.nlm.nih.gov/pmc/articles/PMC4634882/ (visited on 08/13/2018).

[MWU14] Stefan Milz, Jan J. Wilkens, and Wolfgang Ullrich. “A dose error evaluation study for 4D dose calculations”. In: *Physics in Medicine and Biology* 59.21 (Nov. 7, 2014), pp. 6401–6415. ISSN: 1361-6560. DOI: 10.1088/0022-3727/59/21/6401.

[Nic+08] John Nickolls, Ian Buck, Michael Garland, and Kevin Skadron. “Scalable Parallel Programming with CUDA”. In: *Queue* 6.2 (Mar. 2008), pp. 40–53. ISSN: 1542-7730. DOI: 10.1145/1365490.1365500. URL: http://doi.acm.org/10.1145/1365490.1365500 (visited on 08/28/2018).

[Nih+06] Keiji Nihei, Takashi Ogino, Satoshi Ishikura, and Hideki Nishimura. “High-dose proton beam therapy for Stage I non-small-cell lung cancer”. In: *International Journal of Radiation Oncology, Biology, Physics* 65.1 (May 1, 2006), pp. 107–111. ISSN: 0360-3016. DOI: 10.1016/j.ijrobp.2005.10.031.

[NZ15] Wayne D Newhauser and Rui Zhang. “The physics of proton therapy”. In: *Physics in medicine and biology* 60.8 (Apr. 21, 2015), R155–R209. ISSN: 0031-9155. DOI: 10.1088/0031-9155/60/8/R155. URL: https://www.ncbi.nlm.nih.gov/pmc/articles/PMC4407514/ (visited on 07/19/2018).

[Pag02] H. Paganetti. “Nuclear interactions in proton therapy: dose and relative biological effect distributions originating from primary and secondary particles”. In: *Physics in Medicine & Biology* 47.5 (2002), p. 747. ISSN: 0031-9155. DOI: 10.1088/0031-9155/47/5/305. URL: http://stacks.iop.org/0031-9155/47/i=5/a=305 (visited on 07/17/2018).

[Pag12] Harald Paganetti. “Range uncertainties in proton therapy and the role of Monte Carlo simulations”. In: *Physics in Medicine and Biology* 57.11 (June 7, 2012), R99–R117. ISSN: 0031-9155. DOI: 10.1088/0031-9155/57/11/R99. URL: https://www.ncbi.nlm.nih.gov/pmc/articles/PMC3374500/ (visited on 06/28/2018).

[Pag14] Harald Paganetti. “Relative biological effectiveness (RBE) values for proton beam therapy. Variations as a function of biological endpoint, dose, and linear energy transfer”. In: *Physics in Medicine and Biology* 59.22 (Nov. 21, 2014), R419–472. ISSN: 1361-6560. DOI: 10.1088/0031-9155/59/22/R419.

[Pat+18] Annalisa Patriarca et al. “Experimental set-up for FLASH proton irradiation of small animals using a clinical system”. In: *International Journal of Radiation Oncology, Biology, Physics* (July 11, 2018). ISSN: 1879-355X. DOI: 10.1016/j.ijrobp.2018.06.403.

[Per+12] J. Perl, J. Shin, J. Schümann, B. Faddegon, and H. Paganetti. “TOPAS: An innovative proton Monte Carlo platform for research and clinical applications”. In: *Medical Physics* 39.11 (Nov. 1, 2012), pp. 6818–6837. ISSN: 2473-4209. DOI: 10.1118/1.4758060. URL: https://aapm.onlinelibrary.wiley.com/doi/abs/10.1118/1.4758060 (visited on 08/22/2018).

[Pfl+08] Daniel Pflugfelder, Jan J. Wilkens, Simeon Nill, and Uwe Oelfke. “A comparison of three optimization algorithms for intensity modulated radiation therapy”. In: *Zeitschrift Fur Medizinische Physik* 18.2 (2008), pp. 111–119. ISSN: 0939-3889.

[Phi+92] M. H. Phillips, E. Pedroni, H. Blattmann, T. Boehringer, A. Coray, and S. Scheib. "Effects of respiratory motion on dose uniformity with a charged particle scanning method". In: *Physics in Medicine & Biology* 37.1 (1992), p. 223. ISSN: 0031-9155. DOI: 10.1088/0031-9155/37/1/016. URL: http://stacks.iop.org/0031-9155/37/i=1/a=016 (visited on 09/02/2018).

[PK10] Harald Paganetti and Hanne Kooy. "Proton radiation in the management of localized cancer". In: *Expert Review of Medical Devices* 7.2 (Mar. 1, 2010), pp. 275–285. ISSN: 1743-4440. DOI: 10.1586/erd.10.2. URL: https://doi.org/10.1586/erd.10.2 (visited on 09/12/2018).

[Pla+17] Lorenzo Placidi, Alessandra Bolsi, Antony J. Lomax, Ralf A. Schneider, Robert Malyapa, Damien C. Weber, and Francesca Albertini. "Effect of Anatomic Changes on Pencil Beam Scanned Proton Dose Distributions for Cranial and Extracranial Tumors". In: *International Journal of Radiation Oncology*Biology*Physics* 97.3 (Mar. 1, 2017), pp. 616–623. ISSN: 0360-3016. DOI: 10.1016/j.ijrobp.2016.11.013. URL: http://www.sciencedirect.com/science/article/pii/S0360301616334368 (visited on 08/17/2018).

[PWO08] D. Pflugfelder, J. J. Wilkens, and U. Oelfke. "Worst case optimization: a method to account for uncertainties in the optimization of intensity modulated proton therapy". In: *Physics in Medicine and Biology* 53.6 (Mar. 21, 2008), pp. 1689–1700. ISSN: 0031-9155. DOI: 10.1088/0031-9155/53/6/013.

[Qin+16] Nan Qin, Pablo Botas, Drosoula Giantsoudi, Jan Schuemann, Zhen Tian, Steve B. Jiang, Harald Paganetti, and Xun Jia. "Recent developments and comprehensive evaluations of a GPU-based Monte Carlo package for proton therapy". In: *Physics in Medicine & Biology* 61.20 (2016), p. 7347. ISSN: 0031-9155. DOI: 10.1088/0031-9155/61/20/7347. URL: http://stacks.iop.org/0031-9155/61/i=20/a=7347 (visited on 08/20/2018).

[RG41] Bruno Rossi and Kenneth Greisen. "Cosmic-Ray Theory". In: *Reviews of Modern Physics* 13.4 (Oct. 1, 1941), pp. 240–309. DOI: 10.1103/RevModPhys.13.240. URL: https://link.aps.org/doi/10.1103/RevModPhys.13.240 (visited on 09/26/2018).

[RSK15] K.J. Ray, N.R. Sibson, and A.E. Kiltie. "Treatment of Breast and Prostate Cancer by Hypofractionated Radiotherapy: Potential Risks and Benefits". In: *Clinical Oncology (Royal College of Radiologists (Great Britain)* 27.7 (July 2015), pp. 420–426. ISSN: 0936-6555. DOI: 10.1016/j.clon.2015.02.008. URL: https://www.ncbi.nlm.nih.gov/pmc/articles/PMC4465964/ (visited on 09/24/2018).

[San+16] D. Sanchez-Parcerisa, M. A. Cortés-Giraldo, D. Dolney, M. Kondrla, M. Fager, and A. Carabe. "Analytical calculation of proton linear energy transfer in voxelized geometries including secondary protons". In: *Physics in Medicine & Biology* 61.4 (2016), p. 1705. ISSN: 0031-9155. DOI: 10.1088/0031-9155/61/4/1705. URL: http://stacks.iop.org/0031-9155/61/i=4/a=1705 (visited on 09/05/2018).

[Saw+08] Gabriel O. Sawakuchi, Uwe Titt, Dragan Mirkovic, and Radhe Mohan. "Density heterogeneities and the influence of multiple Coulomb and nuclear scatterings on the Bragg peak distal edge of proton therapy beams". In: *Physics in Medicine and Biology* 53.17 (Sept. 7, 2008), pp. 4605–4619. ISSN: 0031-9155. DOI: 10.1088/0031-9155/53/17/010.

[SB64] S.M. Seltzer and M.J. Berger. "Energy loss straggling of protons and mesons". In: *Studies in Penetration of Charged Particles in Matter*. Nuclear Science Series 39. Washington DC: National Academy of Science, 1964. DOI: 10.17226/20066. URL: https://www.nap.edu/read/20066/chapter/10 (visited on 09/25/2018).

[Sch+15] Jan Schuemann, Drosoula Giantsoudi, Clemens Grassberger, Maryam Moteabbed, Chul Hee Min, and Harald Paganetti. "Assessing the Clinical Impact of Approximations in Analytical Dose Calculations for Proton Therapy". In: *International Journal of Radiation Oncology • Biology • Physics* 92.5 (Aug. 1, 2015), pp. 1157–1164. ISSN: 0360-3016. DOI: 10.1016/j.ijrobp.2015.04.006. URL: https://www.redjournal.org/article/S0360-3016(15)00379-X/fulltext (visited on 08/22/2018).

[Sch+17] A. Schiavi et al. "Fred: a GPU-accelerated fast-Monte Carlo code for rapid treatment plan recalculation in ion beam therapy". In: *Physics in Medicine & Biology* 62.18 (2017), p. 7482. ISSN: 0031-9155. DOI: 10.1088/1361-6560/aa8134. URL: http://stacks.iop.org/0031-9155/62/i=18/a=7482 (visited on 08/31/2018).

[Sec+08] Joao Seco, Greg C. Sharp, Ziji Wu, David Gierga, Florian Buettner, and Harald Paganetti. "Dosimetric impact of motion in free-breathing and gated lung radiotherapy: a 4D Monte Carlo study of intrafraction and interfraction effects". In: *Medical Physics* 35.1 (Jan. 2008), pp. 356–366. ISSN: 0094-2405. DOI: 10.1118/1.2821704.

[SGS10] John E. Stone, David Gohara, and Guochun Shi. "OpenCL: A Parallel Programming Standard for Heterogeneous Computing Systems". In: *Computing in Science & Engineering* 12.3 (May 1, 2010), pp. 66–73. ISSN: 1521-9615. DOI: 10.1109/MCSE.2010.69. URL: https://aip.scitation.org/doi/10.1109/MCSE.2010.69 (visited on 08/28/2018).

[Sha+12] James A. Shackleford, Qi Yang, Ana M. Lourenço, Nadya Shusharina, Nagarajan Kandasamy, and Gregory C. Sharp. "Analytic regularization of uniform cubic B-spline deformation fields". In: *Medical image computing and computer-assisted intervention: MICCAI ... International Conference on Medical Image Computing and Computer-Assisted Intervention* 15 (Pt 2 2012), pp. 122–129.

[Sha+14] Gregory Sharp, Karl D. Fritscher, Vladimir Pekar, Marta Peroni, Nadya Shusharina, Harini Veeraraghavan, and Jinzhong Yang. "Vision 20/20: Perspectives on automated image segmentation for radiotherapy". In: *Medical Physics* 41.5 (May 1, 2014), p. 050902. ISSN: 2473-4209. DOI: 10.1118/1.4871620. URL: https://aapm.onlinelibrary.wiley.com/doi/abs/10.1118/1.4871620 (visited on 08/31/2018).

[Sha12] James A. Shackleford. "Plastimatch 1.6 - Current Capabilities and Future Directions". In: *INt Cong Med Image Comput Comput Assist Interv*. INt Cong Med Image Comput Comput Assist Interv. Vol. 15. Int Conf Med Image Comput Comput Assist Interv. MICCAI 2012, Oct. 15, 2012. URL: http://igtpg.spl.harvard.edu/publications/item/view/2371 (visited on 04/04/2017).

[Shi+95] W. U. Shipley et al. "Advanced prostate cancer: the results of a randomized comparative trial of high dose irradiation boosting with conformal protons compared with conventional dose irradiation using photons alone". In: *International Journal of Radiation Oncology, Biology, Physics* 32.1 (Apr. 30, 1995), pp. 3–12. ISSN: 0360-3016. DOI: 10.1016/0360-3016(95)00063-5.

[SKS10] J. A. Shackleford, N. Kandasamy, and G. C. Sharp. "On developing B-spline registration algorithms for multi-core processors". In: *Physics in Medicine and Biology* 55.21 (2010), p. 6329. ISSN: 0031-9155. DOI: 10.1088/0031-9155/55/21/001. URL: http://stacks.iop.org/0031-9155/55/i=21/a=001 (visited on 04/04/2017).

[Sla+04] Jerry D. Slater et al. "Proton therapy for prostate cancer: the initial Loma Linda University experience". In: *International Journal of Radiation Oncology, Biology, Physics* 59.2 (June 1, 2004), pp. 348–352. ISSN: 0360-3016. DOI: 10.1016/j.ijrobp.2003.10.011.

[Smi+11] Benjamin D. Smith et al. "Fractionation for whole breast irradiation: an American Society for Radiation Oncology (ASTRO) evidence-based guideline". In: *International Journal of Radiation Oncology, Biology, Physics* 81.1 (Sept. 1, 2011), pp. 59–68. ISSN: 1879-355X. DOI: 10.1016/j.ijrobp.2010.04.042.

[SS04] V. A. Semenenko and R. D. Stewart. "A fast Monte Carlo algorithm to simulate the spectrum of DNA damages formed by ionizing radiation". In: *Radiation Research* 161.4 (Apr. 2004), pp. 451–457. ISSN: 0033-7587.

[SS06] V. A. Semenenko and R. D. Stewart. "Fast Monte Carlo simulation of DNA damage formed by electrons and light ions". In: *Physics in Medicine and Biology* 51.7 (Apr. 7, 2006), pp. 1693–1706. ISSN: 0031-9155. DOI: 10.1088/0031-9155/51/7/004.

[Ste+11] Robert D. Stewart, Victor K. Yu, Alexandros G. Georgakilas, Constantinos Koumenis, Joo Han Park, and David J. Carlson. "Effects of radiation quality and oxygen on clustered DNA lesions and cell death". In: *Radiation Research* 176.5 (Nov. 2011), pp. 587–602. ISSN: 1938-5404.

[Ste+15] Robert D. Stewart, Seth W. Streitmatter, David C. Argento, Charles Kirkby, John T. Goorley, Greg Moffitt, Tatjana Jevremovic, and George A. Sandison. "Rapid MCNP simulation of DNA double strand break (DSB) relative biological effectiveness (RBE) for photons, neutrons, and light ions". In: *Physics in Medicine and Biology* 60.21 (Nov. 7, 2015), pp. 8249–8274. ISSN: 1361-6560. DOI: 10.1088/0031-9155/60/21/8249.

[SZ08] Jeffrey V. Siebers and Hualiang Zhong. "An energy transfer method for 4D Monte Carlo dose calculation". In: *Medical Physics* 35.9 (Sept. 2008), pp. 4096–4105. ISSN: 0094-2405. DOI: 10.1118/1.2968215.

[Tak02] Yoshihisa Takada. "Optimum solution of dual-ring double-scattering system for an incident beam with given phase space for proton beam spreading". In: *Nuclear Instruments and Methods in Physics Research Section A: Accelerators, Spectrometers, Detectors and Associated Equipment* 485.3 (June 11, 2002), pp. 255–276. ISSN: 0168-9002. DOI: 10.1016/S0168-9002(01)02137-4. URL: http://www.sciencedirect.com/science/article/pii/S0168900201021374 (visited on 08/07/2018).

[Tak94] Yoshihisa Takada. "Dual-Ring Double Scattering Method for Proton Beam Spreading". In: *Japanese Journal of Applied Physics* 33.1 (Jan. 1994), p. 353. ISSN: 1347-4065. DOI: 10.1143/JJAP.33.353. URL: http://iopscience.iop.org/article/10.1143/JJAP.33.353/meta (visited on 08/07/2018).

[TB03] Alexei Trofimov and Thomas Bortfeld. "Optimization of beam parameters and treatment planning for intensity modulated proton therapy". In: *Technology in Cancer Research & Treatment* 2.5 (Oct. 2003), pp. 437–444. ISSN: 1533-0346. DOI: 10.1177/153303460300200508.

[Tes+13] M. Testa, J. Schümann, H.-M. Lu, J. Shin, B. Faddegon, J. Perl, and H. Paganetti. "Experimental validation of the TOPAS Monte Carlo system for passive scattering proton therapy". In: *Medical Physics* 40.12 (Dec. 1, 2013), p. 121719. ISSN: 2473-4209. DOI: 10.1118/1.4828781. URL: https://aapm.onlinelibrary.wiley.com/doi/abs/10.1118/1.4828781 (visited on 08/22/2018).

[TMB15] H. Wan Chan Tseung, J. Ma, and C. Beltran. "A fast GPU-based Monte Carlo simulation of proton transport with detailed modeling of nonelastic interactions". In: *Medical Physics* 42.6 (June 1, 2015), pp. 2967–2978. ISSN: 0094-2405. DOI: 10.1118/1.4921046. URL: http://scitation.aip.org.ezp-prod1.hul.harvard.edu/content/aapm/journal/medphys/42/6/10.1118/1.4921046 (visited on 03/23/2016).

[Tro+05] Alexei Trofimov, Eike Rietzel, Hsiao-Ming Lu, Benjamin Martin, Steve Jiang, George T. Y. Chen, and Thomas Bortfeld. "Temporo-spatial IMRT optimization: concepts, implementation and initial results". In: *Physics in Medicine and Biology* 50.12 (2005), p. 2779. ISSN: 0031-9155. DOI: 10.1088/0031-9155/50/12/004. URL: http://stacks.iop.org/0031-9155/50/i=12/a=004 (visited on 04/03/2017).

[UCB07] Jan Unkelbach, Timothy C. Y. Chan, and Thomas Bortfeld. "Accounting for range uncertainties in the optimization of intensity modulated proton therapy". In: *Physics in Medicine and Biology* 52.10 (May 21, 2007), pp. 2755–2773. ISSN: 0031-9155. DOI: 10.1088/0031-9155/52/10/009.

[UP18] Jan Unkelbach and Harald Paganetti. "Robust Proton Treatment Planning: Physical and Biological Optimization". In: *Seminars in Radiation Oncology*. Proton Radiation Therapy 28.2 (Apr. 1, 2018), pp. 88–96. ISSN: 1053-4296. DOI: 10.1016/j.semradonc.2017.11.005. URL: http://www.sciencedirect.com/science/article/pii/S1053429617301078 (visited on 09/05/2018).

[Ver+16] Joost Mathijs Verburg, Clemens Grassberger, Stephen Dowdell, Jan Schuemann, Joao Seco, and Harald Paganetti. "Automated Monte Carlo Simulation of Proton Therapy Treatment Plans". In: *Technology in Cancer Research & Treatment* 15.6 (2016), NP35–NP46. ISSN: 1533-0338. DOI: 10.1177/1533034615614139.

[Ver+17] Joost Verburg, Thomas Ruggieri, Pablo Botas, E Cascio, Fernando Hueso-Gonzalez, Moritz Rabe, and Thomas Bortfeld. "SU-F-601-2: Clinical translation of prompt gamma-ray spectroscopy for in vivo proton range verification". In: Medical Physics. Vol. 44. 6. Denver: Medical Physics, June 1, 2017, p. 2755.

[Wan+13] Ning Wang, Baldev Patyal, Abiel Ghebremedhin, and David Bush. "Evaluation and comparison of New 4DCT based strategies for proton treatment planning for lung tumors". In: *Radiation Oncology* 8.1 (Mar. 25, 2013), p. 73. ISSN: 1748-717X. DOI: 10.1186/1748-717X-8-73. URL: https://doi.org/10.1186/1748-717X-8-73 (visited on 08/13/2018).

[Wan+16] Hok Seum Wan Chan Tseung, Jiasen Ma, Cole R. Kreofsky, Daniel J. Ma, and Chris Beltran. "Clinically Applicable Monte Carlo–based Biological Dose Optimization for the Treatment of Head and Neck Cancers With Spot-Scanning Proton Therapy". In: *International Journal of Radiation Oncology*Biology*Physics* 95.5 (Aug. 1, 2016), pp. 1535–1543. ISSN: 0360-3016. DOI: 10.1016/j.ijrobp.2016.03.041. URL: http://www.sciencedirect.com/science/article/pii/S0360301616300311 (visited on 08/13/2018).

[Wat+16] Steven van de Water, Iris van Dam, Dennis R. Schaart, Abrahim Al-Mamgani, Ben J. M. Heijmen, and Mischa S. Hoogeman. "The price of robustness; impact of worst-case optimization on organ-at-risk dose and complication probability in intensity-modulated proton therapy for oropharyngeal cancer patients". In: *Radiotherapy and Oncology: Journal of the European Society for Therapeutic Radiology and Oncology* 120.1 (2016), pp. 56–62. ISSN: 1879-0887. DOI: 10.1016/j.radonc.2016.04.038.

[Wil46] Robert R. Wilson. "Radiological Use of Fast Protons". In: *Radiology* 47.5 (Nov. 1, 1946), pp. 487–491. ISSN: 0033-8419. DOI: 10.1148/47.5.487. URL: https://pubs.rsna.org/doi/10.1148/47.5.487 (visited on 08/06/2018).

[WLH13] Minna Wedenberg, Bengt K. Lind, and Björn Hårdemark. "A model for the relative biological effectiveness of protons: the tissue specific parameter α/β of photons is a predictor for the sensitivity to LET changes". In: *Acta Oncologica (Stockholm, Sweden)* 52.3 (Apr. 2013), pp. 580–588. ISSN: 1651-226X. DOI: 10.3109/0284186X.2012.705892.

[WO04] J. J. Wilkens and U. Oelfke. "A phenomenological model for the relative biological effectiveness in therapeutic proton beams". In: *Physics in Medicine and Biology* 49.13 (July 7, 2004), pp. 2811–2825. ISSN: 0031-9155.

[Yas+18] Keisuke Yasui et al. "Evaluation of dosimetric advantages of using patient-specific aperture system with intensity-modulated proton therapy for the shallow depth tumor". In: *Journal of Applied Clinical Medical Physics* 19.1 (Jan. 2018), pp. 132–137. ISSN: 1526-9914. DOI: 10.1002/acm2.12231.

[Yep+18] Pablo Yepes, Antony Adair, David Grosshans, Dragan Mirkovic, Falk Poenisch, Uwe Titt, Qianxia Wang, and Radhe Mohan. "Comparison of Monte Carlo and analytical dose computations for intensity modulated proton therapy". In: *Physics in Medicine & Biology* 63.4 (2018), p. 045003. ISSN: 0031-9155. DOI: 10.1088/1361-6560/aaa845. URL: http://stacks.iop.org/0031-9155/63/i=4/a=045003 (visited on 09/05/2018).

[Zha+13] Ye Zhang, A. Knopf, C. Tanner, D. Boye, and A. J. Lomax. "Deformable motion reconstruction for scanned proton beam therapy using on-line x-ray imaging". In: *Physics in Medicine and Biology* 58.24 (2013), p. 8621. ISSN: 0031-9155. DOI: 10.1088/0031-9155/58/24/8621. URL: http://stacks.iop.org/0031-9155/58/i=24/a=8621 (visited on 02/15/2016).

[Zha+14] Ye Zhang, A. Knopf, C. Tanner, and A. J. Lomax. "Online image guided tumour tracking with scanned proton beams: a comprehensive simulation study". In: *Physics in Medicine and Biology* 59.24 (2014), p. 7793. ISSN: 0031-9155. DOI: 10.1088/0031-9155/59/24/7793. URL: http://stacks.iop.org/0031-9155/59/i=24/a=7793 (visited on 02/15/2016).

[Zie+10] Anthony L. Zietman et al. "Randomized trial comparing conventional-dose with high-dose conformal radiation therapy in early-stage adenocarcinoma of the prostate: long-term results from proton radiation oncology group/american college of radiology 95-09". In: *Journal of Clinical Oncology: Official Journal of the American Society of Clinical Oncology* 28.7 (Mar. 1, 2010), pp. 1106–1111. ISSN: 1527-7755. DOI: 10.1200/JCO.2009.25.8475.

[Zie99] J. F. Ziegler. "Stopping of energetic light ions in elemental matter". In: *Journal of Applied Physics* 85.3 (Jan. 15, 1999), pp. 1249–1272. ISSN: 0021-8979. DOI: 10.1063/1.369844. URL: https://aip.scitation.org/doi/abs/10.1063/1.369844 (visited on 07/10/2018).

[ZS09] Hualiang Zhong and Jeffrey V. Siebers. "Monte Carlo dose mapping on deforming anatomy". In: *Physics in Medicine and Biology* 54.19 (Oct. 7, 2009), pp. 5815–5830. ISSN: 1361-6560. DOI: 10.1088/0031-9155/54/19/010.